Surf zone boundary layer and 2D large scale hydrodynamics

Léandro Suarez Atias

UNIVERSITÉ DE GRENOBLE

THÈSE

Pour obtenir le grade de

DOCTEUR DE L'UNIVERSITÉ DE GRENOBLE

Spécialité : **Mécanique des Fluides, énergétique et procédés**

Arrêté ministériel : 7 août 2006

Et de

DOCTEUR DE LA PONTIFICIA UNIVERSIDAD CATÓLICA DE CHILE

Spécialité : **Engineering sciences degree**

Présentée par

Léandro SUAREZ ATIAS

Thèse dirigée par **Rodrigo CIENFUEGOS** et
codirigée par **Eric BARTHÉLEMY**

préparée au sein du **Laboratoire LEGI**
dans **l'École Doctorale IMEP2**
et du **Departamento de Ingeniería Hidráulica y Ambiental** de la **Facultad de Ingeniería** de la **Pontificia Universidad Católica de Chile**.

La couche limite et l'hydrodynamique 2D à grande échelle de la zone de surf : une étude numérique.

Thèse soutenue publiquement le **vendredi 30 mai 2014**,
devant le jury composé de :

Dr. Cristian VIAL
Professeur Emérite, Pontificia Universidad Católica de Chile, Président
Dr. Philippe BONNETON
Directeur de recherche CNRS, UMR EPOC, Rapporteur
Dr Yarko NIÑO
Professeur titulaire, Universidad de Chile, Rapporteur
Dr Patricio CATALÁN
Professeur Auxiliaire, Universidad Técnica Federico Santa María, Examinateur

Dr Oscar LINK
Professeur associé, Universidad de Concepción, Examinateur
Dr Cristian ESCAURIAZA
Professeur assistant, Pontificia Universidad Católica de Chile, Examinateur
Dr Rodrigo CIENFUEGOS
Professeur associé, Pontificia Universidad Católica de Chile, Directeur de thèse
Dr Eric BARTHÉLEMY
Professeur des universités, Grenoble-INP, co-directeur de thèse

Remerciements

Ce travail de thèse arrive à sa fin, et je voudrais prendre le temps de remercier tout ceux grâce à qui cette thèse a pu voir le jour. Tout d'abord un grand merci à mes deux directeurs de thèse, Éric et Rodrigo qui m'ont aider et poussé à aller au bout de cette thèse. Leurs conseils, leurs expériences m'ont permis d'avancer et de réaliser tout le travail accompli durant ces 5 années et demies.

Je remercie également les membres du jury qui ont pris le temps de lire cette thèse, et de faire des retours pertinents sur le manuscrit.

Du côté grenoblois, je voudrais remercier les membres de l'équipe MEIGE, Hervé, Julien, Céline, Thibault, Jean-Marc, Francois-Xavier. Les discussions autour d'un café ont été très enrichissante et ont permis d'avancer sur le chemin de cette thèse.

Du côté chilien, je voudrais remercier l'équipe du DIHA, Maricarmen, Mauricio, Cuezco, Juan Carlos, Roberto, José et tous ceux que j'ai pu croiser durant ces années, qui ont permis par leurs échanges d'enrichier cette thèse.

Merci également à l'équipe IRD du Bénin qui m'a donné envie de commencer une thèse. Cette année passée en Afrique m'a ouvert de nouveaux horizons, et permis d'arriver où j'en suis actuellement.

Merci à la communauté franco-chilienne ainsi qu'aux amis, Sylvain et Bruno entre autres, que ce soit à Santiago ou à Grenoble, pour tous ces bons moments durant cette thèse.

Merci aussi à ma famille, qui m'a toujours soutenu dans mes choix et m'a souvent aidé durant ces années, malgré la distance.

Merci à Paulina pour son soutien inconditionnel, et à Gabriel qui a apporté beaucoup de joie dans notre monde.

La couche limite et l'hydrodynamique 2D à grande échelle de la zone de surf : une étude numérique.

Résumé :
Ce travail porte sur les processus hydrodynamiques en zone littorale. Deux principaux thèmes sont abordés. Le premier concerne la couche limite oscillante provoquée par l'interaction entre les vagues et le fond à l'approche des côtes. Le second traite de l'évolution de la circulation et la vorticité induite par la bathymétrie et/ou le forçage des vagues. Un modèle de couche limite turbulente a été élaboré et utilisé pour observer l'évolution de la couche limite oscillante sous l'effet de vagues non-linéaires, en s'appuyant sur une modélisation physique menée dans le canal à houle du LEGI. Les profils expérimentaux de vitesse et positions du fond fixe instantanés permettent de définir l'évolution des non-linéarités induites par les vagues au sein de la couche limite. Le modèle numérique couplé à une modélisation du mouvement du lit mobile est capable de reproduire l'évolution de ces non-linéarités, et explique que la diffusion verticale observée expérimentalement est principalement due au mouvement vertical du lit causé induit par les vagues. Pour l'étude de la circulation et de la vorticité en zone côtière, un modèle numérique 2D moyenné sur la verticale de type Shallow Water est validé avec les données d'une expérience menée dans le basin à vagues du Laboratoire Hydraulique de France (ARTELIA). La formation de courants sagittaux a été forcée par un front de vagues avec un déficit d'énergie au centre du bassin. Le modèle numérique est validé par des mesures de surface libre, de vitesse, ainsi que de circulation et vorticité. En utilisant ensuite l'équation de vorticité potentielle comme outil de diagnostic, avec un forçage monochromatique on prédit un équilibre entre la génération de vorticité et son advection par l'écoulement moyen.

Mots clés : circulation moyenne, vorticité, non-linéarités des vagues, dissipation, modèlisation numérique, couche limite turbulente, modélisation en eaux peu profondes.

Surf zone boundary layer and 2D large scale hydrodynamics

Abstract:
This work is about the hydrodynamic processes in the nearshore zone. They are of great importance to estimate the overall dynamics of the coastal zone. This thesis is divided into two main parts; the first one investigates the coastal bottom boundary layer induced by the interaction of the waves and the bottom when approaching the coast; the second one is about the evolution of the mean circulation and vorticity induced by an inhomogeneity in the bathymetry or the wave forcing. A turbulent boundary layer numerical model has been developed and used to simulate the evolution of the oscillating boundary layers under non-linear waves, of a flume experiment at the Laboratoire des Ecoulements Géophysiques et Industriels (LEGI) in Grenoble, France. The experimental instantaneous velocity profiles and still bed positions, allow defining the non-linear velocity distributions induced by the waves within the boundary layer. The numerical model coupled with a ad-hoc modeling of the mobile bed motion is able to reproduce the vertical distribution of the non-linearities, and also indicates that the vertical diffusion observed experimentally is mainly caused by the mobile bed motion induced by the passing waves. A 2D depth-averaged nonlinear shallow water numerical model is used to study the circulation and vorticity in the nearshore zone. This model is validated on a mobile bed experiment in the wave basin of the Laboratoire Hydraulique de France (ARTELIA). The formation of rip currents is forced by a damped wave forcing in the middle of the wave basin. The numerical model is validated with free surface and velocity measurements, and by the circulation and vorticity. Using the potential vorticity balance as a diagnosis tool and with a monochromatic wave forcing, an equilibrium between the vorticity generation and advection is observed in the nearshore zone.

Key words : mean circulation, vorticity, wave non-linearities, dissipation, numerical modeling, turbulent boundary layer, shallow-water modeling.

Capa límite e hidrodinámica 2D a gran escala en la zona de surf: un estudio numérico

Abstract:
Este trabajo trata de los procesos hidrodinámicos en la zona litoral, de grande importancia para la dinámica global del flujo costero. Dos temas principales son estudiados. El primero trata de la capa límite oscilante provocada por la interacción entre el oleaje y el fondo al acercarse a la costa. El segundo tema trata de la evolución de la circulación y la vorticidad inducida por la batimetría y/o el oleaje. Un modelo de capa límite turbulenta ha sido elaborado y validado para analizar la evolución de la capa límite oscilante bajo la influencia de oleaje no-lineal, apoyándose en una modelación física, realizada en el canal de olas del LEGI. Los perfiles experimentales instantáneos de velocidad y posición del fondo fijo, permiten definir la evolución de las no-linealidades inducidas por las olas dentro de la capa límite. El modelo numérico acoplado a una modelación del movimiento del fondo móvil es capaz de reproducir la evolución de estas no-linealidades, y explica también que la difusión vertical observada experimentalmente es principalmente debida al movimiento vertical del fondo inducido por el oleaje. El estudio de la circulación y de la vorticidad en zonas costeras se hace mediante un modelo numérico 2D promediado en la vertical de tipo Shallow Water que es validado con los datos de una experiencia llevada a cabo en la piscina de olas del Laboratoire Hydraulique de France (ARTELIA). La formación de corrientes rip se realiza a través de frentes de olas con un déficit de energía en el medio de la piscina. El modelo numérico es validado con mediciones de superficie libre, de velocidades, y de circulación y vorticidad. Utilizando la ecuación de vortcidad potencial como herramienta de diagnóstico, con un oleaje monocromático se predice un equilibrio entre la generación de vorticidad y su advección por las corrientes.

Palabras Claves: circulación promedio, vorticidad, no-linealidad del oleaje, disipación, modelación numérica, capa límite turbulenta, modelación en aguas someras.

Contents

List of Figures

List of Tables

Chapter 1

Introduction

1.1 General Context

The coast represents the interface between the land and the sea, with great importance as 44 % of the world population lives within 150 km of the coast, and 8 of the 10 most populated cities are found near the coast, according to the UN atlas of the Oceans (`http://www.oceansatlas.org/`) . In a context of global commerce, most of the products are exchanged from ports to ports, producing a natural migration of population toward coastal areas.

As the interest for coastal areas keeps growing, also sustained by increasing tourism activities, the stress on the coastal habitat is also higher. This produces changes in the habitat and ecosystems that are of great importance, and calls for an integrated management of these strategic zones. Another matter that has to be acknowledged is the pollution of the coastal areas, as an increasing amount of waste water is discharged to the coast, due to the coastal areas being more populated, leading to more and more ecological issues, like eutrophication of the littoral zone, which can produce population health hazard.

Another important issue concerning the coastal areas is the global warming, that seems to induce a constant water level rise in the oceans. While this raise of the water level is mild, if we compare it to the total volume of water mass in the planet, the consequences in the long term are still uncertain. A sustained raise in the water level could lead to coastal erosion in some areas, lowland flooding or ground water salinisation [Paskoff, 2004]. The erosion in the coast can be affected by the amount of sediment available, but also by hydrodynamical and climatic factors, such as the water level, the incoming waves and the nearshore circulation associated to it. In Chile though, the coastal erosion is not the main concern [Del Canto et Paskoff, 1983

; Martínez et Salinas, 2009].

Another concern for the Chilean beaches concern tsunamis generated by earthquakes, the last one in February 2010 [Fritz *et al.*, 2011]. Moreover the seismic displacement produced subsidence and uplift in some coastal areas leading to a morphological response influenced by the local hydro-climatic forcing and land level change [Villagran *et al.*, 2013]. The coastal ecosystems response to an earthquake is also very dependent on the local land-level changes [Jaramillo *et al.*, 2012].

Therefore, the coastal management will take a growing importance for countries with coastal areas, and the knowledge of the physical processes that occur near the coast will be important to take wise decisions and to sustain the wealth that can be found in these areas.

One of the main issues concerning the understanding of the physical processes in the coastal areas is the widespread range of space and time scales involved in these processes (Figure 1.1).

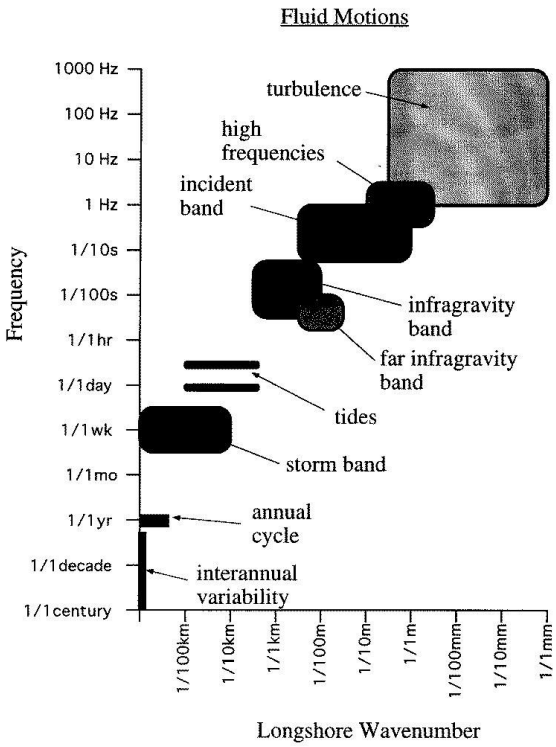

Figure 1.1 – Space-time scales of morphology in the nearshore [Thornton *et al.*, 2000].

As it is difficult to cover all the time and space spectra, in this study we restrain ourselves to some space and time scales processes in the nearshore zone. The sediment transport processes are a product of the nearshore hydrodynamics, hence it is necessary

to get a precise understanding of the hydrodynamics. In our case, we study wave propagation and related processes at two space-time scales:

- at a time scale of wave period and a length scale of centimetres, we study the coastal bottom boundary layer.

- at a time-scale of minutes to hours and a length scale of tens of meters, we study the circulation and vorticity dynamics in the nearshore zone.

1.2 Main concepts

1.2.1 The coastal bottom boundary layer

The knowledge of the coastal bottom boundary layer is essential for the estimation of the sediment transport induced by the bottom shear stress. When waves approach the coast, they feel the influence of the bottom as they propagate, becoming increasingly non-linear. The interactions between the waves and the bottom occur within the turbulent boundary layer, which is why its study represents a mean to understand the evolution of these non-linearities near the coast.

The longshore sediment transport is relatively well understood, being forced by the angle between the wave forcing and the shoreline, producing longshore currents parallel to the shoreline which are able to transport sediments.

The cross-shore sediment transport, normal to the shoreline, is more complicated to estimate due to the sloping bed, the currents, the wave non-linearities, the turbulence induced by wave braking, the presence of bed forms, etc. Several experiments have shown an influence of the wave non-linearities such as velocity and acceleration skewed waves, on the net sediment transport produced by waves leading to an onshore or offshore sand bar migration depending on the waves non-linearities [Dibajnia et Watanabe, 1992 ; Dohmen-Janssen *et al.*, 2002 ; Hsu et Hanes, 2004 ; Grasso *et al.*, 2011 ; King, 1991 ; Elgar *et al.*, 2001 ; Ruessink *et al.*, 2011].

1.2.2 Vorticity and circulation in the nearshore zone

To estimate the sediment transport in the nearshore zone, it is also important to know the evolution of the mean currents produced by either a differential wave breaking or an inhomogeneous bathymetry. These spatio-temporal non-uniformities in wave breaking induce dissipation gradients, that generates currents. These wave-generated currents

produce vorticity, that acts at a much lower time-scale than the waves. These currents are relevant in terms of mixing, dispersion and also for sediment transport.

Among the types of generated circulation, rip-currents are offshore oriented jets that originate in the surf zone (Figure 1.2). These currents constitute a hazard for swimmers as they can be ejected seaward, far from the coast rapidly, and they represent one of the main mechanisms responsible for the mixing and circulation in the surf zone. These currents result from the vorticity generated by the differential wave breaking, generating eddies that travel longshore until two of these eddies meet, creating a dipole that generates these rip currents [Peregrine, 1998].

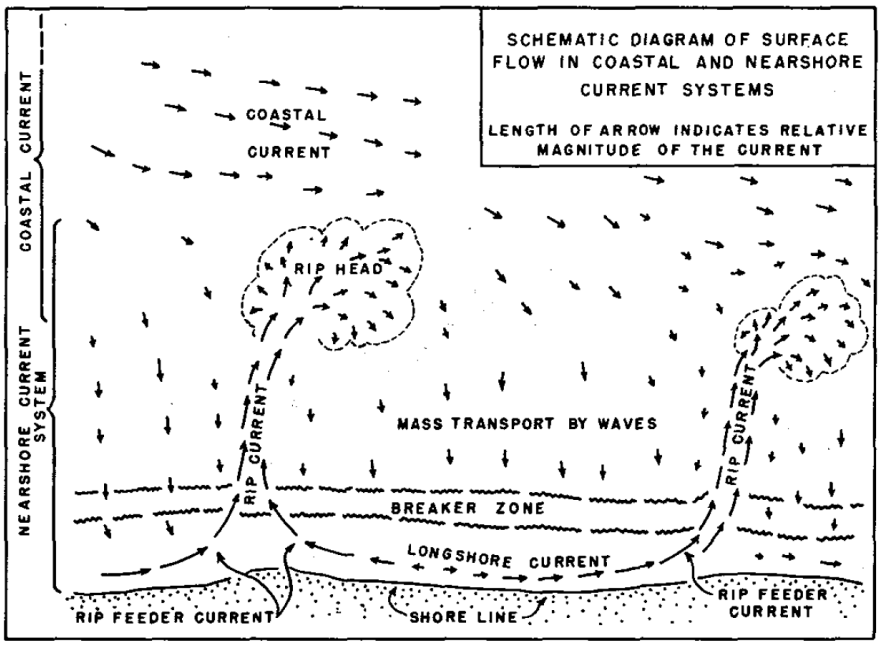

Figure 1.2 – Nearshore current system, from Shepard et Inman [1950]

In nature, these rip currents are always evolving, as natural wave conditions do, and the seabed is also changing due to sediment transport. Hence, there is a feedback between the wave forcing, the beach bathymetry and rip vorticity dynamics, which has not been completely understood so far.

1.3 Objectives

The main objective of this thesis consist in getting an in-depth understanding of the nearshore hydrodynamics, in terms of cross-shore wave propagation and generated circulation by the wave breaking. To this end, the specific objectives are:

- To investigate the mechanisms involved in a turbulent boundary layer under non-linear waves, with a mobile bed. Recent experiments from Berni *et al.* [2013] on a wave flume, under a mobile bed, allowed to observe the evolution of the coastal bottom boundary layer under non-linear waves. Using a $k-\omega$ boundary layer numerical model [Wilcox, 2006], we intend to retrieve some of the main characteristics of the experiment and understand the mechanisms involved in the vertical distribution of these non-linearities.

- to understand the evolution of the circulation and vorticity under a shore-normal wave forcing, on an uneven bathymetry using a 2D depth-averaged Non-linear Shallow Water numerical model [Marche *et al.*, 2007 ; Guerra *et al.*, 2014]. To that purpose, the numerical model is validated using data obtained during the wave basin experiment in ARTELIA (Grenoble) supervised by H. Michallet in the framework of the MODLIT project coordinated by P. Bonneton. These experiment consisted of wave basin with a mobile bed, where a rip current was generated by an alongshore non-uniformity in the wave forcing [Michallet *et al.*, 2010 2013].

1.4 Thesis outline

Chapter 2 presents the numerical model used to investigate the coastal bottom boundary layer. It consist in a 1-D vertical turbulent boundary layer $k-\omega$ model [Wilcox, 2006], which is validated for oscillatory flows.

Chapter 3 presents the results obtained with the $k-\omega$ numerical model compared to experimental measurements [Berni *et al.*, 2013], concerning non-linear waves on a mobile bed, which provide velocity profiles and bed position in a coupled way. These data suggest a transformation within the boundary layer, with a non-dimensional skewness increasing and a non-dimensional asymmetry diminishing as we approach the bottom. Using the $k-\omega$ numerical model, we get a better representation of the non-linear velocity profile distribution inside the turbulent boundary layer. The numerical model is able to determine the velocity within the boundary layer on a fixed bed; by including the bed mobility and coupling it with the $k-\omega$ model, we are able to improve the numerical representation of observed experimental results. The latter is an indication that the bed mobility is responsible for a vertical diffusion within the boundary layer. The numerical model also reproduces the linear relationship between the non-linearities outside the boundary layer and near the bed observed in the experiment.

Chapter 4 presents the 2D depth-averaged numerical model used to obtain the

circulation in the nearshore zone [Marche *et al.*, 2007 ; Guerra *et al.*, 2014]. This numerical model is then validated in terms of free surface, velocities, circulation and vorticity using experimental data [Michallet *et al.*, 2010 2013].

Chapter 5 presents a study of the evolution of vorticity and circulation on an uneven bathymetry that has been validated in chapter 4. Using a JONSWAP wave forcing, representative of the natural state of the sea, as well as monochromatic and bichromatic wave forcing, and using the potential vorticity balance as a diagnostic tool, we aim at understanding the influence of the friction, the wave period, and the wave grouping on the vorticity generation and decay at the nearshore zone.

Finally, Chapter 6 presents the conclusions of this work, along with some perspectives.

Chapter 2

Numerical modelling of oscillatory turbulent boundary layers

2.1 Introduction

2.1.1 Physical processes

Sediment transport in the nearshore is of great importance, as it determines processes such as erosion or accretion on a beach. It is caused by the waves and current, that forces the bed and initiate the sediment transport. This process mainly occurs in the coastal bottom boundary layer, a region usually extending up to 10 cm above the seabed, where friction is predominant. The knowledge of this region is therefore one of the main aspects of the sediment transport, as the non-linear processes occurring in this region can affect the direction of the sediment transport, seaward or shoreward. The study of turbulence in the boundary layer is then a key aspect to understand the processes that take place in the nearshore. We first need to know what is turbulence, then study the different turbulence models that exists, and then determine the use of these turbulence models for coastal bottom boundary layers.

Although the characteristics of turbulence are well known, there is not a clear definition of it, a regime flow where the motion is unsteady and complex, with random changes in velocity or pressure, highly diffusive and dissipative. One of the main characteristic of turbulence is the energy cascade phenomenon. Richardson defined this in 1922 by the following sentence: "Big whorls have little whorls, which feed on their velocity; And little whorls have lesser whorls, And so on to viscosity". This energy transfer keeps on until the eddies are so small that they can only dissipate into heat through molecular viscosity.

Kolmogorov [1941] universal equilibrium theory states that the smallest scales of the eddies does not depend on the larger eddies or the mean flow, as time scales between those two phenomena have different orders of magnitude. Therefore the rate at which the smaller eddies receive energy from the larger eddies should be equal to the rate at which the smallest eddies dissipate energy to heat, and thus at the smallest scale the motion only depend on the rate at which eddies dissipate energy to smaller eddies, $\epsilon = -dk/dt$, k being the kinetic energy per unit mass of the fluctuating turbulent velocity, and the kinematic viscosity, ν .

For very large Reynolds number, he assumed that there is a separation of scales that implies that for some range in eddies size, the energy transferred by inertial effects is predominant. We define the energy spectral density $E(\kappa_e)$ related to the turbulence kinetic energy k:

$$k = \int_0^\infty E(\kappa_e) d\kappa_e \tag{2.1}$$

κ_e being the wavenumber. Using the hypotheses of scale separation, and through dimensional analysis, we obtain an expression for $E(\kappa_e)$ for a certain range:

$$E(\kappa_e) = C_\kappa \epsilon^{2/3} \kappa_e^{-5/3}, \qquad \frac{1}{l} \ll \kappa_e \ll \frac{1}{\eta} \tag{2.2}$$

where C_κ is the Kolmogorov constant, l is the turbulence length scale, and η the Kolmogorov length scale, at which viscosity dominates. The range for κ_e defined in (2.2) is identified as the inertial subrange, i.e. where the inertial transfer of energy dominates. This -5/3 slope can be seen in Figure 2.1.

To obtain the efforts sustained by a turbulent flow over a solid boundary, there is a need to know the interaction between the two. The mean velocity profile near a solid boundary can be determined by the law of the wall [Von Karman, 1930]. This law states that there is a region near the solid boundary where the streamwise velocity has a logarithmic profile.

Let the surface shear stress be τ_w, the friction velocity of the flow near the solid boundary u_τ is then defined as :

$$u_\tau = \sqrt{\frac{\tau_w}{\rho}} \tag{2.3}$$

The law of the wall describe the mean crosswise velocity distribution close to the boundary:

$$\frac{U}{u_\tau} = \frac{1}{\kappa} \ln \frac{z}{z_0} \tag{2.4}$$

where $\kappa \approx 0.41$ is the von Kàrmàn constant, z is the distance from the wall and z_0 is the distance from the boundary at which the velocity is zero. z_0 depends on the

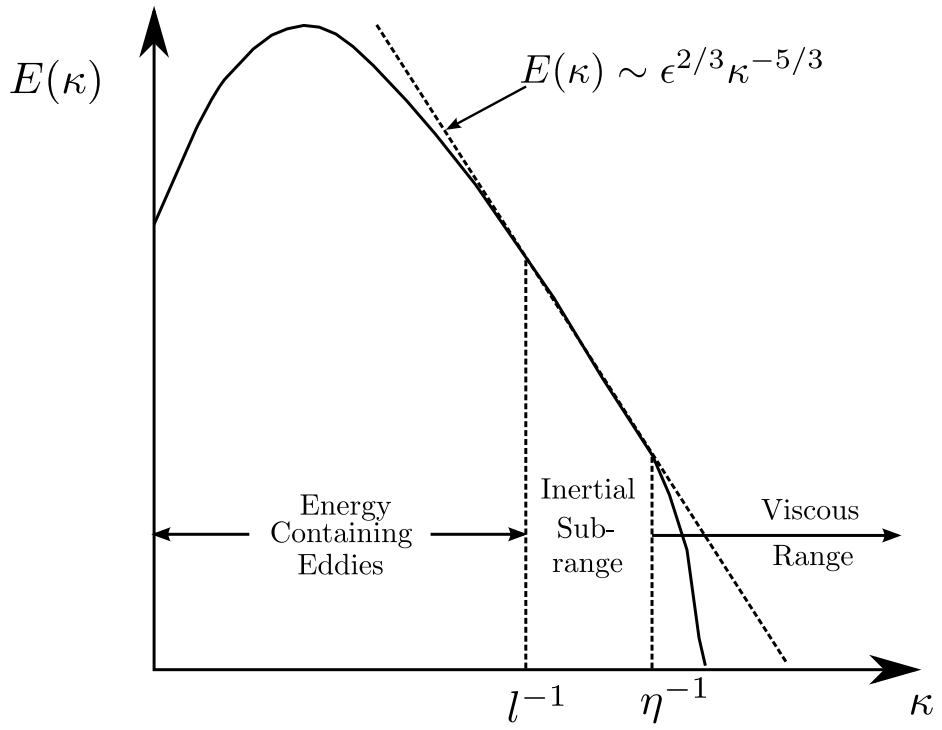

Figure 2.1 – Energy spectrum of a turbulent flow

laminar sublayer thickness δ_v and the characteristic roughness length-scale k_s, found in the boundary Reynolds number $Re_w = u_\tau k_s/\nu$.

- if $k_s < \delta_v$ ($Re_w < 3$) the flow is considered hydraulically smooth, and z_0 is defined as:

$$z_0 = \frac{\nu}{9u_\tau} \tag{2.5}$$

- if $k_s > \delta_v$ ($Re_w > 100$) the flow is considered hydraulically rough, and z_0 is defined as:

$$z_0 = \frac{k_s}{30} \tag{2.6}$$

- if $k_s \approx \delta_v$, the flow is considered transitional.

A velocity profile of a smooth boundary layer under a turbulent flow is shown in Figure 2.2, where the dimensionless velocity $u^+ = U/u_\tau$, with U the mean velocity streamwise component, is plotted as a function of the dimensionless distance to the boundary $z^+ = u_\tau z/\nu$. We can distinguish three different regions in the velocity profile near the boundary layer, the viscous sublayer where $u^+ = z^+$, the log layer where the velocity complies the law of the wall, and the velocity defect layer where the viscosity can be neglected.

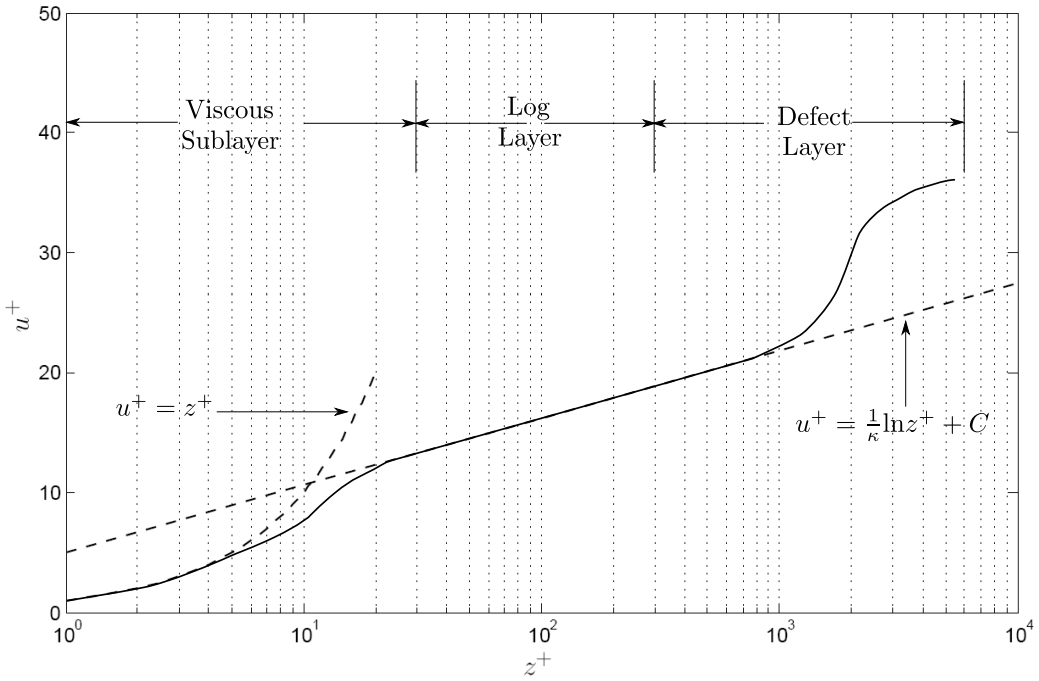

Figure 2.2 – Typical velocity profile of a turbulent flow. The constant C depends on the roughness characteristics.

2.1.2 Turbulence modelling

In most practical situations turbulent flows are very complex. The numerical simulations of flows are required to obtain the characteristics of the flows. One of the most used model turbulence is the Reynolds Averaged Navier-Stokes (RANS) equations. The Reynolds time-averaging consists of splitting the instantaneous variables, for example the velocity $u(x,t)$, in its mean $U(x)$ and its fluctuating part $u'(x,t)$:

$$u(x,t) = U(x) + u'(x,t) \tag{2.7}$$

The mean part $U(x)$ is defined as:

$$U(x) = \frac{1}{T}\int_t^{t+T} u(x,t)dt, \qquad T_1 \ll T \ll T_2 \tag{2.8}$$

where T is the time period at which the averaging is done, T_1 is the time scale of the turbulent fluctuations, and T_2 is the time scale of the slow variations in the flow.

Using this method, we can obtain the RANS:

$$\frac{\partial U_i}{\partial x_i} = 0 \tag{2.9}$$

$$\rho\frac{\partial U_i}{\partial t} + \rho U_j\frac{\partial U_i}{\partial x_j} = -\frac{\partial P}{\partial x_i} + \frac{\partial}{\partial x_j}\left(2\mu S_{ji} - \overline{u_j' u_i'}\right) \tag{2.10}$$

with P the mean pressure, μ the molecular viscosity, and S_{ij} the strain-rate tensor, defined as:

$$\frac{1}{2}\left(\frac{\partial U_i}{\partial x_j} + \frac{\partial U_j}{\partial x_i}\right) \tag{2.11}$$

The fundamental problem of these equations is that there is no simple way to determine the correlation term $\overline{u_j' u_i'}$, defined as the specific Reynolds stress tensor τ_{ij}, and this where the turbulence model is used.

The turbulence models can be separated in four distinct categories:

- the algebraic model or zero-equation model of turbulence, based on the mixing length hypothesis,
- the one-equation models of turbulence, which introduce a partial differential equation approximating the exact equation for the turbulent kinetic energy k,
- the two-equation models of turbulence, which use an additional differential equation, such as the dissipation rate ϵ or the specific rate of dissipation of energy in unit volume and time ω,
- the Stress-Transport models, using a differential equation for the Reynolds-stress tensors.

For additional information on the different types of turbulence models, an extensive overview can be found in Wilcox [2006].

2.1.3 Turbulence modelling for oscillatory flows

The laminar boundary layer for oscillatory flow is found from the linear equation of motion:

$$\rho\frac{\partial}{\partial t}(U - U_\infty) = \frac{\partial \tau}{\partial z} \tag{2.12}$$

where U is the mean part of the horizontal velocity, U_∞ is the free-stream velocity and $\tau(z,t) = \rho\nu\frac{\partial U}{\partial z}$ is the viscous shear stress. By assuming a complex representation for U_∞:

$$U_\infty(t) = A\sigma e^{i\sigma t} \tag{2.13}$$

with A the water particle semi excursion, $\sigma = 2\pi/T$ the radian frequency, T the wave period. The wave formulation for the bed shear stress $\tau(0,t)$ can be deduced ([Nielsen, 1992]):

$$\tau(0,t) = \rho\sqrt{\sigma\nu}A\sigma e^{i(\sigma t+\pi/4)} \tag{2.14}$$

This indicates that the bed shear stress in smooth, laminar oscillatory flow leads the free-stream velocity by $\pi/4$ radians or 45 degrees.

For oscillatory flows, $\delta = \sqrt{\frac{2\nu}{\sigma}}$ is the boundary layer thickness, also known as the Stokes length, which allows to define a Reynolds number for oscillatory flows $Re_\delta = \frac{U\delta}{\nu}$.

When the Reynolds number increases, during one period the velocity covers a wide range of values. This lead to a transition from laminar to turbulent, as well as a relaminarization during one period. The pressure gradient also changes in one period, going from favourable to adverse, and inversely.

As stated by Wilcox [2006], $k-\epsilon$ models are inadequate for flows with adverse pressure gradient, which is not the case for the $k-\omega$ models. This is confirmed by Sana et Tanaka [2000], which compares five Low Reynolds number $k-\epsilon$ models on periodic flows. Although the Low Reynolds Number modifications provide better predictions for the transition, none of the models succeeded in capturing the overall dynamics of the oscillatory boundary layer.

The high Reynolds number version is not able to predict the transition from laminar to turbulent regime. We then need to use a Low Reynolds Number version of the turbulent model to correctly reproduce this transition. The main change of the Low Reynolds number version, is that some closure coefficients of the turbulence model equations, which are constant for fully turbulent flows, now depend on the turbulence Reynolds number Re_T, defined as:

$$Re_T = \frac{k}{\omega\nu} \tag{2.15}$$

As $Re_T \to \infty$, the closure coefficients tend to their fully turbulent values.

The two-equations RANS models of turbulence have been used to observe the evolution of the turbulent bottom boundary layer under oscillatory flows, and its relation with the sediment transport. Suntoyo et Tanaka [2009] studied the influence of the bed roughness under asymmetric waves, showing that the roughness influenced mostly the inner boundary layer, by increasing the turbulence kinetic energy k and the bottom shear stress, and decreasing the mean velocity distribution. The wave non-linearity also has an influence on the bottom shear stress. Recently, Kranenburg *et al.* [2012] observed the influence of the streaming (or net current) on the coastal bottom bound-

ary layer using a $k-\epsilon$ model which includes advection terms, showing the influence of the relative water depth and relative bed roughness on the streaming velocity and the shear stress. Moreover, by adding a sediment concentration to its turbulence closure model, he determined the importance of the progressive wave streaming, but also of the sediment advection in the estimation of the sediment transport rate [Kranenburg *et al.*, 2013]. [Fuhrman *et al.*, 2013] uses a $k-\omega$ turbulence closure model coupled with bed and suspended load transport to study the sheet flow sediment transport processes. The boundary layer streaming due to the convective terms causes an increase of onshore sediment transport in the case of medium sand, and in the case of fine sand they could reverse the the direction of the net transport.

2.2 The $k-\omega$ turbulence model

2.2.1 Governing equations

For clarity purposes, from now on we refer to u, k and ω instead of U, K and Ω as the Reynolds averaged values of the instantaneous velocity, the turbulence kinetic energy and the specific dissipation rate.

Our study focus on the $k-\omega$ model of Wilcox [2006]. This set of equation contains three principal equations, one for the velocity u, one for the turbulence kinetic energy k, and one for the specific dissipation rate ω.

Using the Boussinesq approximation, we have the Reynolds stress tensor τ_{ij}:

$$\tau_{ij} = 2\nu_T S_{ij} - \frac{2}{3}k\delta_{ij} \tag{2.16}$$

where ν_T is defined as the turbulence eddy viscosity and δ_{ij} is the Kronecker delta.

If we sum the three normal Reynolds stresses and multiply by 1/2, we have the turbulence kinetic energy, which we denote by the symbol k. Thus, by definition,

$$k = \frac{1}{2}\left(\overline{u'^2} + \overline{v'^2} + \overline{w'^2}\right) = \frac{1}{2}\overline{u_i' u_i'} \tag{2.17}$$

k represents the kinetic energy of the turbulent fluctuations per unit mass, also called the specific turbulence kinetic energy. We can derive an equation for k using the Reynolds-stress equation.

Concerning ω, Kolmogorov [1942] defined it as "the rate of dissipation of energy in unit volume and time". The dimension of ω is $(\text{time})^{-1}$, and its reciprocal represents the time scale on which dissipation of turbulence energy occurs. There exist several

interpretations of this quantity. Saffman [1970] related ω to the vorticity of the "energy containing eddies", and k to the kinetic energy of the motion induced by this vorticity. Others define ω as the RMS fluctuating vorticity, and ω^2 is twice the enstrophy [Launder et Spalding, 1972], or as the ratio of ϵ to k [Wilcox et Rubesin, 1980].

Although the Wilcox [2006] formulation is the version we use, we implemented several versions of the $k-\omega$ model to obtain a better accuracy in the validations of the model. We assume furthermore that the mass density ρ is constant.

For all these models, we have three main equations, one for the horizontal velocity u, one for the turbulent kinetic energy k, one for the specific dissipation rate ω.

The first equation corresponds to the conservation of momentum:

$$\frac{\partial u_i}{\partial t} + u_j \frac{\partial u_i}{\partial x_j} = -\frac{1}{\rho}\frac{\partial p}{\partial x_i} + \frac{\partial}{\partial x_j}(2\nu S_{ji} + \tau_{ji}) \tag{2.18}$$

The second equation corresponds to the turbulent kinetic energy k:

$$\frac{\partial k}{\partial t} + u_j \frac{\partial k}{\partial x_j} = \tau_{ij}\frac{\partial u_i}{\partial x_j} - \beta^* k\omega + \frac{\partial}{\partial x_j}\left[\left(\nu + \sigma_k \frac{k}{\omega}\right)\frac{\partial k}{\partial x_j}\right] \tag{2.19}$$

The third equation corresponds to the specific dissipation rate ω, and is different according to various versions:

$$\begin{cases} \dfrac{\partial \omega}{\partial t} + u_j \dfrac{\partial \omega}{\partial x_j} = \alpha \dfrac{\omega}{k}\tau_{ij}\dfrac{\partial u_i}{\partial x_j} - \beta\omega^2 + \dfrac{\partial}{\partial x_j}\left[\left(\nu + \sigma_\omega \dfrac{k}{\omega}\right)\dfrac{\partial \omega}{\partial x_j}\right] \\ \text{[Wilcox, 1998 ; Guizien } \textit{et al.}\text{, 2003]} \\ \dfrac{\partial \omega}{\partial t} + u_j \dfrac{\partial \omega}{\partial x_j} = \alpha \dfrac{\omega}{k}\tau_{ij}\dfrac{\partial u_i}{\partial x_j} - \beta\omega^2 + \dfrac{\partial}{\partial x_j}\left[\left(\nu + \sigma_\omega \dfrac{k}{\omega}\right)\dfrac{\partial \omega}{\partial x_j}\right] + \dfrac{\sigma_d}{\omega}\dfrac{\partial k}{\partial x_j}\dfrac{\partial \omega}{\partial x_j} \\ \text{[Wilcox, 2006]} \end{cases} \tag{2.20}$$

The kinematic eddy viscosity, present in the Reynolds stress tensor, reads:

$$\begin{cases} \nu_T = \alpha^* \dfrac{k}{\omega} \\ \text{[Wilcox, 1998 ; Guizien } \textit{et al.}\text{, 2003]} \\ \nu_T = \dfrac{k}{\tilde{\omega}}, \qquad \tilde{\omega} = \max\left[\omega, C_{lim}\sqrt{\dfrac{2S_{ij}S_{ij}}{\beta^*}}\right], \qquad C_{lim} = \dfrac{7}{8} \\ \text{[Wilcox, 2006]} \end{cases} \tag{2.21}$$

The mean rotation tensor Ω_{ij} is defined as:

$$\Omega_{ij} = \frac{1}{2}\left(\frac{\partial u_i}{\partial x_j} - \frac{\partial u_i}{\partial x_j}\right) \tag{2.22}$$

	Wilcox 1998	Wilcox 2006
σ_k	0.5	0.6
σ_ω	0.5	0.5
β_0^*	0.09	-
β^*	$\beta_0^* f_{\beta^*}$	0.09
f_{β^*}	$\begin{cases} 1 \text{ for } (\chi_k \leq 0) \\ \frac{1+680\chi_k^2}{1+400\chi_k^2} \text{ for } (\chi_k > 0) \end{cases}$	-
χ_k	$\frac{1}{\omega^3}\frac{\partial k}{\partial x_j}\frac{\partial \omega}{\partial x_j}$	-
α	13/25	13/25
β	$\beta_0 f_\beta$	$\beta_0 f_\beta$
β_0	9/125	0.0708
f_β	$\frac{1+70\chi_\omega}{1+80\chi_\omega}$	$\frac{1+85\chi_\omega}{1+100\chi_\omega}$
χ_ω	$\left\lvert\frac{\Omega_{ij}\Omega_{jk}S_{ki}}{(\beta_0^*\omega)^3}\right\rvert$	$\left\lvert\frac{\Omega_{ij}\Omega_{jk}\hat{S}_{ki}}{(\beta^*\omega)^3}\right\rvert$
$\hat{S}_{ki}$	-	$S_{ki} - \frac{1}{2}\frac{\partial u_m}{\partial x_m}\delta_{ki}$
σ_d	-	$\begin{cases} 0 \text{ , for } (\frac{\partial k}{\partial x_j}\frac{\partial \omega}{\partial x_j} \leq 0) \\ \frac{1}{8} \text{ for } (\frac{\partial k}{\partial x_j}\frac{\partial \omega}{\partial x_j} > 0) \end{cases}$

Table 2.1 – Closure coefficients and auxiliary relations.

The main differences in the closure coefficients between the versions can be seen in Table 2.1. The Wilcox [2006] formulation introduces a "cross-diffusion term" and a "stress-limiter" modification that makes the eddy viscosity depend on the ratio of turbulence-energy production to turbulence-energy dissipation.

The cross-diffusion term has been added to remove the boundary-condition sensitivity to the free-stream value of ω, by reducing the net production of k and thus the spreading rate for free shear flows. This term becomes zero when approaching the solid boundary, as k increases and ω decreases, and performs well in predicting effects of pressure gradient on attached boundary layers. [Kok, 2000 ; Wilcox, 2008].

The stress-limiter introduced in the eddy viscosity, limits its magnitude when the turbulence energy production exceeds the dissipation, and is more useful for supersonic and hypersonic separated flows [Wilcox, 2008], which is not our case.

2.2.2 Unidimensional version of the $k-\omega$ model

From now on, we assume very large horizontal characteristic flow scales, and use from now on a 1D vertical framework for the $k-\omega$ model. Therefore, the following hypotheses are used:

- the transverse velocity v and vertical velocity w are not taken into account: $v = w = 0$. Only in the case where we incorporate the advection terms, we suppose that there exist a vertical velocity w, but it depends on u, and is not calculated by an equation.
- there is no variation in the x direction and the y direction: $\frac{\partial}{\partial x} = \frac{\partial}{\partial y} = 0$. In the case of the advection terms, the gradients $\frac{\partial}{\partial x}$ are non negligible, and we estimate them using a temporal derivative.
- the mass density is considered constant: $\rho = cte$

The only non-zero terms of the Strain rate tensor S_{ij} and Reynolds stress tensor τ_{ij} are:

$$S_{xz} = \frac{1}{2}\frac{\partial u}{\partial z} \tag{2.23}$$

$$\tau_{xz} = \nu_t \frac{\partial u}{\partial z} \tag{2.24}$$

For the Wilcox [2006] formulation, the stress limiter is reduced to:

$$\tilde{\omega} = \max\left[\omega, C_{lim}\sqrt{\frac{\alpha^*}{2\beta^*}}\left|\frac{\partial u}{\partial z}\right|\right] \tag{2.25}$$

	Wilcox 2006 LRN	Wilcox 1998 LRN	Guizien 2003 LRN
σ_k	0.6	0.5	0.375
σ_ω	0.5	0.5	0.8
β^*	$\frac{9}{100}\frac{100\beta_0/27+(Re_T/R_\beta)^4}{1+(Re_T/R_\beta)^4}$	$\frac{9}{100}\frac{4/15+(Re_T/R_\beta)^4}{1+(Re_T/R_\beta)^4}$	
α	$\frac{13}{25}\frac{\alpha_0+Re_T/R_\omega}{1+Re_T/R_\omega}(\alpha^*)^{-1}$		
α^*	$\frac{\alpha_0^*+Re_T/R_k}{1+Re_T/R_k}$		
Re_T	$\frac{k}{\nu\omega}$		
R_K	6	6	20
R_β	8	8	27
R_ω	2.61	2.95	2.95
α_0	1/9		
α_0^*	$\beta_0/3$		
β_0	0.0708		
ν_t	$\alpha^*\frac{k}{\omega}$		
$\tilde{\omega}$	$max\left[\omega, C_{lim}\sqrt{\frac{2S_{ij}S_{ij}}{\beta_0^*/\alpha^*}}\right]$	-	-
$\left(\nu+\sigma_k\frac{k}{\omega}\right)$	$\left(\nu+\sigma_k\alpha^*\frac{k}{\omega}\right)$		
$\left(\nu+\sigma_\omega\frac{k}{\omega}\right)$	$\left(\nu+\sigma_\omega\alpha^*\frac{k}{\omega}\right)$		

Table 2.2 – Closure coefficients and auxiliary relations

The horizontal velocity $u(z,t)$, the turbulence kinetic energy $k(z,t)$ and the specific dissipation rate $\omega(z,t)$, are described in a 1D framework:

$$\frac{\partial u}{\partial t} = -\frac{1}{\rho}\frac{\partial p}{\partial x} + \frac{\partial}{\partial z}\left((\nu + \nu_T)\frac{\partial u}{\partial z}\right) \tag{2.26}$$

The second equation corresponds to the turbulent kinetic energy k:

$$\frac{\partial k}{\partial t} = \nu_T \left(\frac{\partial u}{\partial z}\right)^2 - \beta^* k\omega + \frac{\partial}{\partial z}\left[\left(\nu + \sigma_k \alpha^* \frac{k}{\omega}\right)\frac{\partial k}{\partial z}\right] \tag{2.27}$$

Notice no vertical advection of k is present, turbulence only diffuses vertically.

The third equation corresponds to the specific dissipation rate w, and is different in the versions:

$$\begin{cases} \dfrac{\partial \omega}{\partial t} = \dfrac{\alpha\omega}{k}\nu_t \left(\dfrac{\partial u}{\partial z}\right)^2 - \beta\omega^2 + \dfrac{\partial}{\partial z}\left[\left(\nu + \sigma_\omega \alpha^* \dfrac{k}{\omega}\right)\dfrac{\partial \omega}{\partial z}\right] \\ \text{[Wilcox, 1998 ; Guizien } \textit{et al.}\text{, 2003]} \\ \dfrac{\partial \omega}{\partial t} = \dfrac{\alpha\omega}{k}\nu_t \left(\dfrac{\partial u}{\partial z}\right)^2 - \beta\omega^2 + \dfrac{\partial}{\partial z}\left[\left(\nu + \sigma_\omega \alpha^* \dfrac{k}{\omega}\right)\dfrac{\partial \omega}{\partial z}\right] + \dfrac{\sigma_d}{\omega}\dfrac{\partial k}{\partial z}\dfrac{\partial \omega}{\partial z} \\ \text{[Wilcox, 2006]} \end{cases} \tag{2.28}$$

The closure coefficients and auxiliary relations in the case of the 1D Low Reynolds Number versions of the $k-\omega$ model can be found in Table 2.2.

2.2.3 Boundary conditions

Condition at the bed

We can define boundary conditions for smooth and rough surface conditions.

Rough Conditions

For rough surface conditions, we have the no-slip condition for the horizontal velocity u , defined at the first grid point z_0, the closest point to the solid boundary :

$$u(z_0) = 0 \tag{2.29}$$

Concerning the boundary condition for the turbulence kinetic energy k, there are two conditions that can be used. The first one is called the no-slip condition, and imposes the following condition:

$$k(z_0) = 0 \tag{2.30}$$

This condition is applicable to smooth boundaries but not consistent with rough boundaries, where turbulence fluctuations can still be present in the wake of the roughness elements. A more physically consistent wall boundary condition for the turbulence kinetic energy k is prescribed by Fuhrman *et al.* [2010]:

$$\left(\frac{\partial k}{\partial z}\right)_{z_0} = 0 \tag{2.31}$$

In the case of smooth walls, using this condition allows to directly integrate through the viscous sublayer, and for rough walls, to avoid the viscous sublayer that is completely disrupted for fully rough conditions [Fuhrman *et al.*, 2010]. The near bed resolution in the rough case can then be deduced from the roughness length, and not the viscous length scale, allowing to reduce the computational cost in terms of necessary nodes near the boundary.

Concerning the specific dissipation rate ω boundary condition, the value is dependent on the friction velocity u_τ near the wall:

$$\omega(z_0) = \omega_{wall} \tag{2.32}$$

With ω_{wall} defined by:

$$\omega_{wall} = \frac{u_\tau^2}{\nu} S_R \tag{2.33}$$

where the dimensionless surface-roughness function S_R is defined as:

$$\begin{cases} S_R &= \left(\frac{200}{k_N^+}\right)^2 & \text{if} \quad k_N^+ \leq 5 \\ S_R &= \frac{K_r}{k_N^+} + \left[\left(\frac{200}{k_N^+}\right)^2 - \frac{K_r}{k_N^+}\right] e^{5-k_N^+} & \text{if} \quad k_N^+ > 5 \end{cases} \tag{2.34}$$

The variable k_N^+ is defined as $k_N^+ = k_N \frac{u_\tau}{\nu}$, where k_N is the Nikuradse roughness parameter, $u_\tau = \sqrt{\tau/\rho}$ is the friction velocity and $\tau = \rho(\nu + \nu_T(z_0)) \left(\frac{\partial u}{\partial z}\right)_{z=z_0}$ is the bottom shear stress. Wilcox [2006] prescribes a value $K_r = 100$ for its base version and $K_r = 60$ for its low Reynolds number version, and Fuhrman *et al.* [2010] uses a value $K_r = 180$, to respect the law of the wall for rough profiles.

The expression of S_R for the Wilcox [1998] and Guizien *et al.* [2003] model is expressed below:

$$\begin{cases} S_R &= \left(\frac{50}{k_N^+}\right)^2 & \text{if} \quad k_N^+ < 25 \\ S_R &= \frac{100}{k_N^+} & \text{if} \quad k_N^+ > 25 \end{cases} \tag{2.35}$$

Smooth Conditions

For perfectly-smooth walls, the specific dissipation rate varies in the sublayer when approaching the wall as z^{-2} . To obtain smooth conditions, we need to specify the value of ω near the wall boundary:

$$\omega(z) = \frac{6\nu_T(z)}{\beta_0 z^2} \ , \qquad z^+ < 2.5 \tag{2.36}$$

Condition at the top of the boundary layer

On the upper boundary $z = z_h$, we have the following conditions for the turbulent kinetic energy and the specific dissipation rate :

$$\left(\frac{\partial k}{\partial z}\right)_{z_h} = 0 \tag{2.37a}$$

$$\left(\frac{\partial \omega}{\partial z}\right)_{z_h} = 0 \tag{2.37b}$$

Concerning the horizontal velocity u, we also have two conditions:

- Either we consider that the velocity outside the boundary layer is constant, which gives:

  $$u(z_h) = U_\infty \tag{2.38}$$

  with U_∞ the free stream velocity.

- Or we express the boundary condition assuming that the velocity gradient is equal to zero at the boundary:

  $$\left(\frac{\partial u}{\partial z}\right)_{z_h} = 0 \tag{2.39}$$

  The forcing term for the equation then corresponds to the horizontal pressure gradient, assumed to be constant in the boundary layer. This pressure gradient is defined as:

  $$-\frac{1}{\rho}\frac{\partial p}{\partial x} = \frac{\partial U_\infty}{\partial t} \tag{2.40}$$

  or

  $$-\frac{1}{\rho}\frac{\partial p}{\partial x} = \frac{\partial U_\infty}{\partial t} + U_\infty \frac{\partial U_\infty}{\partial x} + W_\infty \frac{\partial U_\infty}{\partial z} \approx \frac{\partial U_\infty}{\partial t} + U_\infty \frac{\partial U_\infty}{\partial x} \tag{2.41}$$

  if we add the advection terms.

2.2.4 Additional terms: advection

Influence of the advection terms

The momentum fluxes in the boundary layer should also be considered, as they might play a role in the non-linear processes occurring in the coastal bottom boundary layer, which impact on the sediment transport direction, seaward or shoreward [Henderson *et al.*, 2004]. These momentum fluxes are weak, provided that the ratio of the horizontal linear wave velocity amplitude to the wave celerity is small. Therefore the inclusion of the advection terms can induce a difference in the resolution of the boundary layer.

Estimation of the vertical velocity

The advection terms depend on the horizontal gradient $\partial/\partial x$ and the vertical gradient $\partial/\partial z$. As we want to remain with a unidimensional model in z of the velocity in x for simplicity, the horizontal gradient need to be replaced by another term, and a specific equation for the vertical velocity w is not introduced.

We use the relation:

$$\frac{\partial}{\partial x} = -\frac{1}{c_p}\frac{\partial}{\partial t} \tag{2.42}$$

valid for weakly decreasing waves [Holmedal et Myrhaug, 2009]. In relation (2.42), c_p is the wave celerity propagation.

The vertical velocity w is related to the horizontal velocity u by the conservation of mass:

$$\frac{\partial u}{\partial x} + \frac{\partial w}{\partial z} = 0 \tag{2.43}$$

Using relation (2.42), the spatial and temporal derivatives of u are linked by:

$$\frac{\partial u}{\partial x} = -\frac{1}{c_p}\frac{\partial u}{\partial t} \tag{2.44}$$

by combining equation 2.43 and equation 2.44, we obtain:

$$\frac{\partial w}{\partial z} = \frac{1}{c_p}\frac{\partial u}{\partial t} \tag{2.45}$$

And finally, by integration, we obtain the vertical velocity w:

$$w(z) = \frac{1}{c_p}\int_{z_0}^{z} \left.\frac{\partial u}{\partial t}\right|_z dz + w(z_0) \tag{2.46}$$

For fixed bottom, the relation becomes:

$$w(z) = \frac{1}{c_p}\frac{\partial}{\partial t}\int_{z_0}^{z} u(z)\ dz + w(z_0) \tag{2.47}$$

advection terms

The advection terms are present in the three equations of the velocity, turbulent kinetic energy and specific dissipation rate.

For the horizontal velocity equation, the advection terms are simplified to:

$$\begin{aligned}\frac{\partial}{\partial x_j}(u_j u_i) &= \frac{\partial}{\partial x}(u^2) + \frac{\partial}{\partial z}(uw) \\ &= u\frac{\partial u}{\partial x} + w\frac{\partial u}{\partial z} \\ &= -\frac{u}{c}\frac{\partial u}{\partial t} + w\frac{\partial u}{\partial z}\end{aligned} \tag{2.48}$$

For the turbulent kinetic energy equation, the advection term is:

$$\begin{aligned}\frac{\partial}{\partial x_j}(u_j k) &= \frac{\partial}{\partial x}(uk) + \frac{\partial}{\partial z}(wk) \\ &= u\frac{\partial k}{\partial x} + w\frac{\partial k}{\partial z} + \underbrace{k\frac{\partial u}{\partial x} + k\frac{\partial w}{\partial z}}_{=0} \\ &= -\frac{u}{c}\frac{\partial k}{\partial t} + w\frac{\partial k}{\partial z}\end{aligned} \tag{2.49}$$

For the specific dissipation rate equation, the advection term is:

$$\begin{aligned}\frac{\partial}{\partial x_j}(u_j \omega) &= \frac{\partial}{\partial x}(u\omega) + \frac{\partial}{\partial z}(w\omega) \\ &= u\frac{\partial \omega}{\partial x} + w\frac{\partial \omega}{\partial z} + \underbrace{\omega\frac{\partial u}{\partial x} + \omega\frac{\partial w}{\partial z}}_{=0} \\ &= -\frac{u}{c}\frac{\partial \omega}{\partial t} + w\frac{\partial \omega}{\partial z}\end{aligned} \tag{2.50}$$

2.3 Numerical Resolution

2.3.1 Resolution scheme

We solve the system of equations using the implicit finite control volume method of Patankar [1980] which is described hereafter, on an exponential grid. We improve this method by determining the turbulence kinetic energy k, the specific dissipation rate ω and the turbulent viscosity ν_T in the staggered grid, between the velocity nodes.

The numerical resolution is presented here summarized. For a more detailed version, please refer to Appendix A.

The geometric grid is determined by defining the initial conditions z_0 the bottom boundary, and z_h the upper boundary, and also the number of nodes N_0.

We define the grid with the equation 2.51:

$$\begin{cases} (z)_1 & = z_0 \\ (z)_{j+1} & = (z)_j + z_0 R^j \quad \forall j \geq 1 \end{cases} \tag{2.51}$$

where R represent the common ratio of the geometric series, which is not known beforehand. To determine R we use the properties of a geometric series:

$$(z)_{N_0} = z_0 \sum_{i=0}^{N_0} R^i = z_h \tag{2.52}$$

The midpoints are located at the center of each cell, as shown in Figure 2.3:

$$z_{j+1/2} = z_j + \frac{z_{j+1} - z_j}{2} \tag{2.53}$$

We also define two points that will be used as ghost points in the boundaries:

$$\begin{aligned} z_{-\frac{1}{2}} &= \frac{z_0}{2} \\ z_{N_0+\frac{1}{2}} &= z_h + \frac{z_0 R^{N_0-1}}{2} \end{aligned} \tag{2.54}$$

2.3.2 Discretization of the equations

Horizontal Velocity equation

To solve the system of equation, we discretize and integrate them over a control volume.

We integrate the equation (2.26) over a control volume centered in the point j, and

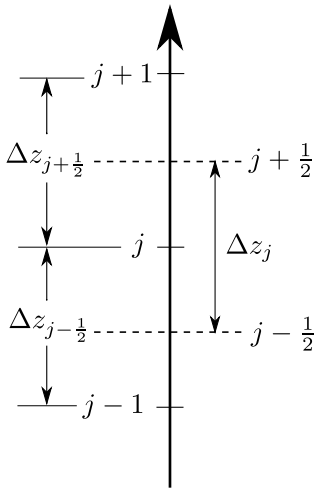

Figure 2.3 – Computational grid sketch. The horizontal velocity u is determined at point j, while the turbulence kinetic energy k and the specific dissipation rate ω are determined on the midpoints $j+1/2$ and $j-1/2$.

over a time step Δt:

$$\int_{j-\frac{1}{2}}^{j+\frac{1}{2}} \int_t^{t+\Delta t} \frac{\partial u}{\partial t}\, dt\, dz = \int_{j-\frac{1}{2}}^{j+\frac{1}{2}} \int_t^{t+\Delta t} \left(\frac{\partial U}{\partial t} - \frac{1}{\rho}\frac{\partial \bar{P}}{\partial x} \right)\, dt\, dz + \int_{j-\frac{1}{2}}^{j+\frac{1}{2}} \int_t^{t+\Delta t} \frac{\partial}{\partial z}\left((\nu + \nu_t)\frac{\partial u}{\partial z} \right)\, dt\, dz \tag{2.55}$$

For time integration, we will use a fully implicit method:

$$\int_t^{t+\Delta t} u_j\, dt = u_j^{t+\Delta t}\Delta t \tag{2.56}$$

For readability purpose, we will drop the superscript $t+\Delta t$, and assume that u, k and ω stand for the new values that are unknown at step $t+\Delta t$:

$$u^{t+\Delta t} \equiv u \ , \ k^{t+\Delta t} \equiv k \ , \ \omega^{t+\Delta t} \equiv \omega \tag{2.57}$$

The non-linear terms are linearised using the variables at the previous iteration. In the end, we obtain the following linear system, where the velocity is the unknown variable, for points $j \in [2 : N_0 - 1]$:

$$A_N(j)u_{j+1} + A_P(j)u_j + A_S(j)u_{j-1} = D_u(j) \tag{2.58}$$

The subscript $_P$ refers to the central point considered, while the $_N$ subscript refers to the point directly above (or "North") and the $_S$ subscript refers to the point directly below ("South"). The coefficients are defined as:

$$A_N(j) = -\frac{\Delta t}{\Delta z_j}\left(\frac{(\Gamma_u)_{j+\frac{1}{2}}}{\Delta z_{j+\frac{1}{2}}}\right) \tag{2.59a}$$

$$A_S(j) = -\frac{\Delta t}{\Delta z_j}\left(\frac{(\Gamma_u)_{j-\frac{1}{2}}}{\Delta z_{j-\frac{1}{2}}}\right) \tag{2.59b}$$

$$A_P(j) = 1 - A_N(j) - A_S(j) \tag{2.59c}$$

$$D_u(j) = -\frac{1}{\rho}\frac{\partial \bar{P}}{\partial x}\Delta t + u_j^t + U - U^t \tag{2.59d}$$

Where $(\Gamma_u)_j = \nu + (\nu_T)_j$.

Boundary conditions

Lower boundary condition: at the bottom boundary, $z = z_0$, corresponding to $j = 0$ (Figure 2.4), the horizontal velocity u is set to zero. The discrete equation for u is straightforward, as it is defined on the regular grid:

$$A_N(1)u_1 + A_P(1)u_0 = 0 \tag{2.60}$$

with

$$A_N(1) = 0\ , \quad A_P(1) = 1 \tag{2.61}$$

Upper boundary condition: at the upper boundary, $z = z_h$, corresponding to $j = N_0$ (Figure 2.5), we can define two different kind of boundary conditions for the horizontal velocity u, the velocity at the boundary can be equal to the velocity outside the boundary layer, or the gradient of velocity in this point can be equal to zero.

- If we define the horizontal velocity at the top boundary to be equal to the velocity outside the boundary layer U_∞, we obtain the following discrete equation for point N_0:

$$A_P(N_0)u_{N_0} + A_S(N_0)u_{N_0-1} = D_u(N_0) \tag{2.62}$$

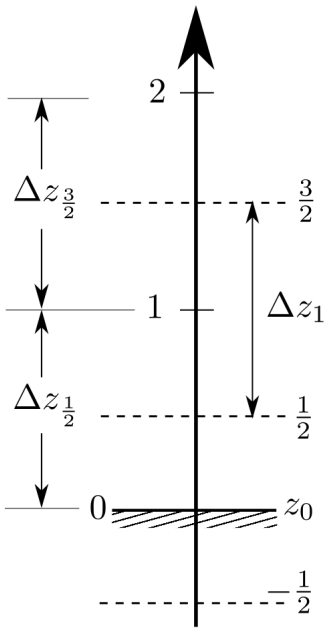

Figure 2.4 – Grid point sketch at the bottom boundary.

Where:

$$A_S(N_0) = -\frac{\Delta t}{\Delta z_{N_0}} \frac{(\Gamma_u)^t_{N_0-\frac{1}{2}}}{\Delta z_{N_0-\frac{1}{2}}} \tag{2.63a}$$

$$A_P(N_0) = 1 \tag{2.63b}$$

$$D_u(N_0) = -\frac{1}{\rho}\frac{\partial \bar{P}}{\partial x}\Delta t + U_\infty(1 + A_S(N_0)) \tag{2.63c}$$

- If we define the boundary condition as $\left.\dfrac{\partial u}{\partial z}\right|_{N_0} = 0$, the resulting equation is quite similar:

$$A_P(N_0)u_{N_0} + A_S(N_0)u_{N_0-1} = D_u(N_0) \tag{2.64}$$

with:

$$A_S(N_0) = -\frac{\Delta t}{\Delta z_{N_0}} \frac{(\Gamma_u)^t_{N_0-\frac{1}{2}}}{\Delta z_{N_0-\frac{1}{2}}} \tag{2.65a}$$

$$A_P(N_0) = 1 - A_S(N_0) \tag{2.65b}$$

$$D_u(N_0) = -\frac{1}{\rho}\frac{\partial \bar{P}}{\partial x}\Delta t + U_\infty - U^t_\infty + u^t_{N_0} \tag{2.65c}$$

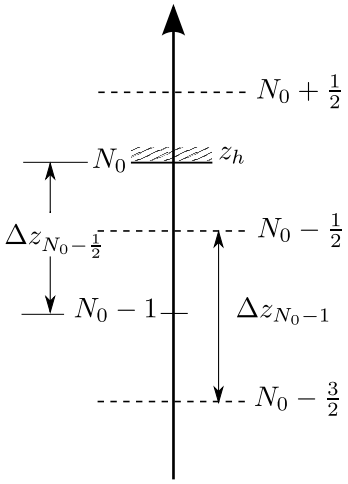

Figure 2.5 – Grid point sketch at the upper boundary $z = z_h$.

Additional terms: advection

We first need to discretize the vertical velocity w. From equation 2.46, we evaluate the integral discretely:

$$\begin{aligned} w_j &= \frac{1}{c_p}\int_{z(1)}^{z(j)} \left.\frac{\partial u}{\partial t}\right|_y dy \\ &= \frac{1}{c_p}\sum_{m=1}^{j-1}\int_{z(m)}^{z(m+1)} \left.\frac{\partial u}{\partial t}\right|_y dy \\ &\sim \frac{1}{c_p}\sum_{m=1}^{j-1} \left.\frac{\partial u}{\partial t}\right|_{m+\frac{1}{2}} \Delta z_{m+\frac{1}{2}} \\ &\sim \frac{1}{c_p}\sum_{m=1}^{j-1} \frac{u^t_{m+\frac{1}{2}} - u^{t-\Delta t}_{m+\frac{1}{2}}}{\Delta t}\Delta z_{m+\frac{1}{2}} \end{aligned} \tag{2.66}$$

The sum starts at $m = 1$ because the vertical velocity is zero at the bottom: $w(z_0) = 0$. The temporal derivative is estimated using the previous time steps t and $t - \Delta t$, as the terms at time step $t + \Delta t$ are unknown, and since it is an implicit discretization, the linear system to be solved would not involve a tridiagonal matrix, making the problem more complicated.

The discretization of the advection terms affect the terms A_P and D_u in equation

2.58:

$$A_P(j) = 1 - A_N(j) - A_S(j) - \frac{u_j^t}{c} \tag{2.67a}$$

$$D_u(j) = -\frac{1}{\rho}\frac{\partial \bar{P}}{\partial x}\Delta t + u_j^t + U_j - U_j^t - \frac{(u_j^t)^2}{c} - w_j^t \frac{\Delta t}{\Delta z_j}(u_{j+\frac{1}{2}}^t - u_{j-\frac{1}{2}}^t) \tag{2.67b}$$

In the lower boundary, the equation is similar to equation 2.60. In the upper boundary, the equation changes with the chosen boundary condition:

- In the case where the boundary condition is $u_{N_0} = U_\infty$, we obtain:

$$\begin{aligned} D_u(N_0) = &- \frac{1}{\rho}\frac{\partial \bar{P}}{\partial x}\Delta t + U_\infty(1 + A_S(N_0)) \\ &+ \frac{1}{c}U_\infty(U_\infty - U_\infty^t) - w_{N_0}^t \frac{\Delta t}{2\Delta z_{N_0}}(U_\infty - u_{N_0-1}^t) \end{aligned} \tag{2.68}$$

  The terms $A_P(N_0)$ and $A_S(N_0)$ remain the same as equations 2.65c and 2.63a

- In the case where the velocity gradient is equal to 0, we have:

$$\int_{N_0-\frac{1}{2}}^{N_0+\frac{1}{2}} \int_t^{t+\Delta t} w\frac{\partial u}{\partial z}\, dtdz = 0 \tag{2.69}$$

  and the coefficients of the discrete equation are changed to:

$$A_P(N_0) = 1 - A_S(N_0) - \frac{u_{N_0}^t}{c} \tag{2.70}$$

$$D_u(N_0) = -\frac{1}{\rho}\frac{\partial \bar{P}}{\partial x}\Delta t + U_\infty - U_\infty^t + u_{N_0}^t - \frac{(u_{N_0}^t)^2}{c} \tag{2.71}$$

Turbulent Kinetic Energy equation

Original terms

We define the turbulent kinetic energy k at the mid-points of the control volume, to insure a better precision in the system. By doing so, we do not need to interpolate the values at the midpoints. The equation (2.27) is integrated over a control volume

centered in the point $j+\frac{1}{2}$, and over a time step Δt:

$$\int_j^{j+1}\int_t^{t+\Delta t}\frac{\partial k}{\partial t}\,dt\,dz = \int_j^{j+1}\int_t^{t+\Delta t}\left(\nu_T\left(\frac{\partial u}{\partial z}\right)^2-\beta k\omega\right)\,dt\,dz + \int_j^{j+1}\int_t^{t+\Delta t}\frac{\partial}{\partial z}\left((\nu+\sigma_k\frac{k}{\omega})\frac{\partial k}{\partial z}\right)\,dt\,dz \tag{2.72}$$

We integrate over time using a first order fully implicit control volume scheme. We obtain the following equation, for point $j+\frac{1}{2}$, with $j\in[2\cdots N-2]$:

$$B_N(j)k_{j+\frac{3}{2}}+B_P(j)k_{j+\frac{1}{2}}+B_S(j)k_{j-\frac{1}{2}}=D_k(j) \tag{2.73}$$

With the terms defined as:

$$B_N(j)=-\frac{\Delta t}{\Delta z_{j+\frac{1}{2}}}\frac{(\Gamma_k)^t_{j+1}}{\Delta z_{j+1}} \tag{2.74a}$$

$$B_S(j)=-\frac{\Delta t}{\Delta z_{j+\frac{1}{2}}}\frac{(\Gamma_k)^t_{j}}{\Delta z_{j}} \tag{2.74b}$$

$$B_P(j)=1-B_N(j)-B_S(j)+(\beta^*)^t_{j+\frac{1}{2}}\omega^t_{j+\frac{1}{2}}\Delta t \tag{2.74c}$$

$$D_k(j)=k^t_{j+\frac{1}{2}}+(\nu_T)^t_{j+\frac{1}{2}}\left(\frac{u^t_{j+1}-u^t_j}{\Delta z_{j+\frac{1}{2}}}\right)^2\Delta t \tag{2.74d}$$

where $(\Gamma_k)_j=\nu+\sigma_k\frac{k_j}{\omega_j}$. As k and ω are defined at the mid-points, the turbulent viscosity ν_T is also defined at those points. Therefore to calculate $(\Gamma_k)_j$ we need to use an interpolation (linear or cubic).

Boundary conditions

Lower boundary condition The turbulent kinetic energy is defined at the point $j=\frac{1}{2}$, therefore we have to find discretization equation in $j=\frac{1}{2}$. There are two kinds of boundary condition for k:

- If we define the boundary condition is $k(z=z_0)=k_0=0$, we obtain the following equation for the boundary condition $j=\frac{1}{2}$:

$$B_N(1)k_{\frac{3}{2}}+B_P(1)k_{\frac{1}{2}}=D_k(1) \tag{2.75}$$

where

$$B_N(1) = -\frac{\Delta t}{\Delta z_{\frac{1}{2}}}\frac{(\Gamma_k)_1}{\Delta z_1} \tag{2.76a}$$

$$B_P(1) = 1 - B_N(1) + \frac{\Delta t}{\Delta z_{\frac{1}{2}}}\frac{\nu}{\Delta z_0} + (\beta^*)^t_{\frac{1}{2}}\omega^t_{\frac{1}{2}}\Delta t \tag{2.76b}$$

$$D_k(1) = k^t_{\frac{1}{2}} + (\nu_T)^t_{\frac{1}{2}}\left(\frac{u^t_1}{\Delta z_{\frac{1}{2}}}\right)^2\Delta t \tag{2.76c}$$

- If we consider the boundary condition with a zero-gradient, the coefficients at point $j = \frac{1}{2}$ becomes:

$$B_N(1) = -\frac{\Delta t}{\Delta z_{\frac{1}{2}}}\frac{(\Gamma_k)_1}{\Delta z_1} \tag{2.77a}$$

$$B_P(1) = 1 - B_N(1) + (\beta^*)^t_{\frac{1}{2}}\omega^t_{\frac{1}{2}}\Delta t \tag{2.77b}$$

$$D_k(1) = k^t_{\frac{1}{2}} + (\nu_T)^t_{\frac{1}{2}}\left(\frac{u^t_1}{\Delta z_{\frac{1}{2}}}\right)^2\Delta t \tag{2.77c}$$

Upper boundary condition

The upper boundary condition for the turbulent kinetic energy k is $\left.\frac{\partial k}{\partial z}\right|_{N_0} = 0$ We obtain the following equation for the boundary condition $j = N_0 - \frac{1}{2}$:

$$B_P(N_0-1)k_{N_0-\frac{1}{2}} + B_S(N_0-1)k_{N_0-\frac{3}{2}} = D_k(N_0-1) \tag{2.78}$$

where

$$B_N(N_0-1) = 0 \tag{2.79a}$$

$$B_S(N_0-1) = -\frac{\Delta t}{\Delta z_{N_0-\frac{1}{2}}}\frac{(\Gamma_k)_{N_0-1}}{\Delta z_{N_0-1}} \tag{2.79b}$$

$$B_P(N_0-1) = 1 - B_S(N_0-1) + (\beta^*)^t_{N_0-\frac{1}{2}}\omega^t_{N_0-\frac{1}{2}}\Delta t \tag{2.79c}$$

$$D_k(N_0-1) = k^t_{N_0-\frac{1}{2}} + (\nu_T)^t_{N_0-\frac{1}{2}}\left(\frac{U^t_\infty - u^t_{N_0-1}}{\Delta z_{N_0-\frac{1}{2}}}\right)^2\Delta t \tag{2.79d}$$

Advection terms

- For the turbulent kinetic energy equation, we integrate the terms between the points j and $j+1$:

$$\begin{aligned}\int_j^{j+1}\int_t^{t+\Delta t} w\frac{\partial k}{\partial z}\,dtdz &= w^t_{j+\frac{1}{2}}\Delta t\int_j^{j+1}\frac{\partial k}{\partial z}\,dz \\ &= w^t_{j+\frac{1}{2}}\Delta t(k^t_{j+1}-k^t_j) \end{aligned} \tag{2.80}$$

$$\begin{aligned}\int_j^{j+1}\int_t^{t+\Delta t} -\frac{u}{c}\frac{\partial k}{\partial t}\,dtdz &= -\frac{u^t_{j+\frac{1}{2}}}{c}\Delta z_{j+\frac{1}{2}}\int_t^{t+\Delta t}\frac{\partial k}{\partial t}\,dz \\ &= -\frac{u^t_{j+\frac{1}{2}}}{c}\Delta z_{j+\frac{1}{2}}(k_{j+\frac{1}{2}}-k^t_{j+\frac{1}{2}}) \end{aligned} \tag{2.81}$$

The coefficients B_P and D_k from equation 2.73 are then changed to:

$$B_P(j) = 1-B_N(j)-B_S(j)+(\beta^*)^t_{j+\frac{1}{2}}\omega^t_{j+\frac{1}{2}}\Delta t-\frac{u^t_{j+\frac{1}{2}}}{c}\Delta z_{j+\frac{1}{2}}(k_{j+\frac{1}{2}}-k^t_{j+\frac{1}{2}}) \tag{2.82}$$

$$D_k(j) = k^t_{j+\frac{1}{2}}+(\nu_T)^t_{j+\frac{1}{2}}\left(\frac{u^t_{j+1}-u^t_j}{\Delta z_{j+\frac{1}{2}}}\right)^2\Delta t-w^t_{j+\frac{1}{2}}\frac{\Delta t}{\Delta z_{j+\frac{1}{2}}}(k^t_{j+1}-k^t_j) \tag{2.83}$$

The values k^t_j and k^t_{j+1} are estimated by linear interpolation.

- In the lower boundary layer, with the boundary condition $k_{z_0}=0$, there is one additional term to the equation:

$$\begin{aligned}\int_0^{1}\int_t^{t+\Delta t} w\frac{\partial k}{\partial z}\,dtdz &= w^t_{\frac{1}{2}}\Delta t\int_0^{1}\frac{\partial k}{\partial z}\,dz \\ &= w^t_{\frac{1}{2}}\Delta t(k^t_1-k^t_0) \\ &= w^t_{\frac{1}{2}}\Delta t k^t_1 \end{aligned} \tag{2.84}$$

$D_k(1)$ is then changed to:

$$D_k(1) = k^t_{\frac{1}{2}}+(\nu_T)^t_{\frac{1}{2}}\left(\frac{u^t_1}{\Delta z_{\frac{1}{2}}}\right)^2\Delta t-w^t_{\frac{1}{2}}\frac{\Delta t}{\Delta z_{\frac{1}{2}}}k^t_1 \tag{2.85}$$

- In the upper boundary, the boundary condition is $\left.\frac{\partial k}{\partial z}\right|_{N_0} = 0$, $D_k(N_0 - 1)$ is changed to:

$$D_k(N_0-1) = k^t_{N_0-\frac{1}{2}} + (\nu_T)^t_{N_0-\frac{1}{2}} \left(\frac{u^t_{N_0} - u^t_{N_0-1}}{\Delta z_{N_0-\frac{1}{2}}} \right)^2 \Delta t - w^t_{N_0-\frac{1}{2}} \frac{\Delta t}{\Delta z_{N_0-\frac{1}{2}}} (k^t_{N_0} - k^t_{N_0-1}) \tag{2.86}$$

2.3.3 Specific dissipation rate equation

Original terms

We define the specific dissipation rate ω at the mid-points of the control volume, like the turbulent kinetic energy k. We first discretize the equation for the Wilcox [1998] formulation, and then add the terms for the Wilcox [2006] formulation.

We need to integrate the equation (2.28) over a control volume centered in the point $j + \frac{1}{2}$, and over a time step Δt:

$$\begin{aligned} \int_j^{j+1} \int_t^{t+\Delta t} \frac{\partial \omega}{\partial t} \, dt \, dz &= \int_j^{j+1} \int_t^{t+\Delta t} \left(\gamma \frac{\omega}{k} \nu_T \left(\frac{\partial u}{\partial z} \right)^2 - \beta \omega^2 \right) \, dt \, dz \\ &+ \int_j^{j+1} \int_t^{t+\Delta t} \frac{\partial}{\partial z} \left(\Gamma_\omega \frac{\partial \omega}{\partial z} \right) \, dt \, dz \end{aligned} \tag{2.87}$$

we obtain the following equation for point $j + \frac{1}{2}$ with $j \in [2 : N - 2]$:

$$C_N(j)\omega_{j+\frac{3}{2}} + C_P(j)\omega_{j+\frac{1}{2}} + C_S(j)\omega_{j-\frac{1}{2}} = D_\omega(j) \tag{2.88}$$

with

$$C_N(j) = -\frac{\Delta t}{\Delta z_{j+\frac{1}{2}}} \frac{(\Gamma_\omega)^t_{j+1}}{\Delta z_{j+1}} \tag{2.89a}$$

$$C_S(j) = -\frac{\Delta t}{\Delta z_{j+\frac{1}{2}}} \frac{(\Gamma_\omega)^t_{j}}{\Delta z_{j}} \tag{2.89b}$$

$$C_P(j) = 1 - C_N(j) - C_S(j) + \beta \omega^t_{j+\frac{1}{2}} \Delta t \tag{2.89c}$$

$$D_\omega(j) = \omega^t_{j+\frac{1}{2}} + \gamma \frac{\omega^t_{j+\frac{1}{2}}}{k^t_{j+\frac{1}{2}}} (\nu_T)_{j+\frac{1}{2}} \left(\frac{u^t_{j+1} - u^t_j}{\Delta z_{j+\frac{1}{2}}} \right)^2 \Delta t \tag{2.89d}$$

where $\Gamma_\omega = \nu + \sigma_\omega \frac{k}{\omega}$. This system is valid for the Wilcox [1998] formulation. If we

want the Wilcox [2006] formulation, we need to add the cross-diffusion term, which has an impact on D_ω:

$$\begin{aligned} D_\omega(j) =& \omega^t_{j+\frac{1}{2}} + \gamma \frac{\omega^t_{j+\frac{1}{2}}}{k^t_{j+\frac{1}{2}}} (\nu_T)_{j+\frac{1}{2}} \left(\frac{u^t_{j+1} - u^t_j}{\Delta z_{j+\frac{1}{2}}} \right)^2 \Delta t \\ &+ \frac{\sigma_d}{\omega^t_{j+\frac{1}{2}}} \frac{k^t_{j+1} - k^t_j}{\Delta z_{j+\frac{1}{2}}} \frac{\omega^t_{j+1} - \omega^t_j}{\Delta z_{j+\frac{1}{2}}} \Delta t \end{aligned} \tag{2.90}$$

Boundary conditions

Lower boundary condition

The specific dissipation rate ω is also defined at the point $j = \frac{1}{2}$. We use the same method as with the turbulent kinetic energy k, and obtain the following equation:

$$C_N(1)\omega_{\frac{3}{2}} + C_P(1)\omega_{\frac{1}{2}} = D_\omega(1) \tag{2.91}$$

with:

$$C_N(1) = -\frac{\Delta t}{\Delta z_{\frac{1}{2}}} \frac{(\Gamma_\omega)_1}{\Delta z_1} \tag{2.92a}$$

$$C_P(1) = 1 - C_N(1) + \frac{\Delta t}{\Delta z_{\frac{1}{2}}} \frac{\nu}{\Delta z_0} + \beta \omega^t_{\frac{1}{2}} \Delta t \tag{2.92b}$$

$$D_\omega(1) = \omega^t_{\frac{1}{2}} + \gamma \frac{\omega^t_{\frac{1}{2}}}{k^t_{\frac{1}{2}}} (\nu_T)_{\frac{1}{2}} \left(\frac{u_1}{\Delta z_{\frac{1}{2}}} \right)^2 \Delta t + \frac{\Delta t}{\Delta z_{\frac{1}{2}}} \frac{\nu \omega_{wall}}{\Delta z_0} \tag{2.92c}$$

If we consider the Wilcox [2006] formulation, the term $D_\omega(1)$ is changed to:

$$\begin{aligned} D_\omega(1) =& \omega^t_{\frac{1}{2}} + \gamma \frac{\omega^t_{\frac{1}{2}}}{k^t_{\frac{1}{2}}} (\nu_T)_{\frac{1}{2}} \left(\frac{u_1}{\Delta z_{\frac{1}{2}}} \right)^2 \Delta t + \frac{\Delta t}{\Delta z_{\frac{1}{2}}} \frac{\nu \omega_{wall}}{\Delta z_0} \\ &+ \frac{\sigma_d}{\omega^t_{\frac{1}{2}}} \frac{k^t_1}{\Delta z_{\frac{1}{2}}} \frac{\omega^t_1 - \omega^t_{wall}}{\Delta z_{\frac{1}{2}}} \Delta t \end{aligned} \tag{2.93}$$

Upper boundary condition

The upper boundary condition for the specific dissipation rate ω is: $\left.\frac{\partial \omega}{\partial z}\right|_{N_0} = 0$. The resulting equation is then:

$$C_P(N_0 - 1)\omega_{N_0 - \frac{1}{2}} + C_S(N_0 - 1)\omega_{N_0 - \frac{3}{2}} = D_\omega(N_0 - 1) \tag{2.94}$$

with:

$$C_S(N_0-1) = -\frac{\Delta t}{\Delta z_{N_0-\frac{1}{2}}}\frac{(\Gamma_\omega)_{N_0-1}}{\Delta z_{N_0-1}} \tag{2.95a}$$

$$C_P(N_0-1) = 1 - C_S(N_0-1) + \beta\omega^t_{N_0-\frac{1}{2}}\Delta t \tag{2.95b}$$

$$D_\omega(N_0-1) = \omega^t_{N_0-\frac{1}{2}} + \gamma\frac{\omega^t_{N_0-\frac{1}{2}}}{k^t_{N_0-\frac{1}{2}}}(\nu_T)_{N_0-\frac{1}{2}}\left(\frac{U_\infty - u_{N_0-1}}{\Delta z_{N_0-\frac{1}{2}}}\right)^2\Delta t \tag{2.95c}$$

If the upper boundary condition for the horizontal velocity is $\frac{\partial u}{\partial z} = 0$, we have to replace the term U_∞ by u_{N_0} in equation 2.95c.

If we consider the Wilcox [2006] formulation, we add the cross diffusion term in D_ω:

$$\begin{aligned} D_\omega(N_0-1) =& \omega^t_{N_0-\frac{1}{2}} + \gamma\frac{\omega^t_{N_0-\frac{1}{2}}}{k^t_{N_0-\frac{1}{2}}}(\nu_T)_{N_0-\frac{1}{2}}\left(\frac{U^t_\infty - u^t_{N_0-1}}{\Delta z_{N_0-\frac{1}{2}}}\right)^2\Delta t \\ &+ \frac{\sigma_d}{\omega^t_{N_0-\frac{1}{2}}}\left(\frac{\partial k}{\partial z}\right)^t_{N_0-\frac{1}{2}}\left(\frac{\partial \omega}{\partial z}\right)^t_{N_0-\frac{1}{2}}\Delta t \end{aligned} \tag{2.96}$$

Advection term

If we add the advection terms, The term D_ω in equation 2.90 is then changed to:

$$\begin{aligned} D_\omega(j) =& \omega^t_{j+\frac{1}{2}} + \gamma\frac{\omega^t_{j+\frac{1}{2}}}{k^t_{j+\frac{1}{2}}}(\nu_T)_{j+\frac{1}{2}}\left(\frac{u_{j+1}-u_j}{\Delta z_{j+\frac{1}{2}}}\right)^2\Delta t \\ &+ \frac{\sigma_d}{\omega^t_{j+\frac{1}{2}}}\frac{k^t_{j+1}-k^t_j}{\Delta z_{j+\frac{1}{2}}}\frac{\omega^t_{j+1}-\omega^t_j}{\Delta z_{j+\frac{1}{2}}}\Delta t \\ &- w^t_j\frac{\Delta t}{\Delta z_{j+\frac{1}{2}}}(\omega^t_{j+1}-\omega^t_j) \end{aligned} \tag{2.97}$$

The values ω^t_j and ω^t_{j+1} are estimated by linear interpolation.

2.3.4 Numerical algorithm

Algorithm used to advance in time

The system of resulting equations consists of three tridiagonal matrices. We can now use the scheme presented in Figure 2.6 to estimate $u^{t+\Delta t}$, $k^{t+\Delta t}$, $\omega^{t+\Delta t}$ from u^t, k^t, ω^t. We first define the matrices and vectors used for the resolution.

For the horizontal velocity equation, we define $\mathbf{A}$, $\mathbf{D_u}$ and $\mathbf{u}$:

$$\mathbf{A} = \begin{pmatrix} A_P(N_0) & A_N(N_0) & 0 & & \dots & 0 \\ A_S(N_0\text{-}1) & A_P(N_0\text{-}1) & A_N(N_0\text{-}1) & \ddots & & \vdots \\ 0 & \ddots & \ddots & \ddots & & \\ & \ddots & & & \ddots & \vdots \\ & & \ddots & \ddots & \ddots & 0 \\ \vdots & & & A_S(2) & A_P(2) & A_N(2) \\ 0 & \dots & & 0 & A_S(1) & A_P(1) \end{pmatrix}$$

$$\mathbf{D_u} = \begin{pmatrix} D_u(N_0) \\ \vdots \\ \\ \\ \\ \vdots \\ D_u(1) \end{pmatrix} \qquad \mathbf{u} = \begin{pmatrix} u_{N_0}^{t+\Delta t} \\ \vdots \\ \\ \\ \\ \vdots \\ u_1^{t+\Delta t} \end{pmatrix}$$

For the turbulent kinetic energy equation we define $\mathbf{B}$, $\mathbf{D_k}$ and $\mathbf{k}$:

$$\mathbf{B} = \begin{pmatrix} B_P(N_0-1) & B_N(N_0-1) & 0 & & \dots & 0 \\ B_S(N_0-2) & B_P(N_0-2) & B_N(N_0-2) & \ddots & & \vdots \\ 0 & \ddots & \ddots & \ddots & & \\ & \ddots & & & \ddots & \vdots \\ & & \ddots & \ddots & \ddots & 0 \\ \vdots & & & B_S(2) & B_P(2) & B_N(2) \\ 0 & \dots & & 0 & B_S(1) & B_P(1) \end{pmatrix}$$

$$\mathbf{D_k} = \begin{pmatrix} D_k(N_0-1) \\ \vdots \\ \\ \\ \\ \vdots \\ D_k(1) \end{pmatrix} \qquad \mathbf{k} = \begin{pmatrix} k_{N_0-\frac{1}{2}}^{t+\Delta t} \\ \vdots \\ \\ \\ \\ \vdots \\ k_{\frac{1}{2}}^{t+\Delta t} \end{pmatrix}$$

For the specific dissipation rate equation we define $\mathbf{C}$, $\mathbf{D}_\omega$ and ω:

$$\mathbf{C} = \begin{pmatrix} C_P(N_0-1) & C_N(N_0-1) & 0 & & \dots & 0 \\ C_S(N_0-2) & C_P(N_0-2) & C_N(N_0-2) & \ddots & & \vdots \\ 0 & \ddots & \ddots & \ddots & & \\ & \ddots & & & \ddots & \vdots \\ & & \ddots & \ddots & \ddots & 0 \\ \vdots & & & C_S(2) & C_P(2) & C_N(2) \\ 0 & \dots & & 0 & C_S(1) & C_P(1) \end{pmatrix}$$

$$\mathbf{D}_\omega = \begin{pmatrix} D_\omega(N_0-1) \\ \vdots \\ \\ \\ \\ \vdots \\ D_\omega(1) \end{pmatrix} \qquad \omega = \begin{pmatrix} \omega^{t+\Delta t}_{N_0-\frac{1}{2}} \\ \vdots \\ \\ \\ \\ \vdots \\ \omega^{t+\Delta t}_{\frac{1}{2}} \end{pmatrix}$$

The values for u, k and ω at $t+\Delta t$ can be estimated by solving the three linear systems:

$$\mathbf{A} \cdot \mathbf{u} = \mathbf{D_u} \tag{2.98}$$

$$\mathbf{B} \cdot \mathbf{k} = \mathbf{D_k} \tag{2.99}$$

$$\mathbf{C} \cdot \omega = \mathbf{D}_\omega \tag{2.100}$$

In the case we use inner iterations, we need to define new matrices and vectors that will depend, on the variables at time t, but also on variables at a intermediate time t_0. We define these matrices $\mathbf{A_1}$, $\mathbf{B_1}$, $\mathbf{C_1}$ and vectors $\mathbf{D_{u_1}}$, $\mathbf{D_{k_1}}$, $\mathbf{D}_{\omega_1}$, that will depend on

new coefficients. For the horizontal velocity equation we have:

$$A_{N_1}(j) = -\frac{\Delta t}{\Delta z_j}\left(\frac{(\Gamma_u)^{t0}_{j+\frac{1}{2}}}{\Delta z_{j+\frac{1}{2}}}\right) \tag{2.101a}$$

$$A_{S_1}(j) = -\frac{\Delta t}{\Delta z_j}\left(\frac{(\Gamma_u)^{t0}_{j-\frac{1}{2}}}{\Delta z_{j-\frac{1}{2}}}\right) \tag{2.101b}$$

$$A_{P_1}(j) = 1 - A_{N_0}(j) - A_{S_0}(j) - \frac{u^{t0}_j}{c} \tag{2.101c}$$

$$D_{u_1}(j) = -\frac{1}{\rho}\frac{\partial \bar{P}}{\partial x}\Delta t + u^t_j + U_j - U^t_j - \frac{u^t_j u^{t0}_j}{c} - w^{t0}_j \frac{\Delta t}{\Delta z_j}(u^{t0}_{j+\frac{1}{2}} - u^{t0}_{j-\frac{1}{2}}) \tag{2.101d}$$

For the turbulent kinetic energy equation, the coefficients are changed to:

$$B_{N_1}(j) = -\frac{\Delta t}{\Delta z_{j+\frac{1}{2}}}\frac{(\Gamma_k)^{t0}_{j+1}}{\Delta z_{j+1}} \tag{2.102a}$$

$$B_{S_1}(j) = -\frac{\Delta t}{\Delta z_{j+\frac{1}{2}}}\frac{(\Gamma_k)^{t0}_{j}}{\Delta z_{j}} \tag{2.102b}$$

$$B_{P_1}(j) = 1 - B_{N_0}(j) - B_{S_0}(j) + (\beta^*)^{t0}_{j+\frac{1}{2}}\omega^{t0}_{j+\frac{1}{2}}\Delta t \tag{2.102c}$$

$$D_{k_1}(j) = k^t_{j+\frac{1}{2}} + (\nu_T)^{t0}_{j+\frac{1}{2}}\left(\frac{u^{t0}_{j+1} - u^{t0}_j}{\Delta z_{j+\frac{1}{2}}}\right)^2 \Delta t - w^{t0}_{j+\frac{1}{2}}\frac{\Delta t}{\Delta z_{j+\frac{1}{2}}}(k^{t0}_{j+1} - k^{t0}_j) \tag{2.102d}$$

For the specific dissipation rate equation, the coefficients are changed to:

$$C_{N_1}(j) = -\frac{\Delta t}{\Delta z_{j+\frac{1}{2}}}\frac{(\Gamma_\omega)^{t0}_{j+1}}{\Delta z_{j+1}} \tag{2.103a}$$

$$C_{S_1}(j) = -\frac{\Delta t}{\Delta z_{j+\frac{1}{2}}}\frac{(\Gamma_\omega)^{t0}_{j}}{\Delta z_{j}} \tag{2.103b}$$

$$C_{P_1}(j) = 1 - C_{N_0}(j) - C_{S_0}(j) + (\beta)^{t0}_{j+\frac{1}{2}}\omega^{t0}_{j+\frac{1}{2}}\Delta t \tag{2.103c}$$

$$\begin{aligned} D_{\omega_1}(j) = {} & \omega^t_{j+\frac{1}{2}} + \gamma\frac{\omega^{t0}_{j+\frac{1}{2}}}{k^{t0}_{j+\frac{1}{2}}}(\nu_T)_{j+\frac{1}{2}}\left(\frac{u^{t0}_{j+1} - u^{t0}_j}{\Delta z_{j+\frac{1}{2}}}\right)^2 \Delta t \\ & + \frac{\sigma_d}{\omega^{t0}_{j+\frac{1}{2}}}\frac{k^{t0}_{j+1} - k^{t0}_j}{\Delta z_{j+\frac{1}{2}}}\frac{\omega^{t0}_{j+1} - \omega^{t0}_j}{\Delta z_{j+\frac{1}{2}}}\Delta t \\ & - w^{t0}_j\frac{\Delta t}{\Delta z_{j+\frac{1}{2}}}(\omega^{t0}_{j+1} - \omega^{t0}_j) \end{aligned} \tag{2.103d}$$

Concerning the advection terms, the vertical velocity is also estimated at each time

step:

$$w_j^{t0} \sim \frac{1}{c}\sum_{k=1}^{j}\frac{u_k^{t0}-u_k^t}{\Delta t}\Delta z_k \tag{2.104}$$

The variables with the superscript ^{t_0} are temporal variables that are used to iterate and get better accuracy.

Iteration steps

The proposed scheme incorporates a loop to improve convergence at each time step. This is required by the non-linear nature of the equations. This scheme is illustrated in the Figure 2.6.

We first define two operators M_u and M_{u_0}:

$$M_u(u^t, k^t, \omega^t) = \mathbf{A^{-1}} \cdot \mathbf{D_u} \tag{2.105}$$

$$M_{u_0}(u^{t_0}, k^{t_0}, \omega^{t_0}, u^t) = \mathbf{A_1^{-1}} \cdot \mathbf{D_{u_1}} \tag{2.106}$$

The operators M_k, M_{k_0}, M_ω and M_{ω_0} are defined similarly.

The different steps required to obtain the values at the time step $t + \Delta t$ that can also be seen in Figure 2.6 are described hereafter:

1. we start with the values at time step t: u^t, k^t and ω^t
2. the values u^{t_0}, k^{t_0} and ω^{t_0} are calculated from the values u^t, k^t and ω^t
3. the values u^{t_1}, k^{t_1} and ω^{t_1} are initialized to begin the loop. The pointer i_s is set to 1.
4. The loop initiates. The values u^{t0}, k^{t0} and ω^{t0} are estimated from the values u^{t0}, u^{t1}, k^{t0}, k^{t1}, ω^{t0}, ω^{t1} using a relaxation coefficient α. This coefficient ranges from 0 to 1, and affects the rate of convergence.
5. The new values u^{t1}, k^{t1} and ω^{t1} are calculated using the previous values u^{t0}, k^{t0} and ω^{t0}, and the values from the initial time step, u^t, k^t and ω^t.
6. the relative error of u, k and ω are calculated.
7. if the maximum of the relative errors is higher than the required precision p_0, and the number of iteration i_s is lower than the maximum number of iterations allowed m_s, we continue the loop and, add 1 to the pointer i_s, and return at step 4.

8. when the maximum relative error is lower than the precision, or the number of iteration reaches the maximum iterations allowed, we get out of the loop.

9. The variables $u^{t+\Delta t}$, $k^{t+\Delta t}$ and $\omega^{t+\Delta t}$ are obtained from u^{t1}, k^{t1} and ω^{t1}.

It is possible to obtain the results without iteration, in that case, the scheme stops at step 2. The convergence of the numerical model is estimated considering that the time-series input length as a pseudo-period. The numerical model is iterated computing its results within the entire time series and pseudo-period, the velocity relative error between 2 pseudo-periods is estimated as:

$$err_{u_0} = \frac{||u_1 - u_0||_2}{||u_0||_2} = \sqrt{\frac{\sum_z \sum_t (u_1(z,t) - u_0(z,t))^2}{\sum_z \sum_t u_0(z,t)^2}} \tag{2.107}$$

where $u_0(z,t)$ represents the solution of the previous pseudo-period, and $u_1(z,t)$ the solution of the current pseudo-period. The convergence is reached by iterating the entire time-series until err_{u_0} is lower than the desired precision taken as 10^{-6}.

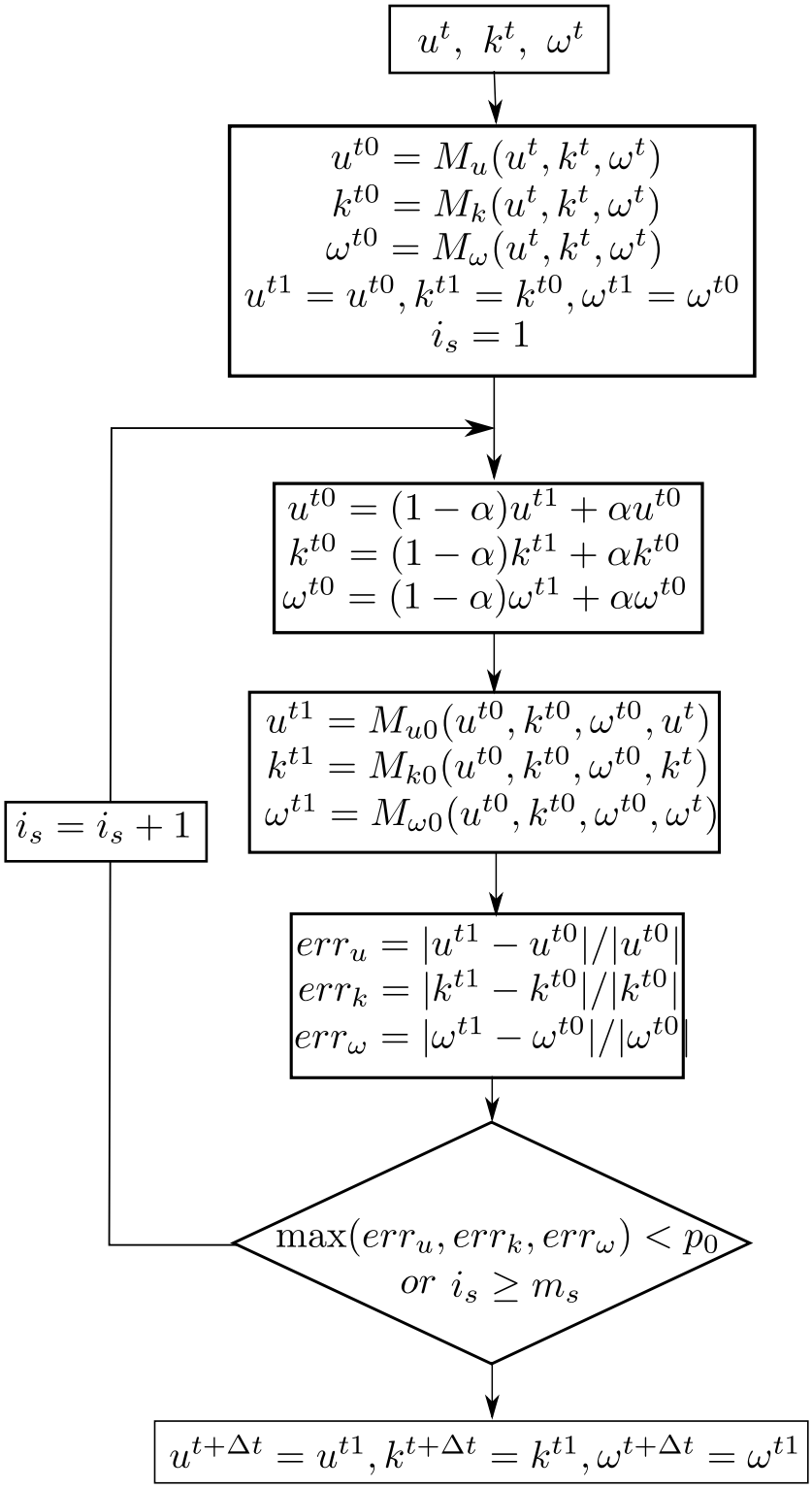

Figure 2.6 – scheme to obtain the values of u, k and ω at time step $t + \Delta t$ from the values at time step t. u^t, k^t and ω^t correspond to the variables at time t, $u^{t+\Delta t}$, $k^{t+\Delta t}$ and $\omega^{t+\Delta t}$ to the variables at time $t + \Delta t$; α is the relaxation coefficient; i_s is an internal loop pointer; p_0 is the precision required to advance to the next step; m_s is the maximum number of iterations.

2.4 Model validation

2.4.1 Validation with sinusoidal flows

The experiments of Jensen *et al.* [1989] are oscillatory flows in a U-tube, on smooth and rough beds. The forcing consist in a sinusoidal velocity in time (Figure 2.7), with a varying Reynolds number defined as $Re = aU_{0m}/\nu$, with a the amplitude of the free-stream motion, U_{0m} the maximum value of the free-stream velocity and ν the kinematic viscosity, ranging from a laminar regime ($Re = 3.3 \times 10^4$) to a fully turbulent regime ($Re = 6.0 \times 10^6$). The bed shear stress is obtained using a hot-film probe, mounted in the middle of the working section. The probe is calibrated using the theoretical solution for the bed shear stress on a laminar boundary layer flow.

The experimental conditions of the different experiments are given in Table 2.3. For all the experiments considered, the kinematic viscosity is $\nu = 1.14 \times 10^{-6}$ m^2.s, and the period is $T = 9.72$ s.

Test no.	U_{0m} (m/s)	a (m)	$Re = aU_{0m}/\nu$	boundary	k_s mm
1	0.073	0.113	7.5×10^3	smooth	-
2	0.152	0.235	3.3×10^4	smooth	-
3	0.23	0.36	7.5×10^4	smooth	-
4	0.34	0.53	1.6×10^5	smooth	-
5	0.45	0.70	2.9×10^5	smooth	-
7	0.68	1.05	6.5×10^5	smooth	-
8	1.02	1.58	1.6×10^6	smooth	-
9	1.55	2.4	3.4×10^6	smooth	-
10	2.0	3.1	6×10^6	smooth	-
13	2.0	3.1	6×10^6	rough	0.84

Table 2.3 – Experimental conditions for [Jensen *et al.*, 1989] experiments. U_{0m} is the maximum value of the free-stream velocity, a is the amplitude of the free-stream motion.

The experimental bed shear stress are compared with the following numerical model, with the Wilcox [2006] formulation, in its normal and Low Reynolds Number version and the Guizien *et al.* [2003] formulation.

For the numerical model, the bed shear stress is defined as:

$$\tau = \rho u_\tau^2 = \rho(\nu + \nu_T(z_0)) \left.\frac{\partial u}{\partial z}\right|_{z=z_0} \tag{2.108}$$

In the experiments from Jensen *et al.* [1989] the bed shear stress was measured with

a hot-film probe, calibrated in a laminar boundary layer flow for the smooth conditions, and using a logarithmic fit of the velocity profile to obtain the friction velocity u_τ and the bed shear stress for the rough conditions.

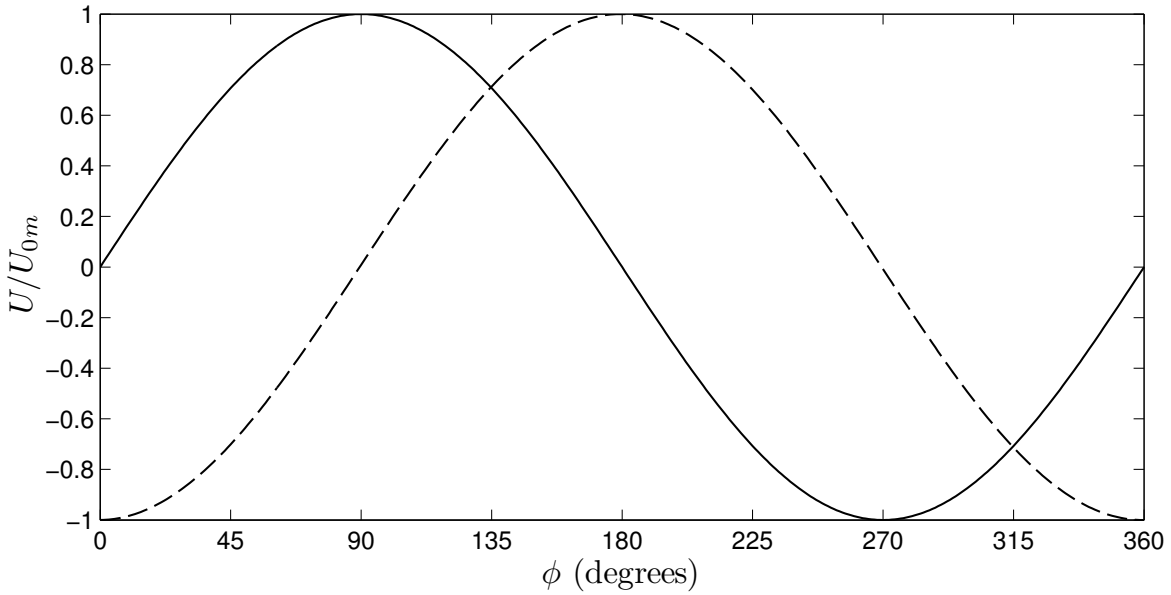

Figure 2.7 – Phase ϕ definition along the oscillatory part of the outer flow velocity $(-)$ and corresponding pressure gradient $(--)$

If we compare the bed shear stress obtained for various Reynolds number on a smooth bed, in Figure 2.8, we observe that the numerical model results are coherent with the experimental results, in terms of bed shear stress magnitude. The experimental results show that the flow is fully laminar for $Re = 3.3 \times 10^4$, $Re = 7.5 \times 10^4$ and $Re = 1.6 \times 10^5$. For $Re = 2.9 \times 10^5$, the bed shear stress shows sign of transition from laminar to turbulent regime, at $\phi = 90^o$ and $\phi = 270^o$, and τ/ρ reaches maximum values of 5 $\mathrm{cm}^2/\mathrm{s}^2$ in the turbulent regime, compared to 4 $\mathrm{cm}^2/\mathrm{s}^2$ in the laminar regime. As we keep increasing the Reynolds number, the transition from laminar to turbulent regime occurs sooner. For $Re = 6.5 \times 10^5$, the transition occurs at $\phi = 60^o$ and $\phi = 240^o$ and for $Re = 1.6 \times 10^6$, the transition occurs at $\phi = 30^o$ and $\phi = 210^o$. For higher Reynolds numbers, $Re = 3.4 \times 10^6$ and $Re = 6.0 \times 10^6$, the flow is fully turbulent over the whole period. Noteworthy, in the experiments where a transition from laminar to turbulent regime occurs, we also observe a relaminarization process during the decelerating phase, that is less apparent in the experimental results, as there is no sudden change in the bed shear stress.

The numerical model is not able to reproduce correctly the right transition from laminar to turbulent. For the Wilcox [2006] formulation, the baseline version shows a

slight transition at $Re = 3.3\times10^4$ at $\phi = 110^o$ and $\phi = 290^o$, and the LRN version shows one at $Re = 3.3 \times 10^4$ at $\phi = 100^o$ and $\phi = 280^o$. As we increase the Reynolds number, the transition begins sooner, and the maximum shear stress is not well reproduced for $Re = 7.5 \times 10^4$, $Re = 1.6 \times 10^5$ and $Re = 2.9 \times 10^5$. For $Re > 2.9 \times 10^5$ the model indicates a fully turbulent regime, and the maximum bed shear stress is of the same order of magnitude than the experimental results, although at high Reynolds numbers, namely $Re = 3.4 \times 10^6$ and $Re = 6.0 \times 10^6$, the bed shear stress is slightly overestimated.

The Guizien *et al.* [2003] formulation is better at predicting the transition between the laminar and the turbulent regime. The model is laminar at lower Reynolds number, at $Re = 3.3 \times 10^4$ and $Re = 7.5 \times 10^4$, and the first transition is observed at $Re = 1.6 \times 10^5$, for $\phi = 110^o$ and $\phi = 290^o$. For intermediate Reynolds numbers, the model is able to reproduce the transition at the correct phase, for $Re = 2.9 \times 10^5$, $Re = 6.5 \times 10^5$ and $Re = 1.6 \times 10^6$, with peaks values similar to the experiment. At higher Reynolds number, at $Re > 3.4 \times 10^6$, the model reproduces a slight transition, for $\phi = 110^o$ and $\phi = 290^o$, that is not apparent in the experimental results. The model also underestimates the shear stress for the higher Reynolds number.

We can observe from these experiments on a smooth bed that the exact time of the transition is difficult to obtain for the $k-\omega$ model, however for almost all experiments, the model reproduces the magnitude of the bed shear stress which is key to estimate the sediment transport.

The mean velocity profiles for the smooth case under a fully turbulent regime, are shown in Figure 2.9.

We observe the experimental log-law region, that starts to develop at $\phi = 15^o$, and increases in height, up to $\phi = 135^o$, then start decreasing to disappear at $\phi = 160^o$, near flow reversal. For $\phi = 15^o$ and $\phi = 160^o$, the velocity profile does not follow a law of the wall because of the strong favourable (respectively adverse) pressure gradients existing at these phases.

Concerning the numerical model, Wilcox [2006] formulation is close to the experimental results, at all phases and we observe a logarithmic region similar to the experimental one. The velocity profile under a favourable pressure gradient is fairly well reproduced, and for the adverse pressure gradient, the velocity is slightly under estimated. Guizien *et al.* [2003] formulation has some discrepancies with the experimental results. As explained before, the numerical model still shows a transition from laminar to turbulent at this Reynolds number, which explain the difference in the velocity profile at $\phi = 15^o$. After that, starting from $\phi = 60^o$, the velocities are over-estimated in the logarithmic region.

If we now look at the same experiment from Figures 2.8 and 2.9, but with a rough bed with $k_s = 0.84$ mm, we can also compare the bed shear stress and the velocity profiles. In the rough bed case, the experimental friction velocity has been estimated when possible, i.e. when a logarithmic region existed, and was obtained by logarithmic fitting (figure 2.10). The Wilcox [2006] formulation tend to obtain similar friction velocities for $15^0 < \phi < 135^0$, but over-estimates them after the flow reversal. On the contrary, Guizien *et al.* [2003] formulation tend to under-estimate the the friction velocity for $\phi < 135^0$, but after the flow reversal, the results are close to the logarithmic fit. We also observe a region of relaminarization, at $160^0 < \phi < 190^0$.

Concerning the mean velocity profiles with a rough bed, the observations are similar to the smooth bed case. The logarithmic region is well reproduced by the Wilcox [2006] formulation, and over-estimated by the Guizien *et al.* [2003] formulation.

From these experiments, we can conclude that the $k - \omega$ model in its different formulations reproduces fairly well the evolution of a periodic flow in a U-tube. If Wilcox [2006] formulation reproduces better the logarithmic region, Guizien *et al.* [2003] formulation is able to better predict the transition from laminar to turbulent.

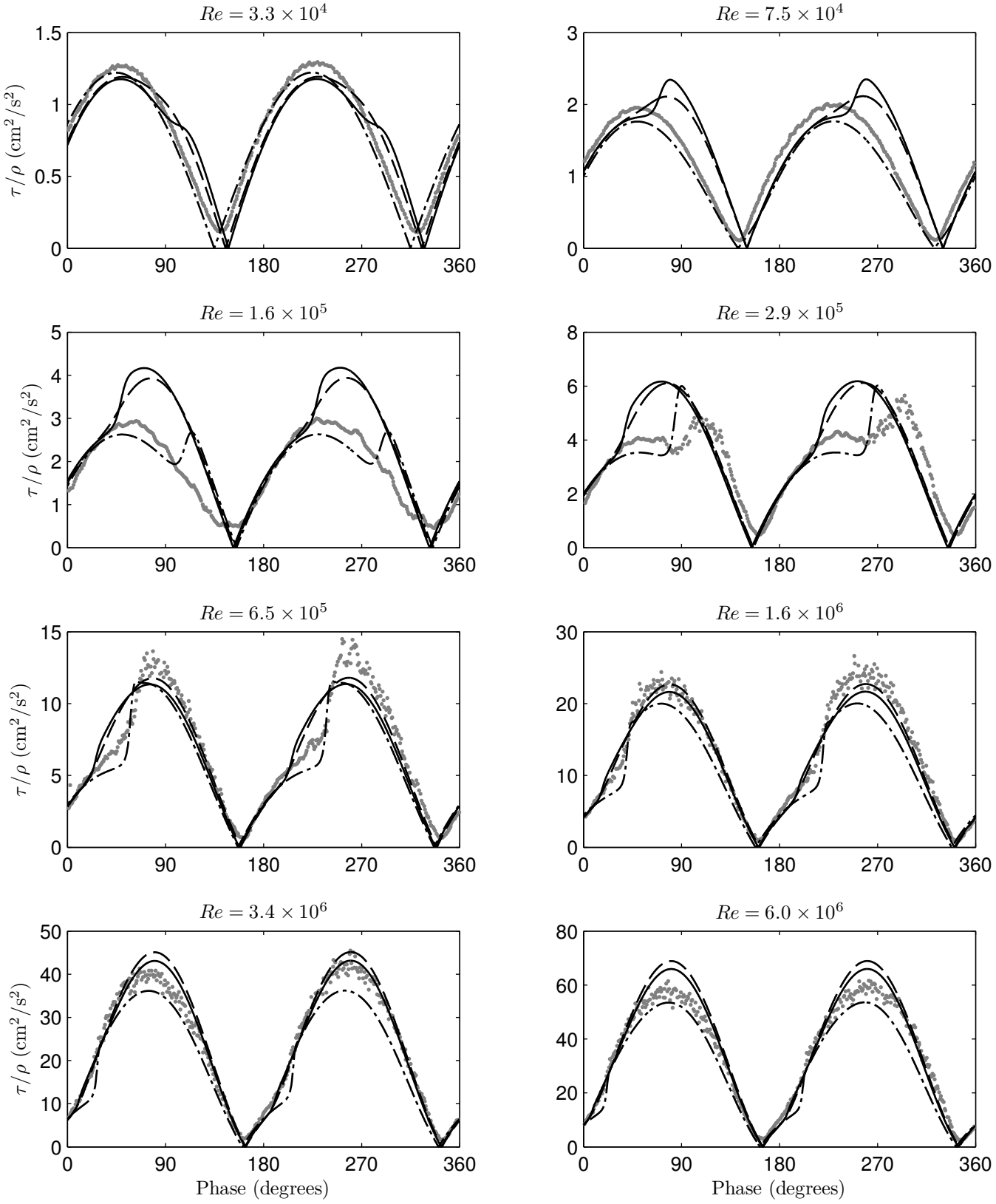

Figure 2.8 – Bottom shear stress over one period, over a smooth bed, for different Reynolds number. Grey dots: experimental measurements [Jensen *et al.*, 1989]; line: Wilcox [2006] $k-\omega$ model, LRN version; dashed line: line: Wilcox [2006] $k-\omega$ model; dot-dashed line: Guizien *et al.* [2003] $k-\omega$ model, LRN version.

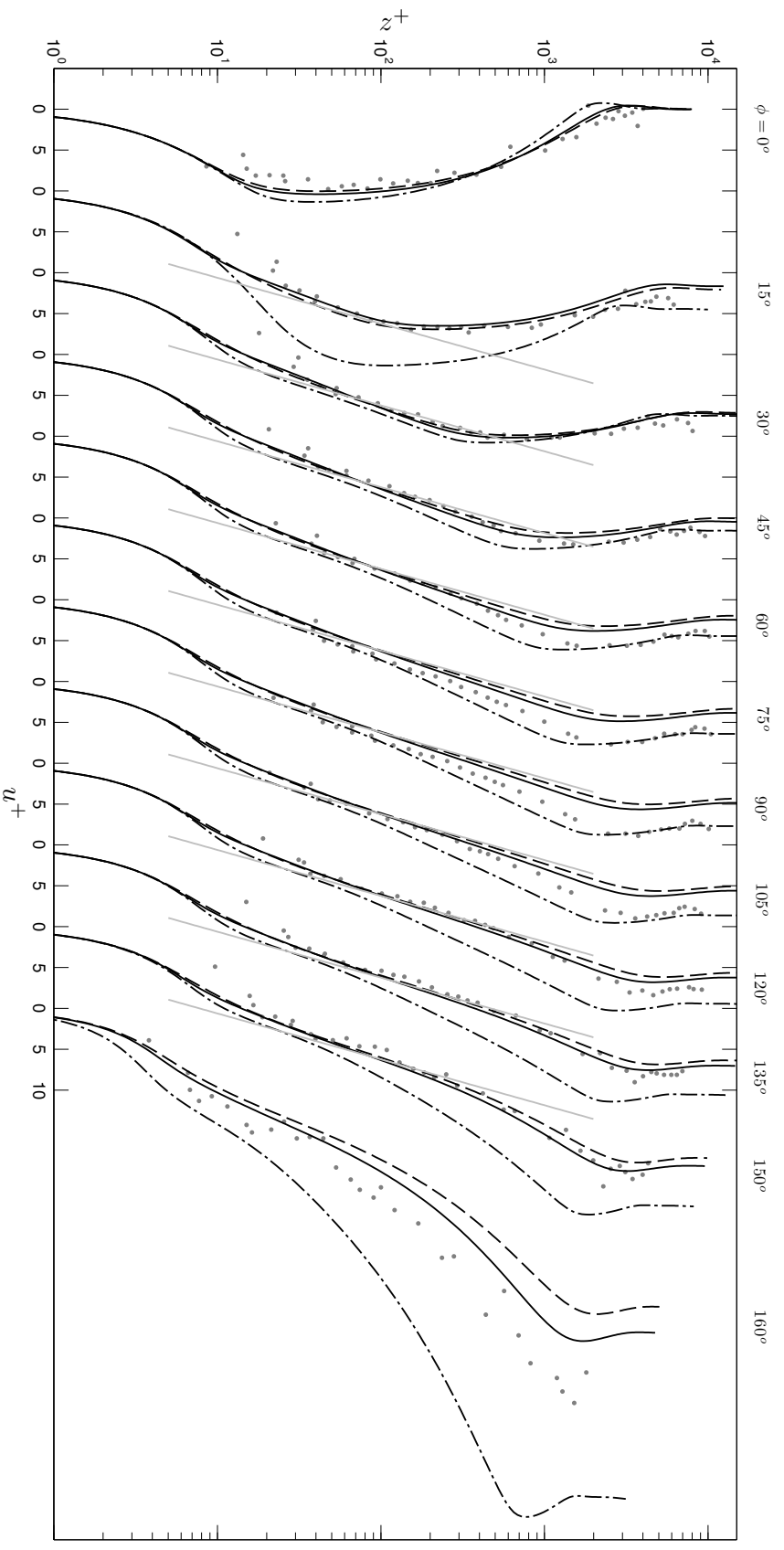

Figure 2.9 – Mean velocity distributions in semi-log plot, at different phases. Smooth bed, $Re = 6 \times 10^6$. Gray dots: Jensen *et al.* [1989] experiment, Test 10; black line: numerical model, Wilcox [2006] formulation, LRN version; black dashed line: numerical model, Guizien *et al.* [2003] formulation, LRN version; black dashed-dotted line: numerical model, Wilcox [2006] formulation; grey line: theoretical log-law for smooth beds.

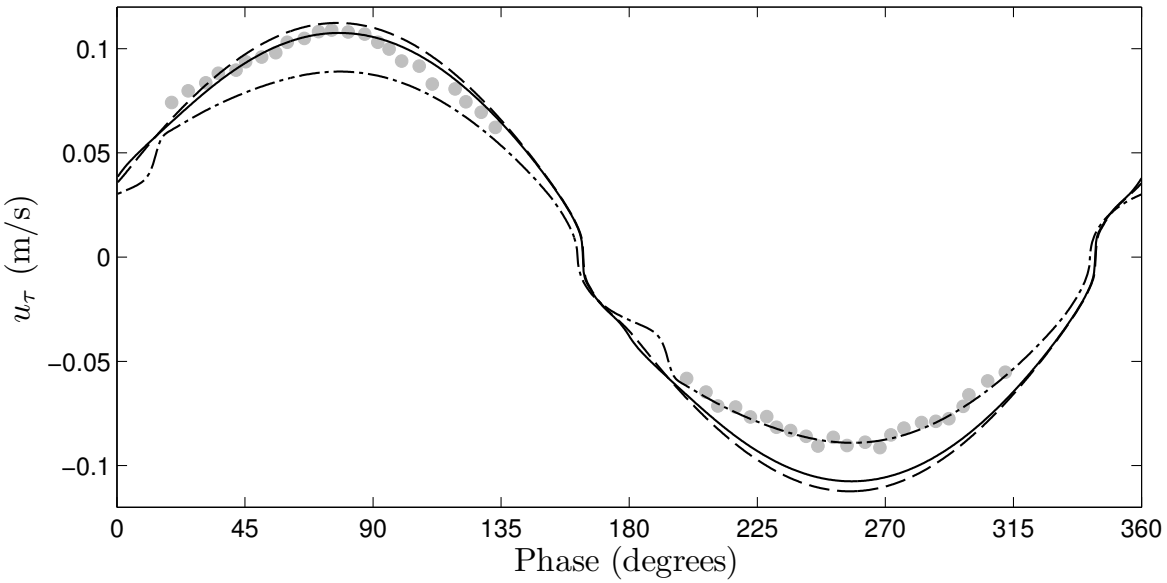

Figure 2.10 – Friction velocity over a rough bed. Grey dots: logarithmic fit, Test 13 [Jensen *et al.*, 1989]; line: Wilcox [2006] $k-\omega$ model, LRN version; dashed line: line: Wilcox [2006] $k-\omega$ model; dot-dashed line: Guizien *et al.* [2003] $k-\omega$ model, LRN version.

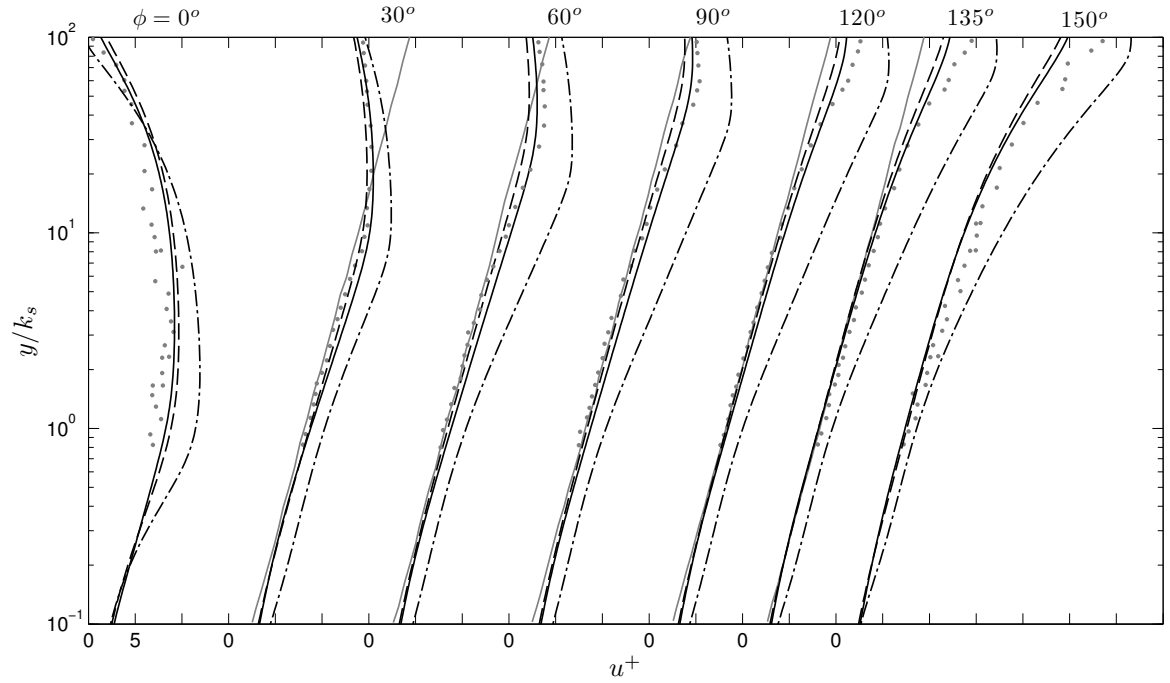

Figure 2.11 – Mean velocity distribution in semi-log plot, over a rough bed. Grey dots: experimental measurements, Test 13 [Jensen *et al.*, 1989]; black line: Wilcox [2006] $k-\omega$ model, LRN version; dashed line: line: Wilcox [2006] $k-\omega$ model; dot-dashed line: Guizien *et al.* [2003] $k-\omega$ model, LRN version; grey line: theoretical log-law for rough beds.

2.4.2 Validation with DNS results

The $k-\omega$ model is also compared to Direct Numerical Simulation (DNS) results , as shown in Guizien *et al.* [2003]. Indeed DNS results provide detailed information on turbulent kinetic and Reynolds Stress vertical distributions. The details from the DNS results, which are phase-averaged, can be found in Vittori et Verzicco [1998]. The hydrodynamical conditions are: $U_0 = 1.1\ m/s$, $T = 4\ s$, $R_\delta = 1241$ and $\delta = 1.128 \times 10^{-3}\ m$, with $\delta = \sqrt{\nu T/\pi}$ the viscous boundary layer thickness, and $R_\delta = U_0\delta/\nu$ is the boundary layer Reynolds number for steady flows. The wave forcing and corresponding pressure gradient are sinusoidal in time as defined in the Figure 2.7, and the bottom is considered smooth.

The DNS results are compared to three formulations of the $k-\omega$ model, the [Wilcox, 2006] formulation in its baseline and LRN version, and the [Guizien *et al.*, 2003] formulation.

If we look at the velocities at 4 distinct phases (Figure 2.12), the $k-\omega$ model is similar to the DNS model for $\phi = -45^o$ and $\phi = 0^o$, with an adverse pressure gradient and a negative velocity. For $\phi = 45^o$, we are after the flow reversal, with positive velocities and an adverse pressure gradient, at this phase the [Wilcox, 2006] formulation has some discrepancies, while the [Guizien *et al.*, 2003] formulation responds quite well compared to the DNS. At $\phi = 90^o$, we have positive velocities and no pressure gradient, and we observe that both the DNS results and the $k-\omega$ model reproduce a logarithmic region in the boundary layer.

The differences observed at $\phi = 45^o$ for the velocity profiles can be clearly explained if we look at the bed shear stress evolution (Figure 2.13). The DNS results show a transition from the laminar to the turbulent regime starting at $\phi = 50^o$ up to $\phi = 70^o$. There is also a period of relaminarization, near the flow reversal at $\phi = 180^o$ that cannot be clearly distinguished as there is no abrupt change in the bed shear stress. We also observe a second transition from laminar to turbulent starting at $\phi = 230^o$ up to $\phi = 250^o$.

The [Guizien *et al.*, 2003] formulation is able to predict the transition from laminar to turbulent, at around $\phi = 50^o$ which is similar to the DNS results, however the transition is much faster. Concerning the [Wilcox, 2006] formulation, the transition is far less important in terms of bed shear stress, and out of phase with the DNS results, as the transition occurs around $\phi = 20^o$. For all the formulations of the $k-\omega$ model considered, the maximum shear stress is under-estimated.

Concerning the turbulent kinetic energy at 4 different phases (Figure 2.14), the variation showed by the DNS results are reproduced by the $k-\omega$ model, the [Wilcox,

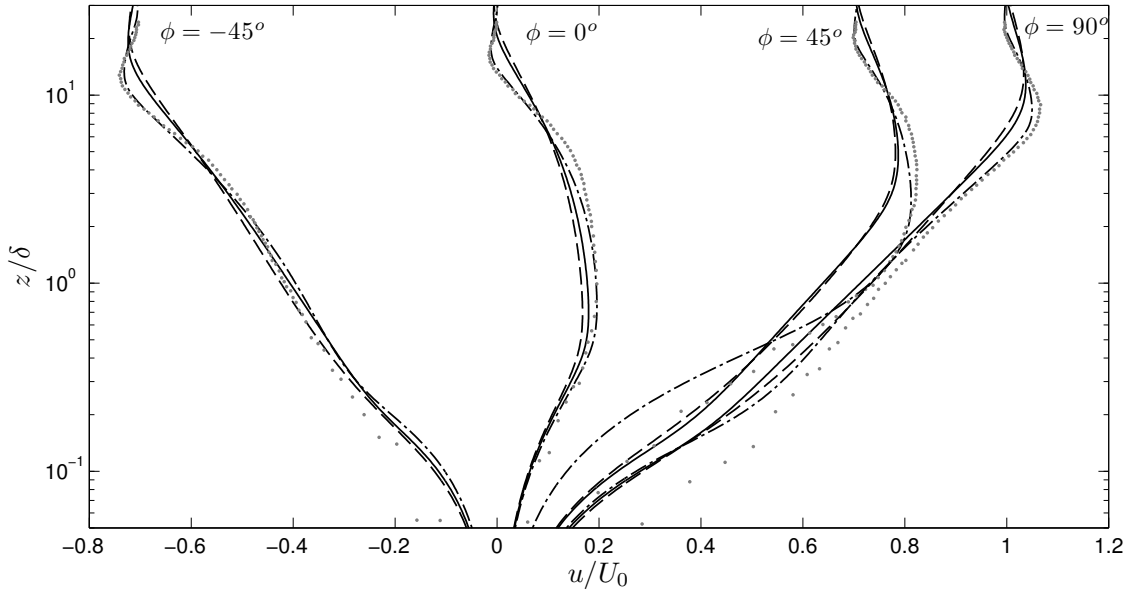

Figure 2.12 – Velocity vertical profiles at different phases; Grey dots : DNS results; black line: [Wilcox, 2006] LRN model (−); dashed line: [Wilcox, 2006] model; dot-dashed line: [Guizien *et al.*, 2003] LRN model.

2006] LRN formulation obtaining the best results in terms of shape and peak values. The Reynolds stress tensor is also plotted for the same 4 phases (Figure 2.15). The profiles obtained by the $k - \omega$ model present a vertical structure similar to the DNS results. From the comparisons with the DNS numerical modelling and the shear stress experimental data at different Reynolds number, we can conclude that the three formulations (Wilcox [1998], Wilcox [2006],Guizien *et al.* [2003]) are able to reproduce fairly well the evolution of the bottom boundary layer, however with slight differences. Although the transition from laminar to turbulent is better reproduced with the Guizien *et al.* [2003] formulation, from now on we choose the Wilcox [2006] formulation, as the vertical profiles at different phases are better reproduced, and additional terms for cross-diffusion and stress limiters are included.

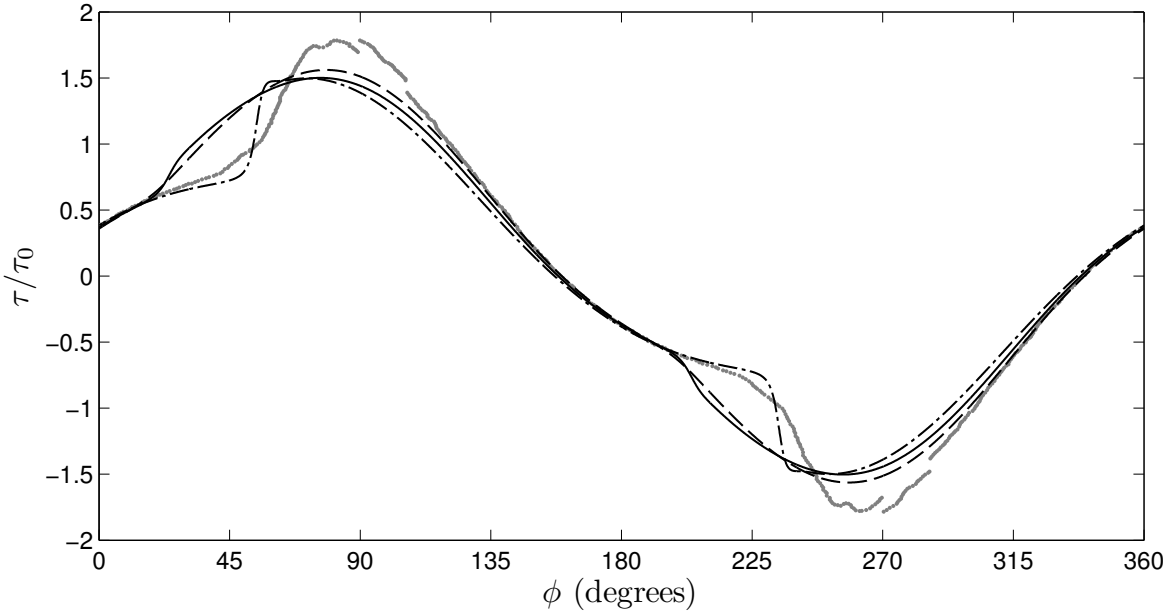

Figure 2.13 – Bottom shear stress time evolution over one period. ; Grey dots : DNS results; black line: [Wilcox, 2006] LRN model (−); dashed line: [Wilcox, 2006] model; dot-dashed line: [Guizien *et al.*, 2003] LRN model. τ_0 is the reference shear stress, defined as $\tau_0 = 2\pi\rho U_0\delta/T$.

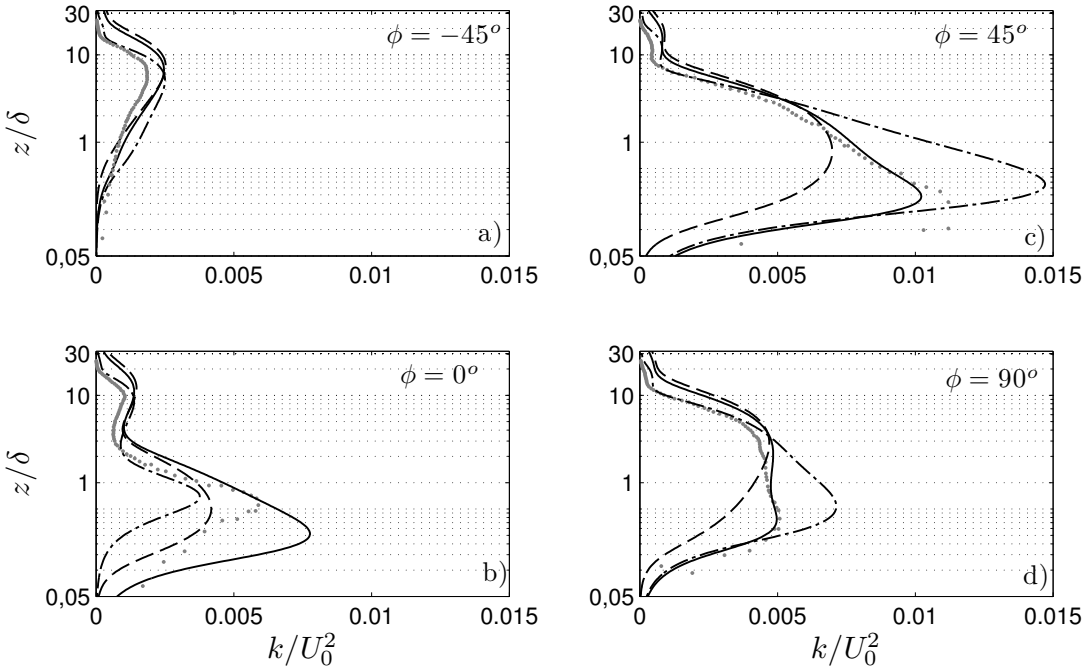

Figure 2.14 – Turbulent kinetic energy vertical profiles at different phases; symbols: see Figure 2.12.

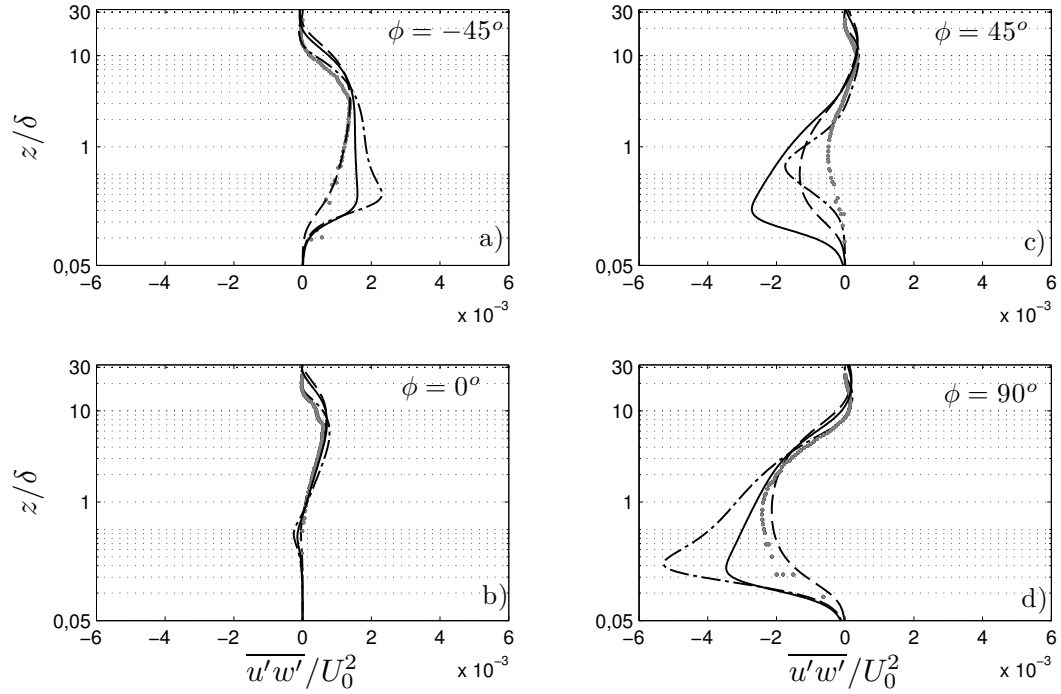

Figure 2.15 – Reynolds stress vertical profiles at different phases; symbols: see figure 2.12.

2.4.3 Asymmetric propagating wave on a fixed uniform slope

Lin et Hwung [2002] experiment

The streaming and horizontal pressure gradients are also important in the bottom boundary layer in the surf zone. To observe the ability of the numerical model to reproduce these features, it is compared to an experiment from Lin et Hwung [2002]. This experiment contains several important aspects of the oscillatory bottom boundary layer in the nearshore zone. The presence of the slope and the wave breaking induces a mean pressure gradient, and it is interesting to observe if this mean pressure gradient is more related to a set-up induced by the waves, or to advection caused by the slope.

The experiment took place in a glass-walled wave flume located at Tainan Hydraulic Laboratory, National Chen Kung University, China. The wave flume had a fixed horizontal smooth bottom of length 3.77 m, followed by a fixed smooth bed, with a slope of 1/15 (see Figure 2.16).

Monochromatic waves of height $H = 0.053$ m and period $T = 1.14$ s were generated over this fixed bathymetry. Velocity profile measurements were made using a one component Laser Doppler Velocimetry. The Stokes length is $\delta = 0.67$ mm for this experiment. Due to the limitations of the experimental facility, all the profiles are obtained in the pre-breaking zone and the bottom boundary layer flow is laminar [Lin et Hwung, 2002].

We focus on three distinct profiles, located at P_4, P_8 and P_{10}. The still water depth at these three positions are $d = 15.7$ cm, $d = 11.0$ cm and $d = 8.5$ cm respectively. The mean horizontal pressure gradient for these three profiles were 0.002 m/s^2, 0.005 m/s^2 and 0.010 m/s^2 respectively.

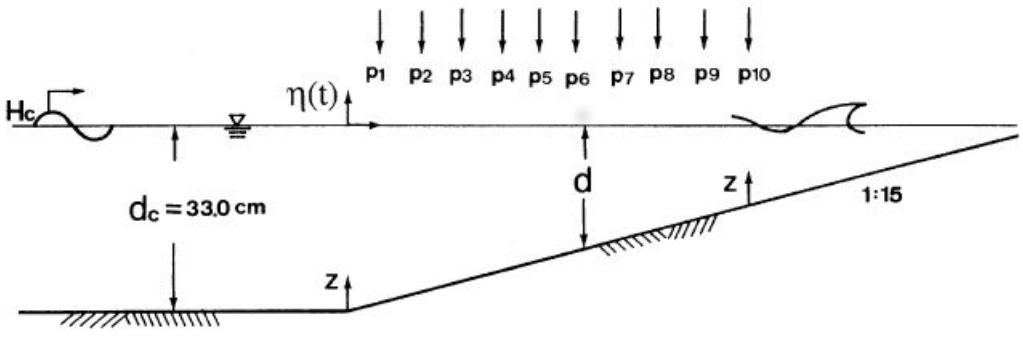

Figure 2.16 – Sketch of wave flume from Lin et Hwung [2002]. H_c is the wave height, d is the still water depth. The generated waves are monochromatic.

Numerical model

We use Wilcox [2006] in its LRN version and compare the results and observe the influence of the mean pressure gradient and the advection on the numerical results. Three different velocity profiles were calculated at three distinct positions, $P4$ (Figure 2.17), $P8$ (Figure 2.18) and $P10$ (Figure 2.19). The velocity at the upper boundary in the numerical model is set to the free-stream velocity, U_∞. The advection terms are deduced from the vertical velocity, w, estimated by equation (2.47), assuming that the vertical velocity at $z = z_0$ is zero, the z-axis being vertical.

The experimental results show that, as the waves come closer to the shoreline, the free-stream velocity becomes increasingly non-linear. In the accelerating phase (profiles a, b, c), we observe a strong overshoot in velocity at $z \approx 2\delta$ for the three gauges considered. We also note that the boundary layer thickness is roughly 8δ, around 5 mm for the three velocity profiles, showing that the bottom boundary layer is restricted to a thin layer near the bottom.

The numerical results show that this overshoot of velocity in the accelerating part is in part due to the mean pressure gradient and the advection produced by the beach slope, as when these terms are incorporated in the model, the velocity profiles are closer to the experimental ones. However, the effects of the sloping bed are not entirely accounted for, explaining the differences in the overshoot. As explained by Fuhrman *et al.* [2009b], the averaged velocity profile over the diverging half period and the converging half period are different, producing a slope-related streaming. This streaming induces an onshore mean velocity near the bottom boundary and an offshore velocity higher in the boundary layer, as shown experimentally by Sumer *et al.* [1993] and validated numerically by Fuhrman *et al.* [2009b]. These mean velocity profiles are similar to the ones from Lin et Hwung [2002] experiment, as we note that in the three profiles considered, the mean velocity profile have a strong similarity, the effect from the bed slope being more important than the streaming induced by the waveform. The streaming induces a translation of the mean vertical profile as it is constant within the bottom boundary layer, which is not the case for the advection terms induced by the slope.

Near the flow reversal (profile e) the numerical model has difficulties in adjusting the experimental velocity profile, probably due to the boundary layer separation that occurs at this phase, that is not modelled.

Except for the maximum velocity and the flow reversal, the numerical velocity profiles matches quite well the experimental results, and the addition of a mean pressure gradient and the advection terms improves the performance of the model. The bed slope effects are harder to match, due to the fact that with a 1D-vertical model the

converging-divergent effects are harder to account for.

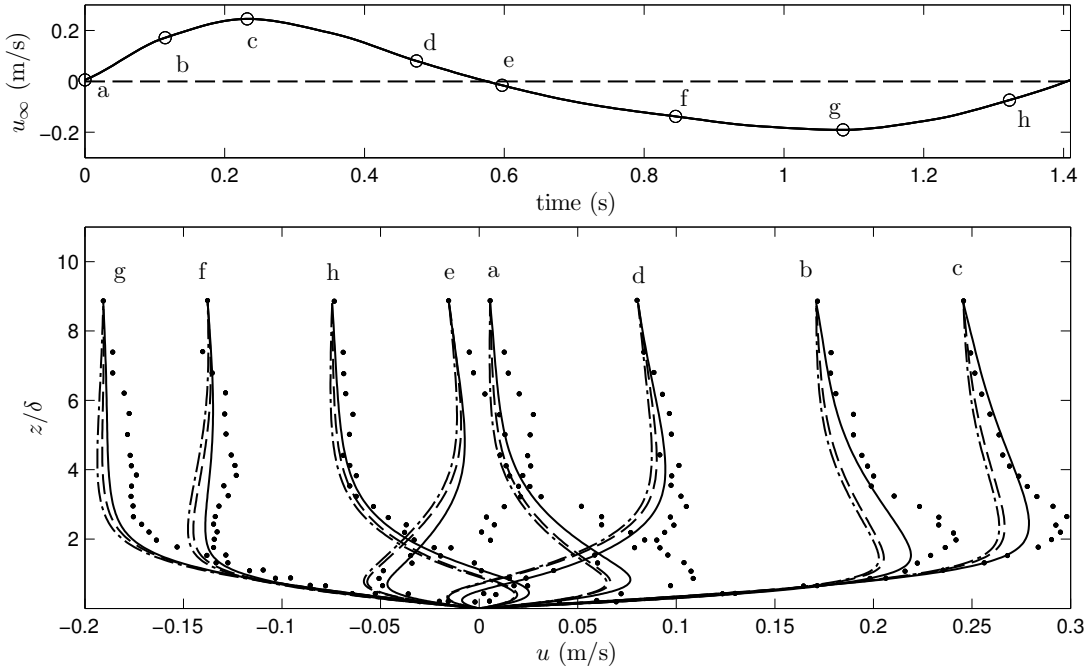

Figure 2.17 – Comparison of instantaneous velocity profiles at gauge P4. Upper panel: free-stream velocity at gauge P4, the circles indicate the time of the velocity profiles. Lower panel: Velocity profiles at the chosen times. $(\cdots)$: Lin et Hwung [2002] experimental results; $(- \cdot -)$: $k-\omega$ model without the mean pressure gradient; $(- - -)$: $k-\omega$ model with the mean pressure gradient; $(-)$: $k-\omega$ model with the mean pressure gradient and the advection terms.

Concerning the mean velocity profiles in Figure 2.20 , we observe that without mean pressure gradient the velocity profiles are negative in the whole boundary layer, whereas the experimental results shows a positive mean velocity for $z < 6\delta$. This positive mean velocity is in part due to the mean pressure gradient and the advection terms, as when incorporating them in the model, the mean velocity profiles improve, and we obtain positive mean velocities near the bottom boundary. There are still some discrepancies, due to the converging-diverging effect of the bed slope, as these terms are not modelled in a 1D vertical model, but the model shows a similar behaviour to the experimental results.

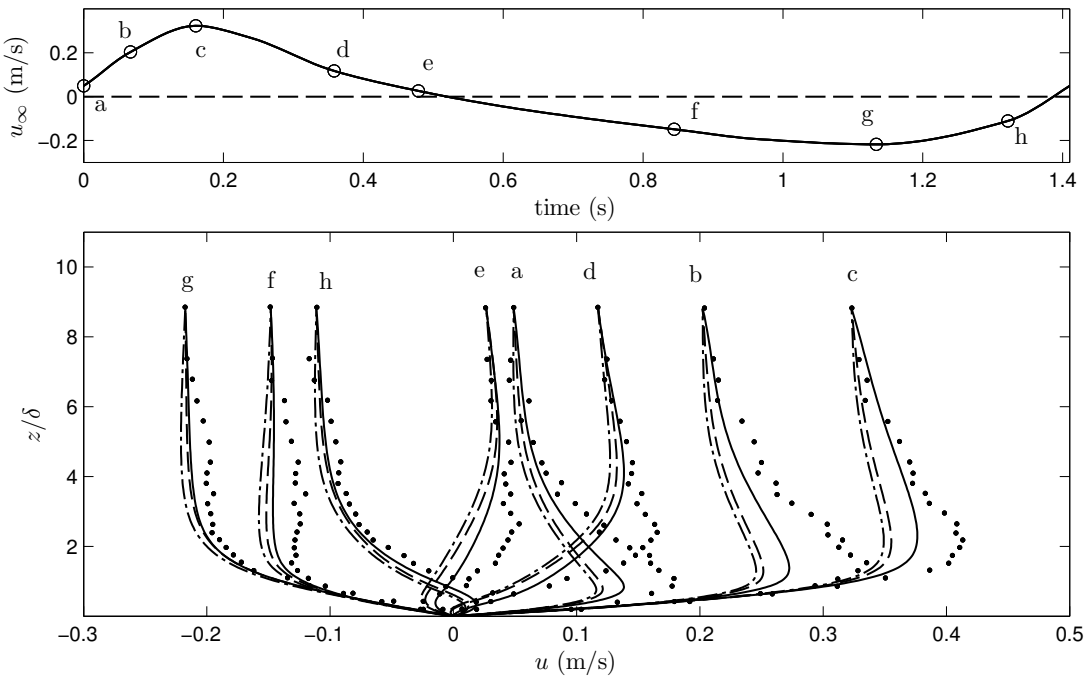

Figure 2.18 – Comparison of instantaneous velocity profiles at gauge P8. Captions, see Figure 2.17.

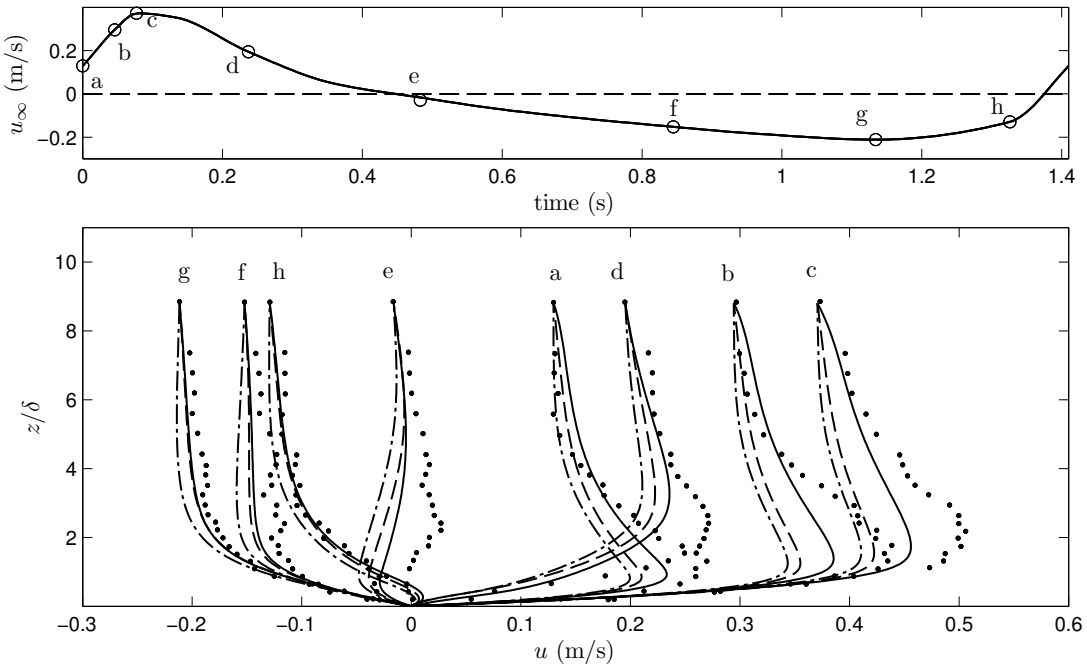

Figure 2.19 – Comparison of instantaneous velocity profiles at gauge P10. Captions, see Figure 2.17.

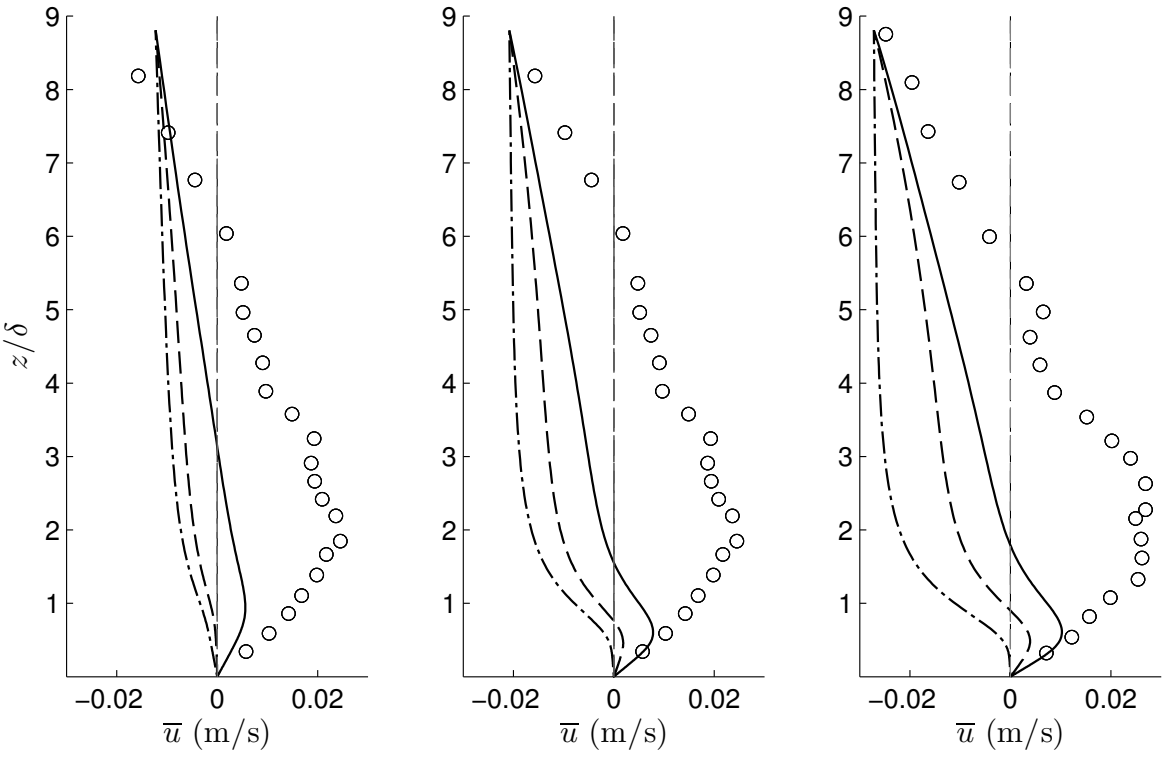

Figure 2.20 – Comparison of mean velocity profiles at gauges P4 (left panel), P8 (middle panel) and P10 (right panel). (o): Lin et Hwung [2002] experimental results; $(- \cdot -)$: $k-\omega$ model without the mean pressure gradient; $(- - -)$: $k-\omega$ model with the mean pressure gradient; $(-)$: $k-\omega$ model with the mean pressure gradient and the advection terms.

2.5 Conclusion

An unidimensional $k-\omega$ model has been proposed and validated on smooth and rough bottoms, against experimental and numerical results. The validation gives confidence in the model to study the evolution of the coastal bottom boundary layer under periodic flows. The incorporation of the advective terms, as well as the mean pressure gradient, improves the model capacity to reproduce the variations of the bottom boundary layer under periodic flows on the beach.

In the next chapter, the $k-\omega$ model is used to study the coastal bottom boundary layer subject to a bichromatic forcing under a mobile bed, and the subsequent evolution of non-linearities in the boundary layer.

Chapter 3

Evolution of non-linearities in the boundary layer

3.1 Introduction

Understanding sediment transport processes that occur in the nearshore zone are fundamental to understand the evolution of beaches. The longshore sediment transport is relatively well understood, but the cross-shore sediment transport remains hard to predict, due to the various non-linear processes occurring in the oscillatory boundary layer, such as the conventional streaming, the bed slope for the gravitational and converging-diverging effects, the shoaling, the wave skewness and asymmetry, the wave breaking, the wave drift and return currents, the undertow, the turbulence, the bottom roughness, the bed forms and percolation [Fuhrman *et al.*, 2009a].

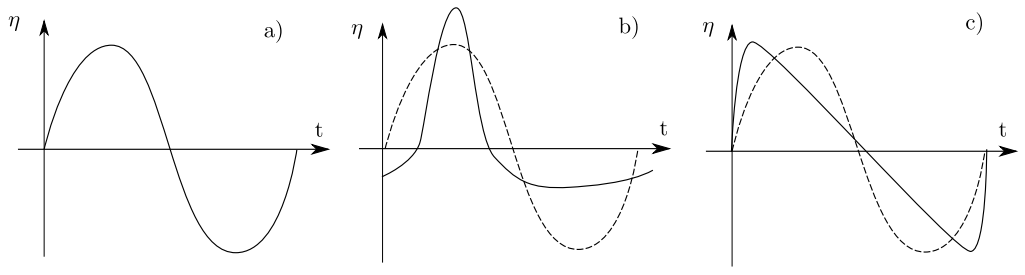

Figure 3.1 – Wave non-linearities. a) sinusoidal wave; b) skewed wave; c) asymmetric wave

In deep water, waves are essentially sinusoidal. When they approach the coast, due to the influence of the bottom, they become increasingly non-linear, showing skewed and asymmetric shapes. In Figure 3.1 we can see the difference between a sinusoidal wave, a skewed and an asymmetric one.

The skewness Sk_0 in free surface displacement which also gives a skewness in horizontal velocity, is characterized by waves with a pinched crest and a wide trough. They are common in the shoaling zone, where the influence of the bottom on the mass flux of water changes the shape of the waves. It is defined as [Nielsen, 2006]:

$$Sk_0 = \frac{\overline{(\eta(t) - \overline{\eta})^3}}{\eta_{\text{rms}}^3} \tag{3.1}$$

where the root-mean square of the free surface η_{rms} is defined as:

$$\eta_{\text{rms}} = \overline{(\eta(t) - \overline{\eta})^2}^{1/2} \tag{3.2}$$

with η the free surface displacement and an overbar stands for a mean value.

The asymmetry As_0 can be understood as a skewness in fluid horizontal acceleration, and is characterized by waves with steeper front, also known as saw-tooth shape waves. Asymmetric waves are mostly found in the inner surf zone, where broken waves have this shape. The asymmetry As_0 is defined as:

$$As_0 = \frac{\overline{\left(\frac{\partial \eta}{\partial t} - \overline{\frac{\partial \eta}{\partial t}}\right)^3}}{\overline{\left(\frac{\partial \eta}{\partial t} - \overline{\frac{\partial \eta}{\partial t}}\right)^2}^{1/2}} \tag{3.3}$$

The asymmetry can also be defined using the third order moment of the Hilbert transform [Elgar, 1987]:

$$As_0 = -\frac{\overline{\Im(\mathcal{H}(\eta))^3}}{\eta_{\text{rms}}^3} \tag{3.4}$$

with the overbar denoting a time-average over the studied interval, $\mathcal{H}(\eta)$ is the Hilbert transform of η and $\Im$ the imaginary part. The skewness and asymmetry of the wave can also be determined by its velocity time-series.

These non-linearities are an important mechanism for sediment transport. In absence of streaming, when the wave is purely sinusoidal, the onshore sediment flux induced by crest velocities balances exactly the offshore flux of the trough velocities. When the waves becomes skewed due to the wave shoaling, the difference of velocities between crests and troughs, as well as the time lapses between crests and troughs, will generate an onshore sediment transport [Dibajnia et Watanabe, 1992 ; Dohmen-Janssen *et al.*, 2002 ; Hsu et Hanes, 2004 ; Grasso *et al.*, 2011]. Concerning non skewed but asymmetric waves, although the onshore velocities balances the offshore velocities over

one period, an onshore sediment transport has also been reported [King, 1991 ; Elgar *et al.*, 2001 ; Ruessink *et al.*, 2011]. One interesting feature outlined by recent laboratory experiments [van der A *et al.*, 2010 ; Ruessink *et al.*, 2011] is that an asymmetric wave shape induces a skewed shear stress in the boundary layer. According to Nielsen [1992] this feature is related to the boundary layer thickness, that grows differently in the rapidly accelerated half cycle, and in the less accelerated one, producing vertical gradients in the flow that lead to an enhanced shear stress. This relation between an asymmetric wave and a skewed shear stress has been observed with a $k-\omega$ numerical model by Fuhrman *et al.* [2009a], and in U-tube laboratory experiments [van der A *et al.*, 2011 ; Abreu *et al.*, 2013].

A theoretical predictor of the relation between the free flow non-linearities and boundary layer ones was suggested by Henderson *et al.* [2004], following a work on bi-spectrum analysis by Elgar [1987], assuming that the phase shift depended on the frequency, thus changing the shape of the wave from asymmetric to skewed. He also found the existence of a linear relation between the near-bed skewness and the free-stream asymmetry.

Another important feature of the bottom boundary layer on beaches is that the bed is mobile and sediment is transported as the waves affect the bottom. It is very common to apprehend boundary layers on mobile beds with the tools of boundary layers on fixed bottom [Sleath, 1987 ; Jensen *et al.*, 1989]. [Dohmen-Janssen *et al.*, 2001] observed the evolution of a mobile bed for oscillatory sheet-flows (when large amounts of sand are transported in a thin layer close to the bed) with an oscillatory water tunnel, and deduced from the measurements that the sheet-flow layer led to an increased resistance in the outer flow and the reduction of the turbulence and sediment mixing in the suspension layer. Sparrow *et al.* [2012] showed that a permeable bed modifies the wave boundary layer dynamics, leading to an increase in the friction and a dependence of the friction on the Reynolds number.

The first part of this chapter has been accepted for publication in La Houille Blanche, International Water Journal [Suarez *et al.*, 2014]. This work investigates the influence of the bed mobility on the bottom boundary layer during a bichromatic wave forcing, inducing a vertical diffusion of the boundary layer [Berni *et al.*, 2013]. In this experiment, the velocity profiles were obtained using an Acoustic Doppler Velocity Profiler (ADVP). The upper limit of the boundary layer was chosen where the root mean square velocity remained constant.

Concerning the vertical distribution of the skewness and the asymmetry in the bottom boundary layer, the linear relation between the near-bed skewness and the free-stream asymmetry Berni *et al.* [2013] has been validated both experimentally and

using the $k-\omega$ numerical model.

To obtain a wide range of skewed and asymmetric waves, the theoretical formula of Abreu *et al.* [2010] has been used. This formula reproduces fairly well the type of waves that occur in the nearshore zone. The velocity related to the wave forcing is defined as:

$$U(t) = U_w f_r \frac{\sin(\sigma t + \frac{r\sin\phi}{1+\sqrt{1-r^2}})}{1 - r\cos(\sigma t + \phi)} \tag{3.5}$$

where U_w is the amplitude of the orbital velocity, $\sigma = 2\pi/T$ the angular frequency, r the index of skewness and ϕ the waveform parameter. The variable f_r is a dimensionless factor function of r, $f_r = \sqrt{1-r^2}$, used to obtain a velocity amplitude equal to U_w.

By allowing the index of skewness r to vary between 0 and 0.75 and the waveform parameter ϕ to vary between $-\pi/2$ and 0, numerous different types of waves were used in the numerical model to relate the near-bed skewness to the free-stream asymmetry. The linear dependence obtained is similar to the one obtained with the experimental results from Berni *et al.* [2012]. This part has resulted in a communication at the International Conference on Coastal Engineering in July 2012 [Berni *et al.*, 2012].

VERTICAL DISTRIBUTION OF SKEWNESS AND ASYMMETRY IN A BOUNDARY LAYER ON A MOBILE BED. EXPERIMENT AND $k-\omega$ MODEL COMPARISON

Leandro SUAREZ[(1)], Eric BARTHELEMY[(2)], Céline BERNI[(3)]
Julien CHAUCHAT[(2)], Hervé MICHALLET[(2)], Rodrigo CIENFUEGOS[(1,4)]

(1) Departamento de Ingeniería Hidráulica y Ambiental, Pontificia Universidad Católica de Chile, Vicuña Mackenna 4860, casilla 306, correo 221, Santiago de Chile, Chile. e-mail: lsuarez2@uc.cl racienfu@ing.puc.cl

(2) Laboratoire des Ecoulements Géophysiques et Industriels (UJF, GINP, CNRS), BP53, 38041 Grenoble Cedex 9, France. e-mail: eric.barthelemy@legi.grenoble-inp.fr; julien.chauchat@legi.grenoble-inp.fr; herve.michallet@legi.grenoble-inp.fr

(3) IRSTEA, UR HHLY, équipe hydraulique des rivières, Centre de Lyon, 5 rue de la Doua, CS 70077, 69626 Villeurbanne Cedex. e-mail: celine.berni@irstea.fr

(4) CIGIDEN, Centro Nacional de Investigación para la Gestión Integrada de Desastres Naturales, Vicuña Mackenna 4860, casilla 306, correo 221, Santiago de Chile, Chile

As the waves approach the coast, non-linearities become increasingly stronger. The interactions between the waves and loose bottoms then generate complex features within the turbulent boundary layer, which are difficult to measure and model. Experiments involving non-linear wave propagation over a mobile bed with detailed boundary layer velocity measurements and bottom elevations are presented. These data suggest a transformation in velocity time series as they are measured closer to the bed within the boundary layer with an increase in velocity skewness and a reduction in asymmetry. Additionally the vertical diffusion of momentum within the boundary layer is shown to be one order of magnitude larger than that over fixed beds. A $k-\omega$ model accounting for the measured bed level variations is used to mimic the flow in the boundary layer. In this work we present a strategy to combine bottom level variations with a $k-\omega$ model and show that it is possible to reproduce the observed experimental results. The bed vertical mobility is shown to be largely responsible for additional vertical diffusion of momentum within the boundary layer.

Key Words: non-linear waves, boundary layer, diffusivity, mobile bed

Distribution verticales d'asymétrie et de skewness dans une couche limite sur fond mobile. Une comparaison expériences - modèle $k-\omega$

Lorsque les vagues se rapprochent de la côte, leurs non linéarités augmentent. Les interactions entre les vagues et un fond mobile produisent des effets complexes sur la couche limite turbulente pariétale qui sont difficiles à mesurer et à modéliser. Des mesures réalisées dans un modèle physique de propagation de vagues non-linéaires sur fond mobile sont présentées. L'analyse conjointe des profils de vitesse et d'évolution du fond suggère une transformation au sein de la couche limite, par laquelle l'asymétrie horizontale des vitesses (skewness) augmente au fur et à mesure que l'asymétrie (skewness de l'accélération) diminue en se rapprochant du fond. De plus on constate que la diffusion verticale dans cette couche limite est plus importante sur fond mobile que sur fond fixe. Dans ce travail nous présentons une stratégie pour combiner les variations verticales du fond avec un modèle $k-\omega$ et montrons que celle-ci permet de reproduire les mesures expérimentales. Nous montrons que la mobilité verticale du fond est responsable de l'augmentation de la diffusion verticale de quantité de mouvement dans la couche limite.

Mots-clefs: houle non-linéaire, couche limite, diffusivité, lit mobile

I INTRODUCTION

Complex flow-sediment interactions are observed within the turbulent boundary layer produced under nearshore waves propagating over loose bottoms. When approaching the coast, the shoaling waves undergo non-linear transformations and dissipation during breaking that impact the boundary layer dynamics. Since the pioneering work by [Bailard, 1981] it is of common understanding that free stream velocity skewness is a key parameter for estimating the rate of sediment transport. In the last decade

it has been suggested that asymmetric waves also produce net sediment transport (see for instance [Ruessink et al., 2009]). Bottom velocity skewness and asymmetry depend on how the boundary layer develops. In this paper we will focus on the study of the turbulent boundary layer resulting from surf zone wave propagation over a mobile bed.

Using the experiments over a scaled sandy bottom of Berni et al. [2013], we attempt to characterize the near bed evolution of velocity profiles and its relation with free stream velocities. The experiments also showed an intriguing strong vertical momentum diffusion in the turbulent boundary layer. Vertical diffusion of momentum is easily quantified by computing the boundary layer thickness defined, for instance, as the height where the defect velocity is 5 % of the free stream velocity.

The laminar boundary layer thickness is a function of the Stokes length δ which reads,

$$\delta = \sqrt{\nu T/\pi} \tag{1}$$

where ν is the water viscosity and T is the wave period. The laminar boundary layer thickness is roughly $3\,\delta$ and is generally very small. For the experimental conditions studied by Berni et al. [2013] its value is of $\simeq 3$ mm. For rough turbulent boundary layers on fixed sand beds the boundary layer thickness δ_t can be estimated empirically as [Sleath, 1987],

$$\frac{\delta_t}{k_s} = 0.27 \left(\frac{A}{k_s}\right)^{0.67} \tag{2}$$

where A is the fluid particle excursion at the bottom, k_s the Nikuradse equivalent roughness. Sleath [1987] recommends the use of $k_s = 2.5\,d_{50}$, d_{50} being the median grain diameter. In the case of the $T = 2.5$ s experiments of Berni et al. [2013] the value of the turbulent boundary layer thickness estimated by (2) is $\delta_t \simeq 6$ mm. None of the two previous estimators pertain to mobile bed boundary layers (as discussed further in section III). Experiments of Berni et al. [2013] indicate that the boundary layer thickness can be as thick as $20\,\delta$ (nearly 2 cm), exceeding the predicted value given by (2). This seems to indicate that vertical momentum diffusion in the case of a mobile bed is stronger than in the fixed bed case.

The aim of this paper is to develop a novel strategy to take into account the effect of loose bottom vertical motions on the near bed velocity profiles and vertical momentum diffusion through a 1D $k-\omega$ RANS model.

II METHODS

II.1 Experimental set-up and wave conditions

The experiments took place in the LEGI wave flume, with nonlinear waves propagating over a scaled beach profile made of loose material (figure 1). The flume is 36 m long, 55 cm wide and 1.30 m high. The bottom granular material is made of plastic particles of low density ($\rho_s = 1,180\,\mathrm{g\,L^{-1}}$) and of median diameter $d_{50} = 0.64$ mm, ensuring a Froude and Shields similitude [see extensive details in Grasso et al., 2009]. The elementary wave forcing used in the experiments is the combination of two single bichromatic wave packets of carrier period $T = 2.5$ s and $T = 3$ s respectively, combined in one wave sequence. In the present paper we will only analyze the dynamics of the boundary layer induced by the 2.5 s wave train (figure 2). The effective experimental forcing consists in 50 repetitions of the wave sequence described above. Before the wave sequence's run, in order to perform reliable phase averages on the free surface and velocity measurements, the experiment was run until the beach profile reached a quasi-equilibrium [Berni et al., 2013]. Phases averages were performed over the last 29 wave trains. Furthermore, in the subsequent analysis we have selected a specific 10 s interval in each of these 29 wave trains. This interval is made out of four waves of similar amplitude and shape in the middle of the wave packet (see figure 3). The average breaking point was roughly stationary at $x \simeq 9$ m. Velocity time series were verified so that spikes associated to the presence of air bubbles (specially in the surf zone) did not represent more than 3 to 5 % of the measured points.

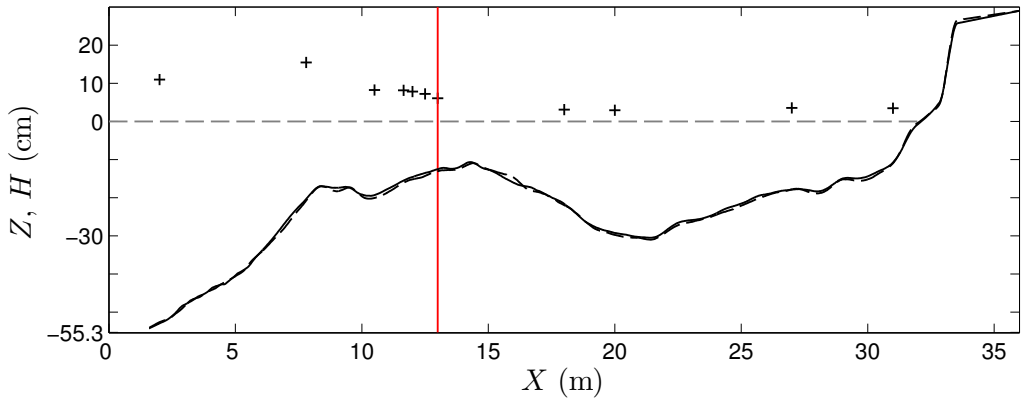

Figure 1: **Experimental cross-shore bed profiles.** Smoothed cross-shore profile of the bed elevation. Solid and dashed black lines correspond to bed profiles separated by 50 wave trains of wave action. The horizontal dashed grey line represents the still water level. The black crosses indicate the mean wave height H of the wave train. The ADVP was located at $x = 13$ m, indicated by the red vertical line.

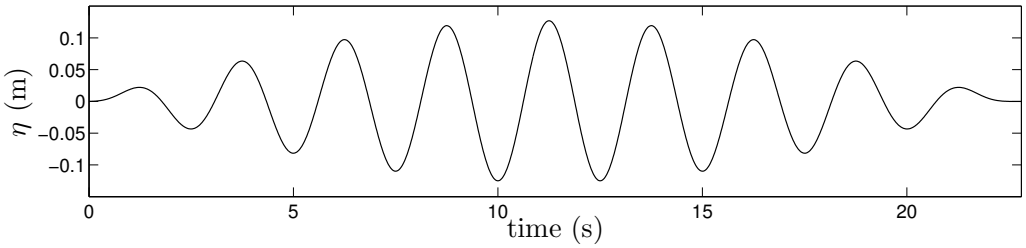

Figure 2: **The wave forcing.** Prescribed bichromatic free surface displacement η at the wavemaker. The carrier wave period is $T = 2.5$ s.

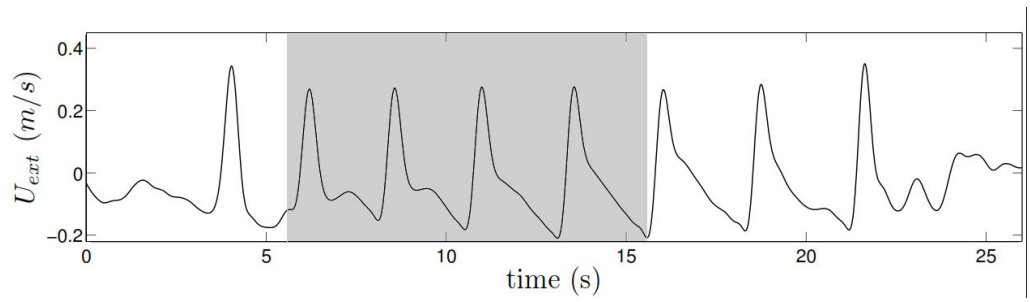

Figure 3: **Free stream velocity**. Phase averaged velocity records of the 2.5 s wave packet at the cross-shore position $x = 13$ m and at an elevation of $z = 3.6$ cm above the mean bed elevation. The grey-tinted box bounds the waves used in the analysis.

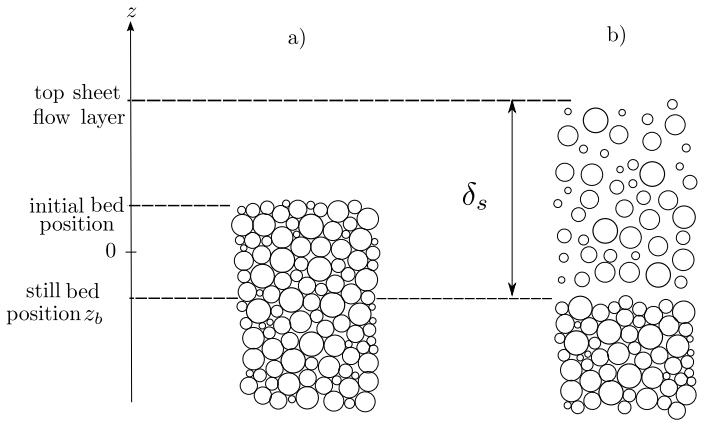

Figure 4: **Schematic of the bed evolution**. $z = 0$ is the average position of the still bed and z_b is the position in time of the still bed level. a) near-bed configuration prior to wave forcing; b) bottom configuration during wave action. δ_s represents the sheet flow layer thickness.

II.2 Bed level measurements

Since the waves propagate on a loose bed, we define the instantaneous still bed position, $z_b(t)$, as the elevation of the limit between the moving fluid-sediment mixture and the motion-less sediment bed (see figure 4). The moving fluid-sediment mixture contains the sheet flow layer. The instantaneous position of the still bed and the evolution of the horizontal cross-shore velocity vertical profile were obtained with a vertical spatial resolution close to 3 mm by using an Acoustic Doppler Velocity Profiler (ADVP). The mean water depth at the location of the velocity measurements (at $x = 13$ m) was $h = 0.125$ m. The procedure for collecting the data presented here has been described thoroughly in Berni et al. [2013]. The ADVP is able to detect the top of the sheet-flow layer as well as the bottom of the sheet flow layer representative of the still bed [Berni et al., 2012]

An example of measured instantaneous still bed position is plotted in figure 5. A filtered time series is computed by applying a low-pass filter with a cut-off at 5 Hz. The filtered time series of still bed elevations shows a still bed evolution qualitatively consistent with the external wave velocity forcing: still bed lowering at phases close to the wave crests at the same time as the sheet flow layer develops with an increase in δ_s.

The evolution of the still bed position z_b can be described by a probability density function (pdf). The mean value of z_b is zero. The standard deviation of the instantaneous still bed elevation is $\sigma_{z_b} = 3.6 \times 10^{-3}$ m. We show in figure 6 two estimations of the still bed elevation pdf. One is directly the pdf of the raw measurements and the other is deduced from a low-pass filtering of z_b. In figure 6 a standard Gaussian distribution, with this same standard deviation σ_{z_b} is also plotted. It appears to be close to the experimental pdf of the non-filtered still bed elevation. The still bed positions are seen to essentially remain in a strip of width $\pm 5\,\delta \simeq \pm 5$ mm (δ being the Stokes length (1)).

II.3 Velocity measurements

As indicated previously the ADVP provides instantaneous velocity measurements at 50 Hz. A clip of the instantaneous velocity time series is shown in figure 5. This clip is a part of the 29 clips used for the ensemble averaging given in figure 3. Notice that the record shows the signature of turbulent fluctuations some of which are stronger at flow reversal (see also the $-5/3$ slope in the power spectra shown in [Berni et al., 2013]). Instantaneous velocities at $x = 13$ m also show pinched crests and secondary crests velocities associated to highly non linear wave propagation inside the surf zone also evidenced by the spectral analysis presented by [Berni et al., 2013]. Waves are also asymmetric with steep wave fronts and gentle seaward slopes. These last features are a consequence of wave breaking occurring a few meters before the measurement point.

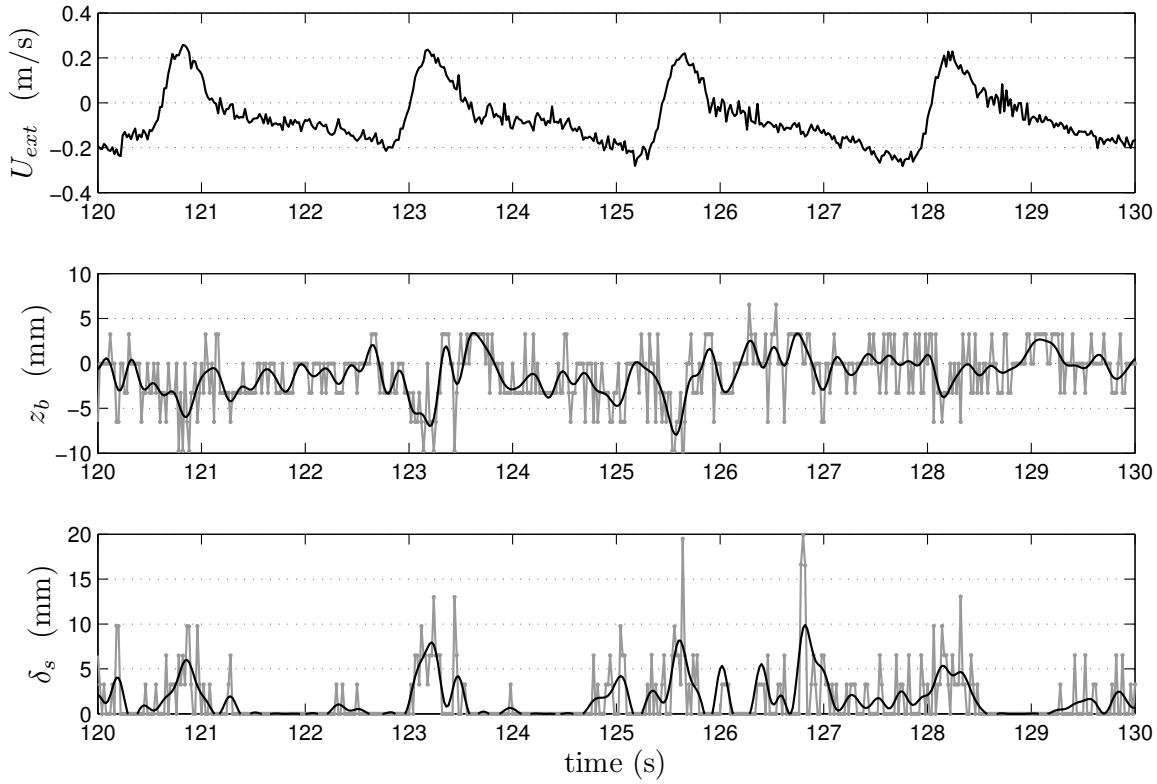

Figure 5: **Instantaneous velocities, still bed levels and sheet-flow layer thickness**. Top panel : one of the 29 records of instantaneous free stream velocity at $z = 3.6$ cm; middle panel : still bed displacements phased with the velocities in the top panel . Bottom panel : sheet flow layer thickness δ_s also phased with the velocities. Thin grey line: instantaneous still bed elevations; Thin black line: low-pass filtered still bed elevations.

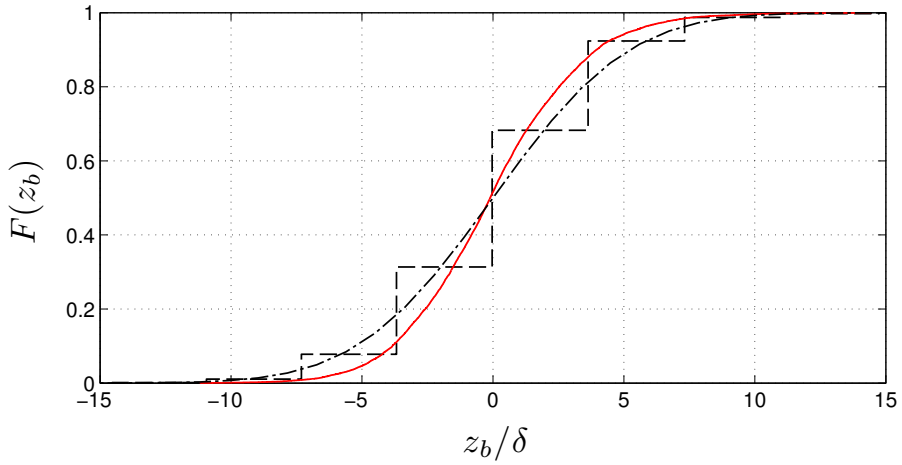

Figure 6: **Cumulative frequency distribution**. dashed line: instantaneous still bed pdf; dot/dashed line: low-pass filtered still bed pdf; plain line: gaussian pdf with the same standard deviation as the instantaneous still bed displacements.

The skewness and the asymmetry are key tools to analyze the nonlinear characteristics of the flow characteristics. The dimensional skewness Sk vertical profile and the dimensional asymmetry As vertical profile of the velocity time series are computed from measured time series using formula (3–4):

$$Sk(z) = \overline{(u(z,t) - \overline{u})^3} \tag{3}$$

$$As(z) = -\overline{\Im(\mathcal{H}(u))^3} \tag{4}$$

where $u(z,t)$ is the cross-shore horizontal velocity, with the overbar denoting a time-average over the studied interval, $\mathcal{H}(u)$ is the Hilbert transform of u and $\Im$ the imaginary part.

The time averaging of velocity measurements at vertical positions that can be alternatively in the flow or inside the bed requires a specific treatment. Indeed some measuring volumes of the ADVP can at some instances be below the still bed level. When this happens the ADVP does not provide a reliable velocity value. It is decided to prescribe a 0 value of the velocity for this cases. It is physically sound to do so since the Eulerian velocity of the sediment/fluid mixture can be reasonably approximated to 0 when the latter occurs. Such a procedure was applied to the data of [Berni et al., 2013] presented here. As the $z = 0$ elevation, corresponding to the mean still bed level, is 50 % of the time below the still bed level, 50 % of the time series is padded with zeros. Moreover the point at $z \simeq -4\,\delta$ (see fig. 7) is found to be in the moving sediment/fluid mixture roughly 20% of the time and therefore about 80 % of the time series is padded with zeros.

The effect of this procedure can be evaluated for the root mean square velocity u_{rms}, computed as:

$$u_{\mathrm{rms}}(z) = \sqrt{\overline{(u(z,t) - \overline{u})^2}} \tag{5}$$

where the time series is padded with zeros following the procedure explained above. The vertical profile of u_{rms} is given in figure 7 and note that below $z = 0$, u_{rms} is very small. The velocity series padded with zeros are also used to compute Sk and As according to equations (3) and (4), respectively.

II.4 Numerical model

The horizontal mean velocities near the bed are numerically computed with a 1DV $k-\omega$ turbulent boundary layer model in a Low Reynolds Number version ([Guizien et al., 2003; Wilcox, 2006]). The turbulent kinetic energy k equation includes cross-correlation terms between the gradient of k and the gradient of ω (specific dissipation rate) to accommodate for adverse pressure gradients. The bottom boundary condition on the turbulent kinetic energy k is $\frac{\mathrm{d}k}{\mathrm{d}z} = 0$ as suggested by [Fuhrman et al., 2010] in order to specifically mimic a rough bottom boundary instead of $k = 0$ that inevitably forces a viscous sub-layer whatever the Reynolds number is. Additionally the boundary Nikuradse equivalent roughness k_s is prescribed in the wall boundary condition for ω.

The nonlinear equations for the horizontal velocity u, the turbulent kinetic energy k and the specific dissipation rate ω are solved using an implicit finite control volume method [Patankar, 1980], with a staggered grid for k and ω.

The model is forced with the time series of the measured (free-stream) velocity at elevation $z = 2$ cm where u_{rms} is maximum. The computational grid on the vertical is a classic geometric grid of 200 nodes from $z_0 = 10^{-6}$ m to $z = 2$ cm. The convergence of the numerical model is estimated considering that the time-series input length as a pseudo-period. The numerical model is iterated computing its results within the entire time series and pseudo-period, the velocity relative error between 2 pseudo-periods is estimated as:

$$err_u = \frac{||u_1 - u_0||_2}{||u_0||_2} = \sqrt{\frac{\sum_z \sum_t (u_1(z,t) - u_0(z,t))^2}{\sum_z \sum_t u_0(z,t)^2}} \tag{6}$$

where $u_0(z,t)$ represents the solution of the previous pseudo-period, and $u_1(z,t)$ the solution of the current pseudo-period. The convergence is reached by iterating the entire time-series until err_u is lower than the desired precision taken as 10^{-6}.

Stratification effects have been neglected in this paper as sediment particles can be considered as massive, the ratio of their settling velocity to the shear velocity is of order unity or lower, therefore

a low suspension is observed. Stratification effects are clearly observed with fine sand (i.e. high ratio of settling velocity to shear velocity) but not with medium sand [O'Donoghue and Wright, 2004]. The processes responsible for the damping of turbulence in the dense sheet-flow layer is still an open question and it is thought that stratification is not the key mechanism.

III RESULTS

Simulations with the $k-\omega$ numerical model on a fixed bed placed at $z=0$, are plotted in figure 7 and 8. On these plots two different runs with two roughness height k_s are given. One is the parametrization by [Wilson, 1989] for uniform steady sheet flows:

$$k_s = 5\,\theta\,d_{50} \tag{7}$$

and the other is the one provided by [Nielsen, 2005] related to measurements on flat sand mobile bed:

$$k_s \simeq 70\,\sqrt{\theta}\,d_{50} \tag{8}$$

where θ is the Shields number of the flow.

The numerical results obtained using relation (8) show a larger vertical diffusion of momentum as expected compared to the simulation with the relation (7) but the maximum computed $u_{\rm rms}$ is located at $z=5\,\delta$, while the maximum experimental $u_{\rm rms}$ is at $z=23\,\delta$. The vertical shape is also qualitatively different. Indeed the fixed bed computations show an over-shoot in orbital velocity not evidenced in the experiments. The dimensional skewness and asymmetry vertical profiles are also qualitatively very different. Moreover maximum skewness value is over-predicted by the model computations on fixed bed. The non-dimensional values of the skewness Sk^* ($Sk^* = Sk/u_{\rm rms}^3$) and asymmetry As^* ($\mathrm{As}^* = As/u_{\rm rms}^3$) are plotted in figure 7. Because $u_{\rm rms}$ decreases towards the bottom more rapidly than the skewness, the Sk^* strongly increases closing up on the bottom. This result already shown by [Berni et al., 2013] is in line with those of [Henderson et al., 2004] for in-situ measurements. Experimental profiles show a much stronger vertical spreading than numerical results not to mention that the model cannot predict velocities below $z=0$ even though fluid flows there from time to time. Above $z=0$ all experimental dimensional values are smaller than the model predicted ones.

To explain such qualitative behavior we hypothesize that the upward vertical motions of the still bed is producing an upward flux of small horizontal momentum in regions of higher momentum while the opposite occurs for downward motions of the still bed. This induces velocities larger than 0 below $z=0$ and velocities smaller than on a fixed bed above $z=0$. This effect acts as a supplementary vertical diffusion that cannot be accounted for even when choosing very strong bed roughnesses. To quantitatively reproduce this phenomenon we combine vertical still bed motion information with the $k-\omega$ computations.

Associated to the free stream velocity time series the model computes times series of the velocity $u(z,t)$ at different elevation. Moreover synchronized with the free stream velocity time series, the experimental data provides $z_b(t)$ which is used to define a new velocity time series as,

$$u'(z,t) = u(z-z_b(t),t) \quad \text{for} \quad z > z_b \tag{9}$$

$$u'(z,t) = 0 \quad \text{for} \quad z \le z_b \tag{10}$$

For this new times series the still bed elevation z_b can either be the low pass filtered or the instantaneous one (fig.6). In replacing the original time series by this new one it is implicitly assumed that the boundary layer adapts instantaneously to each still bed position.

Substituting u' for u in (3), (4) and (5) defines post-processed u_{rms}, skewness and asymmetry. These new estimates are also plotted in figure 7. Dimensional skewness and asymmetry are plotted in 8 along with the mean velocity. The improvement on all quantities is obvious. The novel technique is particularly effective for the mean velocity $\overline{u}$ and the skewness. The improvement on the vertical profile of the asymmetry is not as good. However the qualitative shape is close. The mean velocity $\overline{u}$ vertical profile shows that an undertow is present in the experiments compensating for the Stokes mass flux drift and roller induced mass flux. This undertow is present in the free stream velocity and what the novel 1DV model reproduces is the correct vertical structure within the boundary layer.

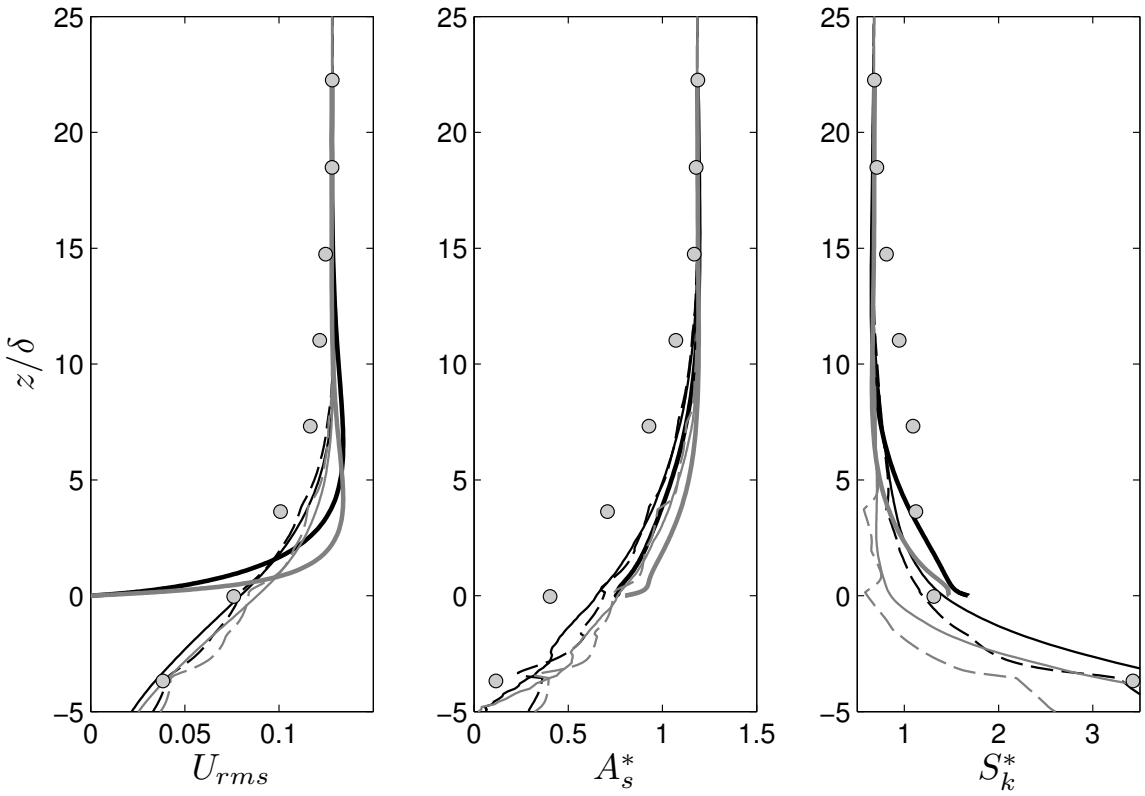

Figure 7: **Orbital velocity, dimensionless asymmetry and dimensionless skewness.** Left panel: orbital velocity; middle panel non-dimensional velocity asymmetry; right panel: non-dimensional velocity skewness. Grey bullets: experimental data; black lines: computations with (8); grey lines: computations with (7); Thick lines: fixed bed computations; thin lines: computations with the low-pass filtered still bed positions in (9); dashed thin lines: computations with the instantaneous still bed positions in (9).

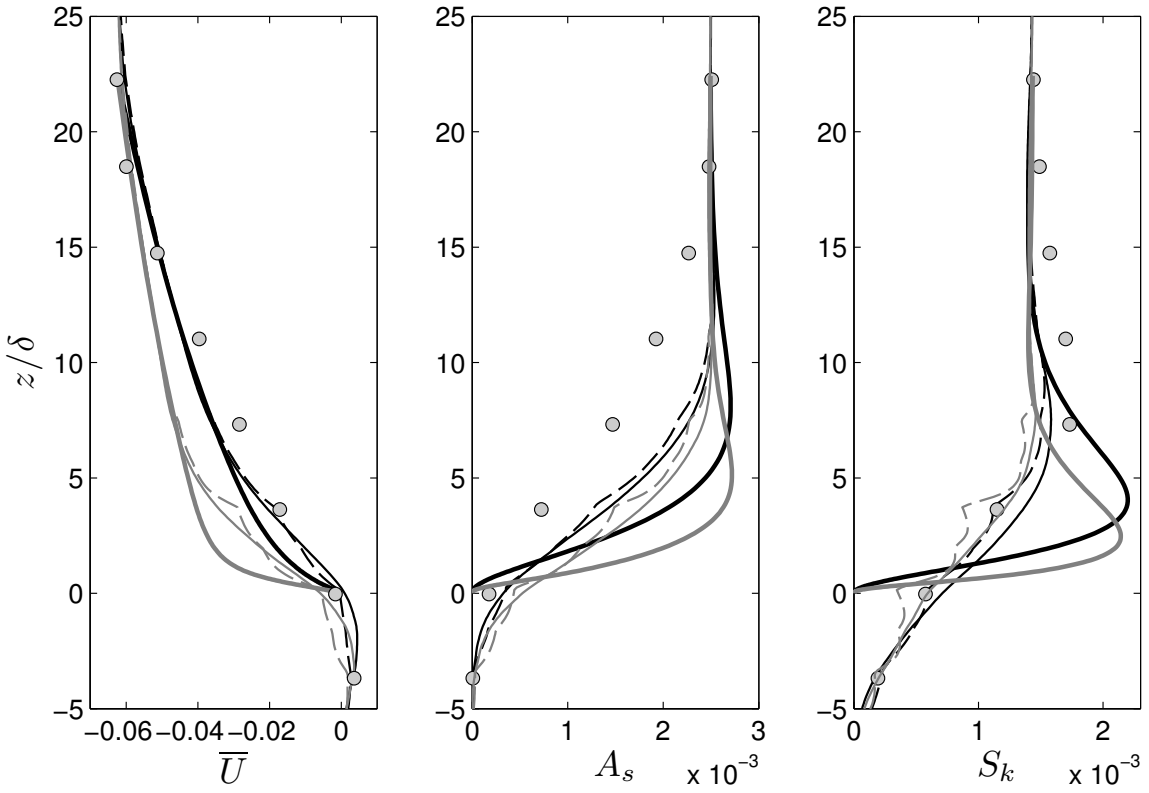

Figure 8: **Mean velocity, dimensional asymmetry and skewness.** Left panel: mean velocity; middle panel dimensional velocity asymmetry; right panel: dimensional velocity skewness. For the rest, same legend as fig. 7.

IV CONCLUSION

A post-processing combining the results of the improved version of a RANS 1DV $k-\omega$ model and data of bottom vertical displacements was successfully used to retrieve vertical profiles at different phases of the horizontal velocity (root mean square velocity, asymmetry and skewness). The enhanced vertical diffusion was found to be due to the vertical motion of the (still bed) boundary rather than to an increase in roughness height. The vertical displacement of the bottom boundary contributes to momentum transfer within the mobile bed and just above. Future work will be focused on the modeling of such vertical bottom motions within the $k-\omega$ framework.

V ACKNOWLEDGMENTS

We are indebted to Jean-Marc Barnoud, Muriel Lagauzère and Pierre-Alain Barraud for providing the technical support of the experiments. This study was partly funded by the project MODLIT (DGA-SHOM/INSU-RELIEFS), the project BARCAN (INSU-LEFE), the BARBEC project (ANR No. 2010JCJC60201) and the MEPIERA project of Grenoble INP. The first author would like to acknowledge the support of CONICYT of Chile through PhD grant No.21100415. R. Cienfuegos acknowledge partial support from Conicyt Fondap program No.15110017

References

Bailard, J. A. (1981). An energetics total load sediment transport model for a plane sloping beach. *Journal of Geophysical Research*, 86(C11). doi:10.1029/JC086iC11p10938.

Berni, C., Barthélemy, E., and Michallet, H. (2013). Surf zone cross-shore boundary layer velocity asymmetry and skewness: an experimental study on a mobile bed. *Journal of Geophysical Research: Oceans*, 118(4):2188–2200.

Berni, C., Michallet, H., and Barthélemy, E. (2012). Measurements of surf zone sand bed dynamics under irregular waves. *European Journal of Environmental and Civil Engineering*, 16(8):981–994.

Fuhrman, D. R., Dixen, M., and Jacobsen, N. G. (2010). Physically-consistent wall boundary conditions for the $k-\omega$ turbulence model. *Journal of Hydraulic Research*, 48(6):793–800.

Grasso, F., Michallet, H., Barthélemy, E., and Certain, R. (2009). Physical modeling of intermediate crossshore beach morphology: Transients and equilibrium states. *Journal of Geophysical Research*, 114(C09001). doi:10.1029/2009JC005308.

Guizien, K., Dohmen-Janssen, C. M., and Vittori, G. (2003). 1dv bottom boundary layer modelling under combined wave and current: suspension ejection events and phase lag effects. *Journal of Geophysical Research*, 108(C1). doi:10.1029/2001JC001292.

Henderson, S. M., Allen, J. S., and Newberger, P. (2004). Nearshore sandbar migration predicted by an eddy-diffusive boundary layer model. *Journal of Geophysical Research*, 109(C05025).

Nielsen, P. (2005). *Coastal bottom boundary layers and sediment transport*. World Scientific Publishing Company Incorporated, third edition.

O'Donoghue, T. and Wright, S. (2004). Flow tunnel measurements of velocities and sand flux in oscillatory sheet flow for well-sorted and graded sands. *Coastal Engineering*, 51:1163–1184.

Patankar, S. V. (1980). *Numerical Heat Transfer and Fluid Flow*. Taylor and Francis Group.

Ruessink, B. G., van den Berg, T. J. J., and van Rijn, L. C. (2009). Modeling sediment transport beneath skewed asymmetric waves above a plane bed. *Journal of Geophysical Research*, 114(C11021). doi:10.1029/2009JC005416.

Sleath, J. F. A. (1987). Turbulent oscillatory flows over rough beds. *Journal of Fluid Mechanics*, 182:369–409.

Wilcox, D. C. (2006). *Turbulence Modeling for CFD*. DCW Industries, Inc., La Canada, Calif., 3rd ed. edition.

Wilson, K. C. (1989). Mobile-bed friction at high shear stress. *Journal of Hydraulic Engineering*, 115(6).

ASYMMETRY AND SKEWNESS IN THE BOTTOM BOUNDARY LAYER : SMALL SCALE EXPERIMENTS AND NUMERICAL MODEL

Céline Berni[1, 2], Leandro Suarez[1], Hervé Michallet[1] and Eric Barthélemy[1]

This study investigates the non-linearities of wave boundary layers in the surf zone. It mainly focuses on the acceleration skewness or asymmetry. Experiments [e.g. Grasso et al., 2011] show that asymmetry influences the sediment transport. Its influence lies in the fact that asymmetry in velocity (acceleration skewness) tends to transform into velocity skewness within the boundary layer. Analysis by Henderson et al. [2004] predicts a linear relation between Sk_b/Sk_∞ and As_∞/Sk_∞ where Sk_b is the dimensionless skewness near the bed, Sk_∞ the free-stream dimensionless skewness and As_∞ the free-stream dimensionless asymmetry. Numerous experiments were carried out in the LEGI wave flume over a mobile bed composed of lightweight sediments. The quasi-random forcing is a repetition of 2 concatenated bichromatic wave packets. Vertical profiles of velocity are measured in the surf zone. A clear linear relation is shown between these two ratios. The experimental results are compared with the numerical results. A linear relation between skewness and asymmetry is also obtained.

Keywords: non linearities, transformation, k-ω model, mobile bed

INTRODUCTION

This study investigates the non-linearities of a wave boundary layer in the surf zone. It mainly focuses on the acceleration skewness or asymmetry. Experiments [e.g. Grasso et al., 2011] show that asymmetry influences the sediment transport. Its influence can be interpreted in different ways. Ruessink et al. [2011] listed several physical processes that can explain this influence, out of which asymmetry in velocity (acceleration skewness) tends to transform into velocity skewness within the boundary layer.

This transformation can be explained as follows: an asymmetric wave is an addition of components of different frequencies that are phase-shifted in order to produce steep fronts. If the phase lead of the near-bed velocity is independent of the frequency, the time shift of each component is proportional to its period. Thus, the time shift between components varies when approaching the bed and asymmetry can transform into skewness in the boundary layer.

This simple model explains qualitatively how non linearities transform through the boundary layer. Further analysis by Henderson et al. [2004] quantifies this transformation. Following his arguments, it can be shown, considering a phase lead ϕ and a velocity amplitude damping between the near-bed velocity and the free-stream velocity independent of the frequency, that [Berni et al., submitted]:

$$\frac{Sk_b}{Sk_\infty} = \cos(\phi) + \sin(\phi)\frac{As_\infty}{Sk_\infty} \tag{1}$$

where Sk_b is the dimensionless skewness near the bed, Sk_∞ the free-stream dimensionless skewness and As_∞ the free-stream dimensionless asymmetry.

The purpose of this paper is to study this transformation, both experimentally and numerically.

NUMERICAL MODEL

The behavior of the wave bottom boundary layer is analyzed using a k-ω turbulence closure model [Wilcox, 2006 ; Guizien et al., 2003]. The low Reynolds number version of the model is chosen. In this model, the horizontal velocity u, the kinetic energy k and the energy dissipation rate ω are solutions of the following equations :

$$\frac{\partial u}{\partial t} = -\frac{1}{\rho}\frac{\partial \bar{P}}{\partial x} + \frac{\partial U}{\partial t} + \frac{\partial}{\partial z}\left((\nu + \nu_t)\frac{\partial u}{\partial z}\right) \tag{2}$$

$$\frac{\partial k}{\partial t} = \nu_t\left(\frac{\partial u}{\partial z}\right)^2 - \beta^* k\omega + \frac{\partial}{\partial z}\left((\nu + \sigma_k\nu_t)\frac{\partial k}{\partial z}\right) \tag{3}$$

$$\frac{\partial \omega}{\partial t} = \alpha\nu_t\frac{\omega}{k}\left(\frac{\partial u}{\partial z}\right)^2 - \beta\omega^2 + \frac{\partial}{\partial z}\left((\nu + \sigma_\omega\nu_t)\frac{\partial \omega}{\partial z}\right) \tag{4}$$

where $\partial\bar{P}/\partial x$ is the mean pressure gradient of the flow, ν the water viscosity, ν_t the turbulent viscosity. The other coefficients and boundary conditions are defined in Guizien et al. [2003]. x is the horizontal direction, z the vertical direction. U is the input velocity of the model.

As we want to study the behaviour of the boundary layer under a non-linear wave, we need to validate the model for such conditions. The results of our model is compared to measurements of Suntoyo et al. [2009] in U-tube. The agreement with measurements is good, attesting the capability of the model to reproduce the dynamic of the wave bottom boundary layer under non-linear waves.

[1]LEGI UMR 5519, Domaine universitaire, BP 53, 38041 Grenoble cedex 9, France
[2]irstea, UR HHLY, Lyon, France

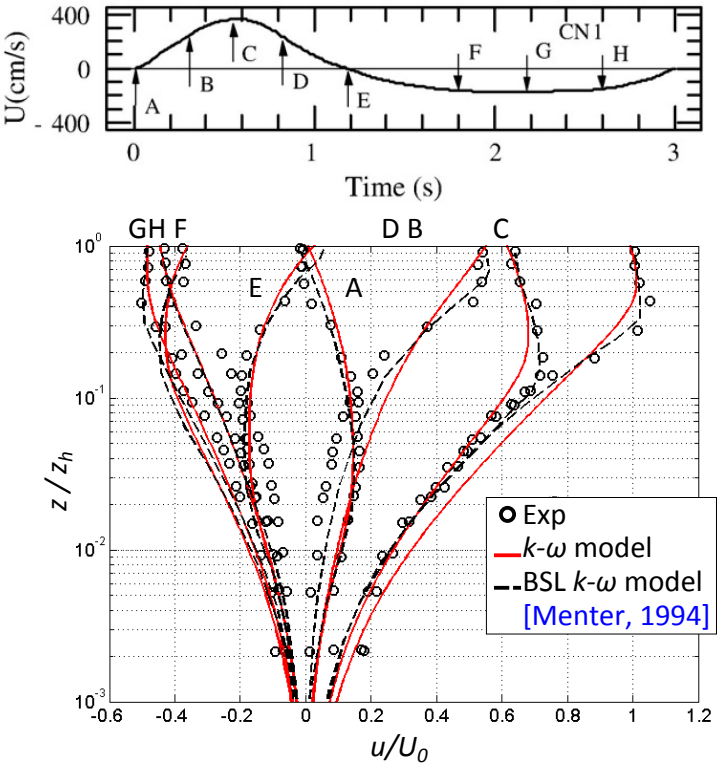

Figure 1: Model validation. Top: time series of the velocity. Bottom: Velocity profiles: comparison between the k-ω model presented in this article (–), experiments of Suntoyo et al. [2009] (o) and a k-ω model of Menter [1994] (- -).

This model will be used in this study to compute the bottom velocity skewness for different free-stream velocities. The bottom velocity skewness is evaluated at approximately $1/10$ of the wave boundary layer thickness over the bed. The free-stream skewness and asymmetry are computed at the maximum value for the orbital velocity. To simulate a wide range of skewness and asymmetries, the formula of Abreu et al. [2010] will be used to compute the input velocity that then will writes:

$$U(t) = U_w \, f_r \, \frac{\sin(\omega t) + \frac{r \, \sin\phi}{1+\sqrt{1-r^2}}}{1 - r \, \cos\left(\omega t + \phi\right)} \tag{5}$$

where U_w is the amplitude of orbital velocity, $\omega = 2\pi/T$ the angular frequency, r the index of skewness ranging from 0 to 0.75 and ϕ the waveform parameter ranging from $-\pi/2$ to 0. The variable f_r is a dimensionless factor, function of r, $f_r = \sqrt{1-r^2}$, allowing the velocity amplitude to be equal to U_w.

EXPERIMENTS

Experimental facility

The experiments took place in a wave flume of 36 m long, 55 cm wide (the LEGI wave flume, see figure 2). The flume is filled with PMMA sediment of low density (1.19 g cm^{-3}) forming a beach. The sediment median diameter is $d_{50} = 0.64$ mm. The corresponding settling velocity is 2.1 cm s^{-1} [see Grasso et al., 2009, for more details on the experimental facility]. The wave forcing is produced by a computer controlled piston-type wave-maker. There is neither wave absorption nor second-order correction on the wave maker motion.

Capacitive wave gauges are placed in the cross-shore direction of the beach to measure free-surface elevations. Beach profiles are recorded between wave series using an acoustic profiler mounted on a motorized trolley. Cross-shore velocity profiles are measured at $X = 13$ m of the wave maker with an acoustic Doppler velocity profiler (ADVP) [Hurther, 2001]. The vertical resolution is 3 mm. The sampling frequency for both velocity and free-surface elevation is 50 Hz.

Experimental conditions

The wave climate is a repetition of a specific wave sequence of duration $T_s = 53$ s. It results of the concatenation of two bichromatic packets with a carrier wave period of 2 s and 2.5 s respectively (see figure 3).

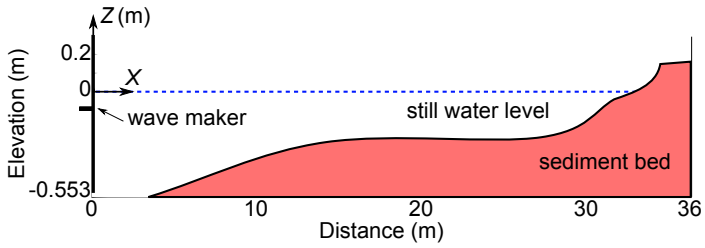

Figure 2: The LEGI wave flume.

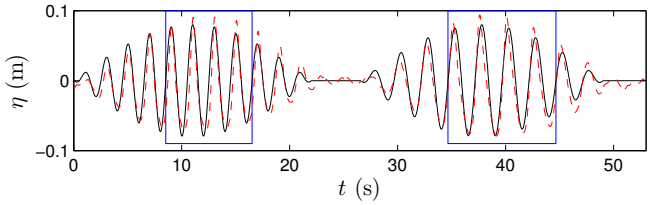

Figure 3: Wave climate: wave maker input data (solid line) and measurements with a capacitive wave gage at $X = 2$ m (dashed line).

The free-surface elevation η for each bichromatic packets writes:

$$\eta(x,t) = A\,\cos\left(\omega_1 t - k_1 x\right) + A\cos\left(\omega_2 t - k_2 x\right) \tag{6}$$

$$= 2\,A\cos\left(\frac{\omega_1-\omega_2}{2}\,t - \frac{k_1-k_2}{2}\,x\right) \times \cos\left(\frac{\omega_1+\omega_2}{2}\,t - \frac{k_1+k_2}{2}\,x\right) \tag{7}$$

where $A = 4$ cm for both packets and x is the cross-shore direction. The angular frequencies for the packet with a wave period of 2 s are $\omega_1 = 3.0$ rad s^{-1} and $\omega_2 = 3.3$ rad s^{-1}; for the packet with a wave period of 2.5 s, $\omega_1 = 2.4$ rad s^{-1} and $\omega_2 = 2.7$ rad s^{-1}. The wave numbers k_1 and k_2 are given by the dispersion relation:

$$\omega_i^2 = g k_i \tanh(k_i h) \tag{8}$$

where h is the water depth, $h \sim 15$ cm in the experiments presented here. The significant wave height at the wave maker is 16 cm for both groups.

The initial, intermediate (after 1350 wave sequences of 53 s) and final (after 4100 wave sequences) beach profiles are plotted in figure 4. During the experiments a bar progressively formed and migrated onshore. The root mean square wave height $H_{\rm rms}$ for the initial and final profiles are plotted in the top plot. The break point was overall stationary at a distance of roughly 8 m from the wave maker. The surf zone extends from there up to the bar trough ($X \sim 20$ m). The measurements analyzed in this paper are all recorded within the surf zone at 13 m.

At this specific position, the different experimental parameters can be summarized as follow:

- the bottom Reynolds number Re_b ranges between 24 000 and 45 000, computed as $Re_b = U_b h/\nu$ where ν is the water viscosity and U_b is the near-bed velocity measured at the wave crest.
- the orbital amplitude a varies between 5 and 10 cm,
- the Shields number is the order of 0.5, estimated by

$$\theta = \frac{1}{2}\,f_w\,\frac{U^2}{g(s-1)d_{50}}, \tag{9}$$

  where U is the amplitude of the free-stream velocity ($U \sim 0.2$ m s^{-1}), s is the relative density of the sediment ($s = 1.19$), d_{50} the median diameter and f_w is the friction coefficient estimated according to Swart [1974] by:

$$f_w = \exp\left[5.213\left(\frac{2.5\,d_{50}}{a}\right)^{0.194} - 5.977\right] \tag{10}$$

- the sheet-flow thickness δ_s is the order of 3 mm, estimated by the Wilson [1987] parameterization

$$\delta_s = 10\,\theta\,d_{50}\,, \tag{11}$$

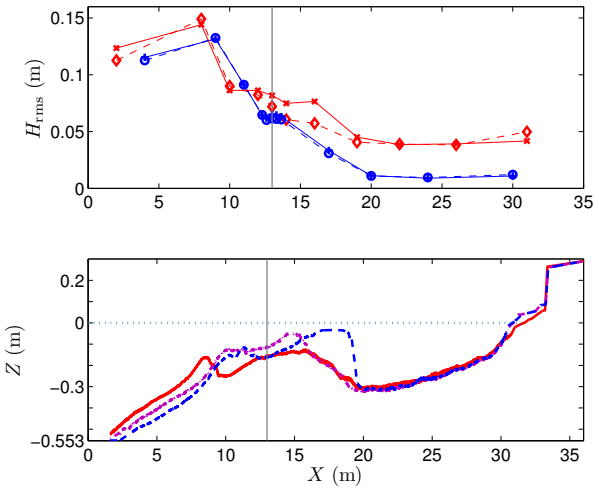

Figure 4: Top: root mean square wave height for the initial ((+): $T = 2$ s; (o): $T = 2.5$ s) and the final ((∗): $T = 2$ s; (◇): $T = 2.5$ s) topography of the beach. Bottom: initial (bold solid line), intermediate (thin solid line) and final (dashed line) topography of the beach. $X = 0$ is the mean position of the wave maker, $Z = 0$ is the still free surface (horizontal dotted line). The vertical line indicates the measurement location.

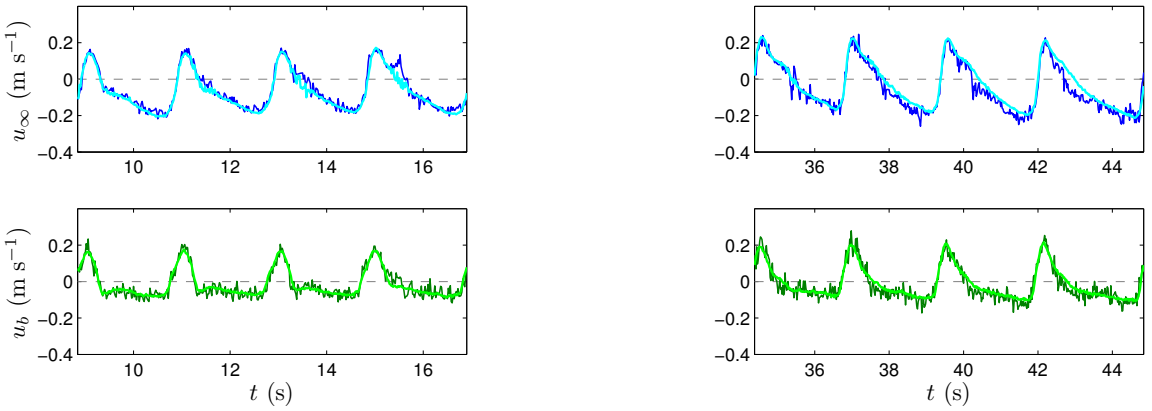

Figure 5: Examples of the time series of the instantaneous free-stream velocity (top) and the instantaneous near-bed velocity (bottom) along with the corresponding ensemble averages (thick light color lines).

- the equivalent roughness length k_s is the order of 2 mm, estimated by the Wilson [1989] parameterization

$$k_s = 5\,\theta\,d_{50}\,. \tag{12}$$

Velocity measurements

Cross-shore velocity profiles are measured over the bar with an acoustic Doppler velocity profiler (ADVP) [Hurther, 2001]. The vertical resolution is 3 mm. Simultaneously with the velocity profile, the ADVP instrument detects the position of the still bed level [Silva et al., 2009 ; Hurther and Thorne, 2011]. The near-bed velocity u_b is defined as the velocity measured in the first sampling volume above the mean position of this still bed level. It is thus measured at an elevation z_b between 0 and 3 mm above the mean still bed level.

Examples of instantaneous velocities at both free-stream and near-bed elevations are given on figure 5. The two groups can be distinguished, the first between $t = 1$ s and $t = 25$ s the second between $t = 25$ s and $t = 53$ s.

The data presented in this article are provided by ensemble averaging over a set of 30 to 50 sequences in a row. The ensemble average on N realizations is computed as :

$$\widetilde{u}(t) = \frac{1}{N}\sum_{n=1}^{N} u(t + (n-1)\,T_s), \tag{13}$$

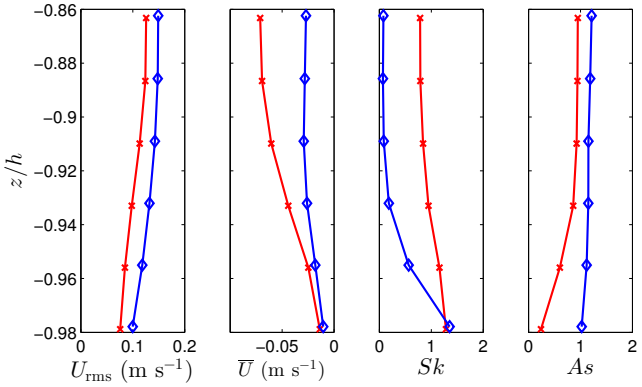

Figure 6: Examples of root-mean-square velocity $U_{\rm rms}$, mean velocity $\overline{U}$, skewness Sk and asymmetry As profiles computed from ensemble averaged velocity, for the two studied intervals specified in figure 3 corresponding to the two wave forcing: (+): $T = 2$ s; (o): $T = 2.5$ s. The vertical axes is the dimensionless elevation, $Z/h = -1$ stands for the mean position of the bed, $Z/h = 0$ for the still free-surface elevation, with the water depth $h = 14$ cm at the measuring location.

where T_s is the duration of the sequence. For clarity, we simplify the notation by using u for $\widetilde{u}$. During each set of sequences (~ 45 minutes) the bottom does not evolve significantly in the mean. Within a sequence it-self, the maximum erosion detected is one volume sampling, *i.e.* 3 mm.

Ensemble averaging reduces the noise and allows reliable velocity measurements. It is superimposed on the instantaneous velocities, on figure 5, as a thin gray line.

Non linearities

Time series of the ensemble average of the free-stream and the bottom velocities at the measurement location are shown in figure 5. These data correspond to one representative example amongst the whole set of 41 experiments. The shape of the waves is typical of the surf zone waves, with pinched crests, long troughs, and pitched-forward waves.

The bottom velocity in figure 5 is in contrast highly skewed. Note that the bottom velocity and the free-stream velocity at each crest are almost of the same value while the near-bed troughs velocities are more than 50 % smaller than their counter parts in the free-stream velocities.

In the following analysis of the non-linearities, we chose to only study the four middle waves of each group, identified by a box on the time series in figure 3. The two time bounds of the box are times with zero-up crossing of the free-stream orbital velocity (without infragravity components). Both intervals are analyzed and studied separately as they correspond to two different periods and therefore to two different forcings. Note that for the example shown on figure 5, asymmetry and skewness are indeed different for both groups. The second group with the 2.5 s period present a larger asymmetry and a smaller skewness of the free-stream velocity.

For this specific experiment, the vertical profiles of the root-mean-square velocity $U_{\rm rms}$, the mean velocity $\overline{U} = \langle u \rangle$, the skewness and the asymmetry are plotted in figure 6 for both bichromatic groups. The root mean square value of the velocity, which offers a quantification of the orbital velocity, decreases down to the bed in the wave boundary layer. The mean velocity $\overline{U}$ is negative in the upper part of the profile, distinctive of the presence of an undertow. It decreases deeper down in the boundary layer. The profile surprisingly concaves downwards but it is probably due to the mobile bed. Indeed, O'Donoghue [2004] found similar profiles over a mobile bed. Besides, the measurements of Sparrow et al. [2012] over impermeable and permeable bed also suggest that permeability induces an inflexion in the velocity profiles. Both forcing of different periods show similar behaviour although the free-stream values of the rms and mean velocity are different. In the third panel of the figure is plotted the dimensionless skewness Sk of the velocity. It increases down to the bed while the asymmetry decreases as shown in the last panel. The increase of the skewness is larger for the wave period of 2.5 s that presents a greater free-stream asymmetry.

For all the experiments (41 groups of at least 30 sequences), dimensionless skewness and asymmetry were computed at the free-stream ($z = \infty$) and the near-bed ($z = z_b$) elevations, corresponding to the upper and lower measure presented on figure 6. The wave boundary layer represents approximately 10 % of the water column and the near-bed elevation is between 1/5 and 1/10 of the wave boundary layer thickness over the bed.

RESULTS

As the beach shape evolves during the 41 experiments, a large range of values for the free-stream skewness and

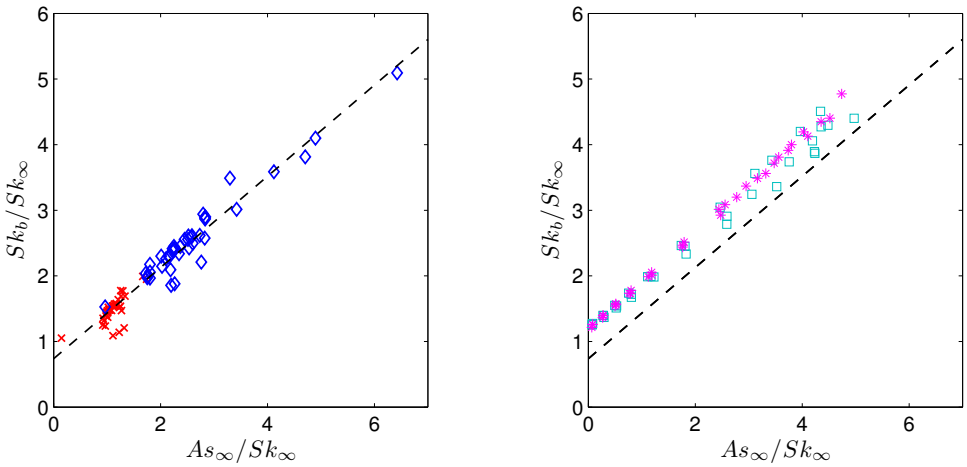

Figure 7: near-bed and free-stream skewness ratio as a function of the ratio between free-stream asymmetry and skewness; left: experimental data (◇ $T = 2.5$ s; x $T = 2$ s) and right: numerical data (□ $T = 2.5$ s; ⋆ $T = 2$ s).

large values of the asymmetry are obtained. In our experiments, the waves of period 2.5 s are more asymmetric and less skewed than the waves of period 2 s.

The ratios appearing in equation (1) are plotted on figure 7. In the experimental case (left), a clear linear relation is shown between these two ratios no matter the forcing. On the right of figure 7, the results of the numerical model also show a clear linear relation with the same slope. This slope can be interpreted as $\sin(\phi)$ according to the relation (1) and leads to $\phi = 44$ degrees. The scatter is similar to the experimental scatter, and larger for the greater period. The y-intercept is quite different between the numerical model and the experiment. Being greater than one in the first case, it can not be interpreted as $\cos(\phi)$ where ϕ is the phase lead. Thus, the analytical relation (1) does not hold for turbulent flow such as the one simulated by the model. Indeed, neither the phase lead nor the attenuation at the bed elevation are independent of the frequency. The linear relation yet holds, offering a way to predict bottom velocity skewness.

The process transforming asymmetry to skewness within the boundary layer is numerically and experimentally confirmed and understood. This transformation results in skewed velocities near the bed that lead directly to net sediment transport.

ACKNOWLEDGMENTS

The technical support of Jean-Marc Barnoud, Muriel Lagauzère and Pierre-Alain Barraud is gratefully acknowledged. The first author's PhD was funded by the French ministry MESR and Grenoble INP, the second author has a PhD Grant of the CONYCIT. This study was partly funded by the project MODLIT (DGA-SHOM/INSU-RELIEFS) and the project BARCAN (INSU-LEFE).

REFERENCES

Abreu, T., P. A. Silva, F. Sancho, and A. Temperville (2010). Analytical approximate wave form for asymmetric waves. *Coastal Eng.*, 57(7):656–667.

Berni, C., H. Michallet, and E. Barthélemy (submitted), Surf zone cross-shore boundary layer velocity asymmetry and skewness: an experimental study on a mobile bed, *J. Geophys. Res.*.

Grasso, F., H. Michallet, E. Barthélemy and R. Certain (2009), Physical modeling of intermediate cross-shore beach morphology: Transients and equilibrium states, *J. Geophys. Res.*, 114, C09001, doi:10.1029/2009JC005308.

Grasso, F. , H. Michallet, and E. Barthélemy (2011). Sediment transport associated with morphological beach changes forced by irregular asymmetric, skewed waves. *J. Geophys. Res.*, 116(C3):C03020.

Guizien, K., M. Dohmen-Janssen and G. Vittori (2003), 1DV bottom boundary layer modelling under combined wave and current: suspension ejection events and phase lag effects. *J. Geophys. Res.*, 108(C1):3016.

Henderson, S. M., J. S. Allen, and P. A. Newberger (2004), Nearshore sandbar migration predicted by an eddy-diffusive boundary layer model. *J. Geophys. Res.*, 109, C05025, 109.

Hurther, D. (2001), 3-D acoustic Doppler velocimetry and turbulence in open-channel flow, Ph.D. thesis, École Polytechnique Fédérale de Lausanne.

Hurther, D. and P. D. Thorne (2011), Suspension and near-bed load sediment transport processes above a migrating, sand-rippled bed under shoaling waves, *J. Geophys. Res.*, *116*, C07001, doi:10.1029/2010JC006774.

Menter, F. R. (1994), Two-equation eddy-viscosity turbulence models for engineering applications. *AIAA Journal*, 32 (8), pp 1598-1605.

O'Donoghue, T. and S. Wright (2006), Flow tunnel measurements of velocities and sand flux in oscillatory sheet flow for well-sorted and graded sands, *Coast. Eng.*, *51*, 1163–1184.

Ruessink, B. G., H. Michallet, T. Abreu, F. Sancho, D. A. Van der A, J. J. Van der Werf, and P. A. Silva (2011), Observations of velocities, sand concentrations, and fluxes under velocity-asymmetric oscillatory flows. *J. Geophys. Res.*, 116(C3):C03004.

Silva, P. A., Abreu T., H. Michallet, D. Hurther, and F. Sancho (2009), Sheet flow layer structure under oscillatory flow, in *River, Coastal and Estuarine Morphodynamics*, Santa Fe, Argentina, 21-25 Sept 2009.

Sparrow, K., D. Pokrajac, and D. van der A. (2012). The effect of bed permeability on oscillatory boundary layer flow, *Proceedings of the International Conference on Coastal Engineering*, 723.

Suntoyo, and H. Tanaka (2009), Effects of bed roughness on turbulent boundary layer and net sediment transport under asymmetric waves, *Coast. Eng.*, *56*, 960–969.

Swart, D.H. (1974), A schematization of onshore-offshore transport, paper presented at the 14th International Conference on Coastal Engineering, Coastal Eng. Res. Counc., Copenhagen, Denmark.

Wilcox, D. C. (2006), *Turbulence modeling for CFD, 3rd edition*. DCW Industries, Inc., La Canada CA.

Wilson, K.C. (1989), Mobile-bed friction at high shear stress, *J. Hydraul. Res.*, *115*6, 825–830.

Wilson, K.C. (1989), Analysis of Bed-Load Motion at High Shear Stress, *J. Hydraul. Eng.*, *113*, 97–0.13.

Chapter 4

Circulation in the nearshore zone

4.1 Introduction

4.1.1 Physical processes

Mean nearshore circulation are mean currents driven by the wave motion. A well known example ins the longshore current forced by the breaking of oblique waves Longuet-Higgins et Stewart [1964]. Waves create mean-currents by transferring momentum to these currents. The most efficient pathway is the breaking of waves. They lose momentum during breaking transferred to other fluid motions. In the case of shore normal waves this transfer can only occur on alongshore non-uniform bathymetries or with non uniform wave forcing. Wave breaking is a process that builds on the shoaling of waves.

In deep waters, the wave shape is roughly sinusoidal. As they approach the nearshore zone, which is the region where the waves are affected by the bottom (Figure 4.1), the waves start feeling the influence of the bottom and their shape becomes non-linear in the shoaling zone. The wave height increases and the wave shape becomes skewed, with a pinched crest and a wide trough. When the wave height is coming close to the water depth under the travelling wave, the wave breaks. As the wave height is different for each wave, the wave breaking does not necessarily occur at the same location, and the breaking zone is defined as the region where the wave breaking occurs.

The wave breaking type can be determined by the Irribaren number ξ_0:

$$\xi_0 = \frac{\tan \beta_0}{(H_0/L_0)^{1/2}} \tag{4.1}$$

with β_0 the beach slope, H_0 the wave height, $L_0 = gT^2/2\pi$ the deep-water wave length,

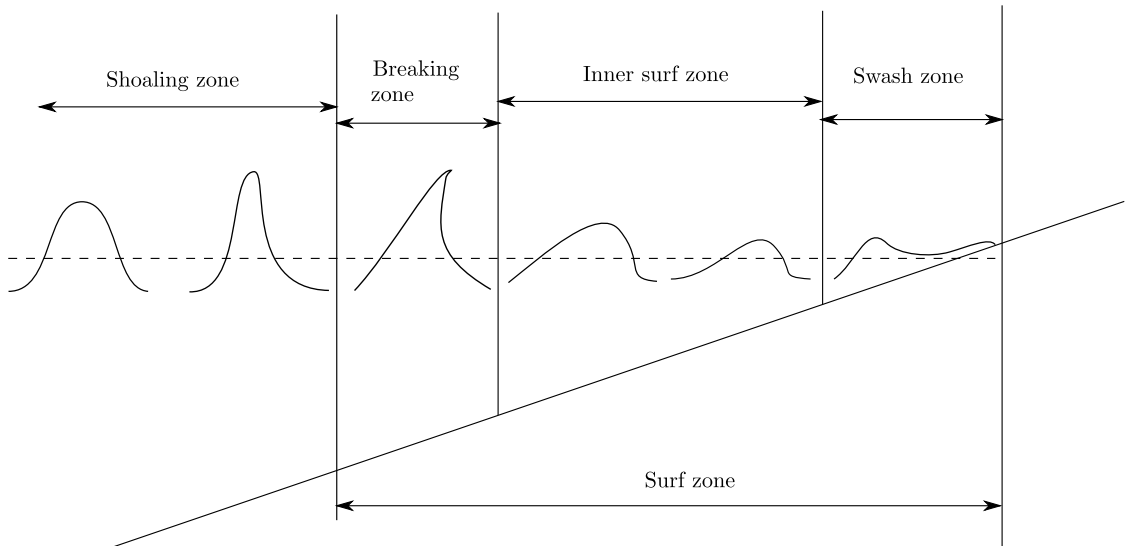

Figure 4.1 – Schematic representation of the nearshore zone, with the wave shape transformation as it propagates toward the shore

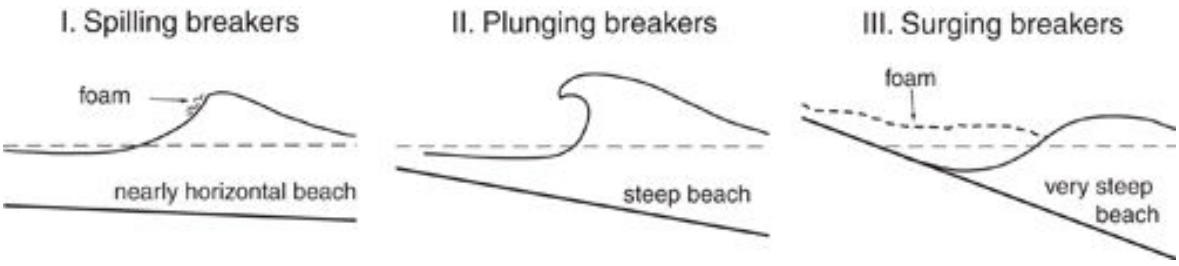

Figure 4.2 – Classification of breaking wave types

T the wave period and g the gravitational acceleration.

For a wave with a specific period and wave height, its wave breaking type then depends on the beach slope. For $\xi_0 < 0.5$, the wave breaking type is spilling, for $0.5 < \xi_0 < 3.3$ it is plunging and for $\xi_0 > 3.3$ it is surging (Figure 4.2). In the case of a spilling wave breaking, the wave crest becomes unstable, white foam appearing on the crest and spilling down the face of the wave. In a plunging wave breaking, the wave crest becomes vertical and then curls over and drop onto the trough of the wave, creating a strong vertical jet that dissipate a great amount of the wave energy. The surging wave breaking corresponds to a wave breaking on the beach itself and the disappearance of the wave crest. The wave breaking is the main source of energy dissipation of the wave energy in the nearshore zone.

After they break, waves keep on propagating in the inner surf zone, in the form of

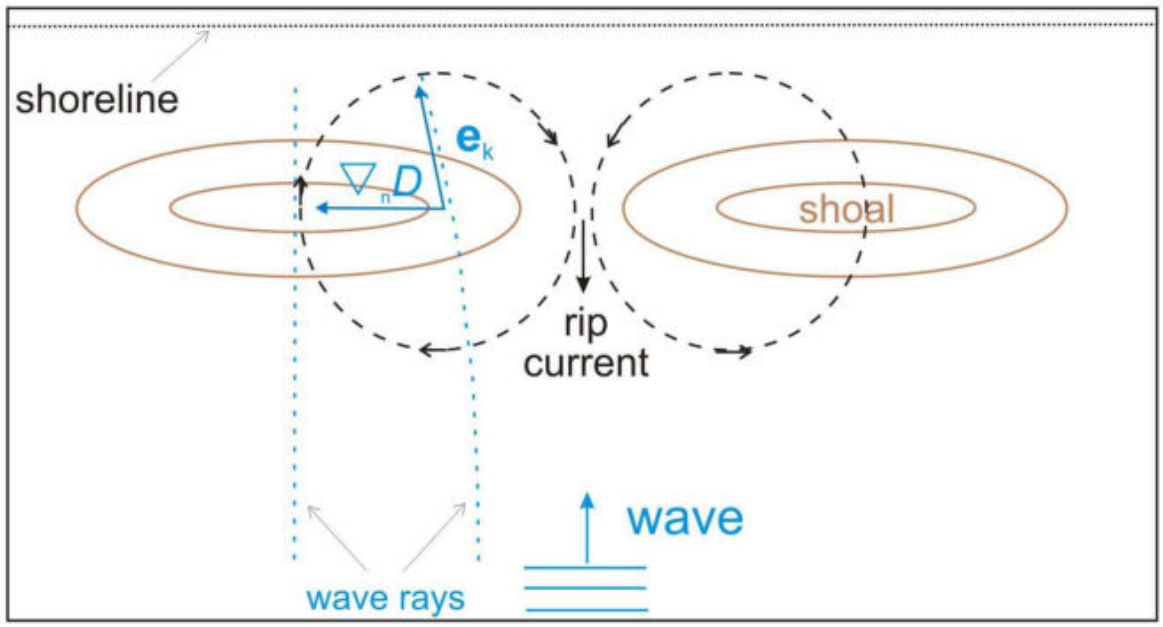

Figure 4.3 – from [Bonneton *et al.*, 2010]

smaller broken waves known as bores, similar to a propagating hydraulic jump. They also dissipate energy as the water becomes shallower, due to the friction of the bottom, resulting in a decrease in the wave height. When these bores reach the beach, the water is pushed towards the beach and then retreats, in the region defined as the swash zone.

There also exist longshore wave transformation processes. The wave celerity in shallow waters is dependent on the water depth, waves propagating slower as the water becomes shallower. In the case of oblique waves, this results in a change of orientation of propagation, the wave front adjusting to the depth contours. The oblique waves also generates longshore currents that can also interact with incoming waves creating circulation patterns, with time and space greater than the wave scales. The waves also generate cross-shore and longshore sediment transport, which changes the bathymetry and modify the circulation patterns.

One important nearshore circulation pattern, is the rip current, which is an offshore oriented water jet, that can occur on a wide variety of beaches under different wave and tidal conditions. The term rip current was first defined by Shepard [1936] as flows travelling "outward almost at right angles to the shore". The rip current is constituted of a feeder region, a ripe neck and a rip head [Shepard *et al.*, 1941]. For a more detailed description of the rip current see the review from Dalrymple *et al.* [2011] and MacMahan *et al.* [2006].

Many theoretical models use the momentum flux induced by the waves called the

Radiation stress as formulated by Longuet-Higgins et Stewart [1964], to explain the appearance of these rip currents: an alongshore variation of wave height introduces a variation in the excess flux of momentum due to the presence of waves, that develops a steady circulation pattern in the nearshore zone [Bowen, 1969]. This wave height alongshore variation can be originated by a wave-wave interaction, by an incoming alongshore heterogeneous wave forcing or by the bathymetry heterogeneity that induces changes in the wave height by shoaling, refraction and wave breaking.

The importance of the vorticity in the generation of rip currents was shown by Peregrine [1998]. Using a discrete wave group forcing, he evidenced the formation of eddies from the longshore currents, and the rip currents originated where two eddies of opposite sign met. The non-linear evolution of these eddies is further studied in Buhler et Jacobson [2001], from its initial generation by wave breaking, until its dissipative decay due to bottom friction. From the vorticity equation, Bonneton *et al.* [2010] obtained a vorticity forcing term related to differential broken-wave energy dissipation (Figure 4.3).

4.1.2 Experiments and models

The nearshore circulation has been studied with a wide variety of numerical models. There are two main types of wave models:

- The phase averaged models, based on the energy balance equation with sources and sinks, that uses the wave spectra statistics and their propagation to the nearshore. They usually use the full radiation stress gradients as driving force. Some examples of these type of models are SWAN [Holthuijsen, 2007] and X-beach [Roelvink *et al.*, 2009]. Bruneau *et al.* [2011] use a vertically integrated time-averaged coupled model, the spectral wave module SWAN coupled with the non-linear shallow water module MARS, using a spatially constant time-varying breaking parameter, to reproduce the nearshore circulation on a well-developed bar and rip morphology. The model correctly reproduces the main evolving behaviours of the rip current.

- the phase-resolving models, which compute at each time-step the free-surface and velocities in the spatial domain, giving access to the intra-phase wave evolution. These models are based on non-linear sets of equation to describe the evolution of the free-surface and velocities in the nearshore zone.

The phase-resolving models are able to compute the non-linear wave transformation processes in the nearshore zone. As stated in the previous chapters concerning the

turbulent boundary layer, the wave skewness and asymmetry during the propagation evolves, and influences the sediment transport [Grasso *et al.*, 2011 ; Elgar *et al.*, 2001 ; Ruessink *et al.*, 2011], hence the need of models able to accurately reproduce the wave non-linearities as well as the wave breaking and run-up.

Numerical models based on the Navier-Stokes equations, such as Direct Numerical simulation (DNS) that resolve all the spatial and temporal scales of the turbulence, or the Large Eddy Simulation (LES) which incorporates a turbulence model for the subgrid scales of the flow allow for a detailed evolution of the wave breaking [Lubin *et al.*, 2003 2006]. However these simulations are very demanding computationally, and are not able to reproduce all the spatial and temporal scales of a realistic nearshore zone.

The vertical scale in the nearshore zone is the water depth, and is little compared to the horizontal scales involved such as the wave length, we can then reduce the complexity by depth-averaging the equations, thus reducing the computational cost with fairly good results. We can distinguish the models using the Boussinesq-type (thereafter BT) equations and the ones using the Non-linear Shallow Water (thereafter NSW) equations.

The BT equations include dispersive terms which provide an accurate description of non-breaking wave transformation. If we note a the order of the free surface amplitude, h_0 the characteristic water depth and L_0 the characteristic horizontal scale, we can define two non-dimensional parameters:

$$\mu = \left(\frac{h_0}{L_0}\right)^2 \tag{4.2}$$

$$\varepsilon = \frac{a}{h_0} \tag{4.3}$$

the parameter μ is characteristic of the non-hydrostatic and dispersive effects and the parameter ε is characteristic of the non-linearity of the flow.

Boussinesq [1872] used a perturbation method on these two non-dimensional parameters to obtain a set of equations. The first assumption is the shallow water condition, implying $\mu \ll 1$. The second assumption is that the dispersion and non-linearities are weak, and that there is a balance between non-linearity and dispersion: $\varepsilon = O(\mu) \ll 1$. These assumptions does not hold on the entire nearshore zone, as the wave shoaling occurs when the wavelength is comparable with the depth ($\mu \sim 1$) and waves break when their amplitude is comparable with the water depth ($\varepsilon \sim 1$). It is therefore necessary to use fully non-linear BT equations to overcome these difficulties. [Serre, 1953] first derived a set of fully non-linear ($\varepsilon \sim 1$) weakly dispersive BT equations

(see [Barthélemy, 2004] for a detailed review), Green et Naghdi [1976] extending these equations to the 2D case on an uneven bottom. Chen *et al.* [1999] use the fully non-linear Boussinesq equations developed by Wei et Kirby [1995] in the FUNWAVE model, including wave breaking and a moving shoreline. They show a good agreement of the numerical simulations with the fixed bar rip current experiments by Haller *et al.* [1997].

The major drawback of this set of equations is that the energy dissipation by wave breaking and the run-up are not included, hence the need to introduce this dissipation by a parametrization, adding extra-terms when the wave breaking is likely to occur ([Cienfuegos *et al.*, 2010 ; Kennedy *et al.*, 2000 ; Madsen *et al.*, 1997a]).

The NSW models provide an accurate description of the broken waves, that are represented as shocks, and of the run-up [Bonneton, 2007 ; Kobayashi *et al.*, 1989 ; Marche *et al.*, 2007]. The main drawback of these models is that the dispersive effects are neglected, restricting them to the inner-surf zone and the swash zone, as the wave shoaling is not well reproduced.

Recently, new models have been developed that use both the BT equations and the NSW equations. [Tissier *et al.*, 2012] use the Serre Green-Naghdi equations, and switch to the NSW equations when a wave is ready to break by removing the dispersive terms, resulting in an appropriate evaluation of the energy dissipation by wave breaking [Bonneton *et al.*, 2011ab]. The FUNWAVE model has also been improved by Shi *et al.* [2012] using a similar technique, the wave breaking being solved by the nonlinear shallow water equations when the Froude number exceeds a threshold, the moving shoreline with a wetting-drying algorithm, and the code parallelized.

These late models were not available at the beginning of this thesis. As we wanted to access to the non-linearities induced by an alonghsore heterogeneous wave forcing, we chose first to use a phase resolving model. The choice of a NSW equation model was then dictated by the fact that we wanted to observe the evolution of the circulation and vorticity, and this type of models does not need further parametrization for the wave breaking dissipation or the run-up. Marche *et al.* [2007] developed a depth-integrated model SURF_WB with a bed slope source term, a treatment for the moving shoreline and accurate bore-capturing abilities.

We intend to simulate with this model the MODLIT experiments ([Michallet *et al.*, 2010 2013]) in order to validate the model in terms of cross-shore and alongshore profiles of flow characteristics. We will also compare model outputs of mean 2D circulation and vorticity with mean circulations determined by experimental Lagrangian drifter motion. These experiments which consider an alongshore varying wave breaking on a mobile bed is representative of an heterogeneous bathymetry of the nearshore zone, and the experimental data provided allows for a comparison between the numerical model

and the experiment. Even though the numerical model is known to have difficulties to reproduce the wave shoaling, the advantage of the MODLIT experiment is that the shoaling zone is reduced, allowing to use a NSW equations model to reproduce the circulation and vorticity in this zone.

4.2 Experiment and methods

4.2.1 Numerical model

Governing equations

The numerical model SURF_WB, from Marche *et al.* [2007] is based on the Non-linear Shallow Water Equations (NSWE), valid for long waves. These equations are obtained by averaging over the water column the Navier-Stokes equation for an homogeneous and incompressible fluid assuming long wave motion.

With all these assumptions, the resulting equations are a system of three hyperbolic conservation laws, with the water depth and the depth-averaged velocities as the variables.

The non-dimensional form of the NSWE can be written:

$$\frac{\partial Q}{\partial t} + \frac{\partial F}{\partial x} + \frac{\partial G}{\partial y} = S(Q) \tag{4.4}$$

where Q is the vector of the non-dimensional hydrodynamic variables, function of h the water depth,u and v respectively the cross-shore and longshore depth-averaged velocities, F and G represent the flux vectors in each Cartesian direction, and S is the source term vector incorporating bed slope and friction. The terms of the equation are defined as:

$$Q = \begin{pmatrix} h \\ hu \\ hv \end{pmatrix}, F(Q) = \begin{pmatrix} hu \\ hu^2 + \frac{1}{2Fr^2}h^2 \\ huv \end{pmatrix}, G(Q) = \begin{pmatrix} hv \\ huv \\ hv^2 + \frac{1}{2Fr^2}h^2 \end{pmatrix} \tag{4.5}$$

$$S(Q) = \begin{pmatrix} 0 \\ -\frac{h}{Fr^2}\frac{\partial z}{\partial x} - S_{fx} \\ -\frac{h}{Fr^2}\frac{\partial z}{\partial y} - S_{fy} \end{pmatrix}$$

where Fr is the Froude number, $\frac{\partial z}{\partial x}$ and $\frac{\partial z}{\partial y}$ are the bed-slopes, S_{fx} and S_{fy} are the friction source terms.

Resolution of the equations

The non-dimensional form of the NSWE, given by Equations (4.5), are solved using a finite volume well-balanced scheme, which incorporates separately the friction and bed-slope in the momentum source terms [Marche *et al.*, 2007] .

The numerical procedure consists of an initial step in which the friction source term in the momentum equations is incorporated employing a semi-implicit method. [Liang et Marche, 2009]. To that end, we solve the following ordinary differential equation:

$$\frac{dQ}{dt} = S_f \tag{4.6}$$

where the friction term S_f is written as:

$$S_f = \begin{pmatrix} 0 \\ -\frac{\tau_{fx}}{\rho} \\ -\frac{\tau_{fy}}{\rho} \end{pmatrix} \tag{4.7}$$

with τ_{fx} and τ_{fy} the bed shear stress in the x and y direction, and ρ the water density. The bed shear stress is estimated as:

$$\tau_{fx} = \rho C_f u \sqrt{u^2 + v^2} \tag{4.8}$$

$$\tau_{fy} = \rho C_f v \sqrt{u^2 + v^2} \tag{4.9}$$

where C_f is a non-dimensional bed friction coefficient, estimated using the Manning formula, valid for uniform flow and ρ the water density.

In a second hyperbolic NSWE step, the variables are reconstructed at the cell interfaces and the fluxes are found through the solution of the Riemann problem at the cell interfaces, using a non-conservative form of the governing equations. This methodology gives the numerical model the well-balanced property by considering the bed-slope in the spatial discretization schemes, using a MUSCL type reconstruction method to reach a second order accuracy. The discretized form of the governing equations is integrated in time using a multi-stage Runge-Kutta scheme.

The model includes a bore capturing method, which allows to dissipate the energy by the wave breaking in the nearshore zone. It has also been improved by Guerra *et al.* [2014] to use a curvilinear grid, suitable for highly variable topography, as can occur in the nearshore zone.

Absorption/generation boundary condition

The absorption/generation condition considers an incoming input wave height and solves a Riemann problem at the boundary, between the incoming invariant "carrying" the incoming wave height and the outgoing invariant, to find the proper wave height at the boundary [Cienfuegos *et al.*, 2007]. This condition is an open boundary as the incoming waves can enter the domain, and the outgoing waves leave freely.

4.2.2 Experiment and model setup

Experiment description

Mobile bed

The experiment [Michallet *et al.*, 2010 2013] took place in the LHF (ARTELIA) wave basin (Figure 4.4), with dimensions of 30×30 m^2. The waves originate from 60 parallel segmented piston-type wavemakers, of 50 cm width each and spanning the 30 m tank width, allowing to produce a differential wave forcing between the segments. The measurement instruments are located on a sliding rail, which can move in the alongshore direction. The cross-shore position of the instruments is fixed during the experiment. The still water level at the wavemaker is $h_0 = 0.765$ m. The experiments where more or less designed to provide a length scale ratio of 1/10 with respect to nature. This implies a time-scale ratio of 1/3 if a Froude scaling is assumed.

The mobile bed used in the experiment is made of sand, of density 2.65 and median diameter $d_{50} = 0.166$ mm. With this type of sand, a Rouse scaling gives a prototype grain size of $d_{50} \approx 0.3$ mm. The Rouse number determines how the sediment is transported in a flowing fluid. Note however that the Shields scaling is not fulfilled. Indeed the experimental Shields is half that of the prototype conditions. The Shields number is important in sediment mobility, and sediment transport regime, and as a result, we observed sand ripples on the bed surface. For the simulation, we consider a fixed bed therefore the Shields scaling is not relevant for our study.

Wave forcing

The wave climate consisted in irregular shore-normal waves with no directional spreading complying with a JONSWAP spectrum. The JONSWAP (Joint North Sea Wave Project) spectrum has been proposed by [Hasselman *et al.*, 1973], using wave data collected in the North Sea. This spectrum can be expressed as:

$$S(f) = \alpha g^2 f^{-5} (2\pi)^{-4} \exp\left[-\frac{5}{4}\left(\frac{f}{f_p}\right)^{-4}\right] \gamma^{\exp\left[\frac{-(f-f_p)^2}{2\sigma^2 f_p^2}\right]} \tag{4.10}$$

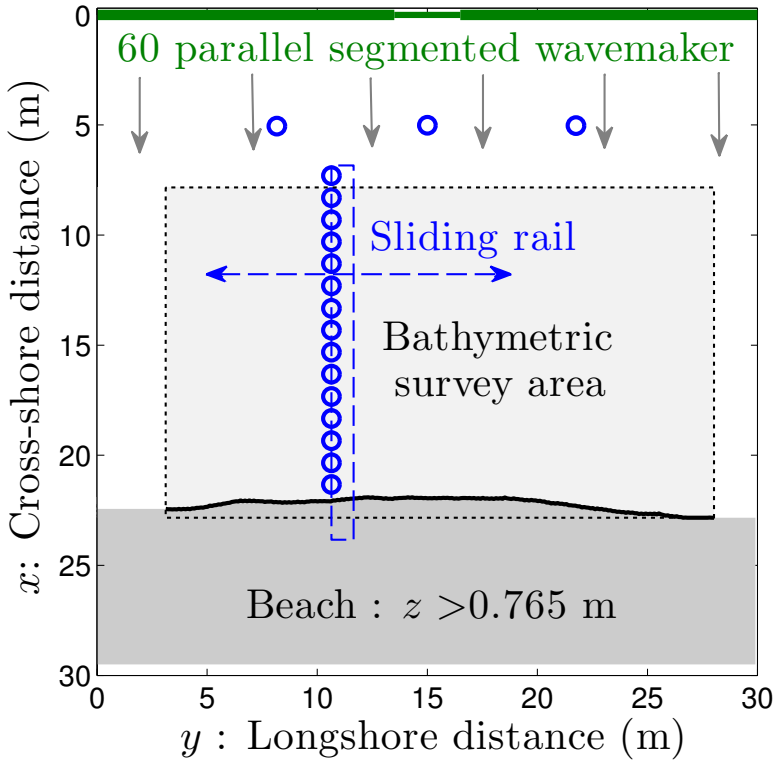

Figure 4.4 – Schematic representation of LHF wave tank. The x axis corresponds to the cross-shore position, the wavemaker is located at $x = 0$ m, the shoreline is at $x \approx 22$ m. The y axis corresponds to the alongshore position. The circles represent wave gauge locations.

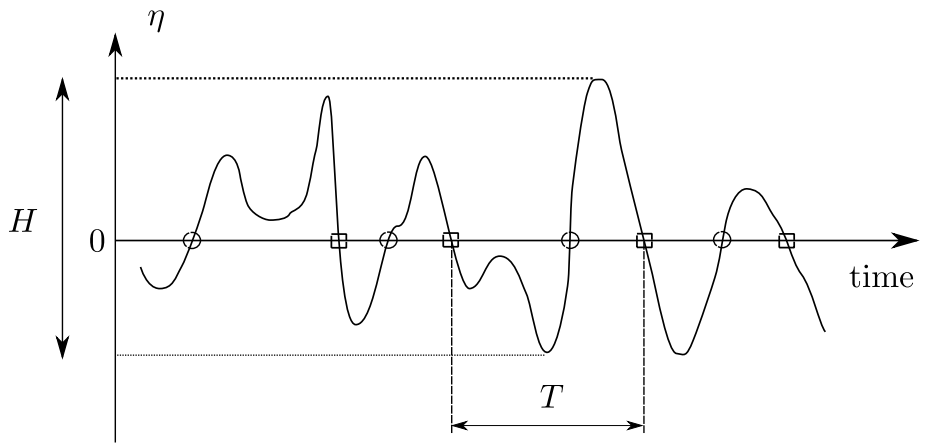

Figure 4.5 – Definition of wave height H, using the zero down-crossing method. The line represents the time-series of the water surface elevation. The wave is defined by two consecutive zero down-crossing, shown by the squares. The wave height can also be defined with a zero up-crossing method, between two consecutive circles. The horizontal axis represents the averaged wave height elevation over the full time series.

where g is the gravity acceleration, $\gamma = 3.3$ is the peak enhancement coefficient, f_p is the peak frequency, σ is the width of the spectrum base before ($\sigma_A = 0.07$) and after ($\sigma_B = 0.09$) the peak frequency, α is the scale factor and is associated with the total spectrum energy, and related to the significant wave height H_{m0}. The spectrum is defined in the frequency band $[0.5f_p, 5f_p]$.

The wave height is defined as explained in Figure 4.5, and can be defined with a zero up-crossing or zero down crossing method. These two methods are equivalent if the surface elevation is a Gaussian process. From the definition of the wave height, we can define the mean wave height $\overline{H}$ over a sequence of N waves:

$$\overline{H} = \frac{1}{N} \sum_{i=1}^{N} H_i \tag{4.11}$$

where i is the i-th wave in the sequence.

We can also define the root mean square of the wave height H_{rms} and the significant wave height H_s as:

$$H_{rms} = \left(\frac{1}{N} \sum_{i=1}^{N} H_i^2 \right)^{1/2} \tag{4.12}$$

$$H_s = H_{1/3} = \frac{1}{N/3} \sum_{j=1}^{N/3} H_j \tag{4.13}$$

where j is the index of the waves ranked by their wave height, meaning that the significant wave height depends on the highest waves only. $H_{1/3}$ is the mean height of the third of the highest waves. By assuming that the probability density function of the wave height is a Rayleigh distribution, it is possible to obtain estimations for $\overline{H}$, H_{rms} and H_s, using the zeroth-moment m_0 [Holthuijsen, 2007]:

$$\overline{H} = \sqrt{2\pi m_0} \tag{4.14}$$

$$H_{rms} = \sqrt{8m_0} \tag{4.15}$$

$$H_s = H_{m_0} = 4.004\sqrt{m_0} \approx 4\sqrt{m_0} \tag{4.16}$$

where

$$m_0 = \int_0^\infty S_{\eta\eta}(f)\mathrm{d}f = E\{\eta^2\} \tag{4.17}$$

with $S_{\eta\eta}(f)$ the variance density spectrum.

In this case, the relation between the significant wave height H_{m_0} and the root mean square of the wave height is $H_{m_0} = 1.416 H_{rms}$.

In order to create an alongshore non-uniformity in the incoming waves, the wave amplitude in the center of the wave crest is damped, resulting in alongshore variations of the wave height H. This alongshore non-uniformity triggered a rip instability. To obtain an estimation of the wave damping in each experiment, we used the three fixed wave gauges at $x = 5$ m. The damping is then calculated as the difference in significant wave height H_{m_0} between the wave gauge located at $y = 15$ m, and the mean of the two wave gauges located at $y = 8.17$ m, and $y = 21.75$ m.

The wave conditions were chosen considering a Dean number Ω_D in the intermediate range. The Dean number ($\Omega_D = H_{m_0}/T_p w_s$, where H_{m0} is the significant wave height, T_p is the peak period, w_s is the settling velocity) can be interpreted as the ratio between the uplifting velocity of sediment particle by waves and the settling velocity w_s of the bed sediment. The Dean number is a macroscopic Rouse number. This number is used to characterize different types of beaches (reflective, dissipative, intermediate, etc.).

Different wave conditions were tested during the experiment, as summarized in Figure 4.6. These wave conditions can be classified in three categories:

- A) An energetic condition A: $H_{m_0} = 23$ cm / $T_p = 2.3$ s / $\Omega_D = 5$, between t=66:00 and t=100:40,
- B) moderate conditions with a longer period : $H_{m_0} = 18$ cm / $T_p = 3.5$ s / $\Omega_D = 2.5$, between t=9:40 and t=66:00,
- C) moderate conditions with a shorter period : $H_{m_0} = 17$ cm / $T_p = 2.1$ s / $\Omega_D =$

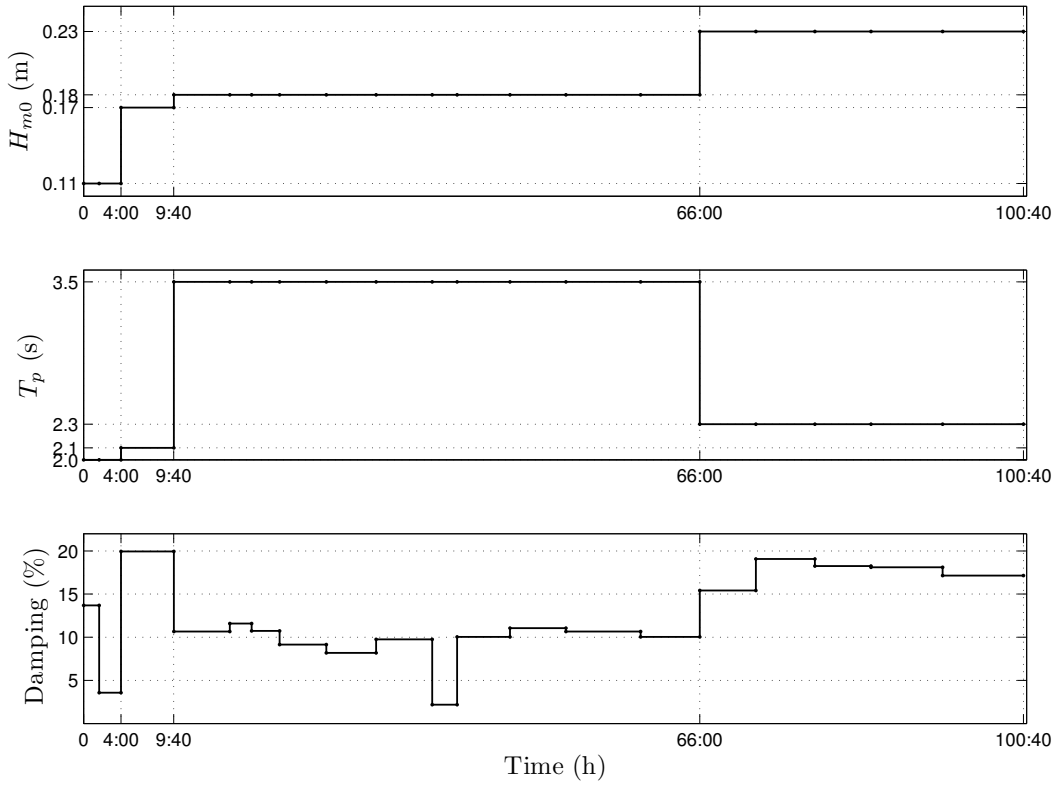

Figure 4.6 – Upper panel: Significant wave height of the wave front H_{m_0}; Middle panel: peak period T_p; Lower panel: wave damping at $x = 5$ m over the full duration of the experiments.

4, between t=4:00 and t=9:40.

The wave conditions at the beginning between 0:00 and 4:00 consisted of relatively small waves (H_{m0} = 11 cm) that served to smooth the bed and determine the best positions for the measuring instruments.

In this chapter we focus on the moderate wave conditions with a larger period (B), thus restraining the analysis to the period between t=9:40 and t=66:00, concerning the bed evolution.

Bed evolution

The bed evolution is detailed and discussed in Michallet *et al.* [2013], we therefore briefly comment the mobile bed evolution during the wave forcing considered.

As we focus on the B wave conditions, we look at the bed evolution between t=9:40 and t=66:00. We consider the initial beach at t=9:40, when the B wave forcing starts. This original bathymetry is relatively uniform alongshore, with a bar at $x \approx 13m$. The wave condition lasts for 50 hours, with a wave sequence of 20 minutes complying a JONSWAP spectrum, repeated continuously. Every 20 minutes the sliding rail was moved alongshore to gather data in the whole survey area.

There are two phenomena that explain the bathymetric evolution. The first one consists in the wave non-uniformity alongshore, which creates rip channels and an heterogeneity alongshore. The second one is related to the moderate wave conditions, and consists in an onshore sediment transport (Figure 4.7). Therefore, during this experiment, the beach never reached a quasi-steady state. The characteristic time of this two phenomena are different, the accretion occurring at a longer time scale than the alongshore non-uniformity.

The alongshore wave forcing non-uniformity results in an alongshore non-uniformity in the bathymetry, and the formation of rip channels (Figure 4.8). At t=9:40 (Figure 4.7 a), we observe two slope change at x = 13 m and x = 22 m in the alongshore averaged bathymetric profile, with three slopes well defined, one between x = 8 m and x = 13 m another one between x = 13 m and x = 22 m and the third one for $x >$ 22 m. At t=21:00 (Figures 4.7 b and 4.8 b), we observe an onshore migration of the bar, as well as the formation of rip channels at y = 10 m and y = 25 m, and shallow shoals. From t=31:20 onward, (Figures 4.7 c and 4.8 c) we observe the filling of the rip channels previously formed, as the accretion phase continues, until the end of the wave condition, at t=66:00.

Choice of the bathymetry and the wave forcing

We want to observe the behaviour of the model for an heterogeneous bathymetry, with a rip current. We then choose the bathymetry corresponding to experiment that

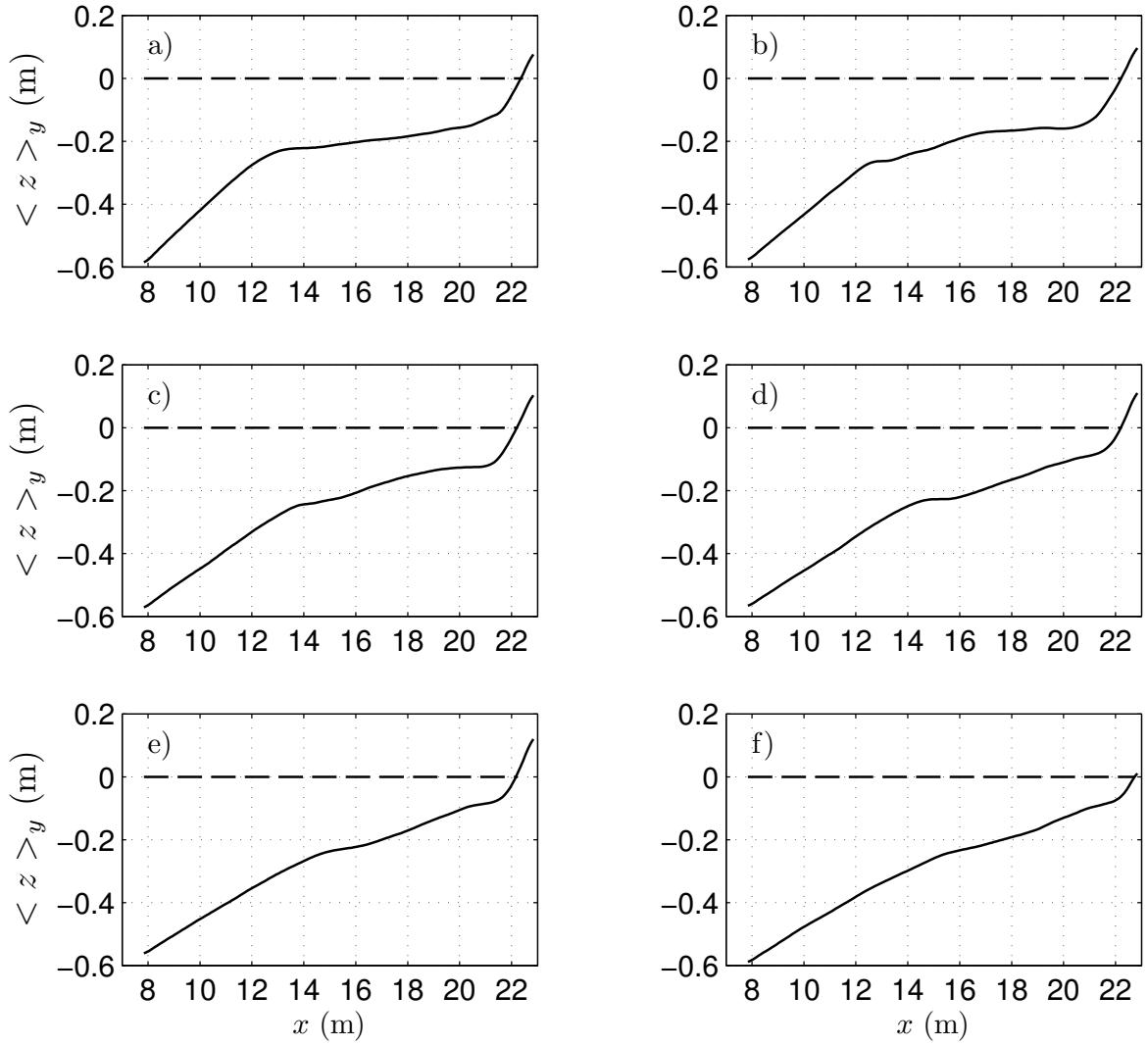

Figure 4.7 – Alongshore averaged bathymetric profiles at different times. a) bathymetry at t=9:40; b) bathymetry at t=21:00; c) bathymetry at t=31:20; d) bathymetry at t=40:00; e) bathymetry at t=51:40; f) bathymetry at t=59:40.

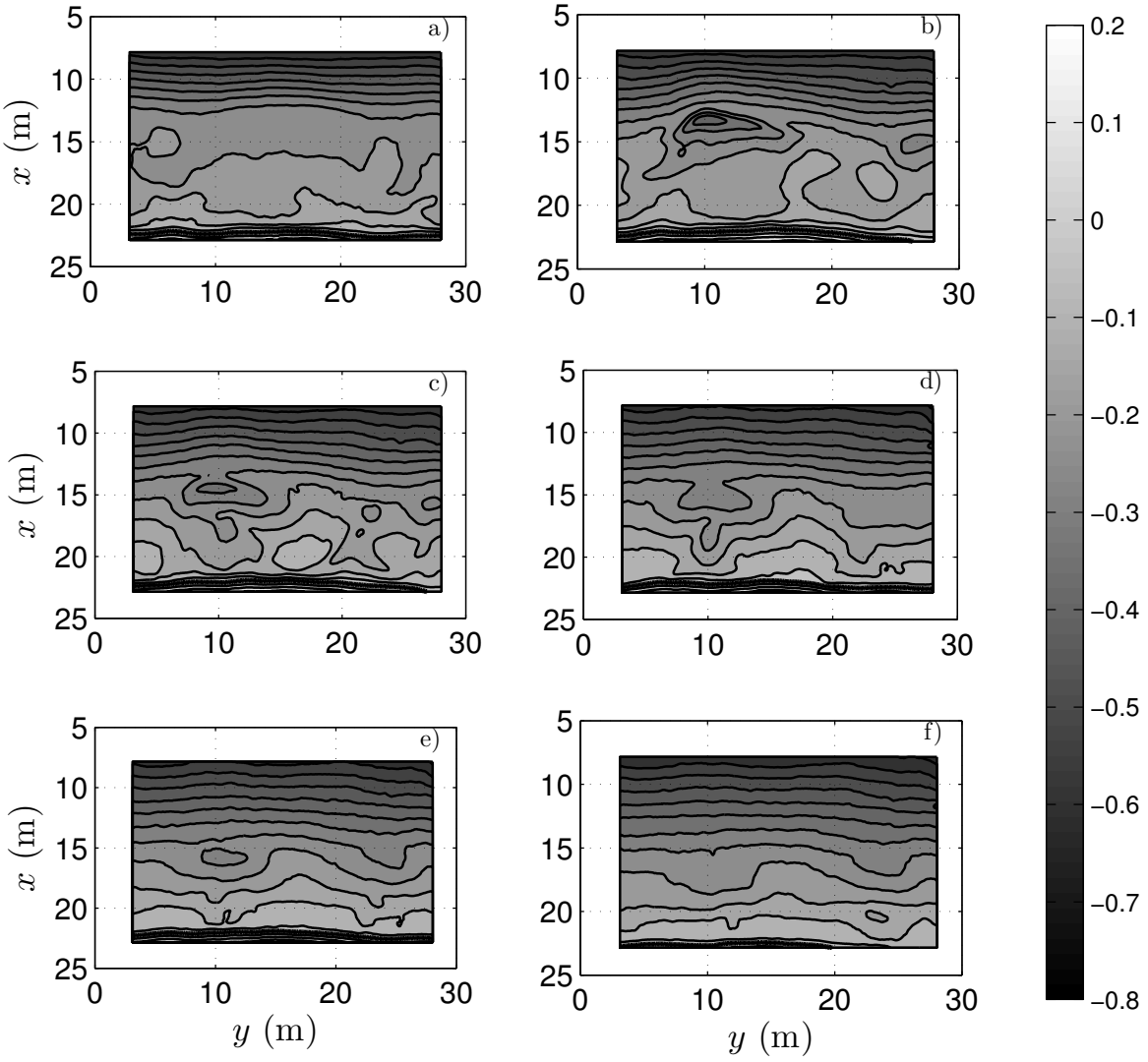

Figure 4.8 – Bathymetry evolutions: bathymetric surveys at different times. The wavemakers are at x=0. a) bathymetry at t=9:40; b) bathymetry at t=21:00; c) bathymetry at t=31:20; d) bathymetry at t=40:00; e) bathymetry at t=51:40; f) bathymetry at t=59:40.

starts at t=21:00 with the largest alongshore non-uniformity. The conditions for this experiment are presented in table 4.1.

starting time	21:00
ending time	26:00
T_p **(s)**	3.5
H_{m0} **(cm)**	18
Positions of the rail	15

Table 4.1 – Conditions for the numerical validation.

The bathymetry during this period is non-uniform alongshore, with 2 rip-channels formed at $y = 10$ m and $y = 25$ m. The wave forcing is also moderate, but with a larger period as explained in the previous subsection.

Measurements and model setup

Bathymetry

The beach morphology is measured by means of a laser mounted on a motorized trolley, located on the sliding rail (Figure 4.4). The basin was emptied every night in order to measure the bathymetry. The emptying was slow enough to prevent mobile bed motion during this draining phase.

The resolution of the bathymetry data is of 1 mm vertically, and respectively 10 cm and 1 cm in the alongshore and cross-shore direction. The complete basin bathymetry could not be surveyed due to the configuration of the sliding rail, and the available surveyed zone is restricted to the area 7.84 m $< x <$ 22.84 m in the cross-shore direction, and 3.12 m $< y <$ 28.02 m in the alongshore direction.

The resulting bathymetry is made of 250 cross-shore profiles, each containing 1501 points.

As stated earlier, the bathymetric survey zone did not cover the entire area of the basin, hence we need to extrapolate the bathymetry for the numerical model. We extrapolate the bathymetry from the area 7.84 m $\leq x \leq$ 22.84 m in the cross-shore direction, 3.12 m $\leq x \leq$ 28.02 m in the alongshore direction, to the area covered by the wave basin, 0 m $< x <$ 30 m in the cross-shore direction, 0 m $\leq x \leq$ 30 m in the alongshore direction.

We define the value $z = -0.765$ m as the position of the fixed bed at the wavemakers. The position $z = 0$ m corresponds to the still water level in the experiment.

The following processing is applied in order to obtain the bathymetry used in the numerical model:

- the bathymetry is filtered from its extreme values, defined as the points where the bed gradient is higher than a given threshold, and replaced by nearby values,

- the bathymetry is spatially smoothed, using a convolution with a 50 cm $\times$ 50 cm mask, in order to remove the ripples,

- The zone between 0 m $\leq x \leq$ 7.84 m in the cross-shore direction is extrapolated by imposing a flat bottom located at $z = -0.765$ m for $x \leq 5$ m, and a linear extrapolation between $x = 5$ m and $x = 7.84$ m, to reach the value $z = -0.765$ m at $x = 5$ m.

- For $x >$ 22.84 m, we estimate the mean slope in the portion 22.35 m $< x <$ 22.84 m, and we extrapolate linearly with these slope in the portion 22.84 m $< x <$ 25.0 m

- The alongshore extrapolation considers the two bands 0 $m < y <$ 3.12 m and 28.02 $m < y <$ 30.0 m. For each lateral boundaries, we consider the mean bed gradient in the 2 meters near the boundary, and consider these gradient to extrapolate linearly a cross-shore profile. We then smooth the resulting profile, and extrapolate linearly from the known profile to the smoothed profile.

The differences between the raw bathymetry and the smoothed one used as an input for the model can be seen in Figure 4.9.

In the experiment, the bed is made of mobile sand and evolves in time with the wave forcing that generates sediment transport. According to Michallet *et al.* [2013], the bottom evolution velocity presents a peak of 1.5 cm/hr located at the rip neck in the bathymetry at t=21:00, with values near 0.5 cm/hr elsewhere. As the numerical simulations last for 20 minutes (unless stated otherwise), we then suppose that the bed variations during each experiment are small enough to use a fixed bathymetry during the numerical simulation.

Surface elevation

To access the water surface elevation, 18 high-accuracy capacitive gauges, designed by Sogreah Consultants were used. The wave gauges are constituted of a conducting wire, whose capacitance is related to the length of the immersed wire, that is converted to a voltage. The acquisition frequency of the wave gauges is set to 50 Hz.

Three of these gauges were installed on a fixed position, at $x = 5.01$ m, $y = 8.17$ m, $x = 5.03$ m, $y = 15.0$ m and $x = 5.05$ m, $y = 21.75$ m. These fixed gauges are located 5 meters onshore from the wavemakers, and allow to observe that the forcing

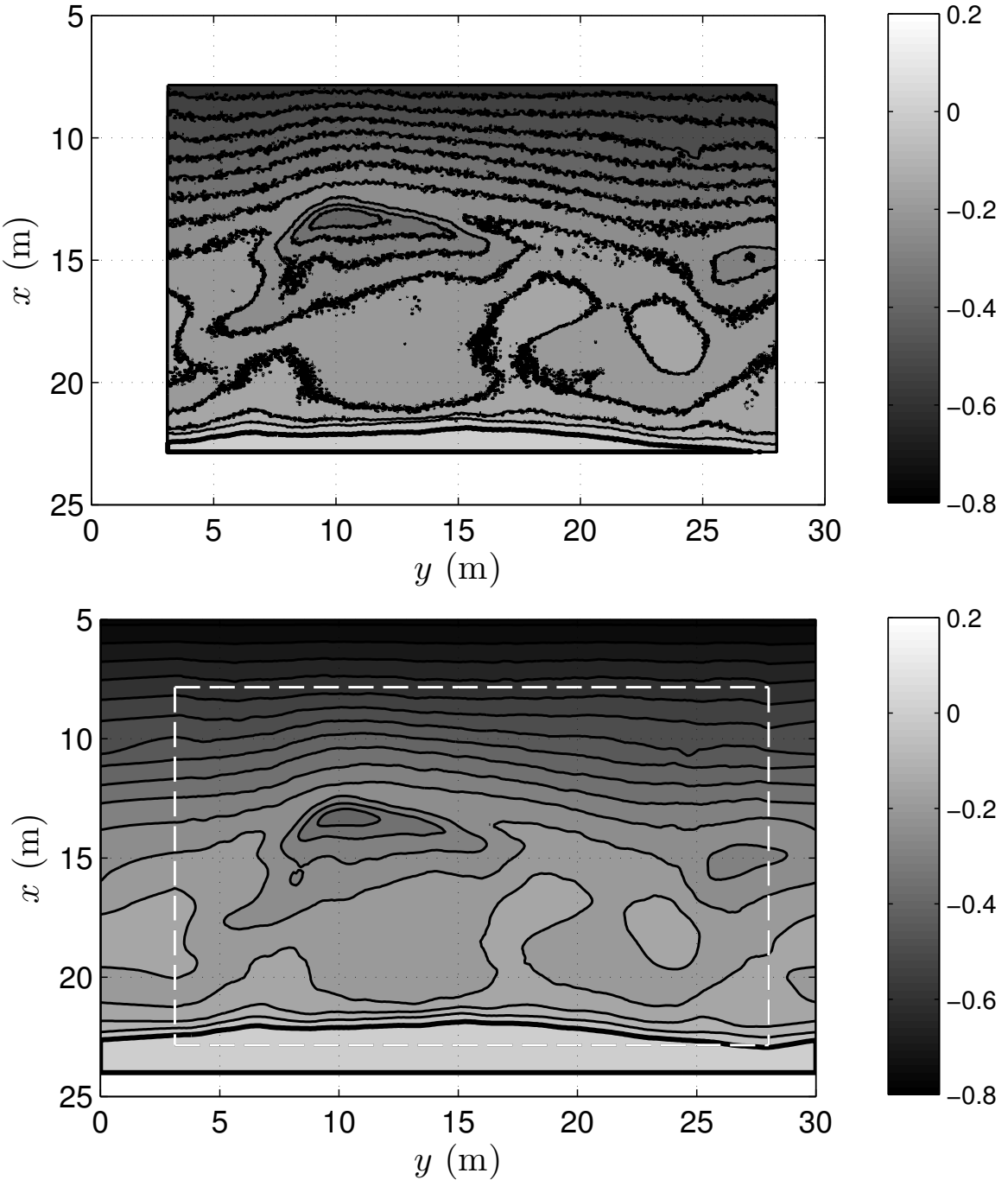

Figure 4.9 – Original bathymetry elevation (upper panel) and input bathymetry elevation for the model (lower panel). The white dashed box represents the limits of the original bathymetry. The isolines are set every 5 cm, the thick black line representing the shoreline.

wave condition remains similar between each run, where a run is defined as a 20 minute sequence of a time-series complying a JONSWAP spectrum.

The remaining 15 wave gauges were fixed on the moving sliding rail at a constant cross-shore distance from the wave maker. The sliding rail could move in the longshore direction, thus allowing to observe cross-shore and longshore profiles of surface evolution. The cross-shore position of these wave gauges is presented in Table 4.2.

Wave gauge	4	5	6	7	8	9	10	11
x **(m)**	7.300	8.305	9.310	10.310	11.300	12.305	13.325	14.320
Wave gauge	12	13	14	15	16	17	18	
x **(m)**	15.315	16.315	17.335	18.330	19.335	20.345	21.325	

Table 4.2 – Cross-shore position of the wave gauges present on the sliding rail. The position $x = 0$ m corresponds to the position of the wavemaker. The cross-shore position of these wave gauges, the longshore position y is variable as the sliding rail changes position

Velocity

The Acoustic Doppler Velocimeter (ADV) provides the three components of the velocity at a fixed elevation in the water column approximately located at 4-8 cm above the bed for the different measurement positions. The measurement volume is approximately of 1 cubic centimetre and the sampling frequency is set to 64 Hz.

During the experiment, 4 ADVs were used, three on the moving sliding rail, and one at a fixed location (Table 4.3).

ADV	1	2	3	4
x **(m)**	10.28	8.50	13.09	14.71
y **(m)**	15	variable	variable	variable

Table 4.3 – Position of the ADVs

Instrument positions

For these experiment, the instrument positions are shown in Figure 4.10. The sliding rail position covers a wide area of the experiment for the chosen run, and the fixed wave gauges are representative of the wave forcing, as the bed position between $x = 0$ m and $x = 5$ m is constant.

Boundary conditions

The model boundary conditions are shown in Figure 4.11: the boundaries 2 ($y = 0$ m) and 3 ($y = 30$ m) correspond to closed boundaries, since the basin is closed. The boundary 4 ($x = 25$ m) corresponds to a moving shoreline, with a dry/wet interface

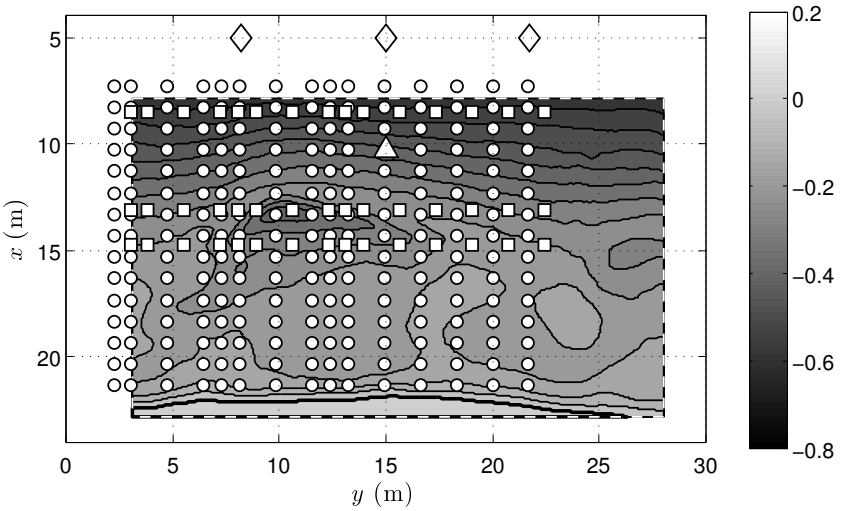

Figure 4.10 – Experiment 30 ($t = 21:00 - 26:00$) - position of the wave gauges and the ADV. Circles: mobile wave gauges; diamond: fixed wave gauges; square: mobile ADVs; Triangle: fixed ADV. The lines represent the isobaths, the thick line corresponds to the shoreline where the free surface intersects the bathymetry.

[Marche *et al.*, 2007]. The boundary 1 ($x = 5$ m) considers an absorption/generation condition [Cienfuegos *et al.*, 2007 ; Mignot et Cienfuegos, 2009].

For the wave height input, the wave height near the wavemaker was not available. Therefore we considered the closest wave gauges to the wavemaker, three static wave gauges located at 5 meters from the wavemaker, precisely at $x = 5$ m, and $y = 8.17$ m, $y = 15$ m, $y = 21.75$ m respectively. The wave input at each node is then interpolated alongshore using the three wave gauges, and assuming at $y = 0$ m and $y = 30$ m the wave forcing are identical to the ones at $y = 8.17$ m and $y = 21.75$ m respectively. The resulting wave forcing is shown in Figure 4.12.

The wave statistics at the three fixed wave gauges at $x = 5$ m varies little during each run. For each run, we then consider the averaged wave forcing over all the 20-minutes time-series in the numerical model.

Wave forcing

The wave forcing for the chosen experimental conditions is shown in Figure 4.12. The wave forcing at the wave-maker is moderate: $H_{m0} = 0.18$ m, with a period $T = 3.5$ s and the damping is of approximately 10 %.

We observe at $x = 5$ m that the wave energy alongshore variation is relatively symmetric, the significant wave height H_{m0} being similar at 8.17 m and $x = 21.75$ m. At $x = 7.30$ m the significant wave height alongshore variation is asymmetric, H_{m0} being higher in the region 10 m $< y <$ 15m than in the region 15 m $< y <$ 20m.

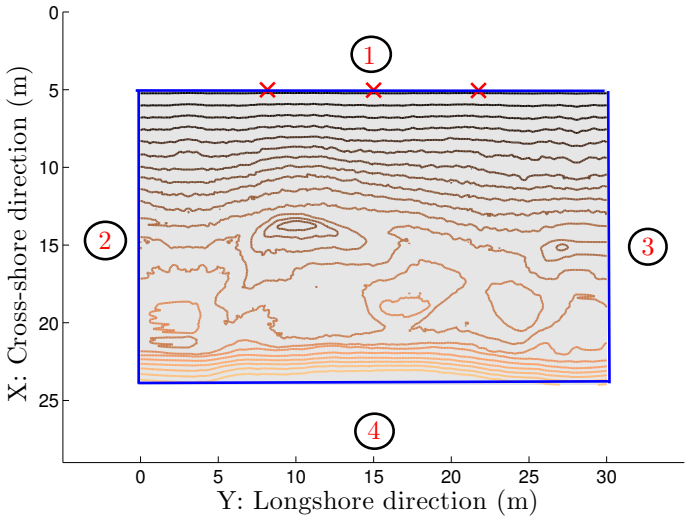

Figure 4.11 – Boundary conditions of the numerical model. The red crosses mark the location of the wave gauges used for estimating the wave forcing input.

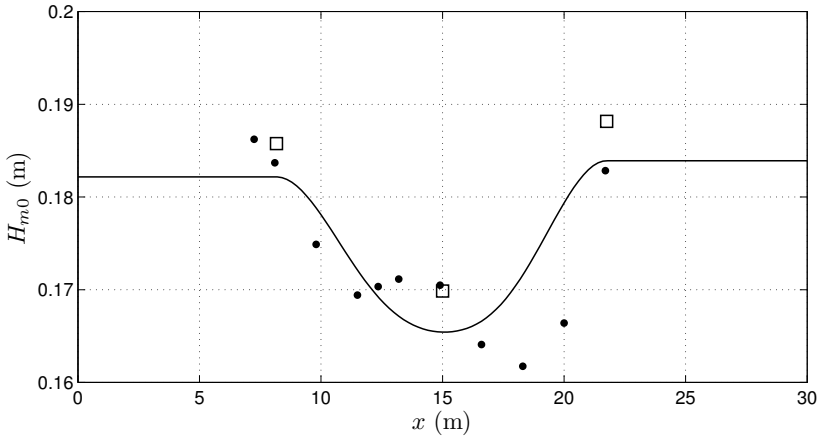

Figure 4.12 – Alongshore variation in significant wave height H_{m0} of the experimental fixed wave gauges at a distance $x = 5\ m$ from the wavemaker (squares), and of the mobile wave gauge located at $x = 7,30\ m$ (dots). The thin line represents the wave forcing input prescribed in the numerical model at $x = 5m$.

The asymmetry in the wave forcing is due to the bathymetry heterogeneity, as a rip channel is formed that increases the circulation toward the band 0 m $< y <$ 15m. This feature can be seen using the mean circulation, as explained in section 4.4.3.

Concerning the incident wave condition, there is a difference between the experimental data, and the numerical model. The absorption/generation condition is an open boundary, and the wave basin is a closed one. The latter implies that reflection at the wavemaker is not included in the numerical model, so that resonant conditions due to the enclosed basin in the experiments will not be amplified in the simulations. The influence of the wavemaker can be seen mostly in the resonant modes of the basin, occurring at low frequencies in a frequency range below the JONSWAP range.

The wave basin resonant modes can be seen in Figure 4.13. We observe two peaks at $f = 0.04$ Hz ($T = 25$ s), and $f = 0.08$ Hz ($T = 12.5$ s), which can be considered as the resonant modes of the wave basin. In the same Figure are shown the results of the numerical model with and without high-pass filtering for the input. The numerical results obtained with the wave input without filtering show a resonant mode amplification for the low frequencies, with two peaks at $f = 0.04$ Hz ($T = 25$ s) and $f = 0.083$ Hz ($T = 12.05$ s), however the same frequencies are three times more energetic than the experimental results. If we look at the numerical model results with high-pass filtering, we observe that the model is able to transfer energy to the low frequency band, without the appearance of resonant mode amplification.

Following these results, we prefer to use a high-pass filter and not to force incident wave conditions with infragravity energy. The infragravity band contains energy of the wave basin modes, that are not reproduced in the model, due to the open absorption/generation condition that is not a resonant condition for the wave basin. The model is able to transfer energy from the short-wave band to the low frequency band, without resonant mode amplification. For that reason, we can obtain information on the infragravity band generated by the model, without the disturbance of the basin seiching modes.

We observe a difference in wave energy between the wave input and the wave gauges at $x = 5$ m in Figure 4.12. This difference is due to the wave forcing filtering, as the energy in the Infragravity band is not taken into account. Resonant modes also named seiching modes will be analysed in more details.

Theoretical seiching modes

As we intend to analyse low frequency motions in the wave basin, we need to determine the wave basin seiching. Seiches occur on enclosed or partially enclosed bodies of

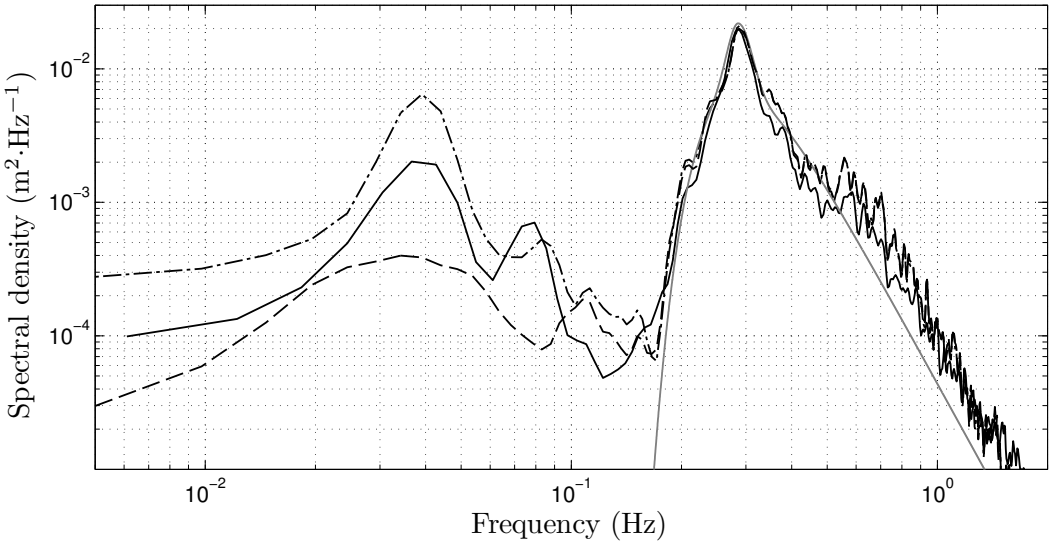

Figure 4.13 – Free surface spectral density for experiment 30 (t=21:00-26:00), at $x = 5$ m, $y = 8.17$ m. The grey line corresponds to the theoretical Jonswap spectrum (equation 4.10) which served as an input for the experiment, the black line to the experimental free surface measured by the wave gauge, the dash-dotted line to the numerical model with experimental results (black line) as input, the dashed line to the numerical model with high-pass filtered input, with a cut-off frequency $f_c = 1.7 \cdot 10^{-2}$ Hz.

water. This body of water resonates to its natural frequencies when excited, allowing the development of a standing wave.

The wave forcing in an enclosed basin produces seiches due to the wave reflection and the wave grouping, allowing a transfer of wave energy to lower frequencies. It is therefore important to estimate these natural frequencies, since they are amplified.

The MODLIT wave basin seiches are determined as explained in Haller et Dalrymple [2001], using the two-dimensional shallow water equation for variable depth:

$$\eta_{tt} - (gh\eta_x)_x - (gh\eta_y)_y = 0 \tag{4.18}$$

with η the water surface elevation, h the water depth, and subscripts representing derivatives.

The details concerning seiching modes can be found in Appendix B. Table 4.4 lists the periods of the waves corresponding to these modes. We observe that the main seiche modes are located in the infragravity band.

T (s)	$n = 0$	$n = 1$	$n = 2$
$m = 0$		33.26	20.28
$m = 1$	25.97	19.48	12.50
$m = 2$	12.42	11.64	9.70

Table 4.4 – Period of the lowest frequency modes. m: cross-shore mode number, n: long-shore mode number.

4.3 Model validation

4.3.1 Set up/Set down and wave height

To observe the differences between the numerical model and the experiment, we will first focus on experiment 30, that starts at t=21:00 and finishes at t=26:00.We will compare cross-shore distribution of flow characteristics along three cross-shore profiles, that are close to the three fixed wave gauges in the alongshore position, at $y = 8.17$ m, $y = 15$ m, $y = 21.75$ m. Thus we can compare the mean values from $x = 5$ m, which is the position of the first gauge, to $x = 21.325$ m, the cross-shore position of the last wave gauge.

We will first look at the differences in wave height. To that end we use the mean water level $\overline{\eta}$, and the mean wave trough $\overline{H_{min}}$ and wave crest $\overline{H_{max}}$, averaged over a period of 20 minutes. These levels are defined in Figure 4.14, $\overline{\cdot}$ is defined as an average over the waves, estimated with the zero down-crossing method, during 1200 seconds.

The results are shown in Figure 4.15, over three cross-shore profiles starting at $x = 5$ m from the wave maker, and finishing at $x = 21.325$ m, just offshore of the swash zone. The numerical values of the mean water level $\overline{\eta}$ compare well with the experimental values with errors lower than 0.01 m. Mean water level profiles show similar behaviour to the other experiments [Michallet *et al.*, 2011]. They all show a set-down followed by a setup. In the numerical model, the mean water level is relatively constant until $x = 11$ m, and then start to increase, results that are consistent with the linear theory, that predicts a mean water level decrease before the breaking and an increase after the breaking. The differences observed in the experimental results could be due to the resonant modes, however the differences are small enough.

If we look at $\overline{H_{min}}$ and $\overline{H_{max}}$, we observe larger differences. The experimental results show an increase in the wave crest level from 0.05 m to $0.10m$, until approximately $x = 12$ m, due to the wave shoaling, and after the breaking, the wave crest level decreases, until reaching values of approximately 0.05 m above the still water level

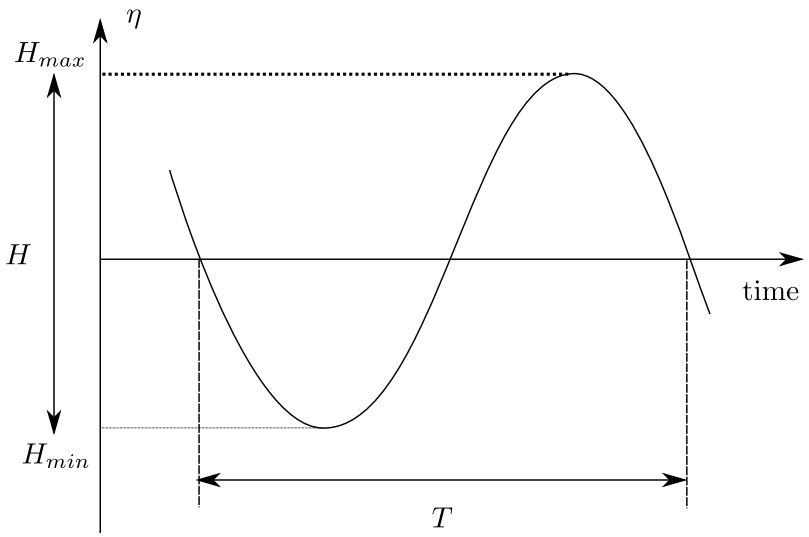

Figure 4.14 – Definition sketch of the wave height H, wave trough H_{min}, wave crest H_{max} and period T of one wave.

at $x = 21.325$ m, before the swash. The wave trough level remains constant in the shoaling zone, with a value of approximately -0.05 m, and after the breaking, the trough level increases, to reach a value of -0.02 m before the swash zone.

Concerning the numerical model results, the wave crest level remains nearly constant at $+0.06$ m in the shoaling zone, instead of increasing. After the breaking, at $x \approx 13$ m, the wave crest level decreases until a value of $+0.03$ m before the swash zone. The wave trough level increases in the nearshore zone, and after the breaking, it decreases from -0.06 m to -0.02 m.

The wave breaking index $\overline{\gamma_0} = \overline{H}/h$ where $\overline{H}$ is the averaged wave height and h the water depth, is an important non-dimensional number. It is often used in wave averaged models to predict the wave height evolution inside the surf zone [Bruneau *et al.*, 2011]. We observe that the spatial distribution of $\overline{\gamma_0}$ in Figure 4.16 is similar in the model and in the experiment, with the peak values in the breaking zone lower in the numerical model, around 0.5 instead of 0.6 in the experiment. This difference is also due to the absence of wave shoaling in the numerical model.

As stated before, there are some differences between the experiment and the numerical model. This can be explained by the fact that the model does not account for dispersive terms effects, hence the wave shoaling does not occur, and the wave crest do not increase in the shoaling zone. Despite this difference, we observe that the wave decrease gradient in the surf zone after the breaking is similar in the numerical model and in the experiments. These gradients are important for the energy balance, the

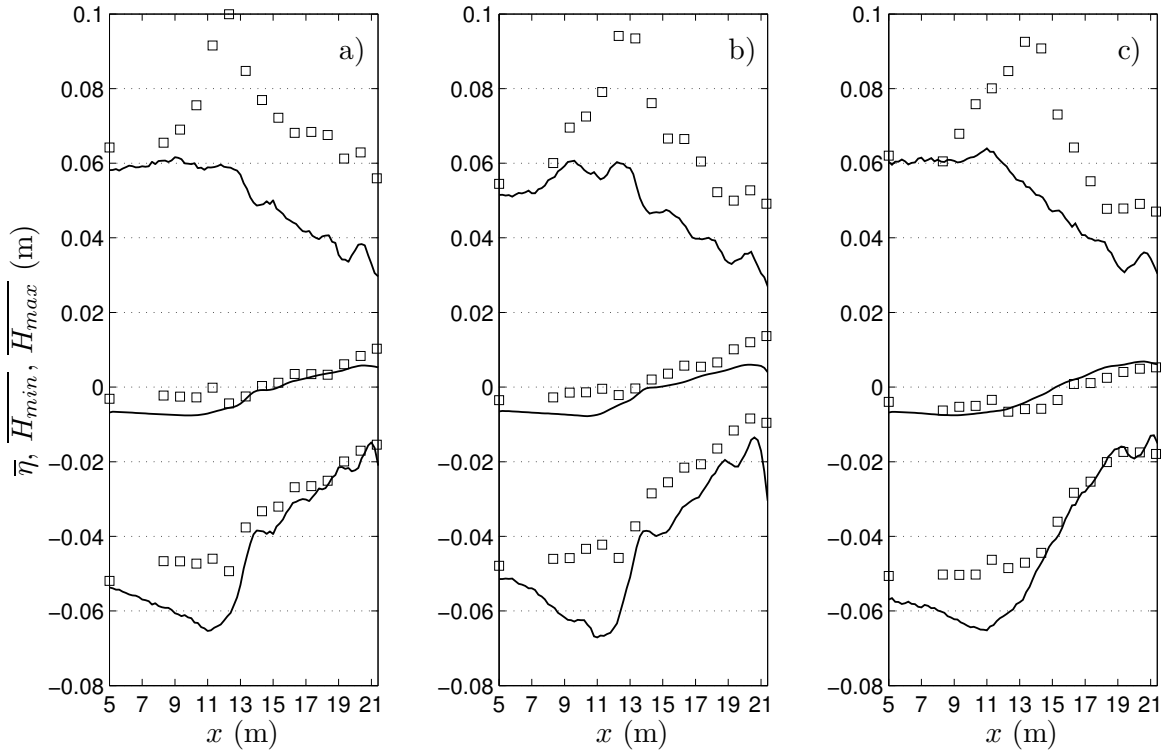

Figure 4.15 – Averaged wave height, over three cross-shore profiles for experiment 30 (t=21:00-26:00). The square correspond to the experimental results, the line to the numerical model. The upper line and square refer to the mean wave crest $\overline{H_{max}}$, the middle line and squares refer to the mean water level $\overline{\eta}$, the lower line and squares refer to the mean wave trough $\overline{H_{min}}$. a) profile at $y = 8.17$ m, b) profile at $y = 15$ m, c) profile at $y = 21.75$ m. The zero altitude corresponds to the still water level.

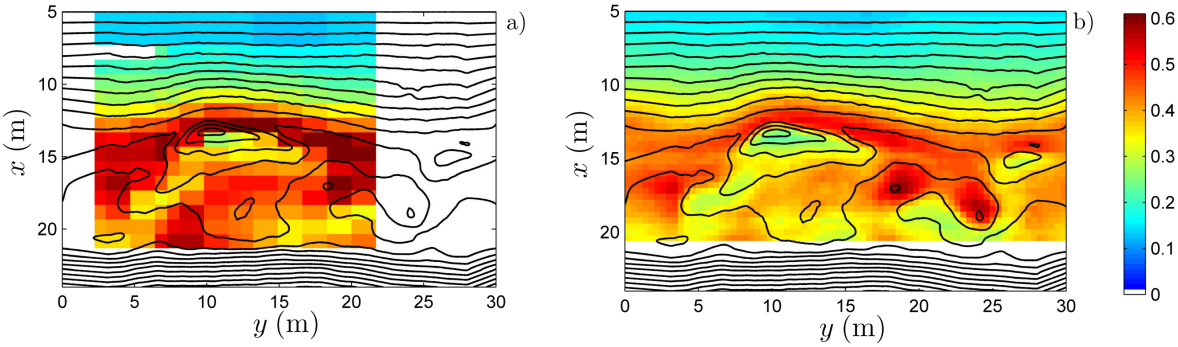

Figure 4.16 – Spatial distribution of the wave breaking index $\overline{\gamma_0}$ for experiment 30 (t=21:00 - 26:00). a) experimental results for experiment 30 (t=21:00-26:00); b) numerical simulation. Line are the isobaths (every 5 cm). Colours for $\overline{\gamma_0}$.

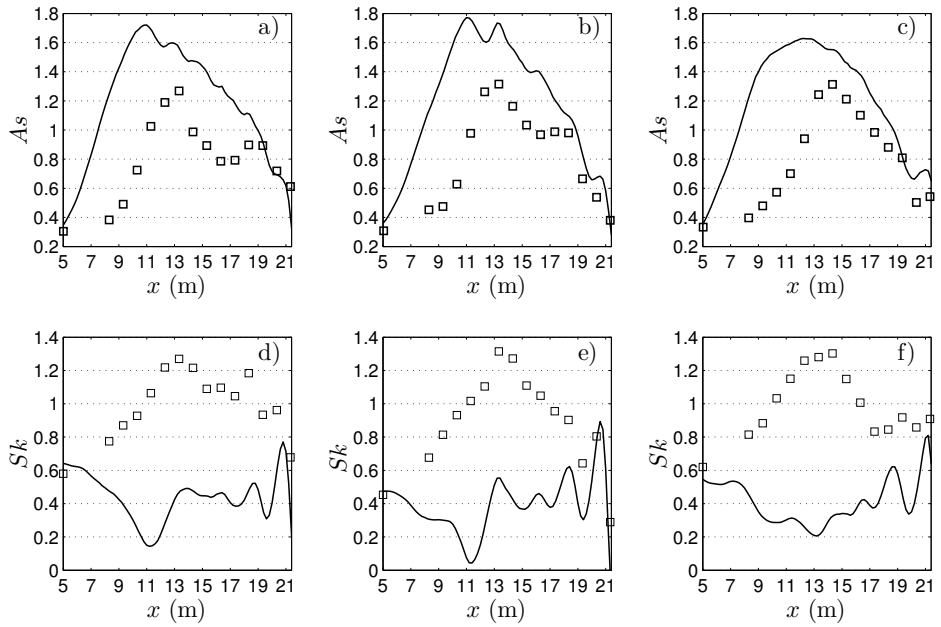

Figure 4.17 – Asymmetry As at profiles a) $y = 8.17$ m , b) $y = 15$ m, c) $y = 21.75$ m and Skewness Sk at profiles d) $y = 8.17$ m , e) $y = 15$ m, f) $y = 21.75$ m. Squares: experimental results; plain line: numerical model.

wave dissipation and current generation.

4.3.2 Non-linearities

We can also compare the asymmetry, A_s, and skewness, S_k, cross-shore evolution in Figure 4.17. The skewness and the asymmetry are key tools to analyse the nonlinear characteristics of the waves. The skewness and the asymmetry of the free surface time series are estimated using formula (4.19–4.20):

$$Sk(x) = \frac{\overline{(\eta(x,t) - \overline{\eta})^3}}{\eta_{rms}^3} \tag{4.19}$$

$$As(x) = -\frac{\overline{\Im(\mathcal{H}(\eta(x,t)))^3}}{\eta_{rms}^3} \tag{4.20}$$

where $\eta(z,t)$ is the free surface time series, $\eta_{rms} = (\eta - \overline{\eta})_{rms}$ the root mean square of the free surface η , with the overbar denoting a time-average over the studied interval, $\mathcal{H}(\eta)$ is the Hilbert transform of η and $\Im$ the imaginary part.

The asymmetry increases slightly in the experiment, from 0.3 at $x = 5$ m to 0.5 at $x = 9$ m, then the increase is stronger, and As goes from 0.5 to 1.3 between $x = 9$ m and $x = 14$ m, just after the breaking. After that, As decreases, and reaches values

between 0.4 and 0.6 at $x = 21$ m.

The skewness in the experiment also increases steadily between $x = 5$ m and $x = 15$ m, from 0.5 to 1.3. After the breaking, Sk decreases in the three profiles, reaching values between 0.6 and 0.8 at $x = 21$ m.

In the numerical model, As increases strongly from $x = 5$ m, with a similar gradient as in the experiment, but not in the same cross-shore position. The maximum As is higher than in the experiment, between 1.6 and 1.8 depending on the profile, and is reached before, at $x = 11$ m. Then As decreases steadily, to reach values between 0.4 and 0.6 at $x = 21$ m.

The skewness decreases, to reach values close to 0.2 before the breaking at $x = 11$ m, and then varies from 0.2 to 0.6. The skewness is related to the wave shoaling and the dispersive terms, and is not well reproduced by the model.

These differences can be explained by the discrepancies in the free surface elevation time series between the simulation and the experimental data as shown for a cross-shore profile, in Figure 4.18. The absence of dispersion terms in the numerical model lowers the wave height peaks, and does not produce secondary peaks, which are responsible for the decrease of the period as waves approach the coast. However wave fronts with bores are relatively well simulated providing asymmetry estimations of better quality than for the skewness.

4.3.3 Significant wave height

We validate the numerical model by checking the free surface elevation spectral properties. To that end, we compare the free surface spectra in a cross-shore profile, located at the middle of the basin alongshore, at $y = 15$ m. The spectra were calculated over a 20 minute sequence, at a 50 Hz frequency for both the wave gauges and the numerical data. The first spectrum (Figure 4.19 a), at a distance $x = 5$ m from the wavemaker, corresponds to the absorption/generation boundary condition of the numerical model. The spectrum indicates that the numerical model is able to reproduce the input wave height in the frequency band between 0.15 Hz and 1 Hz. In the frequency band below 0.15 Hz, the differences in peak frequencies have been explained by the numerical boundary condition, where the reflection by the wavemaker is not included (see section 4.2.2).

The second spectrum (Figure 4.19 b), at a distance $x = 10.31$ m, shows a good concordance in the frequency band between 0.15 Hz and 1 Hz, with some discrepancies under 0.15 Hz. The spectrum at $x = 15.31$ m is located after the wave breaking, and even though the frequency band around the peak frequency, between 0.15 Hz and

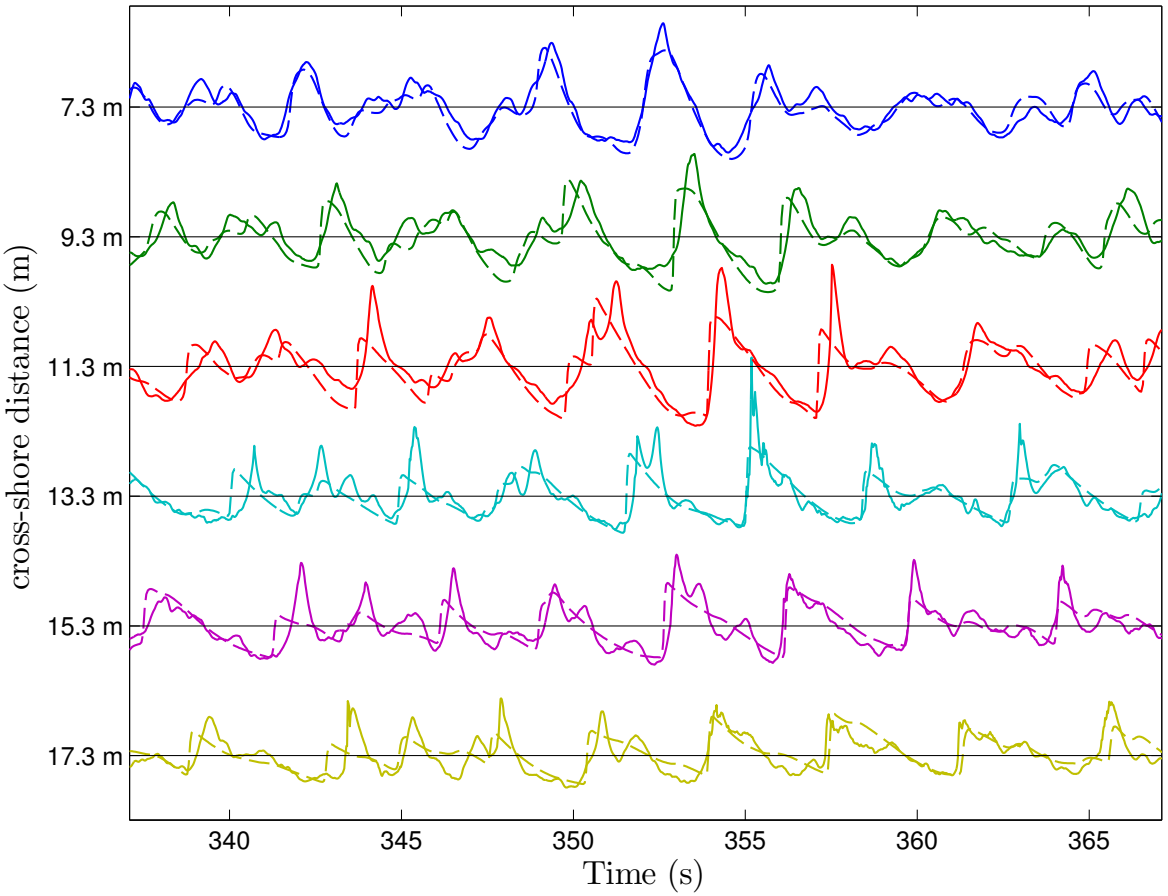

Figure 4.18 – Free surface elevation time-series in a cross-shore profile at $y = 10$ m for 6 different wave gauges located at different cross-shore positions for experiment 30 (t=21:00-26:00). Experimental results (line) and numerical model (dashed line)

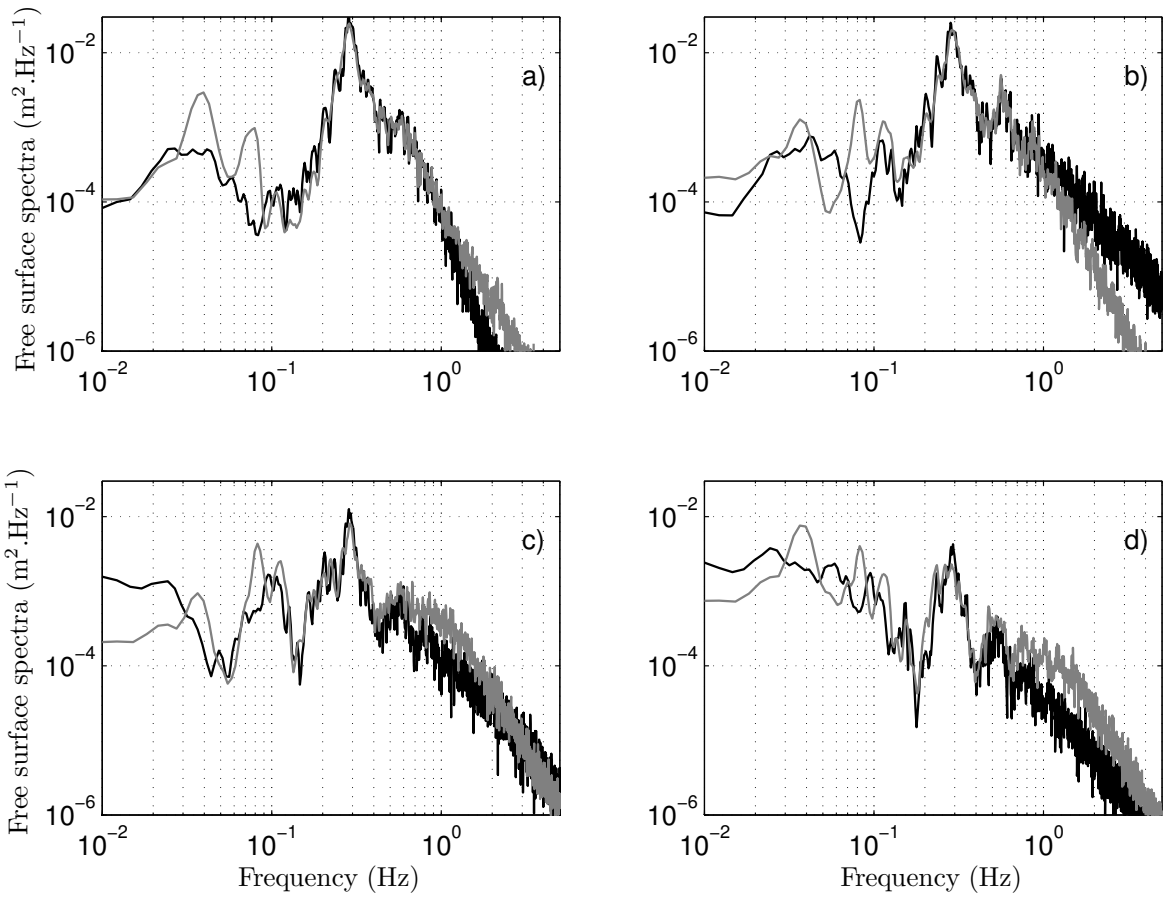

Figure 4.19 – Free surface wave spectra $S\eta\eta$ of experimental wave gauges for experiment 30 (t=21:00-26:00) (grey line) and of the numerical model (black line) at distances (a) $x = 5.01m$, (b) $x = 10.31m$, (c) $x = 15.31m$,(d) $x = 20.34m$, from the wavemaker. The alongshore distance is $y = 15m$, at the center of the basin.

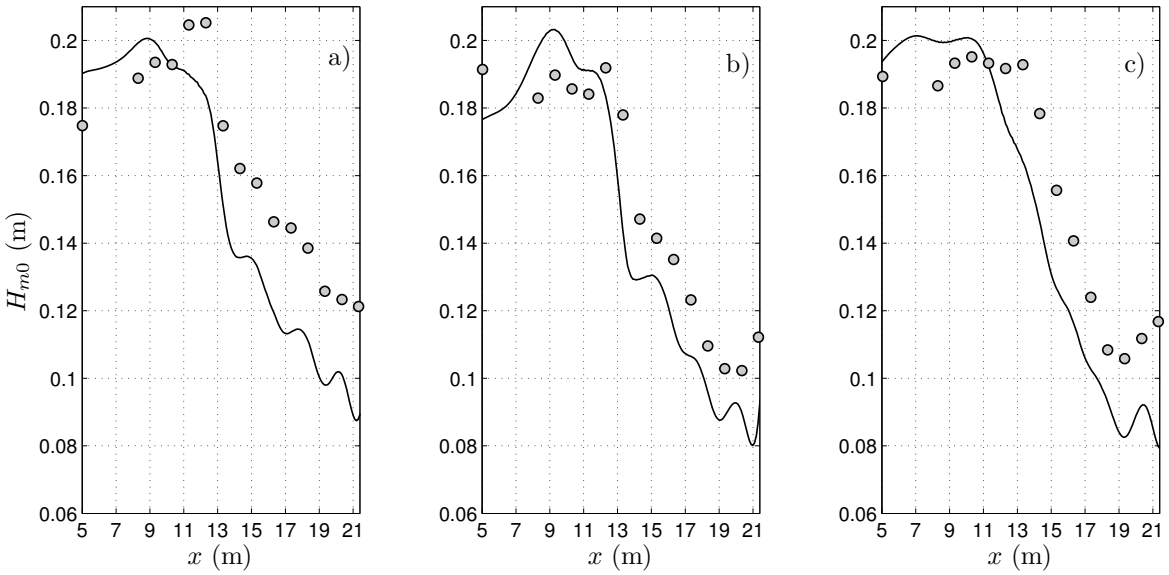

Figure 4.20 – Wave height evolution for experiment 30 (t=21:00-26:00) in three cross-shore profiles at a) $y = 8.17$ m , b) $y = 15$ m, c) $y = 21.75$ m. Grey circle: experimental significant wave height $(H_{m0})_{exp}$ estimated using the wave energy; plain line: modelled significant wave height $(H_{m0})_{mod}$.

0.4 Hz is well reproduced, over 0.4 Hz the numerical model shows more energy than the wave measurements. The infragravity mode at 0.1 Hz is fairly well reproduced by the model. The spectrum at $x = 20.34$ m is located near the shoreline, and the peak frequency band of the numerical model is also concordant with the experimental data. The numerical model reproduces energy transfer to the low frequencies near the shoreline, even though the peaks are not well reproduced.

We can also compare the spectral significant wave height $H_{m_0} = 4\sqrt{m_0}$, as this measure is proportional to the square root of the integral of the wave height spectrum, and is related to the energy dissipated by wave breaking. The cross-shore evolution of the significant wave height in 3 cross-shore profiles is shown in Figure 4.20.

The experimental results show that in the shoaling zone, until $x = 13$ m, $(H_{m0})_{exp}$ remains constant in the $y = 15$ m and $y = 21.75$ m profiles, and increase in the $y = 8.17$ m profile. The significant wave height then decreases after the wave breaking, as the dissipation occurs. In the first profile at $y = 8.17$ m, the wave height increases from 0.17 m, to 0.21 m at the breaking, and then decreases steadily to reach 0.12 m before the swash zone. For the two other profiles, $(H_{m0})_{exp}$ remains constant, between 0.18 m and 0.19 m, and then decreases after the breaking.

The numerical model shows some similarities with a slight increase before the breaking for $y = 15$ m profile, and a constant wave height for the two other profiles, and then

a decrease in wave height, reaching 0.08 m at $x = 21$ m. The decrease in $(H_{m0})_{mod}$ occurs at $x \approx 11$ m, before than in the experiment. The decrease in wave energy corresponds to energy dissipation by wave breaking, and the observed gradient in the spectral H_{m0} decrease is similar in both cases.

4.3.4 Velocities

The numerical model is also validated using velocity observations from ADVs. During the experiment, 3 Acoustic Doppler Velocimeters mounted on the sliding rail, measured the three components of the instantaneous velocities at a frequency of 64 Hz. The ADV was located at a fixed elevation in the water column an therefore in average at roughly 5 cm from the bottom. The numerical model provides cross-shore and alongshore depth averaged velocities, therefore we can only compare the experimental and numerical velocities qualitatively, by assuming that the ADV is outside of the boundary layer and its measurements are representative of depth-averaged velocities.

We compare the averaged cross-shore velocity $\overline{u}$, the averaged longshore velocity $\overline{v}$ and the averaged velocity magnitude $\overline{U}$ over 1200 seconds in two alongshore profiles, at a distance $x = 13.09$ m and $x = 14.71$ m of the wavemaker, where the wave breaking has already occurred. We observe (Figure 4.21) that the numerical model reproduces the velocity variations.

Concerning the cross-shore velocity $\overline{u}$, the experiment shows a maximum off-shore velocity located at approximately $y = 9$ m where the rip channel is located. For both profiles, we observe almost null averaged cross-shore velocity between 0 m $< y <$ 5 m, and then a strong increase, to reach off-shore velocities of -0.15 m/s and -0.19 m/s for the alongshore profiles at $x = 13.09$ m and $x = 14.71$ m respectively. The velocity magnitude decreases slowly, to near-zero values at $y \approx 17$ m for both profiles.

The numerical model also present low velocity intensities in the region 0 m $< y <$ 5 m, and then a strong increase where the rip channel is located, with peak values of -0.14 m/s and -0.16 m/s, for the two alongshore profiles. These peak values are lower than the experimental one, however they are very close. The off-shore velocity decreases also slowly, similar to the experiment, but with a positive peak, not present in the experimental results.

The longshore averaged velocity $\overline{v}$ present lower peaks in the two profiles. For the $x = 13.09$ m profile, $\overline{v}$ decreases from $y = 0$ m to $y = 7$ m, from 0 to -0.03 m/s, then increases steadily until $y = 15$ m at 0.05 m/s, the decreases again. The numerical model reproduces the same tendency with stronger peak values, -0.1 m/s at $y = 7$ m and 0.09 m/s at $y = 15$ m. For the $x = 14.71$ m profile, the longshore averaged

velocities are low for both the experiment and the numerical model, with the same tendencies in increasing and decreasing.

If we look at the averaged velocity magnitude $\overline{U}$, with U defined as $U = \sqrt{u^2 + v^2}$, the profiles are similar between the model and the experiment for the $x = 13.09$ m profile. $\overline{U}$ is around 0.21 m/s at $y = 0$ m, then increases to reach values of 0.25 m/s at $y = 7$ m in the experiment (0.28 m/s in the model) then decreases to a value of 0.19 m/s in the experiment at $y = 10$ m (0.17 m/s in the model). It then increases again to reach a peak value at $y = 15$ m, of 0.22 m/s and 0.25 m/s in the experiment and the model respectively. Between 15 m $< y <$ 30 m, the velocity magnitude remain in a band of $0.2 - 0.22$ m/s.

For the $x = 14.71$ m profile, the velocity magnitude presents similar behaviour, although the peak velocity at $y = 9$ m is under-estimated in the model as the experiment reaches a value of 0.27 m/s and the model a value of 0.23 m/s.

From these alongshore averaged profiles, we can conclude that there is reasonable qualitative agreement between measured and modelled results, concerning the averaged velocities over 1200 seconds.

4.3.5 Model skill

Definition of the model skill

The numerical model will be compared to the experimental results using the model skill σ_k from [Gallagher *et al.*, 1998]. This parameter is defined as:

$$\sigma_k = 1 - \frac{\sqrt{\sum_{i=1}^{i=N}(Q_{c,i} - Q_{m,i})^2}}{\sqrt{\sum_{i=1}^{i=N}(Q_{m,i})^2}} \tag{4.21}$$

with the subscripts c and m corresponding to computed and measured quantities respectively, evaluated at all observed instances i. Here the variable Q is replaced by η_{rms}, or U_{rms}, with η the free surface, $U = \sqrt{u^2 + v^2}$ the velocity magnitude and u, v the cross-shore and longshore velocities respectively.

The model skill is estimated from spectral density distribution on a specific frequency band. MacMahan *et al.* [2004] defined an infragravity band with a low-frequency cut-off at 0.004 Hz and a high-frequency cut-off at 0.04 Hz, and a sea/swell band, with a low cut-off frequency at 0.04 Hz, and a high cut-off frequency at 0.35 Hz.

As there is a 1/3 time-scaling factor for the Froude similarity, we need to multiply these cut-off frequencies by 3. However, if we look at the free surface spectra at $x = 5\ m$, $y = 8.17\ m$ (Figure 4.13), we observe that the infragravity band in the

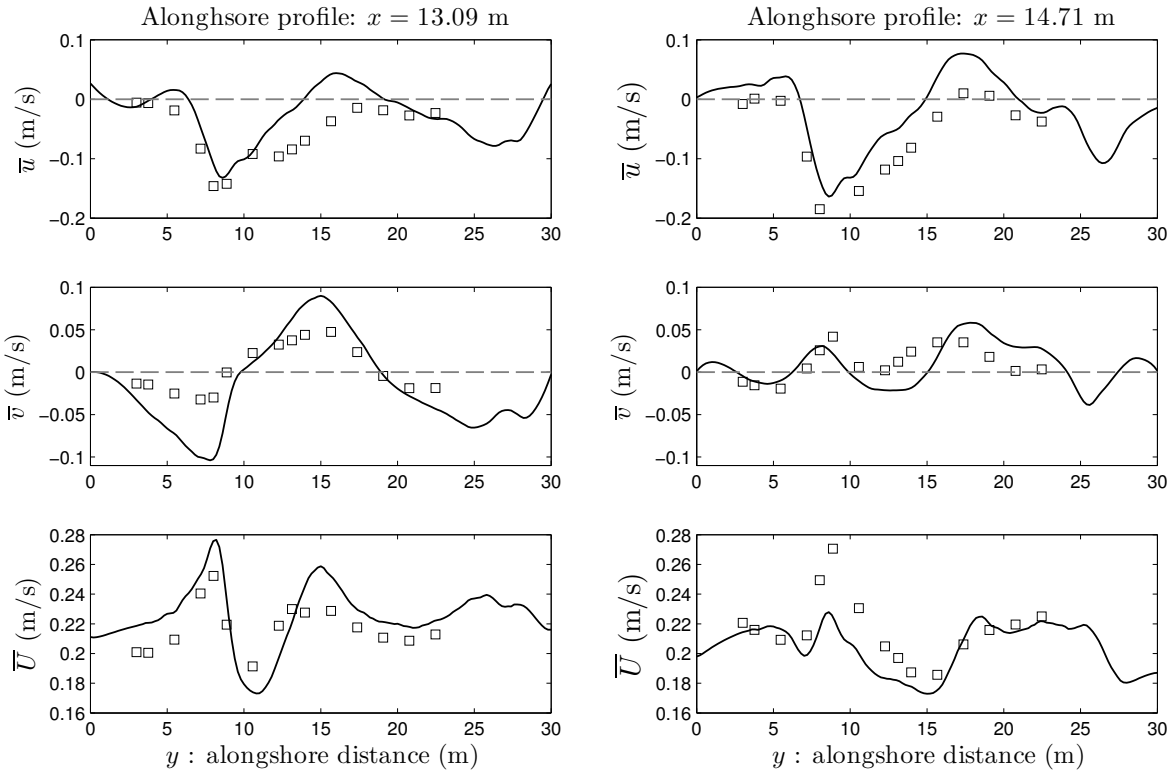

Figure 4.21 – Time-averaged cross-shore velocity $\overline{u}$, longshore velocity $\overline{v}$ and velocity magnitude $\overline{U}$ over two alongshore profiles for experiment 30. Left panels: alongshore profile at $x = 13.09$ m; Right panels: alongshore profile at $x = 14.71$ m. The negative cross-shore velocity represents a seaward oriented velocity, the negative longshore velocity represents velocity towards $y = 0$m.

experiment has a high frequency cut-off of 0.17 Hz, which is the frequency chosen to be the cut-off frequency between Infra-Gravity and sea/swell. The frequency limits between the different bands are then defined for the experiment as:

- the limit between the Very Low Frequency band and the InfraGravity band is $f_{c0} = 0.012$ Hz,
- the limit between the Infragravity band and the sea/swell band is $f_{c1} = 0.17$ Hz,
- the upper limit for the sea/swell band is $f_{c2} = 1.05$ Hz.

The root mean squared values on these bands is then defined as:

$$Q_{rms,hi} = \int_{f_{c1}}^{f_{c2}} S_{QQ}(f)\ df \tag{4.22}$$

$$Q_{rms,lo} = \int_{f_{c0}}^{f_{c1}} S_{QQ}(f)\ df \tag{4.23}$$

$$Q_{rms,tot} = \int_{f_{c0}}^{f_{c2}} S_{QQ}(f)\ df \tag{4.24}$$

where Q and E_Q are replaced by the free-surface η or the velocity magnitude U and the free-surface spectral energy E_η or the velocity magnitude spectral energy E_U respectively.

Concerning the mobile wave gauges located on the sliding rail, most of the time, we only possess one occurrence of the time-series at a specific location, however the cross-shore distance to the wavemaker remains the same. Therefore, we define a skill function $\sigma_{k,\eta}$ for each wave gauge:

$$\sigma_{k,\eta,hi}(i) = 1 - \sqrt{\frac{\sum_{j=1}^{N_{run}} \left((\eta_{rms,hi})_{c,i,j} - (\eta_{rms,hi})_{m,i,j}\right)^2}{\sum_{j=1}^{N_{run}} (\eta_{rms,hi})^2_{m,i,j}}} \qquad i \in [1 : N_g] \tag{4.25}$$

Where N_{run} represents the number of repetition of the 20 minute sequence in each experiment and N_g the number of mobile gauges on the sliding rail. We define the model skill for the other frequency band $\sigma_{k,\eta,lo}$ and $\sigma_{k,\eta,tot}$ in a similar way.

The skill $\overline{\sigma_{k,\eta,hi}}$ is then defined as an average of the differences between the model and the experiment of all the mobile gauges $\sigma_{k,\eta}(i,j)$:

$$\overline{\sigma_{k,\eta,hi}} = \frac{1}{N_g} \sum_{j=1}^{N_g} \sigma_{k,\eta,hi}(j) \tag{4.26}$$

Using the same considerations, we define skills for the ADVs on the mobile rail:

$$\sigma_{k,U,hi}(i) = 1 - \sqrt{\frac{\sum_{j=1}^{N_{run}} \left((U_{rms,hi})_{c,i,j} - (U_{rms,hi})_{m,i,j}\right)^2}{\sum_{j=1}^{N_{run}} (U_{rms,hi})^2_{m,i,j}}} \qquad i \in [1 : N_g] \tag{4.27}$$

$$\overline{\sigma_{k,U,hi}} = \frac{1}{N_g} \sum_{j=1}^{N_g} \sigma_{k,U,hi}(j) \tag{4.28}$$

Model skill cross-shore evolution

The model skill for the cross-shore evolution of the free surface displacement is plotted in Figure 4.22. We do not use the fixed gauges at $x = 5$ m, as they are located in the open boundary, and the last gauge at $x = 21.325$ m as it is close to the swash zone.

For the sea/swell band, we observe that the model skill $\sigma_{k,\eta,hi}$ is high from $x = 7$ m to $x = 11$ m, around 0.9, and then decreases, until reaching a value of around 0.65 between $x = 13$ m and $x = 20$ m. This is explained by the difference in the position of wave breaking between the model and the experiment; before the breaking, the model is consistent with the experimental results, and after the wave breaking the skill decreases, but remains acceptable, of the same order of magnitude as [Reniers *et al.*, 2006b].

Concerning the Infragravity band, the model skill $\sigma_{k,\eta,lo}$ is low before the breaking, with values between 0.5 and 0.6 before $x = 12$ m and then after the breaking increases to reach values of 0.75 between $x = 14$ m and $x = 21$ m. The low model skill is explained by the wave forcing filtering, as mentioned earlier, as the model does not reproduce the wave basin seiching modes, which are present in the infragravity band. However, the energy in the infragravity band is well reproduced by the model after the breaking. One of the possible reasons could be the natural modes correctly simulated that exist between the wave breaking and the surf zone (see section B.2).

The total model skill $\sigma_{k,\eta,tot}$ is consistent with the sea/swell model skill $\sigma_{k,\eta,hi}$, as the majority of the energy is contained in this frequency band.

The averaged free surface model skill is $\overline{\sigma_{k,\eta,tot}} = 0.81$ consistent with the model skill reported by Reniers *et al.* [2006b]. Concerning the velocity model skill $\sigma_{k,U}$, since there is only three mobile ADV (Figure 4.10), cross-shore skill profiles make little sense. Nonetheless velocity measurements where shown to be close the simulations in Figure 4.21. The velocity model skill is quantified by the computation of the averaged skill which is $\overline{\sigma_{k,U,tot}} = 0.74$. This gives confidence in the model capabilities to capture the

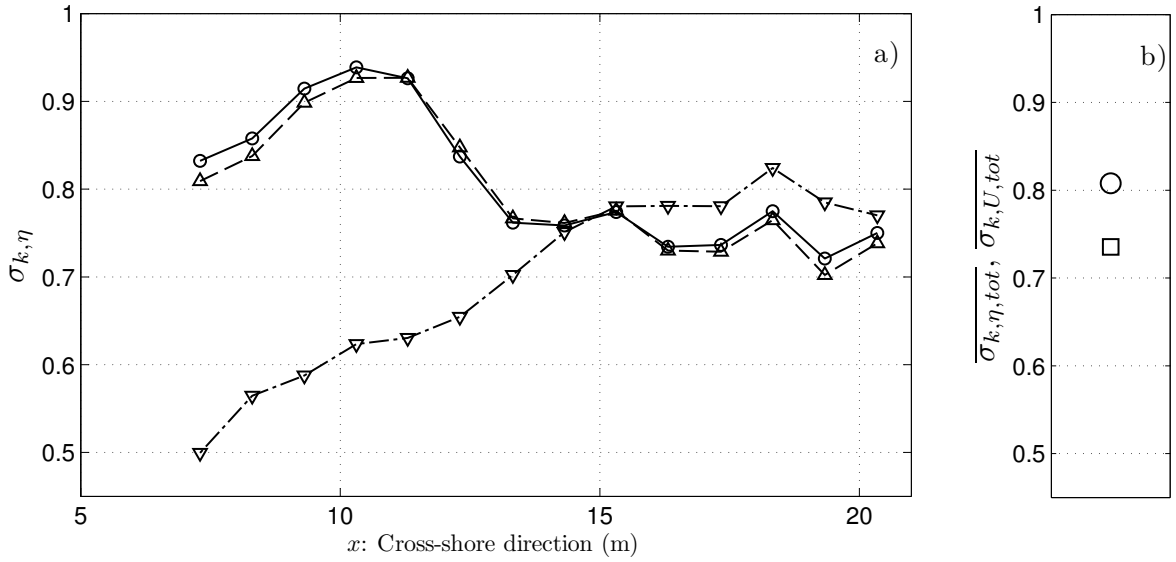

Figure 4.22 – Model skill for free surface and velocity, for the experiment 30. σ_k.a) Cross-shore evolution of the alongshore averaged skill ◯: $\sigma_{k,\eta,tot}$; ▽: $\sigma_{k,\eta,lo}$; △: $\sigma_{k,\eta,hi}$. b) Averaged model skill for the free surface $\overline{\sigma_{k,\eta,tot}}$ (circle) and velocity $\overline{\sigma_{k,U,tot}}$ (square).

overall kinetic energy distribution which is closely related to the average circulation.

4.4 Results

4.4.1 free surface spectral profile

We look at the free surface spectral profiles, in two cross-shore profiles at $y = 6$ m and $y = 10$ m, and an alongshore profile at $x = 16$ m for experiment 30 (t=21:00-26:00) (Figure 4.23). The cross-shore profile at $y = 6$ m is passes through the rip current recirculation cell center at $x = 16$ m, $y = 6$ m. The cross-shore profile at $y = 10$ m is located near the center of the rip current channel, between the two recirculation cells. The alongshore profile passes through the two recirculation cell centres, at $x = 16$ m, $y = 6$ m and $x = 16$ m, $y = 15$ m.

Using this spectral profiles we intend to observe the differences in free surface and velocity in the recirculation cells and in the rip channel.

For that reason we perform a simulation of 1,200 s, forcing the offshore boundary with the measured free surface time series (at $x = 5\ m$) and the interpolation procedure already described. Model results are compared with free surface time series measured by wave gauges, and velocity values recorded with ADVs.

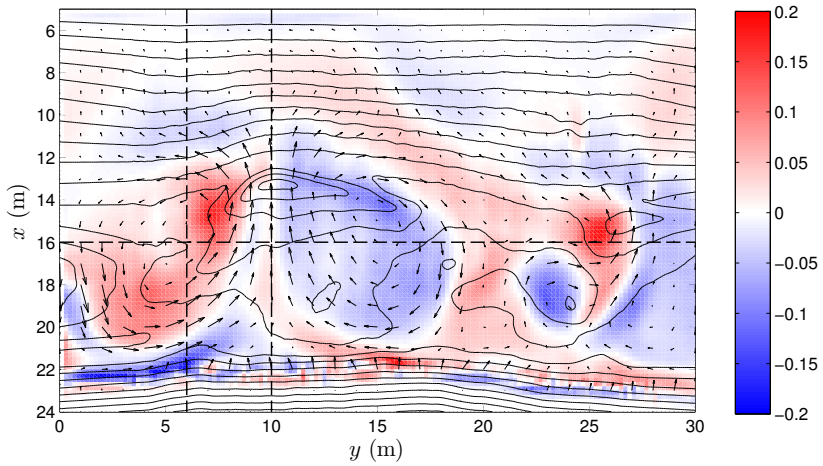

Figure 4.23 – Time averaged circulation (arrows) and vorticity (color) for experiment 30 (t=21:00-26:00), using a JONSWAP wave forcing. The dashed lines represents the two cross-shore profiles at $y = 6$ m and $y = 10$ m, and the alongshore profile at $x = 16$ m used to observe spectral evolution. The black lines represent the isobaths of the bottom with a line every 5 cm.

Alongshore profile

In the longshore spectral distribution of Figure 4.24, we observe that the signature of the JONSWAP spectrum is present in all the positions of the profile, in good agreement with experimental data. We also observe a trough in the spectrum at $y = 15$ m, at a frequency of 0.055 Hz ($T \approx 18.2$ s), and three bumps alongshore, at a frequency of 0.125 Hz ($T \approx 8$ s). The numerical model succeeds in reproducing these features. We observe that the longshore distribution of the free surface spectra is relatively homogeneous, which indicates that the hypothesis for the theoretical seiching modes that the bathymetry is alongshore uniform is not far from the numerical and experimental results. In the numerical model, we observe more energy for lower frequencies for $f < 2 \cdot 10^{-2}$ Hz, that does not appear in the experiment.

Cross-shore profile

Concerning the cross-shore spectral distribution of Figure 4.25, the experimental results show clearly the basin cross-shore seiching, with a fundamental mode at frequency 0.04 Hz ($T = 25$ Hz), lying in the infra-gravity band. This mode does not appear in the numerical model results since an absorbing/generating boundary condition is employed offshore, but overall the spectral distribution is similar in the experiment and in the numerical results. We also observe both, in the data and the model, a modal structure

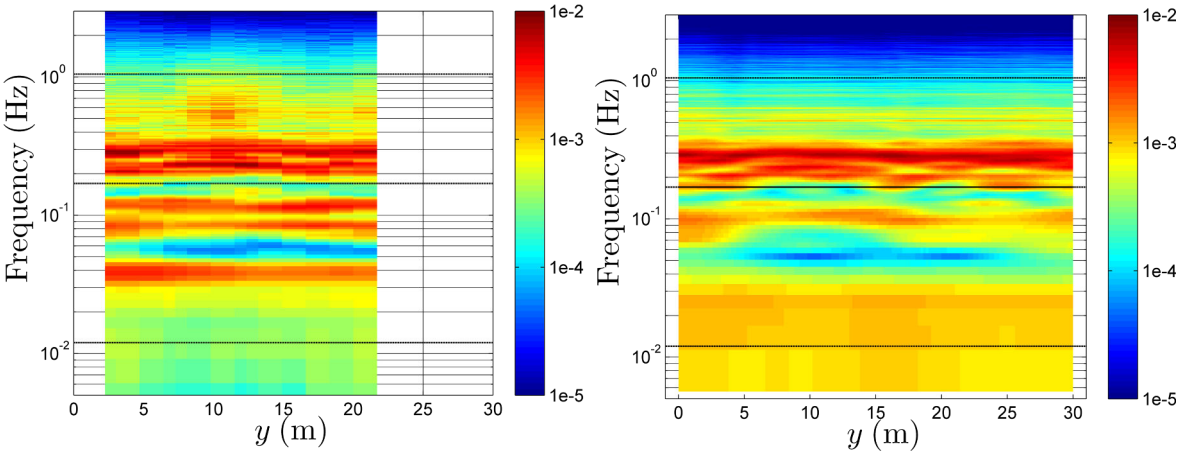

Figure 4.24 – Free surface longshore spectral distribution in $m^2.Hz^{-1}$, at $x = 16$ m. Left panel: Experimental spectral distribution; Right panel: numerical model spectral distribution. The dashed lines represent the frequency limits between the VLF, IG and JONSWAP bands ($f_{c0} = 1.2e-2$ Hz, $f_{c1} = 1.7e-1$ Hz, $f_{c2} = 1.05$ Hz).

at a frequency of 0.07 Hz ($T \approx 14.3$ s). This quasi-standing mode is confined between $x = 12$ m (the breaking point) and the shoreline. It exhibits anti-nodes at the breaking point and the shoreline and a node at $x = 18$ m. It might correspond to a quasi-standing long-wave oscillating between the breaking point and the shoreline.

If we look at the cross-shore velocity spectral distribution (see Figure 4.26), we observe that the some part of the energy is contained in the infragravity band and the VLF band for both profiles. For the $y = 6$ m profile, we observe two peaks in the infragravity band, one at $x = 16$ m at the center of the recirculation cell, and one at $x = 11$ m, in the breaking zone. The energy is contained mainly in frequencies below 0.07 Hz ($T > 14.3$ s), and some energy is contained in the JONSWAP frequency band at a frequency of 0.29 Hz ($T = 3.5$ s).

For the $y = 10$ m profile, we also identify two peaks in the infragravity band, one at $x = 11$ m corresponding to the wave breaking, and another one at $x = 14$ m, in the head of the rip current. In the JONSWAP band, the energy is one order of magnitude lower than in the $y = 6$ m profile, probably due to the strong signature of the rip current. There is energy present in the VLF band, but we require simulations with a longer duration to obtain more information at these frequencies.

Main seiching modes

From the study of the seiching modes, we can conclude that although the model does not reproduce well the basin seiching modes, excepting the main longshore mode, due

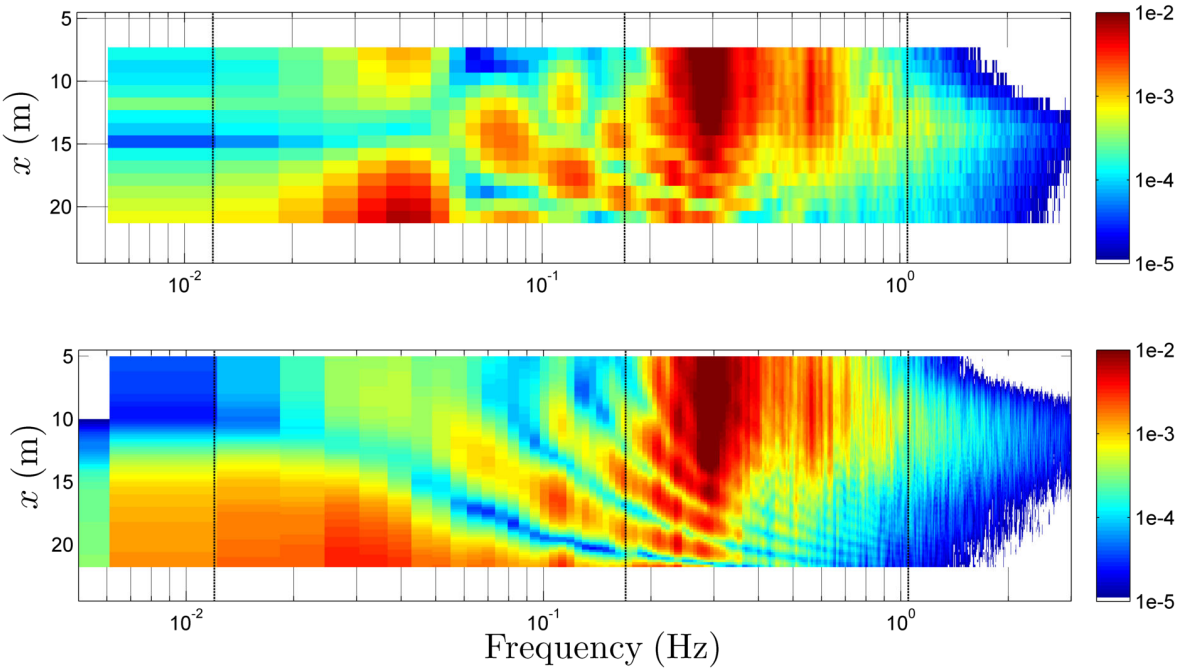

Figure 4.25 – Free surface cross-shore spectral distribution in $m^2.Hz^{-1}$, at $y = 6$ m. Upper panel: Experimental spectral distribution; Lower panel:model spectral distribution. The dashed lines represent the frequency limits between the VLF, IG and JONSWAP bands ($f_{c0} = 1.2e-2$ Hz, $f_{c1} = 1.7e-1$ Hz, $f_{c2} = 1.05$ Hz).

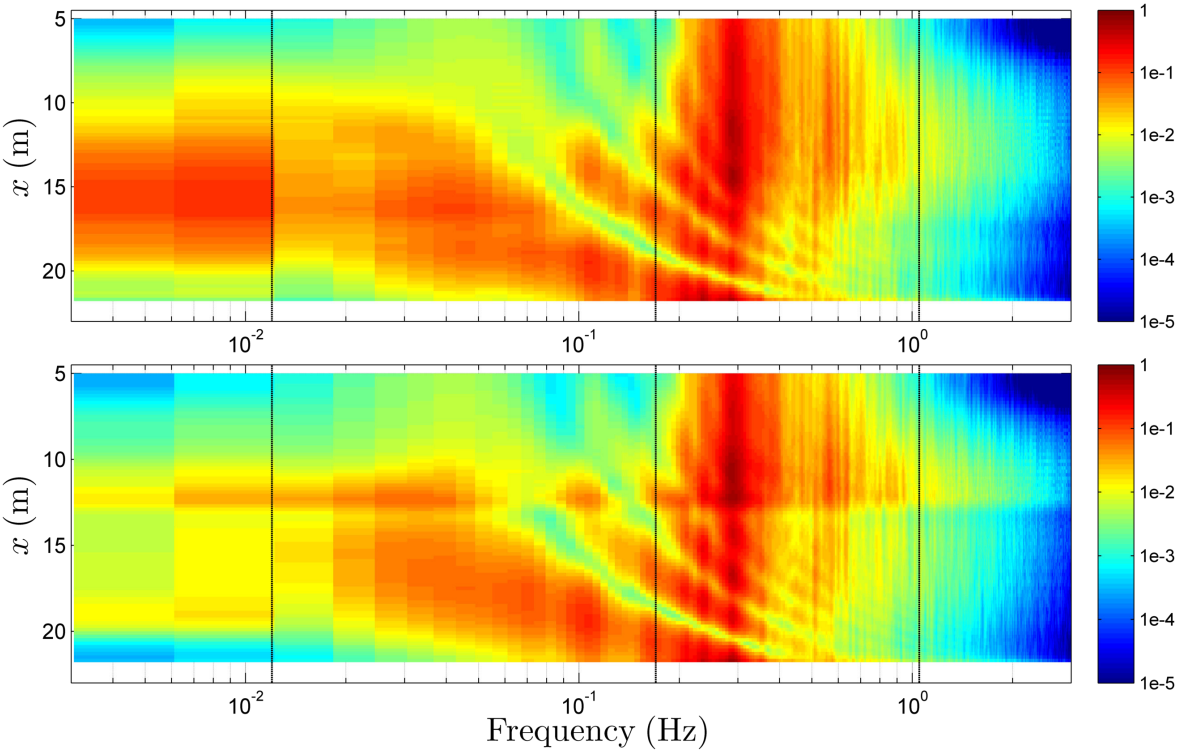

Figure 4.26 – Cross-shore velocity spectral distribution in a cross-shore profile. Upper panel: model spectral distribution at $y = 6$ m. Lower panel: model spectral distribution at $y = 10$ m. The dashed lines represent the frequency limits between the VLF, IG and JONSWAP bands ($f_{c0} = 1.2e-2$ Hz, $f_{c1} = 1.7e-1$ Hz, $f_{c2} = 1.05$ Hz).

to the open boundary condition at $x = 5$ m, we still observe some seiching modes resonating between the shoreline and the breaking point, explaining the presence of energy in the infragravity band. We can observe some of these seiching modes by looking at the free surface spectral profiles, in the previous section. This could be the reason why the numerical model shows some modal structure, even though there is an open boundary condition at $x = 5$ m.

For further details on seiching modes, the reader is referred to Appendix B.

4.4.2 Spectral maps

To understand the spatial distribution of the different spectral range motions, we compute the energy content of free surface displacements, velocities and vorticity. The vorticity is related to kinetic energy of these motions. We focus on the infragravity in the band 0.012 Hz $< f <$ 0.17 Hz and the JONSWAP in the band 0.17 Hz $< f <$ 1.05 Hz, as these band contain the most part of the energy. The values of σ_η, U_{rms} and ω_{rms} in each spectral range (Figure 4.27) are estimated as follows:

$$\sigma_\eta = \sqrt{\int_{band} S_{\eta\eta}(f)df} \tag{4.29}$$

$$U_{rms} = \sqrt{\int_{band} S_{UU}(f)df} \tag{4.30}$$

$$q_{rms} = \sqrt{\int_{band} S_{qq}(f)df} \tag{4.31}$$

where $S_{\eta\eta}$ is the power density spectrum of the free surface displacements, S_{uu} and S_{vv} are the power density spectra of the cross-shore and alongshore velocity respectively, S_{qq} is the power density spectrum of the vorticity q and f is the frequency. We also estimate the total $\sigma_\eta = m_0$ and U_{rms}, and obtain a spatial map of the total energy content in this variables (Figures 4.27).

In the energy map of the free surface displacements restricted to the JONSWAP band σ_η (Figure 4.27 a) and b)) we observe the wave damping in the middle, at $x = 5$ m and $y = 15$ m. At $x \sim 12$ m the differential breaking produced by the bathymetry combined with the wave forcing is clearly evidenced as the gradients have different cross-shore positions alongshore. This is the source of the vortices generation, that will be explained in detail in the next Chapter. The infragravity band motion shows a spatial structure of U_{rms} with higher amplitudes at the horns of the shore-attached bars located near $x = 18 - 19$ m. This could be explained by wave amplification over

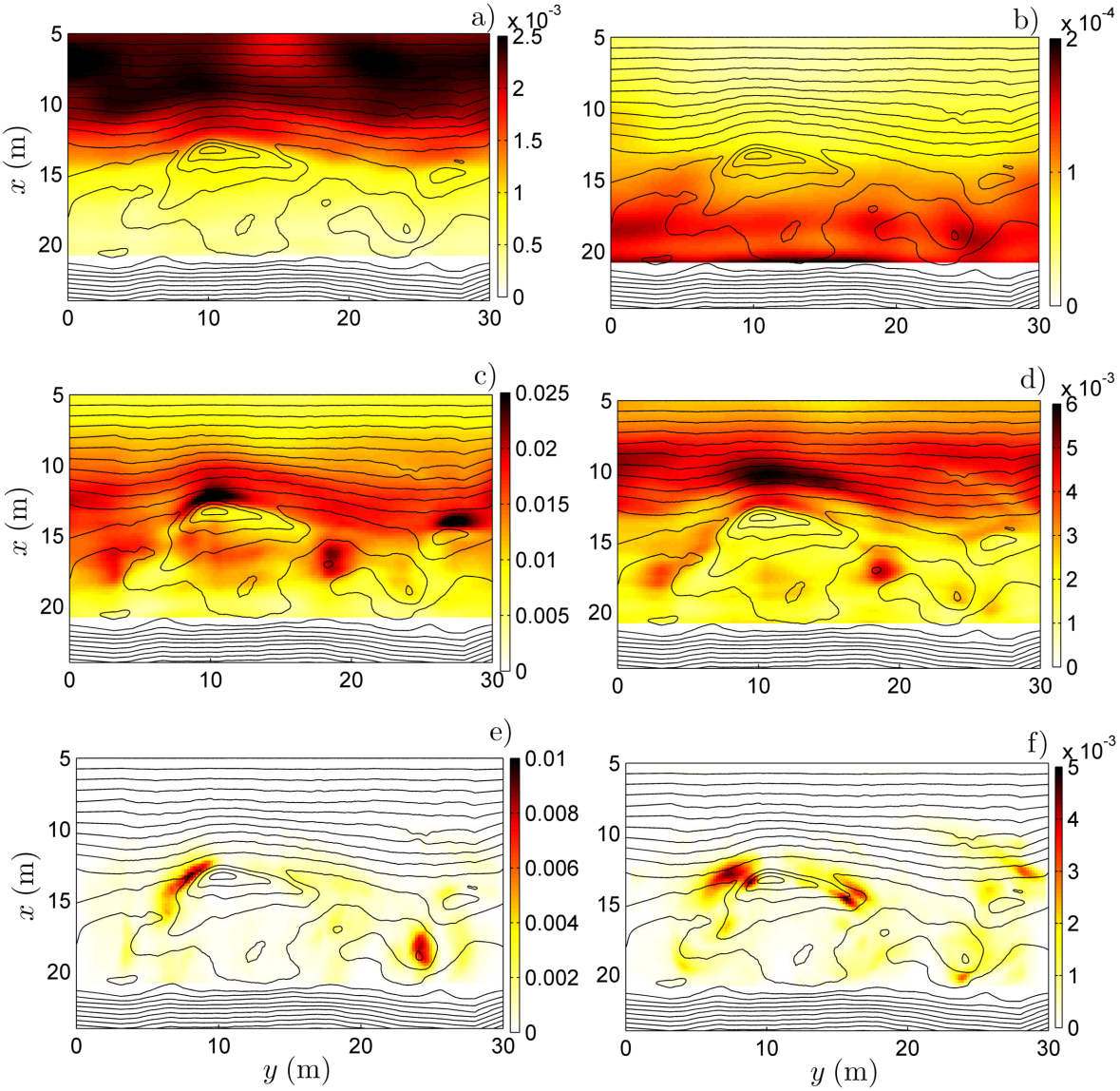

Figure 4.27 – Spectral maps of σ_η, U_{rms} and q_{rms} obtained with equations 4.29, 4.30 and 4.31 respectively. a), c), e): respectively σ_η, U_{rms} and q_{rms} integrated in the JONSWAP high-frequency spectrum range . b), d), f): respectively σ_η, H_{rms} and q_{rms} integrated in the InfraGravity range.

the shoal, since at the same location U_{rms} is also maximum (Figure 4.27 c) and d)).

The U_{rms} maps are plotted in Figure 4.27 c) and d). The shoaling of the waves is evidenced in the JONSWAP U_{rms} map where U_{rms} is the strongest near the breaking point. There are peaks near the breaking point, at $y = 10$ m and $y = 27$ m. The peaks at $y = 10$ m and $y = 27$ m correspond to strong off-shore averaged velocities, as evidenced by the mean circulation in Figure 4.23. We also observe two peaks at ($x = 18$ m, $y = 3$ m) and ($x = 18$ m, $y = 19$ m), located at the horns. In the Infragravity band, we also observe peaks at the horns, and a band of energy between 8 m $< x <$ 11 m.

In the q_{rms} maps (Figure 4.27 e) and f)), we observe localized peaks, both in the JONSWAP band and in the infragravity band. In the JONSWAP band, there is one peak at $x = 13$ m, $y = 9$ m, and another at $x = 19$ m, $y = 25$ m. In the infragravity band, we observe two strong peaks, one located at $x = 13$ m, $y = 9$ m, and another located at $x = 15$ m, $y = 16$ m. These two peaks correspond to the maximum vorticity in the two recirculation cells of the rip current located at $y = 10$ m.

4.4.3 Averaged circulation

During the LHF experiment, rip currents characteristics were investigated with the use of drifters measurements [Castelle *et al.*, 2010]. Those drifters consisted in balloons filled with water, of diameter 5-10 *cm* deployed in the surf zone during the different runs, that lasted between 30 and 60 minutes which is a smaller time period than the morphological time scales of few hours. It can therefore be assumed that the measured drifter pattern is associated with a given bathymetry.

A shore-mounted video-camera was used to track the drifters during the wave forcing (see Figure 4.28). The images obtained were then rectified to obtain the Cartesian coordinates of the drifters. The drifters motions were obtained by a semi-automatic method, by pointing manually the drifter position every 6 seconds on the video records.

Cross-shore and alongshore drifter velocities were estimated from a linear interpolation in position and time of each sequential position of the drifter at a 1 s time step over a 30 s duration.

The mean currents were estimated at eight different moments, therefore with eight different bathymetries, shown in table 4.5. The mean flow patterns of the lagrangian estimation using the drifters and the numerical model, as well as the estimated and modelled vorticity can be seen in Figure 4.29 and Figure 4.30.

For the lagrangian drifters, the vorticity is estimated from the curl of the mean flow velocity, and computed discretely with a weighted central difference scheme detailed in [MacMahan *et al.*, 2010]. For the numerical model, the vorticity is also estimated

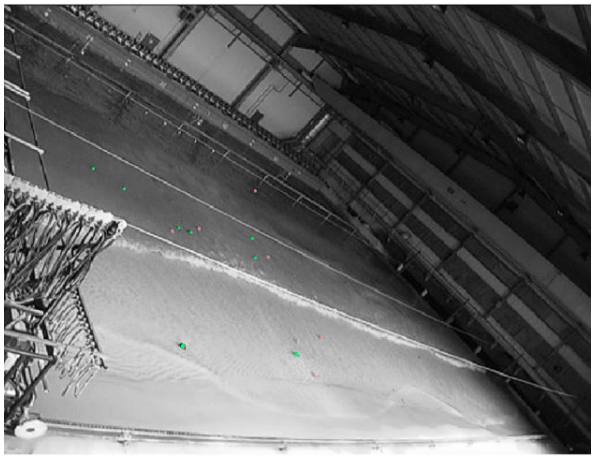

Figure 4.28 – Sample of captured video images with drifters (from Castelle *et al.* [2010]).

Simulation	time
27	15:40-18:00
30	21:00-26:00
31	26:00-31:20
33	31:20-37:20
36	40:00-45:40
37	45:40-51:40
38	51:40-59:40
41	59:40-66:00

Table 4.5 – Experiments considered for the estimation of the circulation with the drifters.

from the mean flow velocity, using a 4th order centered difference scheme to compute the curl of the velocity.

For experiments 27-30-31-33 (Figure 4.29), we observe a strong rip current at the alongshore position $y = 10$ m, with strong offshore currents exceeding 0.1 m/s. A smaller rip is positioned on the far right of the basin at an alongshore position of roughly $y = 25$ m. The two recirculation cells of the rip current at $y = 10$ m reach their maximum area for the experiments 30 and 31, with strong vorticity values and then start to decrease.

The vorticity estimated from the lagrangian drifters is fairly well reproduced by the numerical model. For experiment 27 (Figure 4.29 a) and b)) we observe a patch of negative vorticity at $x = 17$ m, $y = 10$ m, that is reproduced by the model. At this time, we observe that the recirculation cells are starting to develop near the breaking zone, but they do not reach the shoreline yet, as the vortices are found in the area 11 m $<$

$x < 17$ m. For experiments 30, 31 and 33 (Figure 4.29 c-h)), the two recirculation cells of the rip channel at $y = 10$ m are well reproduced, both in terms of area and magnitude. Noteworthy, for experiment 33 (Figure 4.29 g-h)) the weaker dipole located at $y = 22$ m shown by the lagrangian drifters is also visible in the same region in the numerical model.

For experiments 36-37-38-41 (Figure 4.30), we observe a decrease in the vorticity field for the rip current located at $y = 10$ m, as the rip channel is filled by the accretion process due to the wave forcing. We start to observe an onshore jet, at $y = 18$ m, as two rip currents are about the same strength, at $y = 10$ m and $y = 23$ m. The rip channels were initiated by the wave forcing damping, and enhanced by the currents. However, at a much larger scale we observe that the beach is not in equilibrium with the wave forcing, causing this accretion phenomenon.

Looking at the vorticity, we still observe the two recirculation cells, but with reduced occupied area. For experiment 37 (Figure 4.30 c-d)) the secondary dipole at $y = 25$ m is also visible in the numerical model.

The qualitative agreement between the numerical model and the flow patterns determined with the drifters is quite good, as it shows similar positions for the rip currents, and the recirculation cells. The comparison of the vorticity also shows a similar structure, both in spatial distribution and in magnitude, giving confidence in using the numerical model to investigate the vorticity and circulation in the nearshore zone.

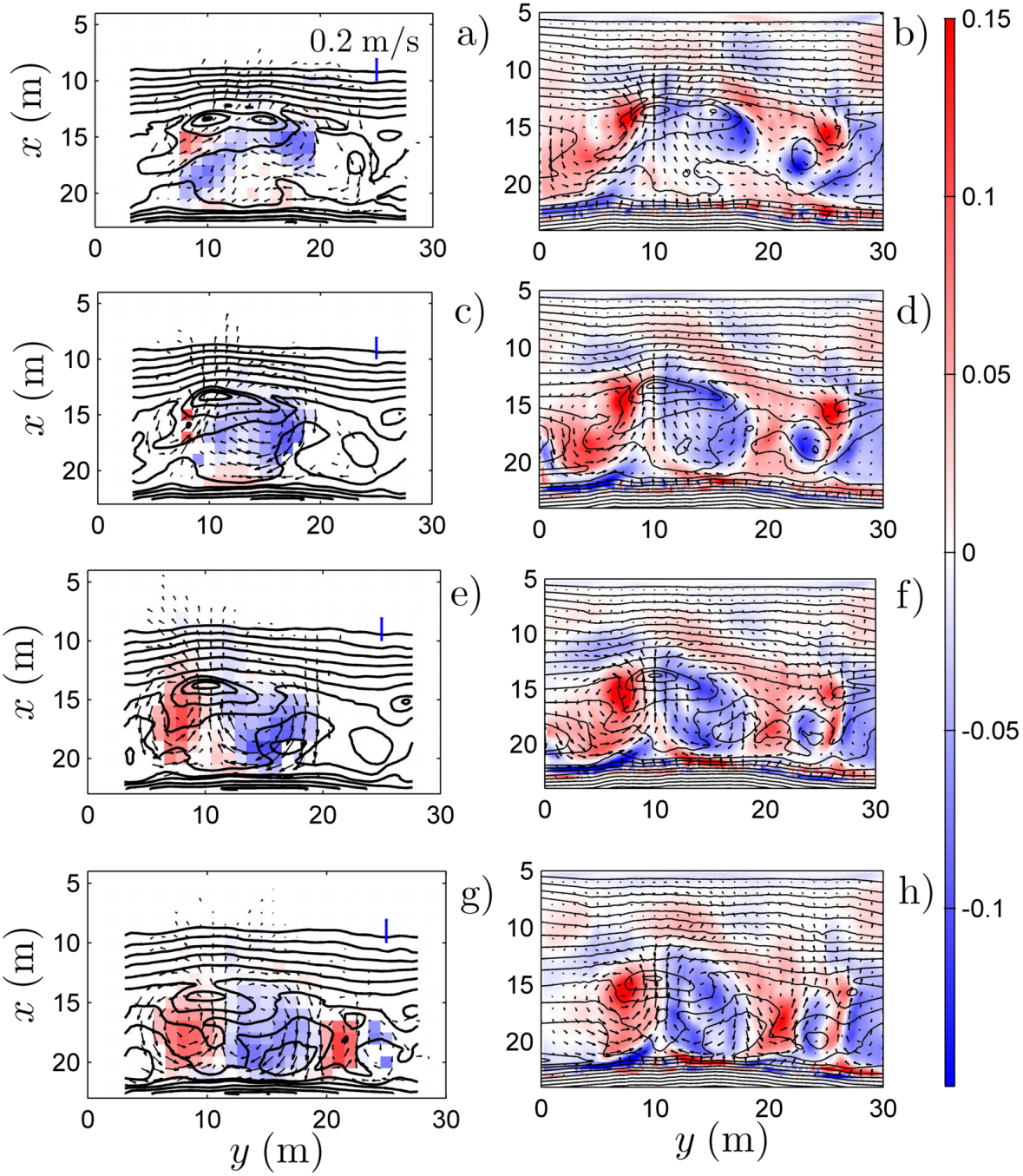

Figure 4.29 – Mean circulation: time averaged velocity magnitude over 3600 s (experiment) and 1200 s (model), and time averaged vorticity. Left panels (a-c-e-g): experimental results [Castelle *et al.*, 2010]; Right panels (b-d-f-h): numerical model; a-b)experiment 27 ($t = 15:40$); c-d)experiment 30 ($t = 21:00$); e-f) experiment 31 ($t = 26:00$); g-h) experiment 33 ($t = 31:20$). The blue line in a) represents a net velocity of 0.2 m/s. Colours are for vorticity, units in s^{-1}.

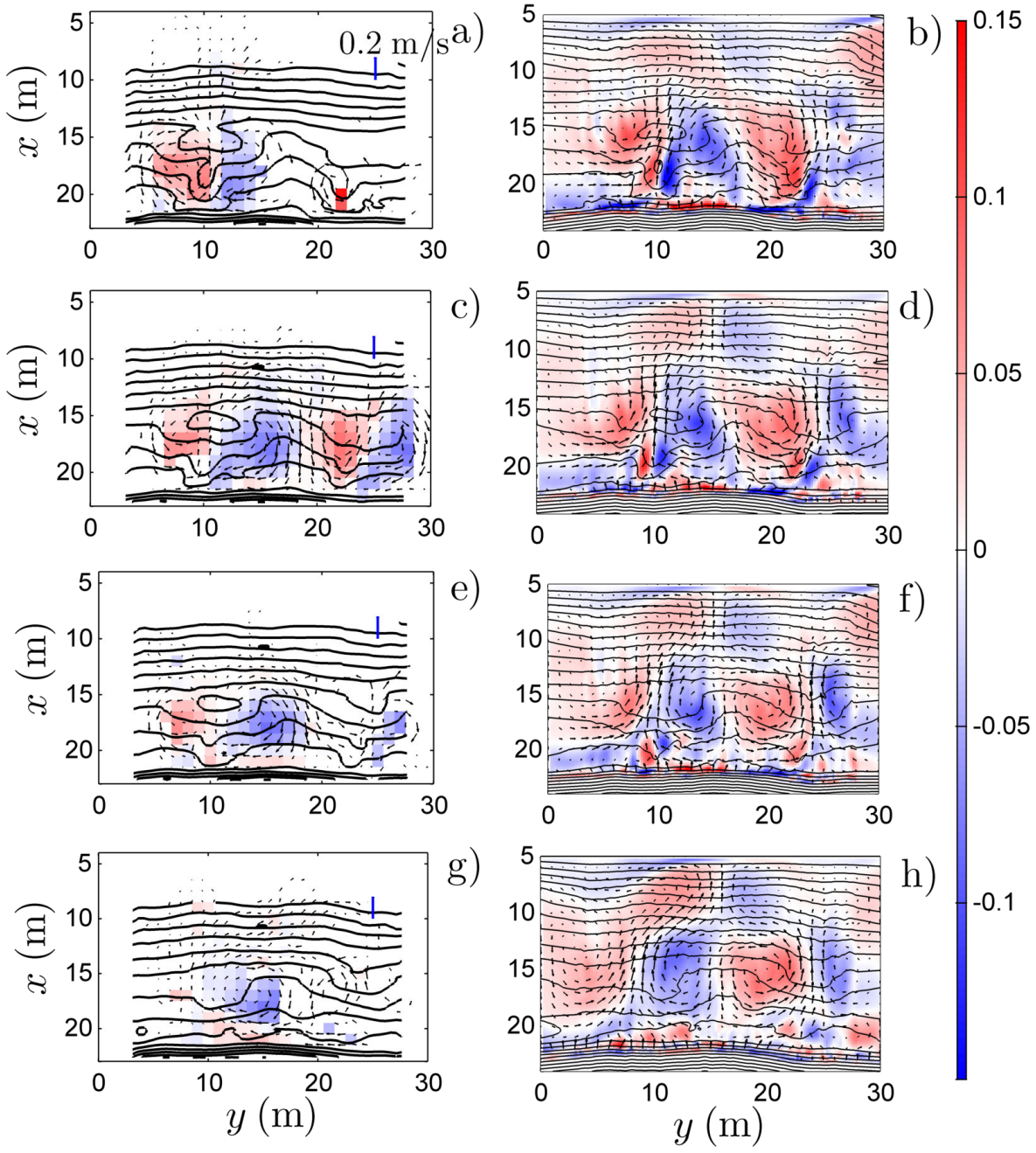

Figure 4.30 – Mean circulation: time averaged velocity magnitude over 3600 s (experiment) and 1200 s (model), and time averaged vorticity. Left panels (a-c-e-g): experimental results [Castelle *et al.*, 2010]; Right panels (b-d-f-h): numerical model; a-b)experiment 36 ($t = 44 : 40$); c-d)experiment 37 ($t = 50 : 40$); e-f) experiment 38 ($t = 58 : 40$); g-h) experiment 41 ($t = 65 : 00$). The blue line in a) represents a net velocity of 0.2 m/s. Colours are for vorticity, units in s^{-1}.

4.5 Conclusion

The model hydrodynamics have been validated with a wide set of data, of free surface and velocity evolution. The model is able to reproduce the energy dissipation gradients related to wave breaking, as well as the energy transfer from the JONSWAP band to the infragravity band. These energy dissipation gradients are an important proxy for vorticity generation [Brocchini *et al.*, 2004 ; Bonneton *et al.*, 2010] . The numerical model is also accurate in estimating the nearshore circulation and vorticity associated, compared to the lagrangian drifters [Castelle *et al.*, 2010]. The model also reproduces some of the seiching modes that occur between the breaking point and the shoreline.

In the next chapter, we start from the equations of the potential vorticity in the nearshore zone, and then observe the spatial evolution of the different terms of these equation. We then try to observe the time evolution of enstrophy related to vorticity in the nearshore zone.

Chapter 5

Mean circulation and vorticity dynamics in the nearshore zone.

5.1 Introduction

The circulation and vorticity are important in the nearshore region, as it they influence the evolution of the dispersion and mixing in this region, as well as the transport of sediment. These processes are important in several aspects of the nearshore zone management, for example in terms of pollution, benthic life, and tourism. The knowledge of this circulation is thus primordial if we want to predict the beaches evolution due to sediment transport or the contamination of the nearshore due to one pollutant.

In the nearshore and surf zone the horizontal scales are larger than the vertical scales, hence the vorticity possesses some similarities with 2D turbulent fluid [Chavanis et Sommeria, 2002]. The vorticity q, considered as a pseudo-scalar in 2D flows, can be defined as the rotation or curl of the vertically integrated averaged horizontal velocity field:

$$q = \frac{\partial v}{\partial x} - \frac{\partial u}{\partial y} \tag{5.1}$$

In a 2D flow, the energy that is injected at a specific length scale cascades to other length scales, either by vortex merging which creates vortices of larger length scale, or by inviscid processes that transfer energy from vortex to vortex of lower dimensions. The latter energy cascade called the inverse-energy cascade with an energy spectrum slope $E \sim k^{-5/3}$ is the classic transfer cascade. The former is the enstrophy cascade, with an energy slope $E \sim k^{-3}$ [Kraichnan et Montgomery, 1980].

Using Lagrangian drifter dispersion analysis, both numerically and experimentally, Spydell et Feddersen [2009] showed that the circulation nearshore under directionally

spread and normally incident waves is similar to a 2D turbulent flow field. Furthermore, by separating the rotational from the irrotational part they observed that the dispersion is mainly due to the rotational part. They also show that, similarly to 2D turbulence flow field, the vorticity is generated at a single length scale (approximately 10-20 m) and then cascade to other length scales, an enstrophy cascade for 5-10 m length scales, and an inverse energy cascade for 20-100 m length scales.

To study the nearshore circulation, we have access to experimental data, and numerical modelling. The experimental data is of great interest, however the nearshore zone can be at times highly energetic, complicating the data extraction. Furthermore, these data are most of the time limited to a few positions in space and time, which makes it difficult to understand the overall dynamic. To study the nearshore circulation, in addition to eulerian data, that is available on fixed points, the use of lagrangian data by the means of drifters has been taking importance [Castelle *et al.*, 2010 ; Reniers *et al.*, 2006a ; Spydell et Feddersen, 2009 ; MacMahan *et al.*, 2010]. However even using the eulerian and lagrangian observations, it is difficult to obtain instantaneous data of the whole field. For this reason, numerical modelling of the nearshore zone has been increasingly used to understand the evolution of the circulation.

The numerical modelling is an idealization of the physics that occurs in the nearshore zone, however some set of equations allow for a fairly good representation of the phenomenons, for example with the Boussinesq equations [Wei et Kirby, 1995] or the Non-linear Shallow Water Equations (N.S.W.E.) [Marche *et al.*, 2007].

There are two identified mechanisms for the generation of circulation and vorticity in the nearshore zone, that is caused by inhomogeneities either in the wave forcing or in the bathymetry, for normal incident or oblique wave forcing. [Peregrine, 1998]. Bruneau *et al.* [2011] observed that for topography controlled circulation, the spatial gradients in the breaking wave energy dissipation are the major source of vorticity generation. Buhler et Jacobson [2001] also observed that the mean vorticity generation is due to a dissipative force induced by non-uniform or differential wave breaking.

Bonneton *et al.* [2010] obtained from the vertically-integrated and time-averaged momentum equations an expression for the vorticity forcing term, that depends on the energy dissipation by wave breaking and the direction of the wave rays. This forcing term appears when the energy dissipation due to wave breaking is non-collinear with the wave rays, producing vorticity locally.

This vorticity forcing term generates vorticity locally near the wave breaking that is advected by the circulation induced by the bathymetry, and merge into large scale dipoles to create a rip current. The motion of this dipole is then dictated by mutual advection and self-advection due to the sloping topography [Buhler et Jacobson, 2001]

The bottom dissipation by friction in the nearshore zone is also an important mechanism, one of the main sink of vorticity [Bowen, 1969]. However, the life span of a vortex group is not dictated by the friction but is the result of the sequence of the passing wave group, which increase or decrease the vortices, depending on their direction of propagation [Long et Ozkan-Haller, 2009].

The friction term also dictates the stability of the rip current. Yu [2006] observed that the instability of the rip current is related to the rate of vorticity generation and the rate of dissipation by bottom friction. Using a pseudospectral 2D Navier-Stokes solver Geiman et Kirby [2013] showed that the frequency oscillations of an out of equilibrium asymmetric vortex dipole on a plane beach are related to a frictional time scale and an advective time scale.

In this chapter, we focus on understanding the mechanisms of generation, sustainability and decay of vorticity in the nearshore zone, using the model from Marche *et al.* [2007] and improved by Guerra *et al.* [2014] alongside with the exact formulation for the vorticity production by Bonneton *et al.* [2010]. The equations of Bonneton *et al.* [2010] are also used as a diagnostic tool to study the potential vorticity balance from the numerical results.

The numerical shallow water model is first used to understand vorticity generation and dynamics in the conditions of the MODLIT experiment [Michallet *et al.*, 2010 2013], then with monochromatic wave forcing, to analyse the influence of the friction coefficient and the period of the waves and the spatial variation of the potential vorticity balance terms. Using a scaling law, we find an equilibrium between the vorticity advection and the vorticity production with a monochromatic wave forcing. Finally, the wave groupiness role on the vorticity dynamics and spatial variation is investigated using a bichromatic wave forcing.

5.2 Diagnosis equations

5.2.1 Vorticity equation

Definitions

To understand the dynamics of the vorticity in the nearshore zone, we first need to define the variables involved. The definition of the variables in the surf zone in Figure 5.1 shows the space variables. The axis x represent the cross-shore direction, the axis y the longshore direction, and the axis z the vertical direction. The bottom $b(x, y)$ is the interface between the water and the sediment, and is supposed here fixed in time.

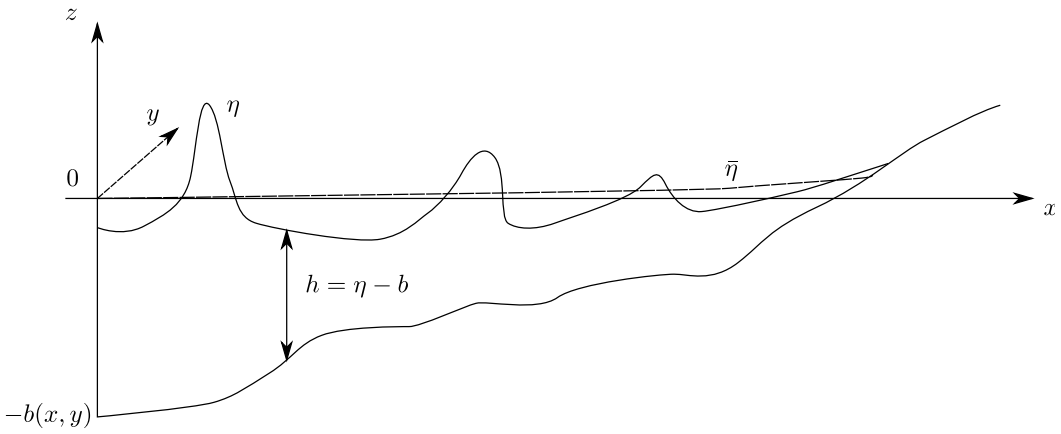

Figure 5.1 – Definition sketch of the surf zone

η represents the free surface displacement, and $h = \eta - b$ represents the water depth.

Concerning the velocity fluctuations, we need to define spatial variables and integrated variables over the water depth. The spatial velocities are defined with a subscript "$_0$": $u_0(x, y, z, t)$, $v_0(x, y, z, t)$, $w_0(x, y, z, t)$. The integrated variables over depth h are defined as $u(x, y, t)$, $v(x, y, t)$. The velocity vectors associated are $\mathbf{u}_0 = [u_0, v_0, w_0]$ and $\mathbf{u} = [u, v] = [|\mathbf{u}| \cos\theta, |\mathbf{u}| \sin\theta]$, with θ the direction of the wave propagation.

The time averaging need also to be defined, as we use different kinds of time averaging:

- the time averaging over one wave period T is defined as:

$$\overline{(.)} = \frac{1}{T} \int_t^{t+T} (.)\, \mathrm{d}\tau \tag{5.2}$$

  Using this time averaging, we can deduce for each variable a steady and fluctuating part, for example:

$$\eta = \bar{\eta} + \tilde{\eta} \tag{5.3}$$

  where $\overline{\tilde{\eta}} = 0$.

- the time-averaging over n_0 periods is defined as:

$$< . >_{n_0} = \frac{1}{n_0 T} \int_t^{t+n_0 T} (.)\, \mathrm{d}\tau \tag{5.4}$$

- the time-averaging over a time period t_1 is defined as:

$$< . >_{t=t_1} = \frac{1}{t_1} \int_t^{t+t_1} (.)\, \mathrm{d}\tau \tag{5.5}$$

- the time-averaging over the duration of one simulation, typically 1200 seconds, is defined as:

$$< . >= \frac{1}{1200} \int_{t=0}^{t=1200} (.)\ \mathrm{d}\tau \tag{5.6}$$

The spatial averaging is defined as:

$$< . >_{x,y}= \frac{1}{L_x L_y} \int_{x_1}^{x_2} \int_{y_1}^{y_2} (.)\ \mathrm{d}x\ \mathrm{d}y \tag{5.7}$$

where x_1,x_2 and y_1,y_2 are respectively the cross-shore and longshore boundaries, and $L_x = x_2 - x_1$, $L_y = y_2 - y_1$.

Conservation of mass

Drawing upon Bonneton *et al.* [2010] analysis, we start from the conversation of mass in an incompressible fluid:

$$\nabla \cdot \mathbf{u}_0 = \frac{\partial u_0}{\partial x} + \frac{\partial v_0}{\partial y} + \frac{\partial w_0}{\partial z} = 0 \tag{5.8}$$

The kinematic boundary conditions at the free surface η and the bottom b are defined as:

$$\frac{\partial \eta}{\partial t} + u_0 \frac{\partial \eta}{\partial x} + v_0 \frac{\partial \eta}{\partial y} - w_0 = 0 \qquad \text{at} \qquad z = \eta \tag{5.9}$$

$$u_0 \frac{\partial b}{\partial x} + v_0 \frac{\partial b}{\partial y} + w_0 = 0 \qquad \text{at} \qquad z = -b \tag{5.10}$$

We now integrate equation 5.8 over water depth and time-average over one period:

$$\overline{\nabla \cdot \int_{-b}^{\eta} \mathbf{u}_0\ \mathrm{d}z} = 0 \tag{5.11}$$

The horizontal terms of this equation are split into a mean part and fluctuating part:

$$\overline{\frac{\partial}{\partial x} \int_{-b}^{\eta} u_0\ \mathrm{d}z} = \frac{\partial}{\partial x} \left(\int_{-b}^{\bar{\eta}} \overline{u_0}\ \mathrm{d}z + \overline{\int_{\bar{\eta}}^{\eta} u_0\ \mathrm{d}z} \right) \tag{5.12}$$

The first term of this equation is the mean current continuity, and assuming that the horizontal velocity is depth uniform, we obtain:

$$\frac{\partial}{\partial x} \int_{-b}^{\bar{\eta}} \overline{u_0}\ \mathrm{d}z = \bar{h} \frac{\partial \bar{u}}{\partial x} \tag{5.13}$$

The second term of equation 5.12 is the net wave momentum and represents the Stokes transport induced by waves. By using a Taylor expansion from the mean surface $\bar{\eta}$, we obtain an estimation of this term:

$$\overline{\int_{\bar{\eta}}^{\eta} u_0 \, \mathrm{d}z} \approx \overline{\tilde{\eta}\tilde{u}} \tag{5.14}$$

For the vertical velocity, the integration and time-averaging gives:

$$\begin{aligned}\overline{\frac{\partial}{\partial z}\int_{-b}^{\eta} w_0 \, \mathrm{d}z} = \overline{\int_{-b}^{\eta} \frac{\partial w_0}{\partial z} \, \mathrm{d}z} = \overline{[w_0]_{-b}^{\eta}} &= \overline{\frac{\partial \eta}{\partial t} + u_0\frac{\partial \eta}{\partial x} + v_0\frac{\partial \eta}{\partial y} - u_0\frac{\partial b}{\partial x} - v_0\frac{\partial b}{\partial y}} \\ &= \frac{\partial \bar{\eta}}{\partial t} + \mathbf{u}\cdot\nabla\bar{h} \\ &= \frac{\partial \bar{h}}{\partial t} + \mathbf{u}\cdot\nabla\bar{h}\end{aligned} \tag{5.15}$$

We finally obtain the equation for mass conservation, integrated over water depth and time-averaged over one period:

$$\frac{\partial \bar{h}}{\partial t} + \bar{\mathbf{u}}\cdot\nabla\bar{h} = -\nabla\cdot\widetilde{\mathbf{M}} \tag{5.16}$$

where $\widetilde{M} = [\tilde{\eta}\tilde{u}, \tilde{\eta}\tilde{u}]$ is the wave mass-induced flux also called Stokes drift.

Vorticity equation

To obtain the vorticity equation, we start from the Nonlinear Shallow Water Equations with friction and bed slope source term used by the model SURF-WB, in its dimensional form (equations 5.17 - 5.18 - 5.19) :

$$\frac{\partial \eta}{\partial t} + \frac{\partial}{\partial x}(hu) + \frac{\partial}{\partial y}(hv) = 0 \tag{5.17}$$

$$\frac{\partial u}{\partial t} + u\frac{\partial u}{\partial x} + v\frac{\partial u}{\partial y} + g\frac{\partial h}{\partial x} = -g\frac{\partial b}{\partial x} - \frac{1}{h}S_{f_x} \tag{5.18}$$

$$\frac{\partial v}{\partial t} + u\frac{\partial v}{\partial x} + v\frac{\partial v}{\partial y} + g\frac{\partial h}{\partial y} = -g\frac{\partial b}{\partial y} - \frac{1}{h}S_{f_y} \tag{5.19}$$

Using the Lorentz linearisation of Mei [1989], the friction source term $\mathbf{S_f} = [S_{f_x}, S_{f_y}]$ can be defined as:

$$\frac{1}{h}\mathbf{S_f} \approx \frac{8}{3\pi}\frac{c_f}{h}u_{rms}\mathbf{u} \approx \frac{c_f}{h}u_{rms}\mathbf{u} \approx \beta\mathbf{u} \tag{5.20}$$

The variable $\beta = \frac{c_f}{h}u_{rms}$ is the linearised friction coefficient, u_{rms} is called the orbital

velocity due to the wave component of the motion, and is defined as:

$$u_{rms} = \sqrt{\widetilde{u^2} + \widetilde{v^2}} \tag{5.21}$$

We now time-average equation 5.18 over one period T:

$$\begin{aligned} &\frac{1}{T}\int_t^{t+T} \frac{\partial u}{\partial t} d\tau + \frac{1}{T}\int_t^{t+T} u\frac{\partial u}{\partial x} d\tau + \frac{1}{T}\int_t^{t+T} v\frac{\partial u}{\partial y} d\tau + \frac{1}{T}\int_t^{t+T} g\frac{\partial h}{\partial x} d\tau \\ &= -\frac{1}{T}\int_t^{t+T} g\frac{\partial b}{\partial x} d\tau - \frac{1}{T}\int_t^{t+T} \frac{1}{h} S_{f_x} d\tau \end{aligned} \tag{5.22}$$

In the inner surf zone, the broken-wave solution can be approximated by representing wave fronts as a discontinuity [Bonneton, 2007]. This discontinuity satisfies the jump conditions, with the conservation of the mass and momentum across the shock:

$$-c_b[h] + [h\mathbf{u} = 0 \tag{5.23}$$

$$-c_b[h\mathbf{u}] + [h\mathbf{u}^2 + \frac{1}{2}gh^2] = 0 \tag{5.24}$$

where the brackets [] indicate a jump in the quantity, $c_b = [c_b \cos\theta, c_b \sin\theta]$ is the shock velocity, θ is the angle of the propagation of the wave front with $\theta = 0$ defined as the normal direction to the shoreline.

We obtain the following equation for the time-averaged vorticity originally derived by Bonneton *et al.* [2010]:

$$\frac{\partial \bar{q}}{\partial t} + \bar{\mathbf{u}} \cdot \nabla \bar{q} = \nabla \times (\bar{D}\mathbf{e}_k) \cdot \mathbf{e}_z - \nabla \cdot (\overline{\tilde{q}\tilde{\mathbf{u}}}) - \beta \bar{q} \tag{5.25}$$

where $\bar{D}$ is determined using shock conditions.

5.2.2 Potential vorticity equation

The potential vorticity ζ defined by $\zeta = q/h$ is a quantity that is conserved along a streamline, in absence of friction. Therefore, as a vortex moves offshore into deeper water, the vorticity increases, but the area of the vortex decreases, because the potential vorticity is conserved. The potential vorticity has been widely used to describe the evolution of the circulation in the nearshore [Arthur, 1962 ; Peregrine, 1998 ; Buhler et Jacobson, 2001 ; Johnson et Pattiaratchi, 2006 ; Long et Ozkan-Haller, 2009].

The averaged potential vorticity equation is obtained, by multiplying equation

(5.16) by $(\bar{q}/\bar{h}^2)$, equation (5.25) by $(1/\bar{h})$ and summing them, resulting in:

$$\frac{\partial\bar{\zeta}}{\partial t} + \underbrace{\bar{u}\frac{\partial\bar{\zeta}}{\partial x} + \bar{v}\frac{\partial\bar{\zeta}}{\partial y}}_{\text{advection}} = \underbrace{\frac{\bar{\zeta}}{\bar{h}}\nabla\bar{M}}_{\substack{\text{Stokes drift}\\ \text{advection}}} - \underbrace{\frac{1}{\bar{h}}\nabla(\overline{\tilde{q}\tilde{\mathbf{u}}})}_{\substack{\text{wave scale}\\ \text{vorticity}\\ \text{diffusion}}} + \underbrace{\frac{1}{\bar{h}}\nabla\times(\bar{D}\mathbf{e}_k).\mathbf{e}_z}_{\substack{\text{vorticity}\\ \text{production}}} - \underbrace{\beta\bar{\zeta}}_{\substack{\text{friction}\\ \text{dissipation}}} \tag{5.26}$$

where the averaged flow potential vorticity over one period is $\bar{\zeta} = \bar{q}/\bar{h}$.

The terms of equation (5.26) can be interpreted in this manner:

- The vorticity production term is directly related to potential vorticity generation induced by the differential wave breaking. The advantage of this set of equation is that we can directly determine this term.

- The friction dissipation term is the term linked to the dissipation of potential vorticity by the bottom. When the wave forcing ceases, which means that no more energy is introduced to the system, this term is responsible for the potential vorticity decay.

- the advection term does not generate potential vorticity, and transport it with the averaged circulation,

- the Stokes drift advection is the flux induced by the waves. This term arises from the mass conservation equation, to balance the extra flux induced by the waves. This flux represents a potential vorticity transport term.

- the wave scale vorticity diffusion term is related to the diffusion of the potential vorticity gradients, it is the diffusion of the potential vorticity by the wave induced motions.

Estimation of the dissipative force

The dissipative force D in equation (5.26) is related to the wave energy dissipation by breaking. This force is defined as

$$D = \frac{D_{bm}}{c\bar{h}} \tag{5.27}$$

with c the norm of the phase velocity, and D_{bm} the broken-wave energy dissipation. We estimate D_{bm} using two different techniques, by analogy with an hydraulic jump or by the energy flux gradients dissipation. The hydraulic jump analogy is used to estimate D_{bm} with the experimental data, as the energy spatial gradients cannot be estimated

easily. In the numerical model, as the energy fluxes can be estimated at each point, we use the energy flux gradients to estimate D_{bm}. The first one is by analogy between the breaking wave and a hydraulic jump Thornton et Guza [1983] ; Bonneton *et al.* [2010], and D_{bm} is expressed as:

$$D_{bm} = \frac{g}{4T}\frac{H^3}{\bar{h}} \tag{5.28}$$

with H the wave height. In this case, if we assume the shallow water, we have $c = \sqrt{g\bar{h}}$ and the dissipative force is defined as:

$$D = \frac{g}{4cT}\frac{H^3}{\bar{h}^2} = \frac{\sqrt{g}}{4T}\frac{H^3}{\bar{h}^{5/2}} \tag{5.29}$$

Dissipation can also be estimated from the energy fluxes on an elementary control volume $dx \cdot dy$. At this end the NSW equations can be written in non-conservative form:

$$\frac{\partial \eta}{\partial t} + \frac{\partial}{\partial x}(hu) + \frac{\partial}{\partial y}(hv) = 0 \tag{5.30}$$

$$\frac{\partial u}{\partial t} + u\frac{\partial u}{\partial x} + v\frac{\partial u}{\partial y} + g\frac{\partial \eta}{\partial x} = 0 \tag{5.31}$$

$$\frac{\partial v}{\partial t} + u\frac{\partial v}{\partial x} + v\frac{\partial v}{\partial y} + g\frac{\partial \eta}{\partial y} = 0 \tag{5.32}$$

with $h = \eta - \bar{b}$ the total water depth.

By multiplying equation 5.30 by $(g\eta + \frac{u^2+v^2}{2})$, equation 5.31 by (hu), equation 5.32 by (hv) we obtain:

$$g\eta\left(\frac{\partial \eta}{\partial t} + \frac{\partial}{\partial x}(hu) + \frac{\partial}{\partial y}(hv)\right) + \frac{u^2+v^2}{2}\left(\frac{\partial \eta}{\partial t} + \frac{\partial}{\partial x}(hu) + \frac{\partial}{\partial y}(hv)\right) = 0 \tag{5.33}$$

$$hu\frac{\partial u}{\partial t} + hu^2\frac{\partial u}{\partial x} + huv\frac{\partial u}{\partial y} + ghu\frac{\partial \eta}{\partial x} = 0 \tag{5.34}$$

$$hv\frac{\partial v}{\partial t} + huv\frac{\partial v}{\partial x} + hv^2\frac{\partial v}{\partial y} + ghv\frac{\partial \eta}{\partial v} = 0 \tag{5.35}$$

By adding these three terms, we obtain an equation for the conservation of energy. If we look at the terms containing the time derivative, we have:

$$g\eta\frac{\partial \eta}{\partial t} + \frac{u^2+v^2}{2}\frac{\partial \eta}{\partial t} + hu\frac{\partial u}{\partial t} + hv\frac{\partial v}{\partial t} = \frac{\partial}{\partial t}\left[g\eta^2 + h\frac{u^2+v^2}{2}\right] \tag{5.36}$$

The terms containing a x spatial derivative can be simplified:

$$g\eta\frac{\partial(hu)}{\partial x}+\frac{u^2+v^2}{2}\frac{\partial(hu)}{\partial x}+ghu\frac{\partial\eta}{\partial x}+hu^2\frac{\partial u}{\partial x}+huv\frac{\partial v}{\partial x}=\frac{\partial}{\partial x}\left[gh\eta u+hu\frac{u^2+v^2}{2}\right] \quad (5.37)$$

We operate similarly with the terms containing the y derivative:

$$g\eta\frac{\partial(hv)}{\partial y}+\frac{u^2+v^2}{2}\frac{\partial(hv)}{\partial y}+ghv\frac{\partial\eta}{\partial y}+huv\frac{\partial u}{\partial y}+hv^2\frac{\partial v}{\partial y}=\frac{\partial}{\partial y}\left[gh\eta v+hv\frac{u^2+v^2}{2}\right] \quad (5.38)$$

We finally obtain an equation for the conservation for energy:

$$\frac{\partial F_t}{\partial t}+\frac{\partial F_x}{\partial x}+\frac{\partial F_y}{\partial y}=0 \quad (5.39)$$

with the energy fluxes F_x, F_y, F_t defined as

$$F_t=g\eta^2+h\frac{u^2+v^2}{2} \quad (5.40)$$

$$F_x=gh\eta u+hu\frac{u^2+v^2}{2} \quad (5.41)$$

$$F_y=gh\eta v+hv\frac{u^2+v^2}{2} \quad (5.42)$$

If no dissipation occurs, equation 5.39 is valid and the spatial flux gradients are exactly balanced with the temporal flux gradient. In our case, there exist energy dissipation through breaking, therefore the equation reads:

$$\frac{\partial F_t}{\partial t}+\frac{\partial F_x}{\partial x}+\frac{\partial F_y}{\partial y}=-D_{bm} \quad (5.43)$$

In the case of a regular wave forcing, by time-averaging over several periods the equation 5.43, the first term disappear and we can obtain the averaged dissipation by estimating the averaged energy flux gradients:

$$< D_{bm} >_n=-\frac{\partial < F_x >_n}{\partial x}-\frac{\partial < F_y >_n}{\partial y} \quad (5.44)$$

In the case of an irregular forcing, the temporal flux gradient cannot be neglected, hence we estimate the dissipation over a time duration t_1, supposed greater than the wave peak period:

$$< D_{bm} >_{t=t_1}=-\frac{\partial < F_t >_{t=t_1}}{\partial t}-\frac{\partial < F_x >_{t=t_1}}{\partial x}-\frac{\partial < F_y >_{t=t_1}}{\partial y} \quad (5.45)$$

We then suppose that this averaged dissipation is similar to the time-averaged dissipation over one period as we have a monochromatic wave forcing:

$$\overline{D_{bm}} \approx < D_{bm} >_n \approx < D_{bm} >_{t=t_1} \tag{5.46}$$

Refraction map

To estimate the vorticity production terms in (5.26) also require the estimation of the waves rays, as the vector $\mathbf{e}_k$ is collinear with the wave rays. To obtain the refraction map necessary to obtain the direction of the wave rays, we use the hypothesis that the wave propagation is co-linear with the energy fluxes:

$$\overrightarrow{c} \propto (F_x, F_y) \tag{5.47}$$

These fluxes are averaged over a time duration t_1 , and the refraction angle is then estimated as:

$$\theta_r = \arctan\left(\frac{< F_y >_{t=t_1}}{< F_x >_{t=t_1}}\right) \tag{5.48}$$

where $\mathbf{e}_k = [\cos\theta_r, \sin\theta_r]$ is the vector collinear with the wave rays.

Estimation of the potential vorticity balance terms

The terms of the potential vorticity balance require gradient estimations. Sensitivity analysis have showed us that it is necessary to use a 4th order central finite difference scheme. For any function f(x,y) this reads:

$$\frac{\partial f(x_i, y_j)}{\partial x} = \frac{1}{12\Delta x}\left(-f(x_{i+2}, y_j) + 8f(x_{i+1}, y_j) - 8f(x_{i-1}, y_j) + f(x_{i-2}, y_j)\right) \tag{5.49}$$

In the case of a regular wave forcing (monochromatic), the mean part is the averaged quantity over the wave period considered, and the fluctuating part is the difference between the signal and its mean.

In the case of an irregular wave forcing, the mean part of the variable, denoted by a bar $(\bar{.})$ is the high-pass filtered variable, with a cut-off frequency f_c, while the fluctuating part is denoted by a tilde $(\tilde{.})$, and represents the low-pass filtered variable, with the same cut-off frequency f_c.

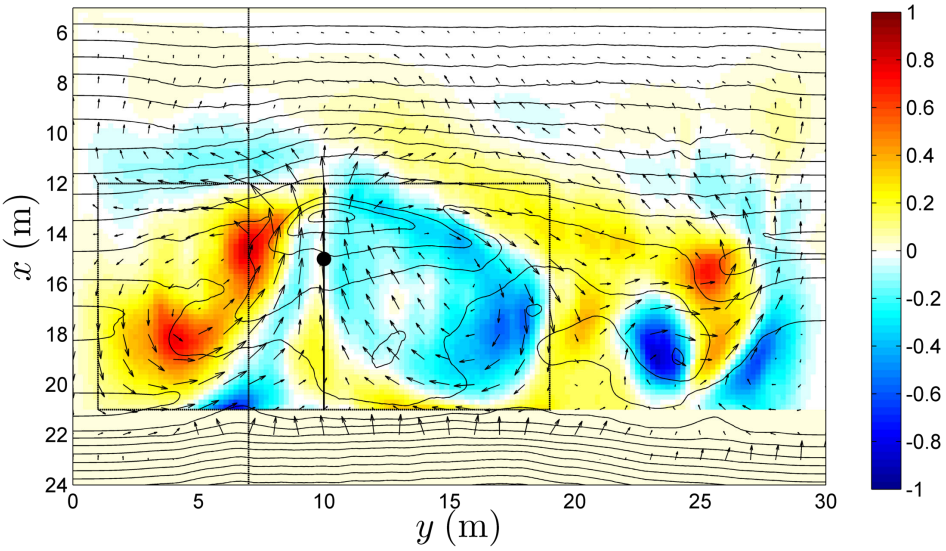

Figure 5.2 – Potential vorticity field for a JONSWAP wave forcing of significant wave height $H_{m_0} = 0.18$ m and peak period $T = 3.5$ s, with an alongshore energy damping at $y = 15$ m (simulation J_0). The black lines represent the isocontours of the bathymetry, the arrows the averaged circulation over 800 s, between $t = 300$ s and $t = 1100$ s. The dotted line represents the cross-shore section used to do the vorticity time-stack.

Enstrophy

If we define the system composed by the bathymetry and the wave forcing, we define the enstrophy ϵ as:

$$\epsilon(t) = \int_S q(t)^2 dS \tag{5.50}$$

Where S represents the area defined as 7 m $< x <$ 20 m and 1 m $< y <$ 29 m. This area starts before the breaking zone located at $x \approx 11$ m, and stops before the swash zone located at $x \approx 22$ m.The vorticity present near the lateral boundaries is also not included. This quantity is directly related to the kinetic energy in the flow and is used to estimate the spin-up and decay time of the mentioned system.

5.3 Model set-up and analysis methods

5.3.1 circulation cells position

The evolution of the circulation cells also provides valuable information for the evolution of the vorticity in the nearshore zone, especially in term of wave grouping. We then define two delimited regions, corresponding to the circulation cells (Figure 5.2). We choose the boundaries to detect the circulation cells at 12 m $< x <$ 21 m,

2 m $< y <$ 10 m and 12 m $< y <$ 19 m for the positive and negative vortices respectively.

For each circulation cell, we define at each time step the vorticity averaged over one wave period, and find the vortices extrema. For the positive vortex, the vorticity extrema is:

$$\overline{q_m^+} = \max\,(\overline{q(x,y)}), \qquad x \in [12,21], \qquad y \in [2,10] \tag{5.51}$$

For the negative vortex we have:

$$\overline{q_m^-} = \min\,(\overline{q(x,y)}), \qquad x \in [12,21], \qquad y \in [10,19] \tag{5.52}$$

To estimate the center of mass of the circulation cells, we define the vortices boundaries as the points where the value is higher (respectively lower) than 0.25 of the maximum (respectively minimum) value for the positive vortex (respectively negative vortex), similarly to Long et Ozkan-Haller [2009]. The center of mass coordinates of the positive vortex $[x_v^+, y_v^+]$ and the negative vortex $[x_v^-, y_v^-]$ are then estimated as:

$$x_v^+ = \frac{\sum\limits_{\overline{q}>0.25\overline{q_m^+}} \overline{q(x,y)}x}{\sum\limits_{\overline{q}>0.25\overline{q_m^+}} \overline{q(x,y)}}, \qquad x \in [12,21], \qquad y \in [2,10] \tag{5.53}$$

$$y_v^+ = \frac{\sum\limits_{\overline{q}>0.25\overline{q_m^+}} \overline{q(x,y)}y}{\sum\limits_{\overline{q}>0.25\overline{q_m^+}} \overline{q(x,y)}}, \qquad x \in [12,21], \qquad y \in [2,10] \tag{5.54}$$

$$x_v^- = \frac{\sum\limits_{\overline{q}<0.25\overline{q_m^-}} \overline{q(x,y)}x}{\sum\limits_{\overline{q}<0.25\overline{q_m^-}} \overline{q(x,y)}}, \qquad x \in [12,21], \qquad y \in [10,19] \tag{5.55}$$

$$y_v^- = \frac{\sum\limits_{\overline{q}<0.25\overline{q_m^-}} \overline{q(x,y)}y}{\sum\limits_{\overline{q}<0.25\overline{q_m^-}} \overline{q(x,y)}}, \qquad x \in [12,21], \qquad y \in [10,19] \tag{5.56}$$

The distance between the two centres of mass d_v is defined as:

$$d_v = \sqrt{(x_v^+ - x_v^-)^2 + (y_v^+ - y_v^-)^2} \tag{5.57}$$

5.3.2 rip current velocities

One of the main feature of the rip current are the rip current ejections, which are unsteady velocity increase seaward oriented, a great hazard for swimmers. To observe the variation in the rip current velocity, we focus on point at $x = 15$ m, $y = 10$ m. This point is located in the center of the rip channel, visible in the averaged circulation in Figure 5.2. The cross-shore and longshore velocities at this point are defined as $[u_{rip}, v_{rip}]$.

5.3.3 numerical simulations considered

Concerning the numerical modelling, all the simulations considered in this chapter use the same bathymetry from the experiment at $t = 21:00$. This bathymetry has been used in the previous chapter to validate the model, therefore we can have confidence in the simulation results.

We first consider the results in terms of vorticity with wave forcing similar to the experiment. This wave forcing consists of a JONSWAP spectrum of duration 1200 s, with significant wave height $H_{m0} = 0.18$ m, peak period $T = 3.5$ s, and a wave energy damping in the middle.

We then use monochromatic and bichromatic alongshore uniform wave forcing, to observe the evolution of vorticity in these cases. As we want to obtain a similar wave forcing energy in all the cases considered, we use the same significant wave height $H_{m0} = 0.18$ m. When the wave height distribution can be approximated by a Rayleigh distribution [Longuet-Higgins, 1952], the significant wave height H_{m0} can be approximated by [Holthuijsen, 2007]:

$$H_{m0} = 4\ \sigma_\eta \tag{5.58}$$

where σ_η represents the free surface variance. Although this relation is only valid in the case of a Rayleigh distribution, we use it to determine the significant wave height in a monochromatic case or bichromatic case, in order to compare the wave forcing energy in all these cases.

The numerical simulations considered are expressed in Table 5.1. All the simulations were performed using a grid step $\Delta x = \Delta y = 0.1$ m, which led to a variable time step of approximately $\Delta t \approx 0.01$ s, determined at each time step to ensure a Courant-Friedrich-Lewy condition.

The considered monochromatic wave forcing time-series of period T_0 s corresponding

Simulation name	wave forcing	Alongshore variation	T (s)	C_f	H_{m0} (cm)	A (cm)	T_g (s)
J_0	JONSWAP	damped	3.5	$2.1 \cdot 10^{-2}$	18	5.56	-
M_1	monochrome	uniform	3.5	$1.6 \cdot 10^{-2}$	18	6.36	-
M_2	monochrome	uniform	3.5	$2.1 \cdot 10^{-2}$	18	6.36	-
M_3	monochrome	uniform	3.5	$2.6 \cdot 10^{-2}$	18	6.36	-
M_4	monochrome	uniform	2.5	$2.1 \cdot 10^{-2}$	18	6.36	-
M_5	monochrome	uniform	4.5	$2.1 \cdot 10^{-2}$	18	6.36	-
M_6	monochrome	uniform	3.5	$2.1 \cdot 10^{-2}$	12.6	5.56	-
M_7	monochrome	uniform	2	$2.1 \cdot 10^{-2}$	18	6.36	-
M_8	monochrome	uniform	4	$2.1 \cdot 10^{-2}$	18	6.36	-
B_1	bichromatic	uniform	3.5	$2.1 \cdot 10^{-2}$	18	8.99	35
B_2	bichromatic	uniform	3.5	$2.1 \cdot 10^{-2}$	18	8.99	70
B_3	bichromatic	uniform	3.5	$2.1 \cdot 10^{-2}$	18	8.99	105
B_4	bichromatic	uniform	3.5	$2.1 \cdot 10^{-2}$	18	8.99	140
B_5	bichromatic	uniform	3.5	$2.1 \cdot 10^{-2}$	18	8.99	175
B_6	bichromatic	uniform	3.5	$2.1 \cdot 10^{-2}$	18	8.99	210
B_7	bichromatic	uniform	3.5	$2.1 \cdot 10^{-2}$	18	8.99	245
B_8	bichromatic	uniform	3.5	$2.1 \cdot 10^{-2}$	18	8.99	280

Table 5.1 – Simulation conditions for the JONSWAP, the monochromatic and the bichromatic cases.

to simulation M_2 is determined as

$$\eta_0(t) = A\sin(\sigma_0 t) \tag{5.59}$$

where $\sigma_0 = 2\pi/T_0$ and $A = 6.36$ cm is the amplitude of the waves.

If we consider a simulation with the same averaged wave height over 1200 seconds as the JONSWAP run, we obtain a different wave amplitude, as $< H >= 0.112$ m, with H the wave heights determined by a zero-down-crossing method. Therefore, for the simulation M_5 we have $A = 5.56$ cm.

For the bichromatic case, we define the wave group period T_g as the time between two nodes of the group, and obtain the following expression:

$$\eta_1(t) = \frac{A}{2}\left(\sin(\sigma_1 t) + \sin(-\sigma_2 t)\right) \tag{5.60}$$

where:

$$\sigma_1 = \frac{\pi(2T_g + T_0)}{T_0 T_g} \tag{5.61}$$

$$\sigma_2 = \frac{\pi(2T_g - T_0)}{T_0 T_g} \tag{5.62}$$

The coefficient $A = 8.99$ cm is determined to ensure that the wave forcing contains the same significant wave height H_{m_0}, and compare the monochromatic forcing with the bichromatic and the JONSWAP ones.

5.4 Potential vorticity in the LHF experiment

5.4.1 Vorticity

The potential vorticity equation (5.26) is just a consequence of the NSWE on which the numerical model is also based. Using the methods described in section 5.2 we can diagnose the importance of the different terms and determine their spatial distribution.

We first estimate the enstrophy on the numerical simulation J_0, with the parameters from the experiment. The evolution of enstrophy (Figure 5.3) reveals three distinct phases. The first one corresponds to the spin-up of the system starting from a rest state and lasts for the first 200 seconds approximately. After the spin-up phase, we observe a quasi equilibrium regime where the enstrophy varies with time, but around a mean value of 1 $m^2.Hz^2$ in our case. During this phase, we can see an arrangement of vorticity, as enstrophy variations present semi-periodic behaviour with periods of the

order of 100 seconds, induced by the wave groupiness of the wave forcing. The third phase corresponds to the decay, when the wave forcing ceases. We observe that the decay rate is high at the beginning, losing 50 % of its value before decay in 30 seconds, and this rate starts decreasing, as it takes 200 seconds to reach 10% of its value before decay.

If we compare the results obtained with the JONSWAP forcing (simulation J_0) with the ones obtained with monochromatic wave forcing different wave amplitudes. The M_2 simulation with an amplitude of $A = 6.36$ cm provides the same significant wave height as the JONSWAP. The monochromatic wave is energetically equivalent. The M_6 simulation for $A = 5.56$ cm gives a wave height equal to the JONSWAP mean wave height. We observe a spin-up time of about 75 seconds for both simulations, then the enstrophy decreases to reach a quasi-equilibrium state. We note that the enstrophy for the JONSWAP simulation seems to oscillate near a value of 1 $\mathrm{m}^2.\mathrm{s}^{-2}$, close to the monochromatic simulation with the same wave height, while the monochromatic simulation with an equivalent significant wave height reaches a higher value of enstrophy, around 1.3 $\mathrm{m}^2.\mathrm{s}^{-2}$. This could be due to the fact that in the JONSWAP simulation, the breaking occurs at varying cross-shore positions, hence the vortices have to adapt constantly to the incoming waves, whereas in the monochromatic case the forcing is constant and the vorticity generated by the differential wave breaking occurs at the same position, maximizing the vorticity generation.

The averaged circulation and vorticity are estimated on a duration of 800 s, between $t = 300$ s and $t = 1100$ s, to avoid the spin-up period and the decay. We can see in Figure 5.2 the rip channel at $y = 10$ m, with the two circulation cells, the positive with a center near $x = 16$ m, $y = 6$ m, and the negative one with a center near $x = 16$ m, $y = 16$ m. The averaged circulation shows a strong offshore oriented jet between these two cells. We also observe another dipole near $y = 24$ m, however the circulation near this dipole seems to be affected by the lateral boundary, therefore we will focus our analysis to the dipole on the left. Concerning this dipole, we also note that the peak averaged vorticity is not found in the center of the vortex, where the averaged circulation is zero, but rather in the vortices edges.

We can also observe the evolution of the potential vorticity compared to the wave forcing in one cross-shore profile (Figures 5.4-5.5). We time-stack instantaneous potential vorticity profile on a cross-shore transect that goes roughly through the center of the positive vortex (red). In Figure 5.4 middle panel we observe that free surface waves have periods close to the peak period, but wave height and wave groupiness are more widely distributed. in the top panel of Figure 5.4 the propagation of the waves is observed as thin lines with a negative slope, and we see that the generation of vorticity

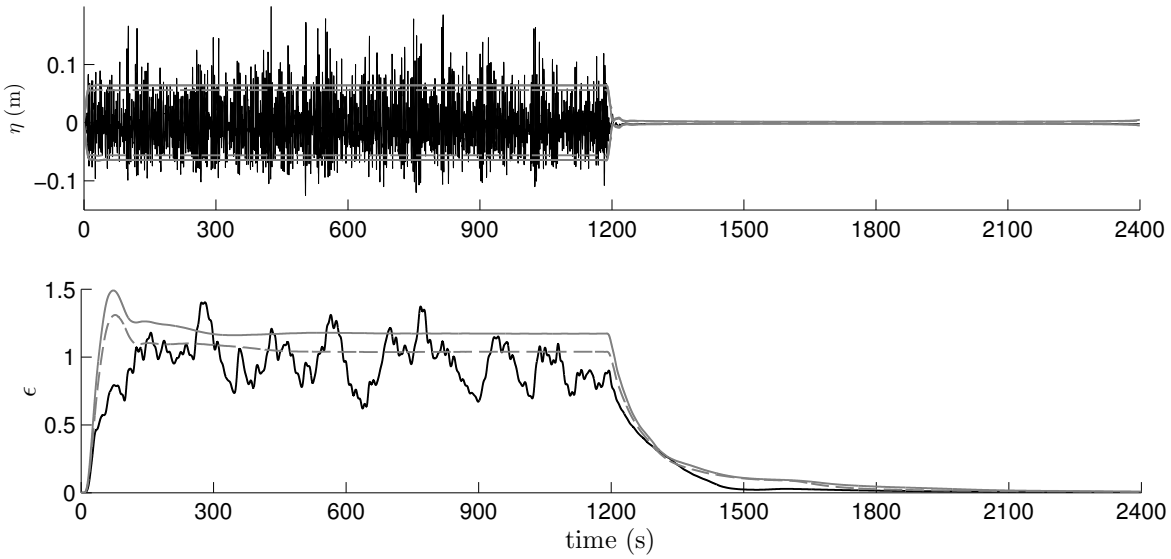

Figure 5.3 – Wave forcing time-series (upper panel) and low-pass filtered enstrophy time-series with a cut-off frequency of 10 s (lower panel). The black line represents a Jonswap wave forcing, of significant wave height $H_{m0} = 0.18$ m and peak period $T = 3.5$ s (simulation J_0). The wave forcing ceases at $t = 1200$ s to observe the enstrophy decay. The grey line represents a monochromatic wave forcing with the significant wave height $H_{m0} = 0.18$ m and period $T = 3.5$ s (simulation M_2), the grey dashed line represents a monochromatic wave forcing with the same amplitude as the JONSWAP wave forcing $A = 0.056$ m (simulation M_6). In the upper panel related to free surface evolution $\eta(t)$, the grey line and dashed line represent the monochromatic wave envelope.

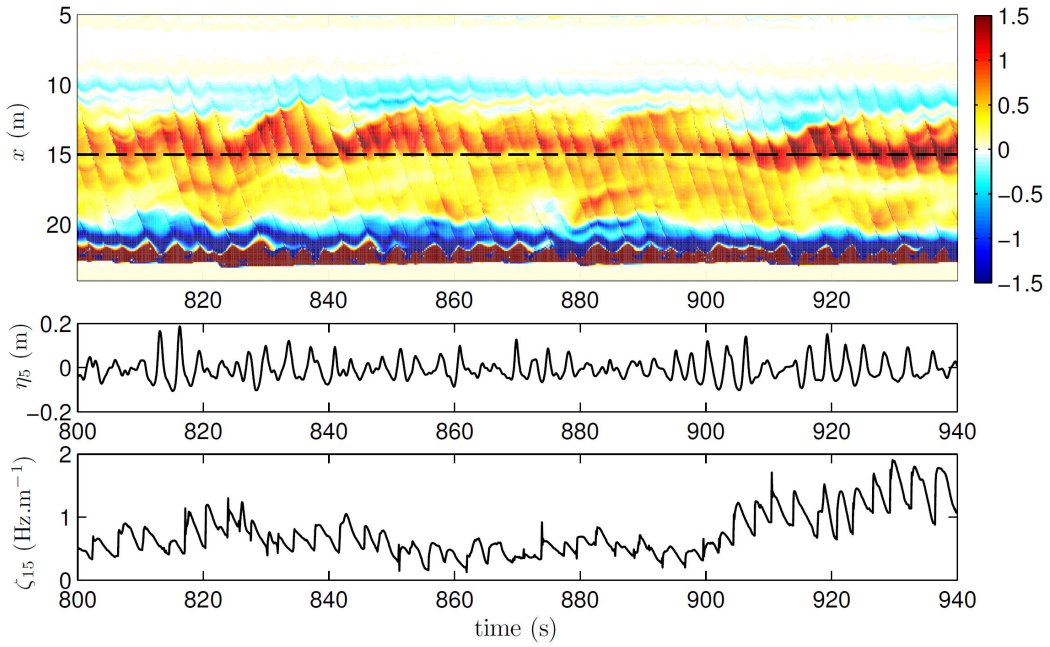

Figure 5.4 – Cross-shore vorticity time stack at $y = 7$ m (upper panel), corresponding free surface water height at $x = 5$ m (middle panel) and potential vorticity evolution at $x = 15$ m (lower panel) for simulation J_0 (Jonswap wave forcing). The dashed line in the upper panel represents the vorticity time series shown in the lower panel.

within the vortex for each wave is different: for 920 s $< t <$ 940 s the vorticity reaches peaks of 2 Hz.m^{-1} with each passing wave at $x = 15$ m, and for 870 s $< t <$ 900 s the peaks in vorticity are closer to the value 0.5 Hz.m^{-1}.

The positive shoreward boundary of the vortex moves at a lower period than the waves, as we can see some modulations of period 10 s and 20 s in the time-stack. This is due to the fact that the vorticity generated by each wave is proportional to the power of 3 of the wave height.

By doing a close-up on a 50 second period (Figure 5.5) and with a lower time step, we note that the passing waves generate a peak in potential vorticity. These peaks does not seem to correlate with an enhanced potential vorticity in the vortex, as between $t = 825$ s and $t = 835$ s, we observe an increased vorticity, but the peaks are not relatively high.

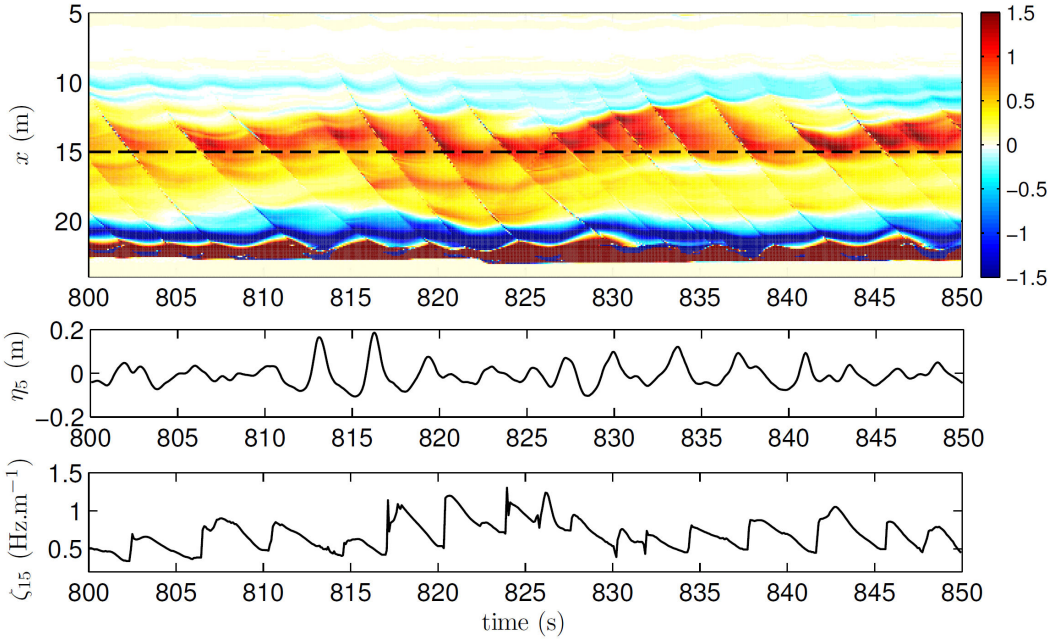

Figure 5.5 – Cross-shore vorticity time stack at $y = 7$ m (upper panel), corresponding free surface water height at $x = 5$ m (middle panel) and potential vorticity evolution at $x = 15$ m (lower panel) for simulation J_0 (Jonswap wave forcing). The dashed line in the upper panel represents the vorticity time series shown in the lower panel.

5.4.2 Dissipative force estimations: hydraulic jump and energy gradients

As stated in the previous section, The dissipation induced by the wave breaking can be estimated in different ways. We can then compare the dissipation term estimated using a hydraulic jump analogy both for the numerical model and the experiment.

Hydraulic jump analogy

Using an analogy between the wave breaking and an hydraulic jump, the results from the experiment and from the numerical model with the same conditions can be found in Figure 5.6.

We observe that the dissipative force in the numerical model and in the experiment are found approximately in the same region, between $x = 12$ m and $x = 15$ m for the experiment. At $y = 10$ m, where the rip channel exits, the dissipative force is stronger at $x = 12$ m, with a maximum of 0.04 , whereas at $y = 5$ m or $y = 20$ m, the dissipative force occurs at $x = 15$ m in the experiment. The numerical model dissipative force term shows a similar behaviour, but the magnitude of the dissipative force is different, as the maximum dissipative force, at the rip channel exit is about 0.02, a half of the experimental result.

The wave height H is determined by a zero-downcrossing method to determine the waves and then averaging over all the waves. The period is determined with the significant wave period $T_{1/3}$. As noted by Holthuijsen [2007], for swell wave forcing with narrow spectrum, $T_{1/3} \approx T_{peak}$, where T_{peak} is the peak wave period of the JONSWAP. In our case, we observe that the significant wave period is slightly lower around $T = 3.2$ s at $x = 5$ m. However, we focus on the period evolution when approaching the shoreline, and not the exact values. If we compare the spatial variation of wave height and period , we observe that the significant wave period decreases in the experiment, from $T = 3.2$ s at $x = 5$ m, to $T = 2.7$ s at $x = 15$ m, and the wave height increases from $H = 0.11$ m at $x = 5$ m, to $H = 15$ m at $x = 15$ m. The numerical model shows a different behaviour concerning the significant wave period, as the period is approximately $T = 3.2$ s at $x = 5$ m, and increases to $T = 4$ s at $X = 20$ m. The wave height increases before the breaking, but the maximum water height is $H = 0.13$ m, lower than the experimental results.

These differences can be explained if we look at the free-surface elevation time-series in a cross-shore profile, in Figure 5.7. The absence of dispersion terms in the numerical model lowers the wave height peaks, and does not produce secondary peaks, which are responsible for the increase in wave height and decrease of the period as we approach

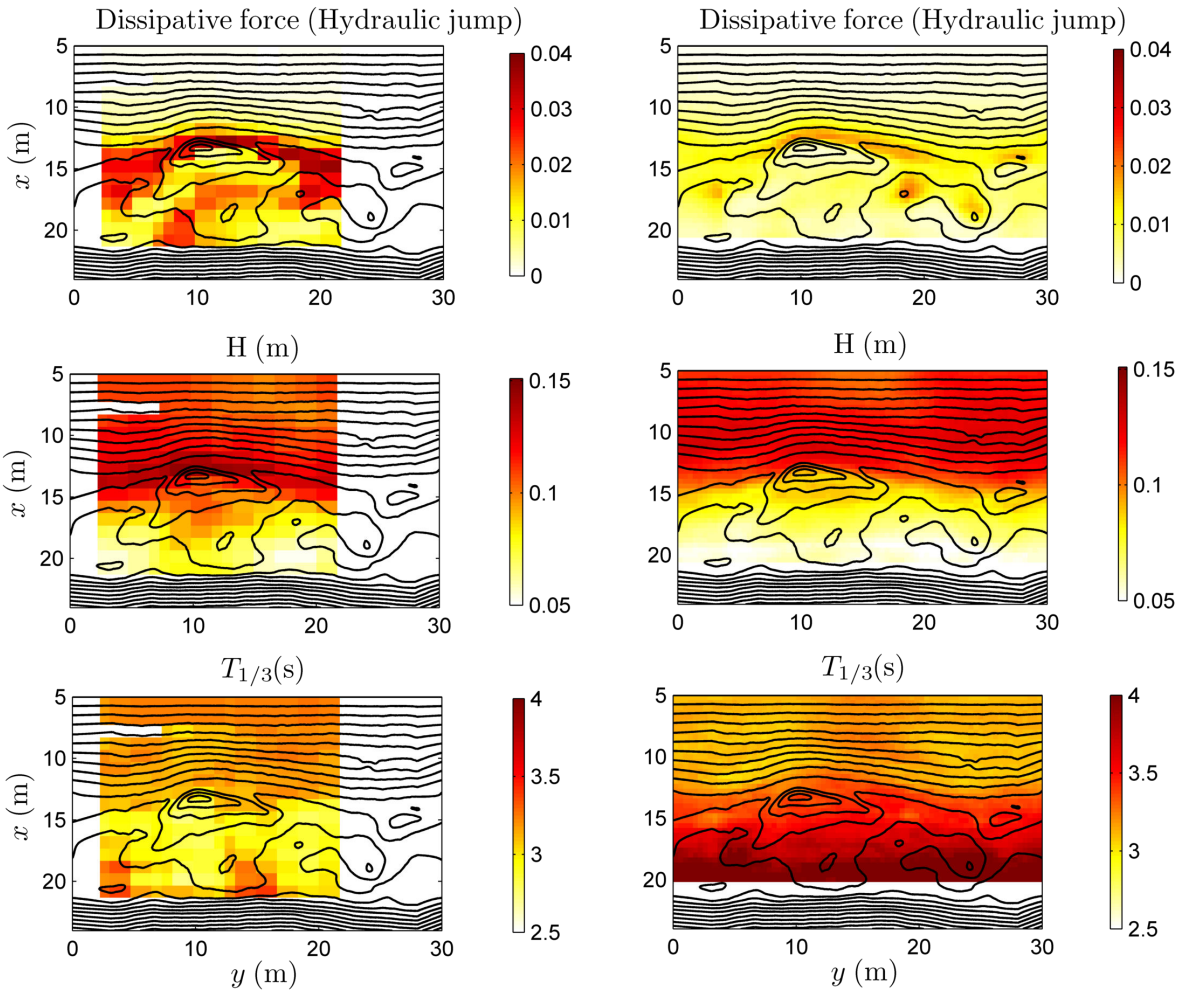

Figure 5.6 – Spatial distribution of the dissipative force D estimated with a hydraulic jump analogy (Upper panels), of the wave height (Middle panels), and of the significant wave period $T_{1/3}$ (Lower panels). The left panels corresponds to experimental results, from experiment 30 (t=21:00-26:00), using a JONSWAP spectrum, damped in the middle . The right panels corresponds to the numerical model, using a similar forcing (simulation J_0).

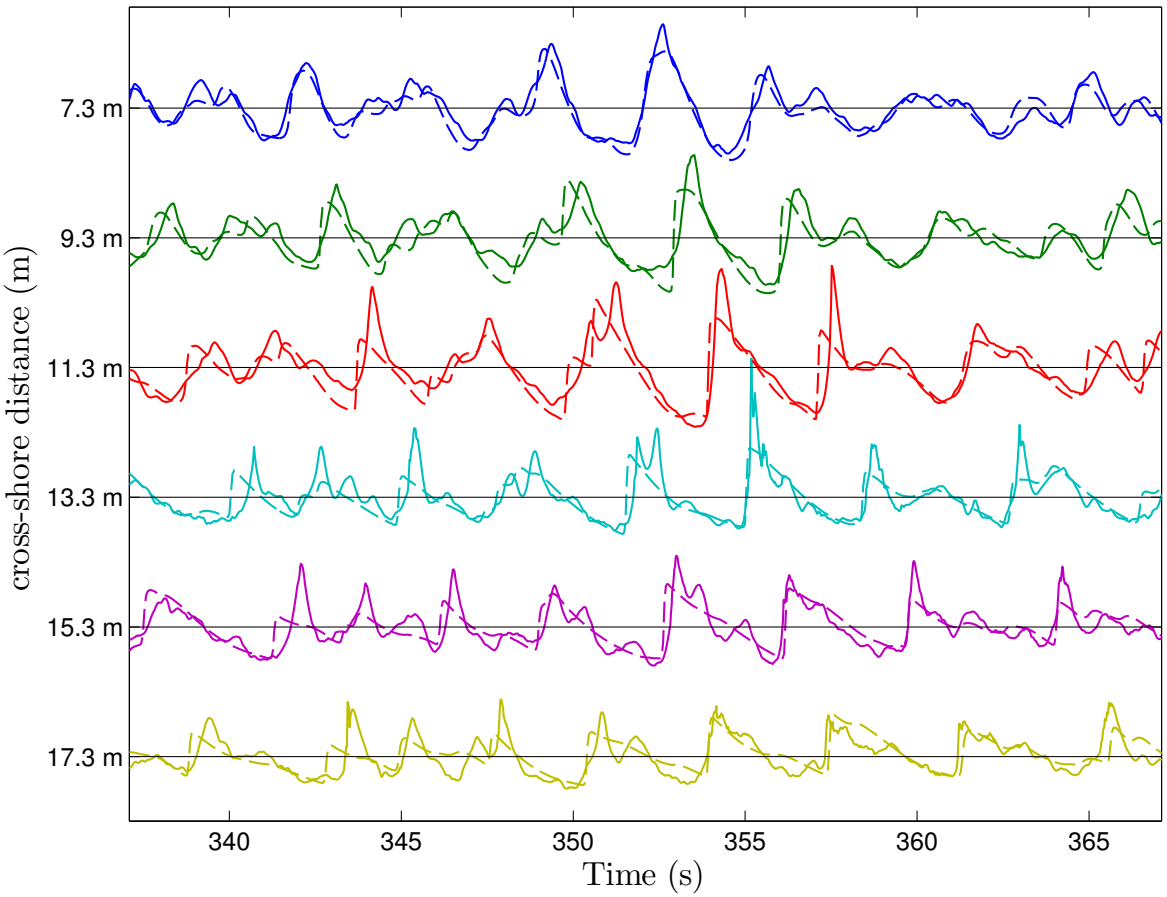

Figure 5.7 – Free surface elevation time-series in a cross-shore profile at $y = 10$ m, difference between the experimental results for experiment 30 (t=21:00-26:00) (line) and the numerical simulation J_0 (dashed line)

the shoreline. The estimation of the dissipative force using an hydraulic jump analogy is lower than expected, mainly due to the reduced wave height before breaking, and the different period evolution in the domain, that also tends to decrease the dissipative force. However, the spatial distribution of the dissipative force is fairly good.

Energy fluxes gradient

If we use the energy flux gradients, we can also estimate the dissipative force. We suppose that for a long enough duration, here 60 wave periods (210 s), the flux gradient are equal to the dissipative force. If we look at the dissipative force estimated by the energy fluxes (Figure 5.8), we see that the values and spatial distribution of the dissipative force is similar to the experimental dissipative force estimated with the hydraulic jump analogy. The areas where the dissipative force is high consist in the

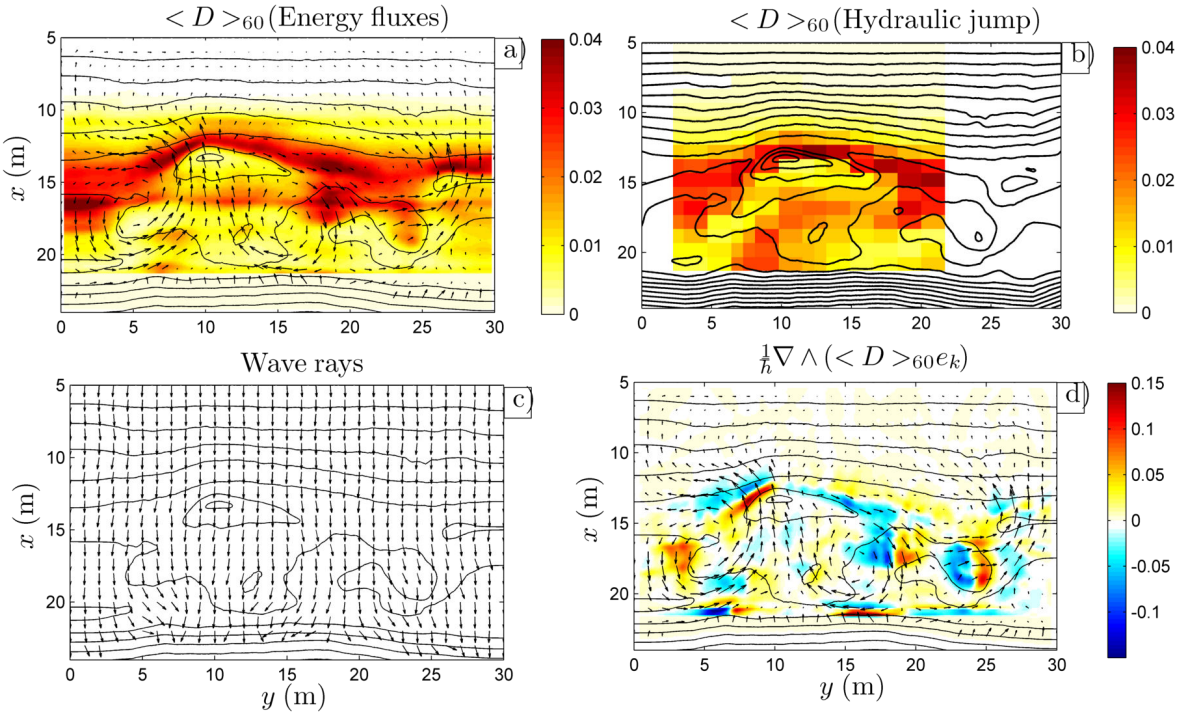

Figure 5.8 – Averaged dissipative force and vorticity production term estimated over 60 wave period. The black lines represent the isocontours of the bathymetry. a) arrows: averaged circulation over 60 wave period; colors: dissipative force estimated using the energy fluxes for the numerical simulation J_0; b) Experimental dissipative force estimated with the hydraulic jump analogy for experiment 30 (t=21:00-26:00). c) arrows: direction of the wave ray vector $\mathbf{e}_k$ for simulation J_0; d) colors: vorticity production term $1/h\nabla \wedge D\mathbf{e}_k$ for simulation J_0, arrows: averaged circulation over 60 wave period.;

breaking zone, between $x = 12$ m and $x = 14$ m. For the region of the rip channel, for 9 m $< y <$ 15 m, the dissipative force is moved seaward, at $x = 12$ m, as the bathymetry induces an earlier wave breaking.

Vorticity production

The refraction map estimated with the energy fluxes (Figure 5.8) shows that the refraction angles are lower than 10 degrees up to $x = 14$ m, and lower than 15 degrees up to $x = 18$ m. For $x > 18$ m, the refraction angles increase rapidly.

We estimate the vorticity production term, from the equation 5.26:

$$\nabla \times (D\mathbf{e}_k).\mathbf{e}_z \approx (\nabla D \times \mathbf{e}_k).\mathbf{e}_z \approx \frac{\partial D}{\partial x}\sin\theta - \frac{\partial D}{\partial y}\cos\theta \tag{5.63}$$

In the breaking zone, where the dissipative force is important, we showed that the refraction angles are lower than 10 degrees, therefore the vorticity generation comes mainly from the alongshore dissipative force gradient $\frac{\partial D}{\partial y}$, and not so much on the cross-shore dissipative force gradient, corresponding to the wave energy. This is consistent with Peregrine [1998], who showed that the lateral gradients were responsible for the vorticity generation.

We observe that the peak values of the vorticity production term are near the rip neck at $x = 13$ m, $y = 7$ m, where the wave breaking is more intense, and in the horns at $x = 20$ m, $y = 17$ m, where the water depth is lower.

Chapter 4 has provided a sound validation of the mean circulation and mean vorticity fields. In this section we have gained insight on the transient spin-up under jonswap forcing compared to the monochromatic wave forcing. Moreover, we have gained a first understanding of the different time scales of the vorticity production by wave breaking by analysing vorticity time-stacks, at the scale of the waves and at large time scales related to the advection by the mean circulation.

5.5 Potential vorticity under a monochromatic wave forcing

In the present section we aim at understanding what controls the vorticity production in a bathymetry with a rip channel and rip bar head. At this end we will use a alongshore uniform monochromatic wave forcing. The circulation in this configuration is entirely controlled by the bathymetry, as the wave forcing is alongshore uniform.

The differential wave breaking, motor of the vorticity generation, is caused by the bathymetry heterogeneity. With the monochromatic wave forcing, we will observe the influence of several parameters:

- we will as previously analyse the different time scales involved in the vorticity evolution.
- we will see how friction changes the vorticity spin-up and spin-down.
- we will also analyse the influence of the wave period at constant wave height.

5.5.1 Vorticity

Averaged circulation and vorticity

We now use simulations with the same bathymetry from experiment 30 (t=21:00-26:00), but with an alongshore uniform monochromatic forcing. This way, the circulation reaches a quasi-equilibrium after the spin-up period, oscillating with the wave period and we can estimate the terms of the potential vorticity balance by averaging over a period.

The averaged potential vorticity for simulation M_2, with the same significant wave height than the JONSWAP simulation J_0, can be seen in Figure 5.9. The rip channel at $y = 10$ m is the main feature, with two circulation cells marked with opposite vorticity. The centres of the cells which correspond the the averaged vorticity maximum, are at $x = 16$ m, $y = 7$ m and $x = 17$ m, $y = 16$ m for the positive and the negative vortex respectively. There is little vorticity within the rip channel, except at the rip neck, at $x = 13$ m, where the two cells meet. Due to the bathymetry heterogeneity, where the bed gradients are higher in the region 5 m $< y <$ 10 m than in the region 10 m $< y <$ 20 m, the circulation cells are asymmetric. The positive vortex is closer to the rip channel with a strong maximum, whereas the negative vortex is further from the rip channel with an expanding arm reaching the rip neck.

If we compare this Figure with the JONSWAP simulation J_0 (Figure 5.2), we observe that the vorticity values are stronger in the recirculation cells in the monochromatic case. This is probably due to the smoothing induced by the irregular wave forcing: as waves do not break exactly at the same position, the averaged quantities are spatially smoothed, and the values are lower than in the monochromatic case.

If we look at the potential vorticity time-stack for simulation M_2 in a cross-shore profile at $y = 7$ m (Figure 5.10) we observe that the potential vorticity is in quasi-equilibrium, oscillating with the wave period. Each wave generates potential vorticity,

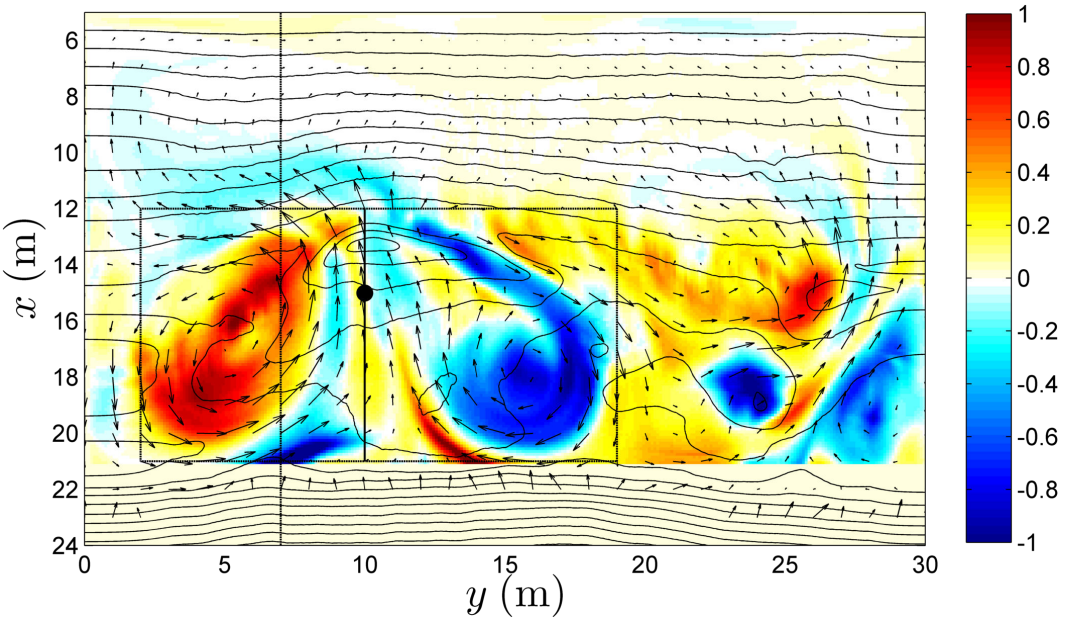

Figure 5.9 – Time-averaged potential vorticity field and circulation with the bathymetry from experiment 30 (t=21:00) and a monochromatic wave forcing (simulation M_2) over a duration of 800 s. The black lines represent the isocontours of the bathymetry, the arrows the averaged circulation. The dotted boxes represents the region used to estimate the center of mass of each vortex.

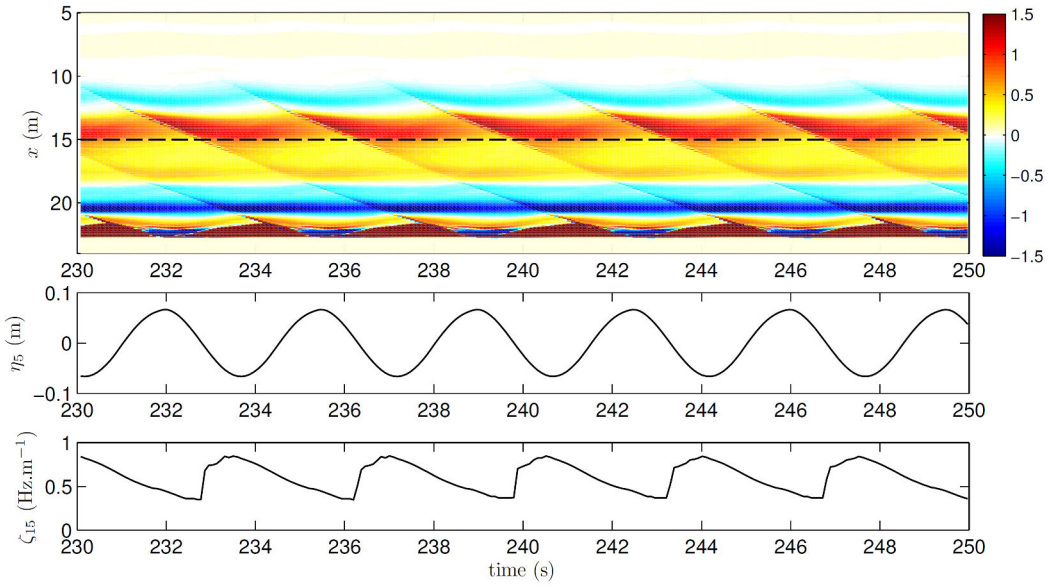

Figure 5.10 – Cross-shore potential vorticity time stack at $y = 7$ m (upper panel), corresponding free surface water height time series at $x = 5$ m (middle panel) and potential vorticity time-series at $x = 15$ m, $y = 7$ m (lower panel) corresponding to the black dashed line in the potential vorticity time-stack, for a monochromatic wave forcing (simulation M_2)

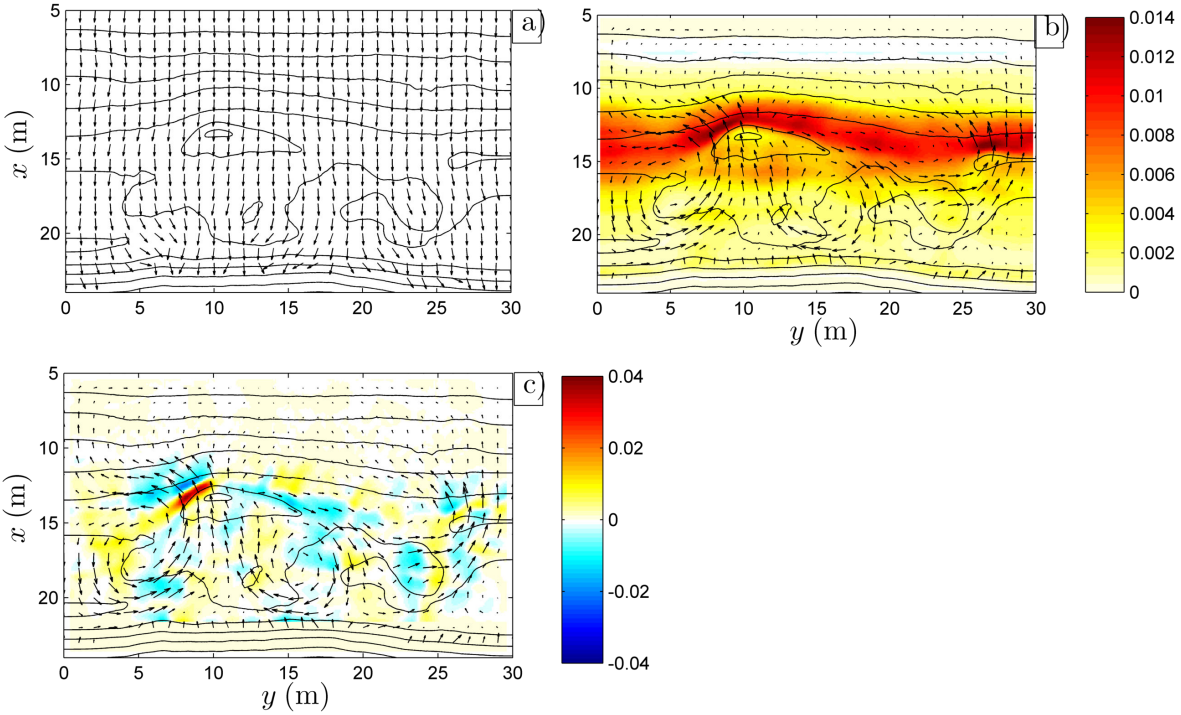

Figure 5.11 – Averaged Vorticity production term estimated over 60 wave period for a monochromatic wave forcing (simulation M_2). The black lines represent the isocontours of the bathymetry. a) arrows: direction of the wave ray vector $\mathbf{e}_k$; b) arrows: averaged circulation over this 60 wave period, colors: Dissipation estimated using the energy fluxes; c) colors: Vorticity production term $1/h\nabla \wedge D\mathbf{e}_k$; arrows: averaged circulation over this 60 wave period.

with a peak at $x = 15$ m, but the vortex boundaries are only affected by the passing waves, and do not modulate at a larger period.

5.5.2 Potential vorticity balance

For the estimation of the different terms of the potential vorticity equation, we focus on the time range 900 s $< y <$ 1110 s. The system is considered in quasi equilibrium, and we have approximately 60 wave periods, to estimate the averaged quantities.

If we look at the potential vorticity production term (Figure 5.11), we clearly observe a peak, at $x = 14$ m, $y = 9$ m, located near the rip neck, where the bottom gradients are the strongest, and the longshore dissipation gradient is significant. We also note that the vorticity production term is not symmetric, as it is stronger in one of the two vortices.

Having estimated the vorticity production term, we compare it with the remaining terms of the potential vorticity balance (equation 5.26). The spatial evolution of these

terms can be seen in Figure 5.12. We focus on the two circulation cells between $y = 1$ m and $y = 20$ m. We define the positive vortex as the circulation cell with positive potential vorticity with a center at $x = 16$ m, $y = 7$ m, and the negative vortex the circulation cell with a center at $x = 16$ m, $y = 15$ m. Concerning the different terms of the potential vorticity balance, we observe that the peak values are located near the rip neck, at $x = 12$ m, $y = 10$ m, except for the friction that is more widely spread, near the regions of strong vorticity.

We also observe the rip asymmetry as the advection , the wave induced mass flux, the wave scale vorticity diffusion and the vorticity production are stronger in the positive vortex than in the negative vortex. For the positive vortex, the mentioned terms are strong near the ripple neck, and form a line toward the center of the vortex. For the negative vortex, we also observe that the extrema form a line, which starts in the ripple neck at $x = 13$ m, $y = 10$ m, and extend through the negative vortex arm up to $x = 15$ m, $y = 19$ m.

In terms of peak values, the stronger values are observed in the advection and wave scale vorticity diffusion, with 0.1 $m^{-1}.s^{-2}$. The vorticity production term shows a peak value of 0.04 $m^{-1}.s^{-2}$ and the wave induced mass flux shows a peak value of -0.03 $m^{-1}.s^{-2}$ near the ripple neck.

The friction dissipation shows lower extrema values, at 0.02 $m^{-1}.s^{-2}$ but it is more uniformly distributed. Whereas all the other terms are important in the breaking zone, the friction term is important near the shoreline, as it increases with decreasing depth.

The areas where most of the term are relevant correspond to the seaward boundaries of the vortices, where the circulation and the wave breaking occur. From the spatial organization of these terms, we can deduce an organization of the potential vorticity under monochromatic wave. Starting the numerical experiment from rest and imposing a monochromatic wave forcing, the following steps occur:

1. at first the potential vorticity is negligible, therefore the only important term is the vorticity production term, dependent of wave breaking dissipation gradient and the water depth h. If there is no such gradient, for example with an alongshore uniform beach with alongshore uniform normal wave forcing, no vorticity is created. In our case, the vorticity is generated near the rip neck, for both vortices, and at the horns, where the water depth is lower, at $x = 17$ m, $y = 3$ m and $x = 17$ m, $y = 17$ m. The vorticity generated at the horns has lower values, but contribute to the global vorticity generation

2. The vorticity generated near the rip neck and the horns is then moved in the system by advection or diffusion. These two terms are also important in the rip

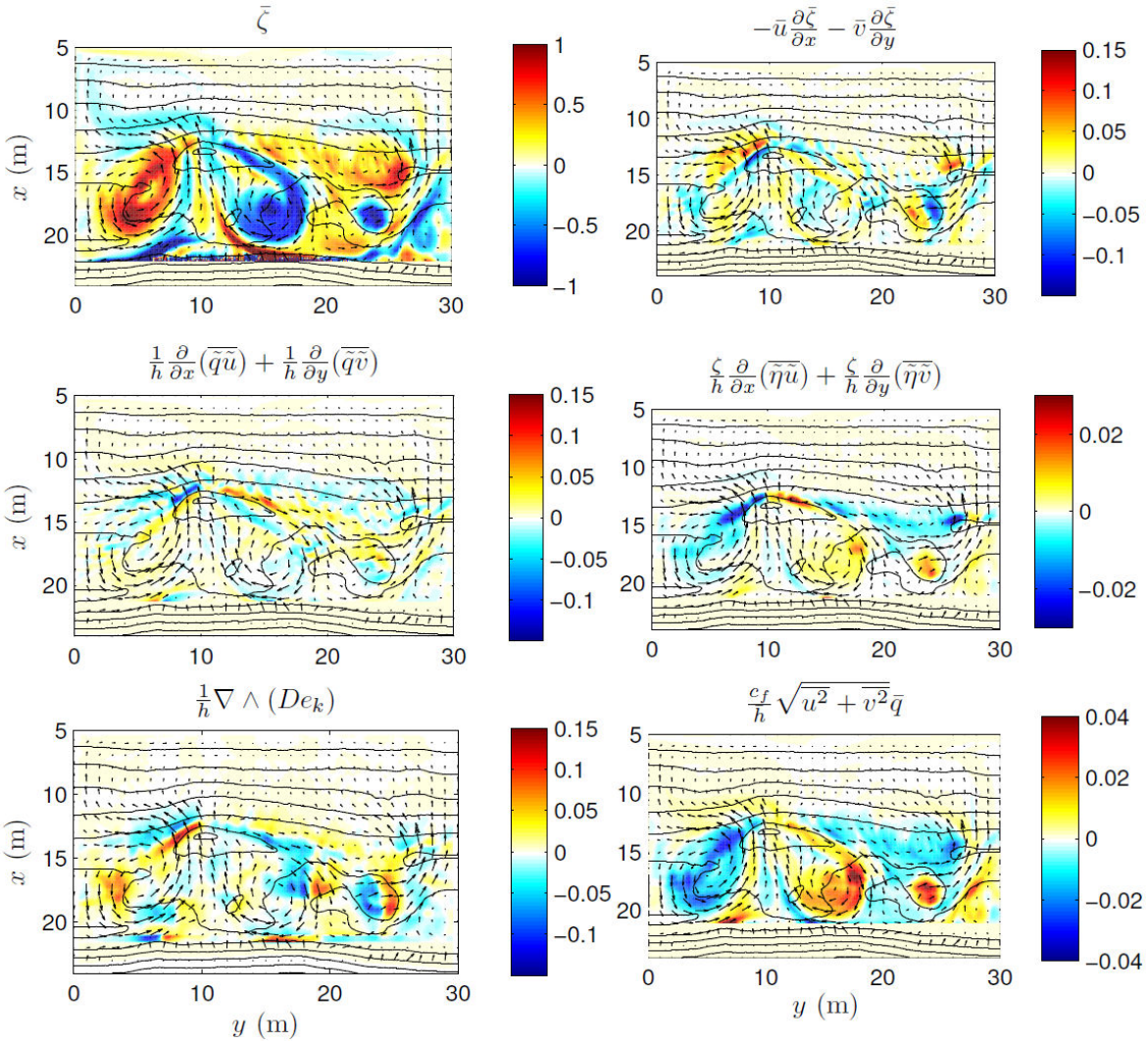

Figure 5.12 – Importance of the terms of the potential vorticity balance for a monochromatic wave forcing (simulation M_2). The black lines represent the isocontours of the bathymetry, the arrows the averaged circulation over this 60 wave period. The scale color can be different. The potential vorticity unit is $\mathrm{m}^{-1}.\mathrm{s}^{-1}$ and the unit for the potential vorticity balance terms is $\mathrm{m}^{-1}.\mathrm{s}^{-2}$

neck, as it is the region where the vorticity is generated.

3. The circulation induced by the bathymetry create a rotational circulation that has a positive feedback on the generated vorticity. The vorticity generated at the rip neck is of the same sign as the vortices of the recirculation cells, therefore the vorticity adds up to the greater vortices.

4. as vorticity keeps increasing, the wave induced mass flux and the friction terms are no longer negligible. The friction term spatial distribution is very similar to the distribution of the mean circulation. This points at a general equilibrium between bottom friction and the mean circulation. As for the wave induced mass flux it seems to have a negative feedback on vorticity, which would tend to decrease the vorticity levels, however the magnitude is much lower than the other terms.

5. in its equilibrium state, the two vortices have well defined boundaries close to elliptic shapes, with maximum vorticity at the edges of the vortices. The vorticity in the system is at equilibrium, being generated near the rip neck and at the lateral horns, being advected and diffused in the whole system, and being dissipated by friction in the whole area.

If we now focus on the order of magnitude of the terms of the potential vorticity equation restricted to the the area of the positive and negative vortex, we obtain an estimation of the relative importance of these terms in the vortex by averaging spatially over the area occupied by the whole vortices.

For the positive vortex (Figure 5.13) we observe that the production term has an area-averaged value of $6.08 \cdot 10^{-3}$ $\mathrm{m}^{-1}.\mathrm{s}^{-2}$ with peak values at 0.15 $\mathrm{m}^{-1}.\mathrm{s}^{-2}$. is the main source of vorticity with and the friction is the main sink of vorticity with $-5.85 \cdot 10^{-3}$ $\mathrm{m}^{-1}.\mathrm{s}^{-2}$. Even though the area-averaged value of the advection is an order of magnitude less than that of the production, the peak values are of same magnitude. Moreover an interesting feature is that the color patterns of these advection and production terms have similar shapes. All these characteristics indicate that advection redistributes vorticity to produce an equilibrium. In this system bottom friction is the only sink of energy. We probably can state that the rate of production of vorticity at wave scale is compensated by the rate at which it is destroyed by friction at the scale of the mean circulation.

For the negative vortex (Figure 5.14), we also observe a similar behaviour, the area-averaged potential vorticity production term and the friction term being the main

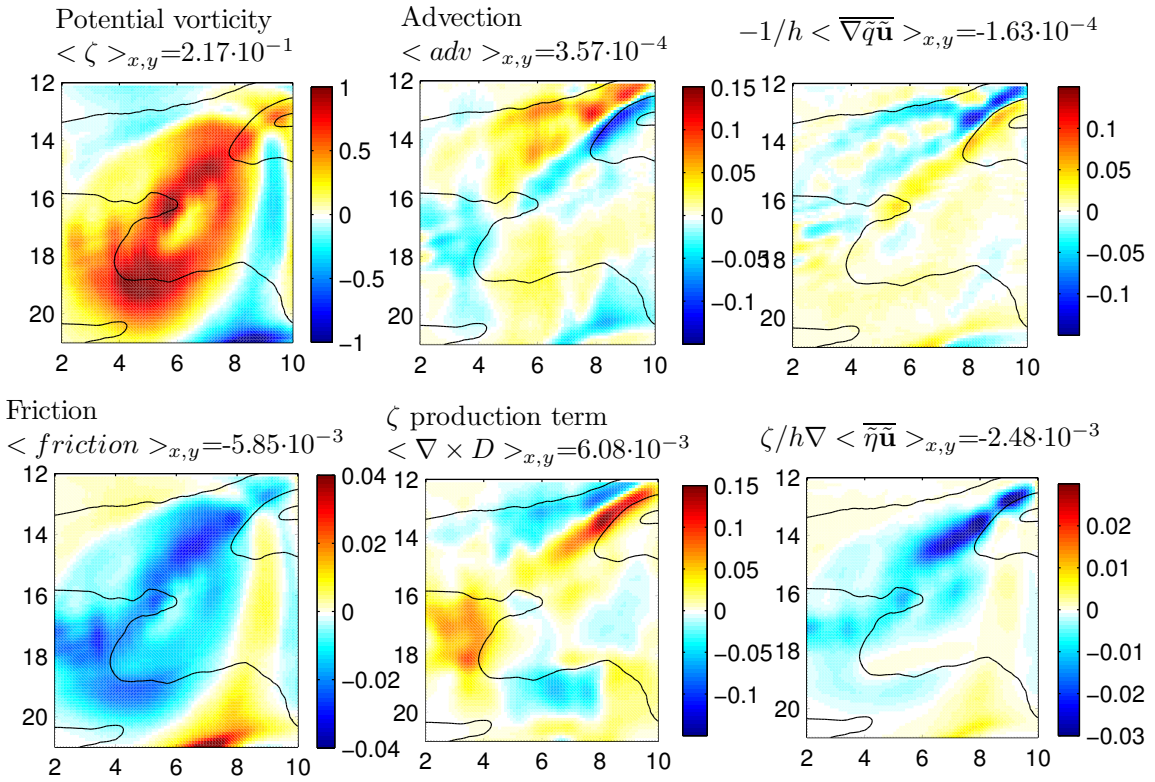

Figure 5.13 – Potential vorticity balance (5.26) terms for a monochromatic wave forcing (simulation M_2), for the positive vortex located at 12 m $< x <$ 21 m, 2 m $< y <$ 10 m. The black lines represent the isobaths. The potential vorticity unit is m^{-1}.s^{-1} and the unit for the potential vorticity balance terms is m^{-1}.s^{-2}

contributors to the potential vorticity balance. The patterns of the spatial distribution of the advection and the production are also similar.

5.5.3 Influence of friction

The friction is important as it is the only sink of the energy of the mean circulation in the nearshore zone. Yu et Slinn [2003] using a linear bottom friction with normal incident wave forcing observes that it has only a slight influence on the flow patterns, as the offshore extent and the width of the rip current are barely affected by a change in the bottom friction. Long et Ozkan-Haller [2009] observed that the friction coefficient does not dictate the temporal variability of the vortical motions.

In our study the influence of friction in the vorticity field is estimated using a monochromatic wave forcing with significant wave height $H_{m_0} = 0.18$ m and period $T = 3.5$s, and different friction coefficients: $c_f = 1.6 \cdot 10^{-2}$, $c_f = 2.1 \cdot 10^{-2}$, $c_f =$

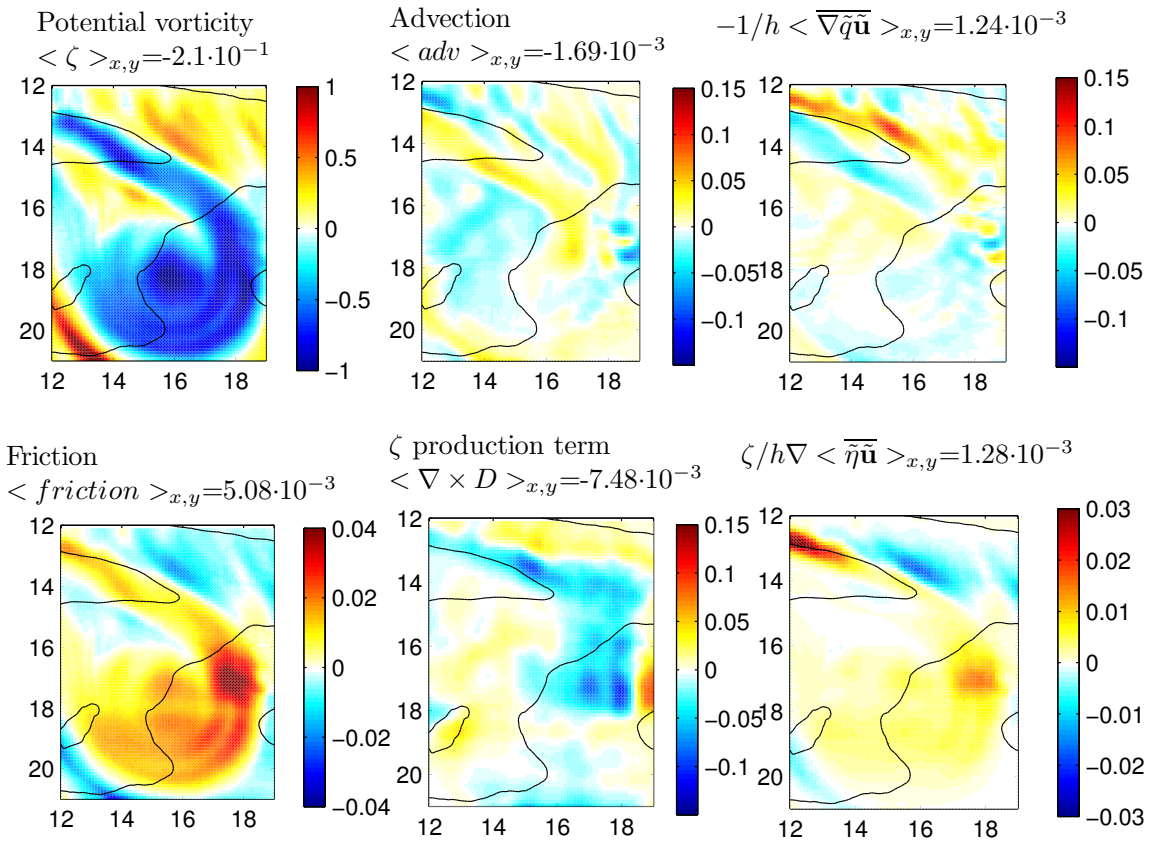

Figure 5.14 – Potential vorticity balance (5.26) terms for a monochromatic wave forcing (simulation M_2), for the negative vortex located at 12 m $< x <$ 21 m, 12 m $< y <$ 19 m. The black lines represent the isocontours of the bathymetry. The scale color can be different. The potential vorticity unit is m^{-1}.s^{-1} and the unit for the potential vorticity balance terms is m^{-1}.s^{-2}

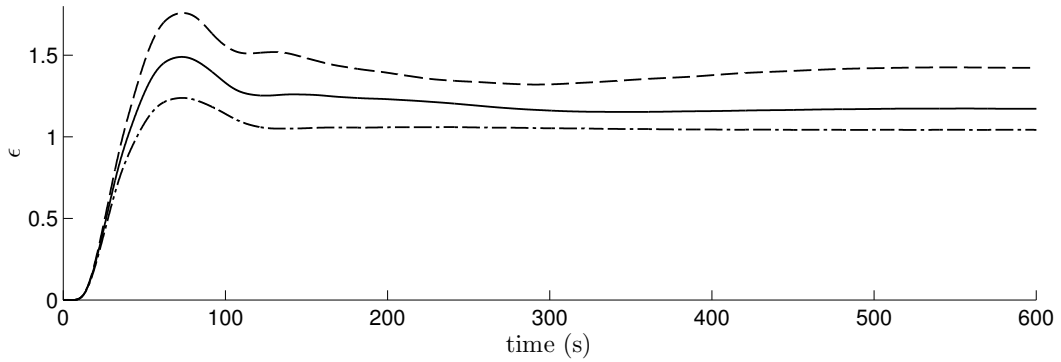

Figure 5.15 – Time evolution of high-pass filtered enstrophy for a uniform monochromatic wave forcing, for different friction coefficients. $(--)$: $c_f = 1.6 \cdot 10^{-2}$ (simulation M_1); $(-)$: $c_f = 2.1 \cdot 10^{-2}$ (simulation M_2); $(- \cdot -)$: $c_f = 2.6 \cdot 10^{-2}$ (simulation M_3).

$2.6 \cdot 10^{-2}$ (respectively simulations M_1, M_2, M_3). The evolution of the low-pass filtered enstrophy for the monochromatic wave forcing is shown in Figure 5.15 for these friction coefficients. We observe a spin-up time of about $t = 75$ during which the enstrophy increases with a steady rate. This rate does not really depend on the friction coefficient, meaning that the friction is not the important factor in the spin-up. After this period of spin-up, the enstrophy decreases and reaches a quasi-steady state at approximately $t = 200$ s.

To analyse how friction influences vorticity decay, we run the simulation for $t = 1200$ seconds in order to reach a quasi-equilibrium state and set the wave forcing to zero at $t = 1200$ seconds, and observe the evolution of enstrophy (Figure 5.16). To compare the decay with different friction coefficients, we define the equilibrium enstrophy ϵ_{eq} as the enstrophy reached after a duration of 1200 s and normalize the enstrophy with this value.

We observe that the enstrophy decay is directly related to the friction coefficient, as the time to reach half of the equilibrium enstrophy in the system is of approximately 50 seconds for $c_f = 2.6 \cdot 10^{-2}$, 70 seconds for $c_f = 2.1 \cdot 10^{-2}$ and 100 seconds for $c_f = 1.6 \cdot 10^{-2}$. For the simulation with the lower friction, we observe after 100 seconds that the enstrophy decrease accelerates, whereas the two other simulations have a relatively smoother behaviour, with no sudden change in the rate of enstrophy decay. The spatial and temporal evolution of the enstrophy decay are shown at several instants after the wave forcing ceases in Figure (5.17). For the early stage of decay, between 1200 and 1350 seconds we first observe that the enstrophy is higher when the friction coefficient is lower, due to the potential vorticity balance at equilibrium where the friction is the main sink.

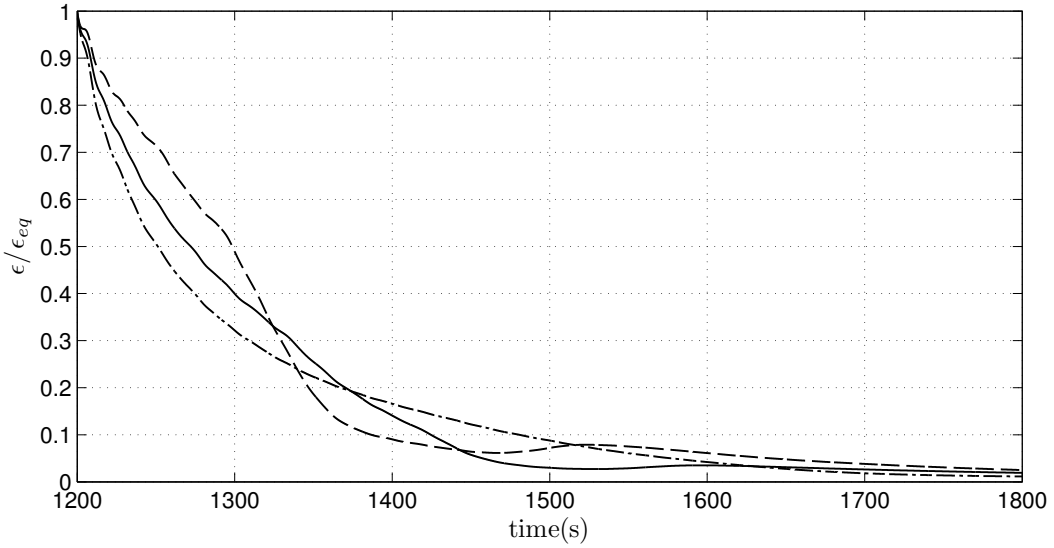

Figure 5.16 – Time evolution of enstrophy decay for a uniform monochromatic wave forcing, for different friction coefficients. $(--)$: $c_f = 1.6 \cdot 10^{-2}$ (simulation M_1); $(-)$: $c_f = 2.1 \cdot 10^{-2}$ (simulation M_2); $(- \cdot -)$: $c_f = 2.6 \cdot 10^{-2}$ (simulation M_3).

For the three simulations, after the wave forcing ceases, there is a self-advection of the two vortices, reducing their distance and advecting themselves seaward. The advection is slowed when increasing the friction, which in turn reduces vorticity, giving a negative feedback to the vortices. Concerning the dipole at $y = 25$ m, the positive vortex (red) is stronger than the negative one (blue) and is advected with a greater velocity seaward, the negative vortex circling around it. This positive vortex moves seaward due to the velocity induced by its image with respect to the close right lateral boundary. This vortex is probably the reason of the increased decay in Figure 5.16) for $c_f = 1.6 \cdot 10^{-2}$, as the vortex goes near the boundaries, and part of it goes out of the integration zone for the vorticity (Figure 5.17 a-d).

For the latter stages between $t = 1400$ s and $t = 1550$ s, we observe that the dipole is slowly advected seaward for $c_f = 2.1 \cdot 10^{-2}$ (m-p) and $c_f = 2.6 \cdot 10^{-2}$ (u-x). For $c_f = 1.6 \cdot 10^{-2}$ (e-h), we observe that the positive vortex (red) is trapped by the bathymetry, staying in the trough, while the negative vortex (blue) is still advected seaward. This has been reported by Buhler et Jacobson [2001], who stated that the favourite positions for the vortices were at bar trough, as it is difficult for them to "climb" out of these bathymetric troughs.

If we focus on the motion of the dipole defined by the vortices at $y = 7$ m and $y = 15$ m, we can look at the trajectories of the center of mass of these vortices for different friction coefficient (Figure 5.18). We see that the displacement of the vortices

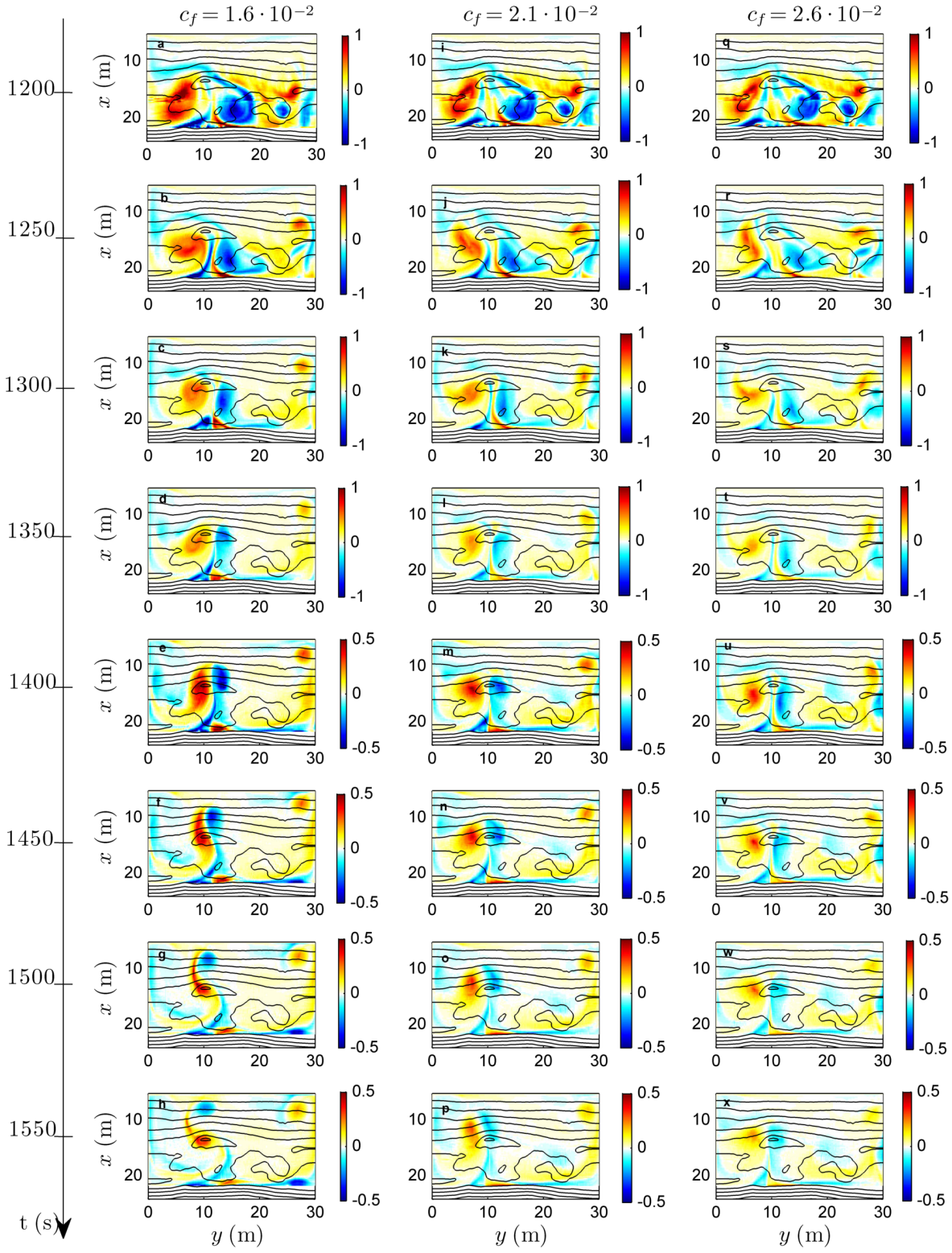

Figure 5.17 – Potential vorticity snapshots during the decay, for different friction coefficients c_f. (a-h) $c_f = 1.6 \cdot 10^{-2}$ (simulation M_1); (i-p) $c_f = 2.1 \cdot 10^{-2}$ (simulation M_2); (q-x) $c_f = 2.6 \cdot 10^{-2}$ (simulation M_3); $t = 1200$ s corresponds to the moment where the wave forcing ceases; the left vertical axis corresponds to the time of the snapshots, every 50 seconds ; The color scale changes for $t > 1350$ s to observe the evolution of the vortices, the potential vorticity unit is Hz.m^{-1}.

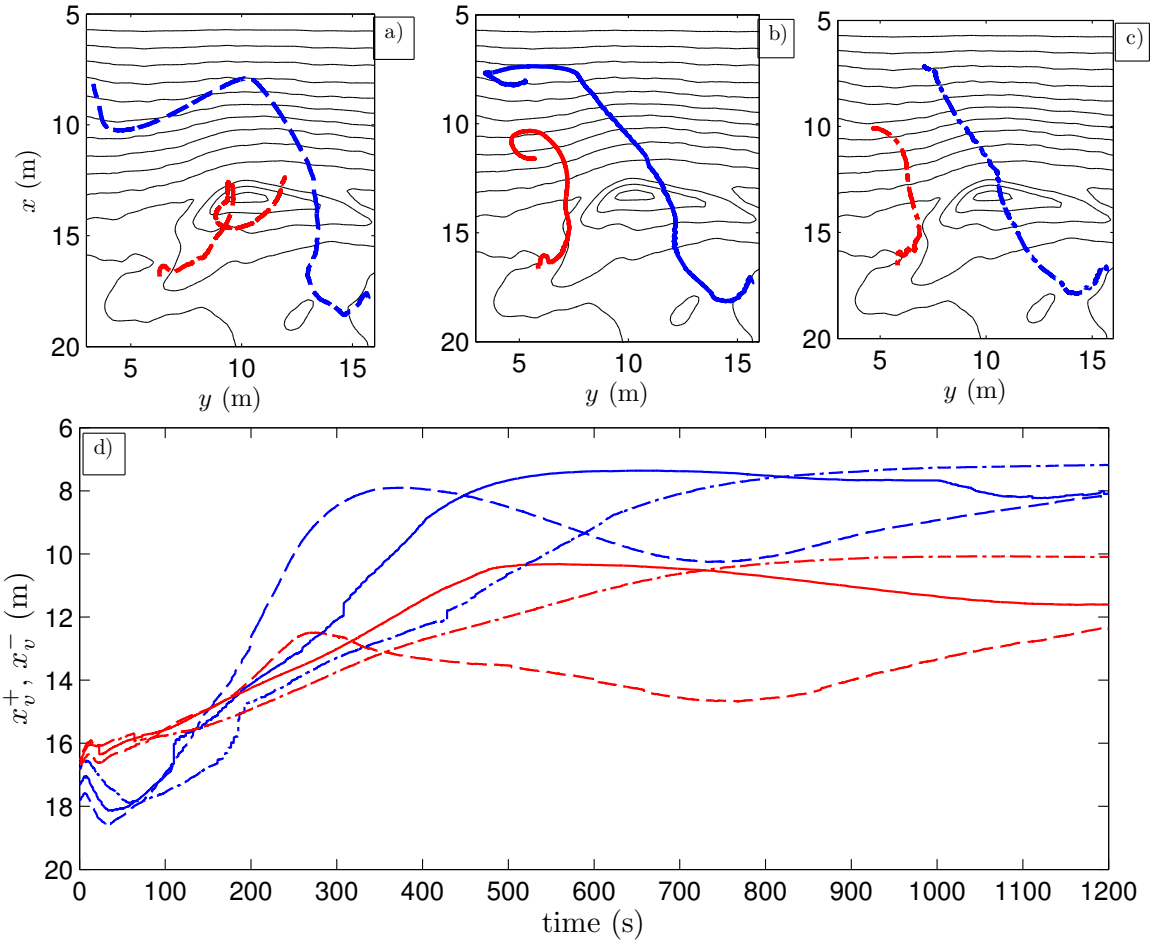

Figure 5.18 – Trajectories of the center of mass of the vortex dipole during the decay over 1200 seconds, for different friction coefficients c_f. a) $c_f = 1.6 \cdot 10^{-2}$ (simulation M_1); b) $c_f = 2.1 \cdot 10^{-2}$ (simulation M_2); c) $c_f = 2.6 \cdot 10^{-2}$ (simulation M_3); d) Evolution of the center of mass cross-shore position for the positive vortex x_v^+ (red) and negative vortex x_v^- (blue) for different frictions; $(--)$: $c_f = 1.6 \cdot 10^{-2}$ (simulation M_1); $(-)$: $c_f = 2.1 \cdot 10^{-2}$ (simulation M_2); $(- \cdot -)$: $c_f = 2.6 \cdot 10^{-2}$ (simulation M_3).

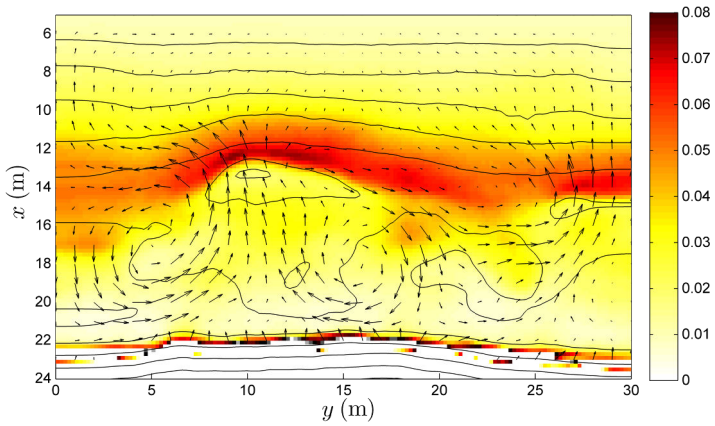

Figure 5.19 – Estimation of the Stokes Drift for a monochromatic wave forcing (simulation M_2). The arrows represent the averaged circulation over the simulation, the lines the isocontour of the bathymetry.

center of mass is influenced by the friction, as the friction slows them and reduce their strength. For $c_f = 1.6 \cdot 10^{-2}$ (a), we observe that the positive vortex (red) is trapped for some time in the trough or the rip neck and as a result the negative vortex (blue) starts moving around this position. When the negative vortex is far enough, the dipole separates and each vortex starts moving freely.

For $c_f = 2.1 \cdot 10^{-2}$ (b) and $c_f = 2.6 \cdot 10^{-2}$ (c), we observe that the vortices start moving closer, and then the mutual advection start to drive them seaward. For these two cases, the vortices are advected toward $y = 0$, as the positive vortex (red) is stronger than the negative one (blue), the negative vortex is slowly rotating around the red one.

If we look at the evolution of the cross-shore position of the vortices, we also observe the influence of the friction on the displacement of the vortices. From these positions, we can estimate an order of magnitude of the vortices displacement velocity, between 1 cm/s and 4 cm/s. These velocities are of the order of magnitude of the Stokes drift (Figure 5.19) indicating that the seaward motion of the self-advected vortices is countered by the Stokes drift who traps them between the shoreline and the breaking zone. We observe that the Stokes drift produces high velocities in the breaking zone of approximately 7 cm/s, preventing the vortices to move seaward.

5.5.4 Influence of period

The enstrophy present in the system also depends on the period of the wave. To observe this dependence, we use monochromatic simulations with the same significant

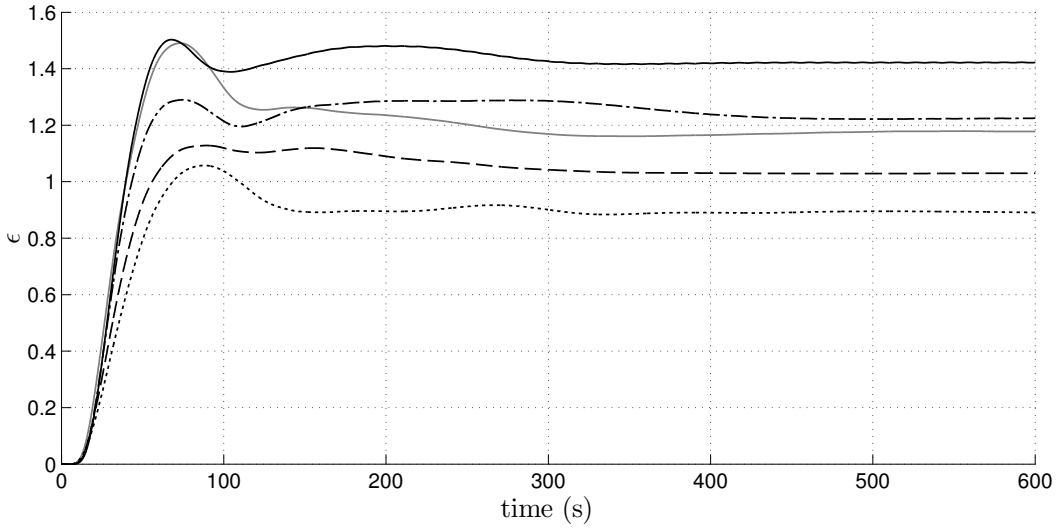

Figure 5.20 – Time evolution of enstrophy for a uniform monochromatic wave forcing, with different wave periods. $(\cdots)$: $T = 2.5$ s (simulation M_7); $(--)$: $T = 3$ s (simulation M_4); $(-)$: $T = 3.5$ s (simulation M_2); $(- \cdot -)$: $T = 4$ s (simulation M_8); $(-)$: $T = 4.5$ s (simulation M_5).

wave height $H_{m_0} = 0.18$ m and periods ranging from $T = 2.5$ s to 4.5 s. The time evolution of enstrophy indicates that the spin-up is similar for all the simulations, and that a quasi-equilibrium state is reached in all cases, after approximately 400 seconds.

If the value of the enstrophy at the equilibrium increases with the period, for the spin-up, we observe that for the wave forcing with $T = 3.5$ s, the maximum value reached during the spin-up is higher than the one for the $T = 4$ s simulation and similar to the $T = 4.5$ s simulation (simulations M_8 and M_5 respectively). This is probably caused by the influence of the incident and reflected wave field. By using a radon transform [Almar *et al.*, 2013] to separate these wave fields (Figure 5.21) we see that the reflected wave field has an influence on the local wave height for longer periods, as it creates patches for the wave height and the wave breaking index, which can increase the vorticity generation locally. By looking now at vorticity time-stacks at $y = 7$ m (5.22), near the positive vortex center, we also observe that the vorticity generated by each passing increases with the period. The boundaries of the vortex in this cross-shore profiles are quite steady. The reason for the increase of enstrophy in the system with longer wave periods, is due to the increase in the vorticity production term (Figure 5.23). An increase in the wave period induces an increase in the dissipation, which in turn generates higher vorticity.

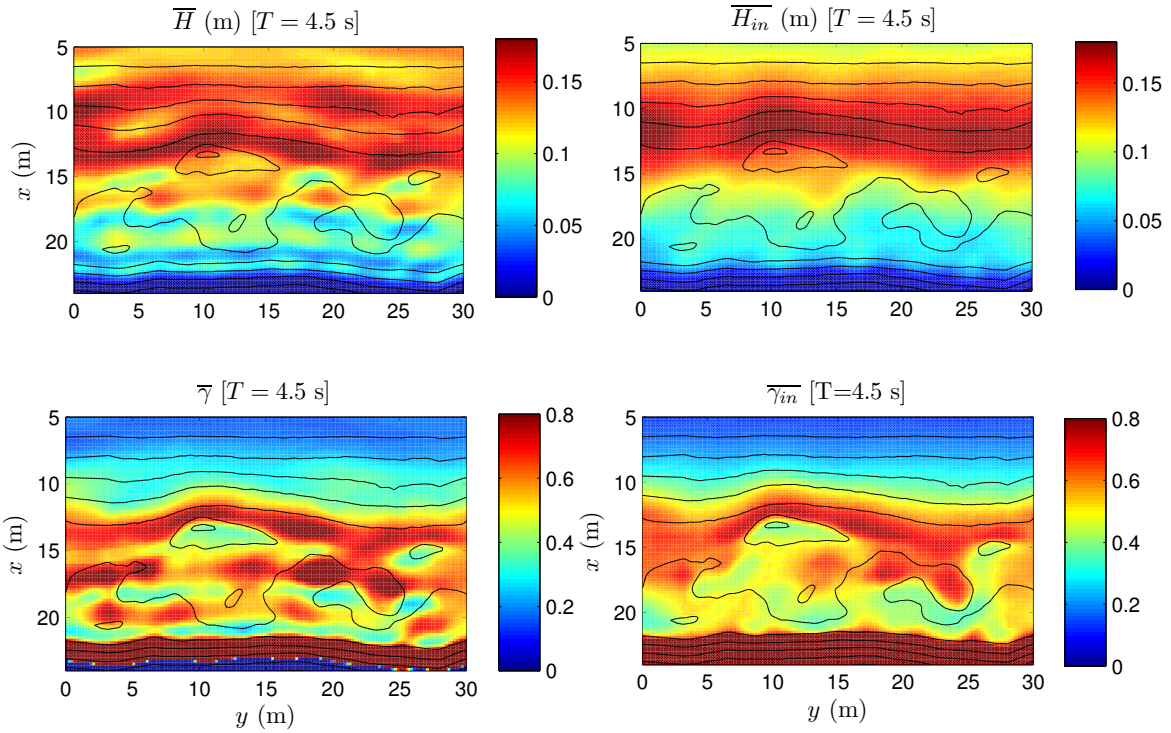

Figure 5.21 – Estimation of the averaged wave height $\bar{H}$ and the averaged wave breaking index $\bar{\gamma}$ for a monochromatic wave forcing of period $T = 4.5$ s (simulation M_5). Left panels: Total wave field; Right panel: incident wave field, separated using the radon transform

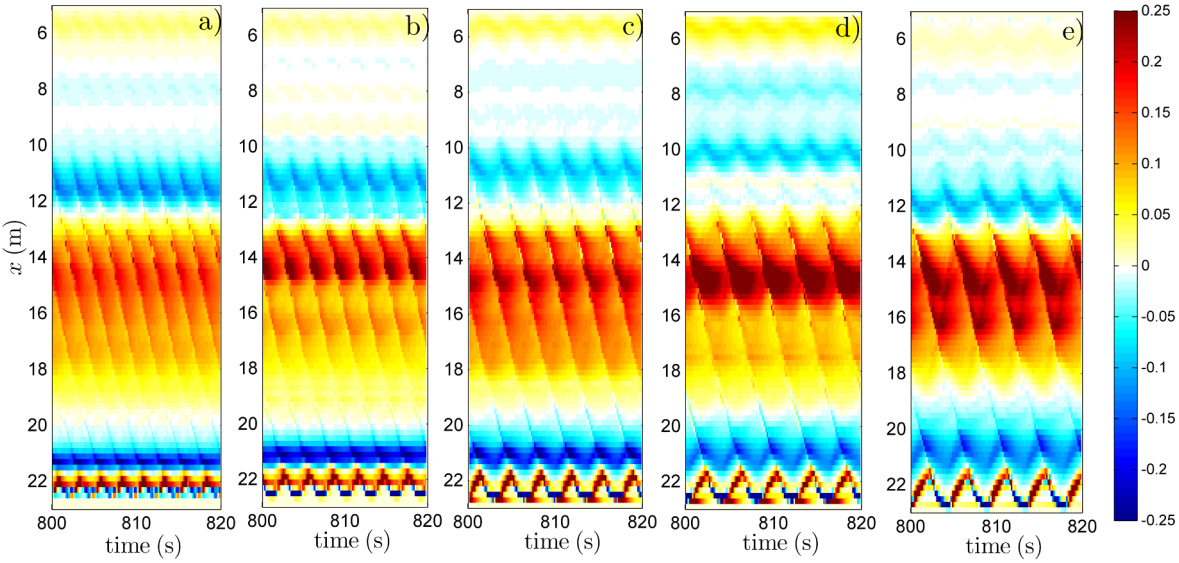

Figure 5.22 – Vorticity time-stack of a cross-shore profile at $y = 7$ m for a monochromatic wave forcing, with different wave periods. a) $T = 2.5$ s (simulation M_7); b) $T = 3$ s (simulation M_4); c) $T = 3.5$ s (simulation M_2); d) $T = 4$ s (simulation M_8); e) $T = 4.5$ s (simulation M_5);

5.5.5 Scaling law of the mean vorticity

Concerning the mean vorticity on the nearshore zone, averaged in space and over a long period of time, Bowen [1969] suggested an equilibrium between the production and the dissipation due to the friction. If we admit that the inverse-energy non-linear cascade is dominant in the equilibrium, as noted by Chavanis et Sommeria [2002], we can assume that the mean vorticity is the result of the equilibrium between the production and the advection by the mean currents.

In equation 5.26, this equilibrium writes:

$$\mathbf{u} \cdot \nabla \left(\frac{q}{h} \right) \sim \frac{1}{h} \nabla \times (D\mathbf{e}_k) \cdot \mathbf{e}_z \tag{5.64}$$

we now suppose that the orders of magnitude for the variables are defined as:

$$q \sim Q \qquad \mathbf{u} \sim U_0 \qquad \frac{\partial}{\partial x} \sim \frac{\partial}{\partial y} \sim \frac{1}{L_y} \qquad h \sim h_0 \tag{5.65}$$

where L_y is the length scale of the energy deficit which in the experiment is $L_y \sim 5$ m, and h_0 is the characteristic the water depth near the breaking point taken here as $h_0 \sim 0.2$ m. The dissipative force is estimated using the hydraulic jump analogy defined in equation 5.29. The gradients of the production term are mainly alongshore

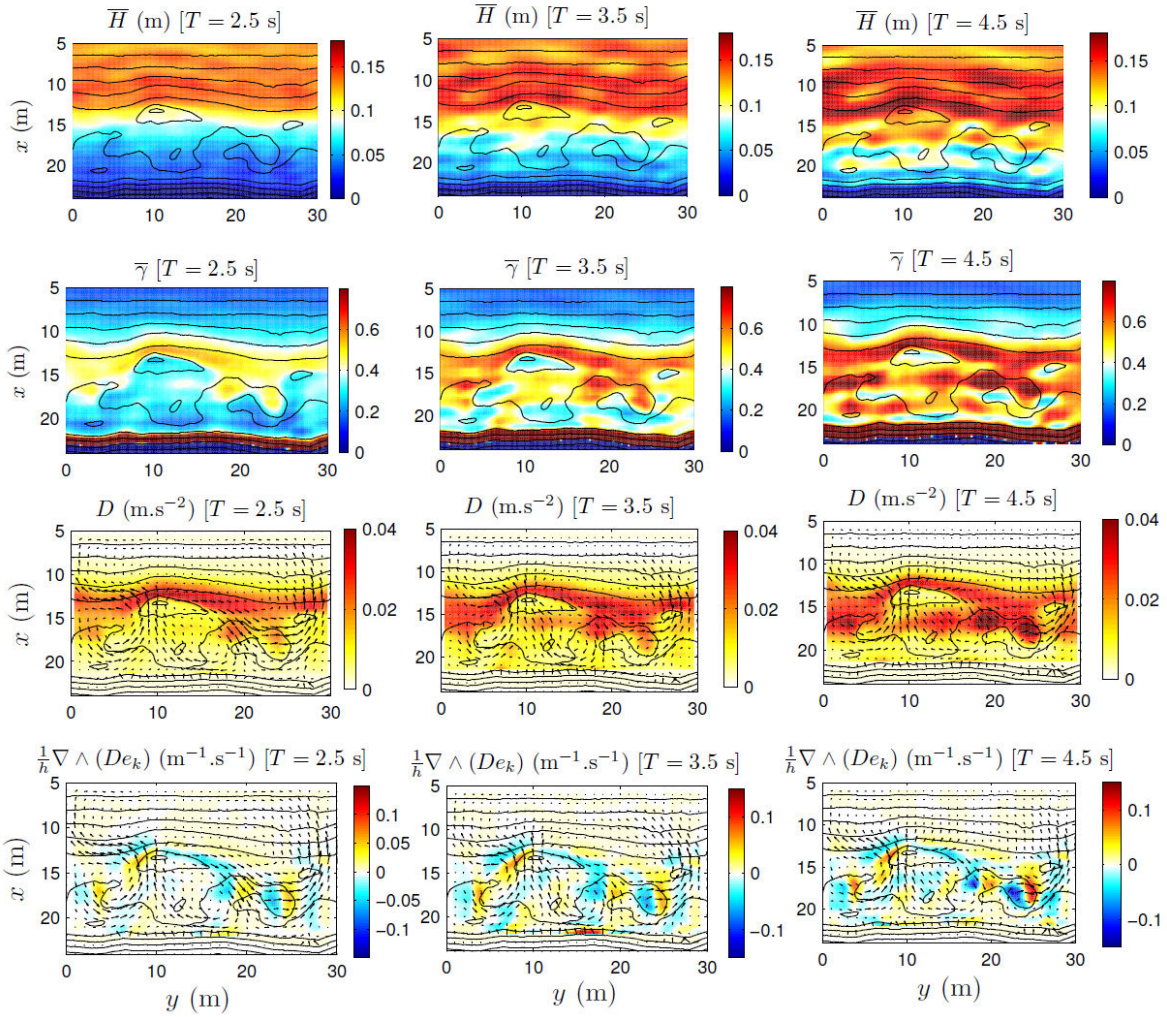

Figure 5.23 – Estimation of the averaged wave height $\bar{H}$, the averaged wave breaking index $\bar{\gamma}$, the dissipative force D and the vorticity production term, with monochromatic wave forcing with different periods. Left panels: T=2.5 s (simulation M_4); Middle panels: T=3.5 s (simulation M_2); Right panels: T=4.5 s (simulation M_5).

and therefore associated to either the energy deficit length scale or the bathymetry alongshore gradients as shown in the previous analysis. The advection term is associated to gradients in the potential vorticity which are on the scale of the vortex radius R.

We then obtain the following order of magnitude relation:

$$U_0 \frac{1}{R} \frac{Q}{h_0} \sim \frac{1}{h_0 L_y} \frac{g}{4cT} \frac{H^3}{h_0^2} \tag{5.66}$$

If we suppose that the velocity magnitude is related to the vortices and that these are of the Rankine type, the velocity increases with vortex radius as $U_1(r) \approx \frac{r}{R} U_0$, with U_1 the velocity in the vortex, r the distance from the vortex center, R the vortex radius. The order of magnitude for the vorticity Q is then

$$Q \sim \frac{1}{r} \frac{\partial (r U_1)}{\partial r} \sim \frac{U_0}{R} \tag{5.67}$$

The relationship 5.66 the becomes:

$$Q^2 \sim \frac{g h_0}{4cTL_y} \gamma^3 \tag{5.68}$$

where $\gamma = H/h_0$ is the wave breaking index. By integrating in the surf zone represented by the area S and time-averaging we obtain an equivalence for the mean enstrophy:

$$< \epsilon > \sim \frac{g h_0}{4cTL_y} \int_S < \gamma >^3 \equiv \Gamma_r \tag{5.69}$$

Using the scaling law between the vorticity generation and the vorticity advection, we observe that for Γ_r there is a linear relationship with the enstrophy, indicating the quasi-equilibrium between the vorticity generation and the vorticity advection.

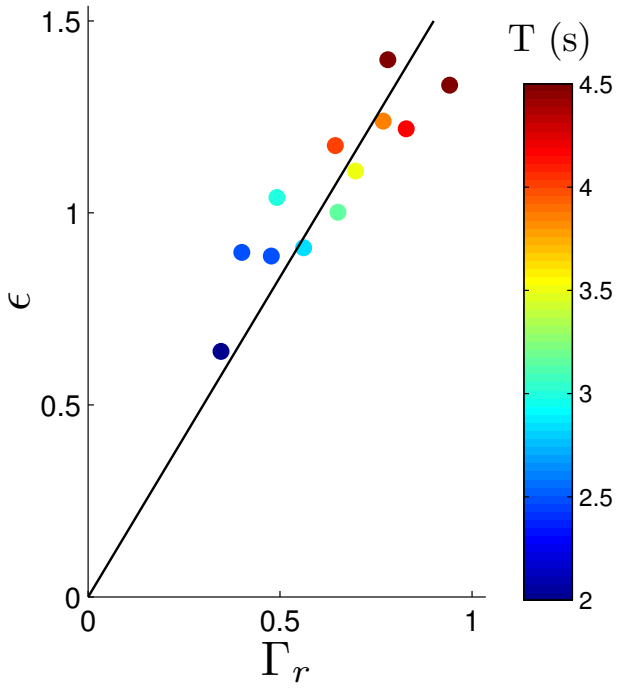

Figure 5.24 – Scaling law of the mean enstrophy $< \epsilon >$ versus Γ_r $(\cdot)$ using simulations with a monochromatic wave forcing and different periods. The line represents the linear relationship. The colours represent the period of the monochromatic wave forcing.

5.6 Bichromatic wave forcing

5.6.1 Vorticity

Using the bichromatic simulations we want to observe the influence of the wave grouping on the evolution of vorticity in the nearshore zone. The bichromatic wave forcing allows to observe the spin and decay of the vorticity for each wave group, and to observe the evolution of vorticity for wave groups with different wave group periods.

To that end, we perform simulations with the same significant wave height $H_{m_0} = 0.18$ m and same wave period $T = 3.5$ s, but with a different wave grouping ranging from $T_g = 35$ s, with 10 wave periods between two nodes (simulation B_1), to $T_g = 280$ s with 80 wave periods between two nodes (simulation B_8). We observe that the averaged circulation and potential vorticity are similar for the bichromatic simulations, allowing to compare the variations forced by the wave grouping. The two vortices are located in the same areas and the point where the rip velocity is estimated is located within the rip channel for all the simulations.

The averaged quantities being similar, we can compare the different simulations. We first look at the evolution of the enstrophy in the system, in Figure 5.26. The wave envelope at $x = 5$ m shows the wave groups for the monochromatic case, and the different bichromatic cases. The main difference apart from the wave grouping is that the monochromatic wave amplitude is of 0.0636 m, whereas the maximum amplitude in the bichromatic case is of 0.09 m, to obtain the same significant wave height H_{m_0} for all the simulations considered. Concerning the enstrophy, in the monochromatic case the spin-up has already been commented in Figure 5.15, with an increase up to $t = 70$ s, then a decrease to the quasi equilibrium value, at $t = 200$ s. The bichromatic wave forcing shows a similar enstrophy gradient in the spin-up, with a time-lag between the different cases, due to the fact that the greater the wave group period, the longer the time to attain the sufficient wave amplitude to break and generate vorticity. After that, all the bichromatic case reach an oscillatory state, where the modulation in enstrophy is directly related to the modulation in the wave group.

For the shorter wave group period $T_g = 35$ s (simulation B_1), the enstrophy reaches an oscillatory state lower than in the monochromatic case (simulation M_2). This limit could be related to the spin-up time of the monochromatic case, around 70 s, and if the wave group period is lower than this limit, then the circulation does not oscillate around the equilibrium value of the monochromatic case. For the other bichromatic cases, the oscillatory phase in enstrophy is modulated around the equilibrium enstrophy value of the monochromatic case. We also note that the longer the wave group period,

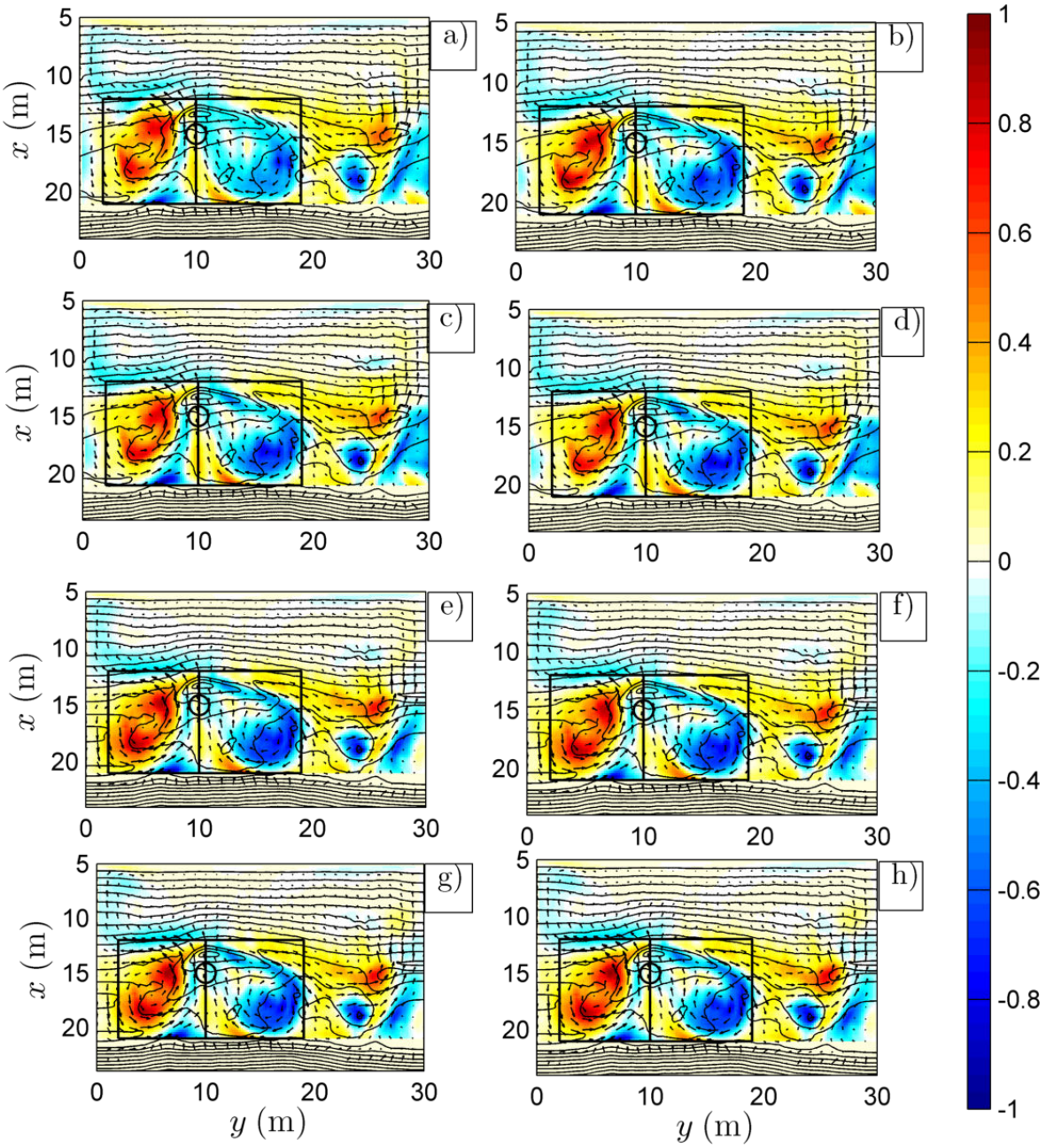

Figure 5.25 – Averaged Potential vorticity field and circulation over one to several wave group periods, depending on the simulation for a bichromatic wave forcing. The black lines represent the isocontours of the bathymetry, the arrows the averaged circulation over one group period T_g. The boxes represent the areas where the center of mass of the vortices is searched. The circle represent the position of the point where u_{rip} and v_{rip} are estimated. a) $T_g = 35$ s (simulation B_1); b) $T_g = 70$ s (simulation B_2); c) $T_g = 105$ s (simulation B_3); d) $T_g = 140$ s (simulation B_4); e) $T_g = 175$ s (simulation B_5); f) $T_g = 210$ s (simulation B_6); g) $T_g = 245$ s (simulation B_7); h) $T_g = 280$ s (simulation B_8).

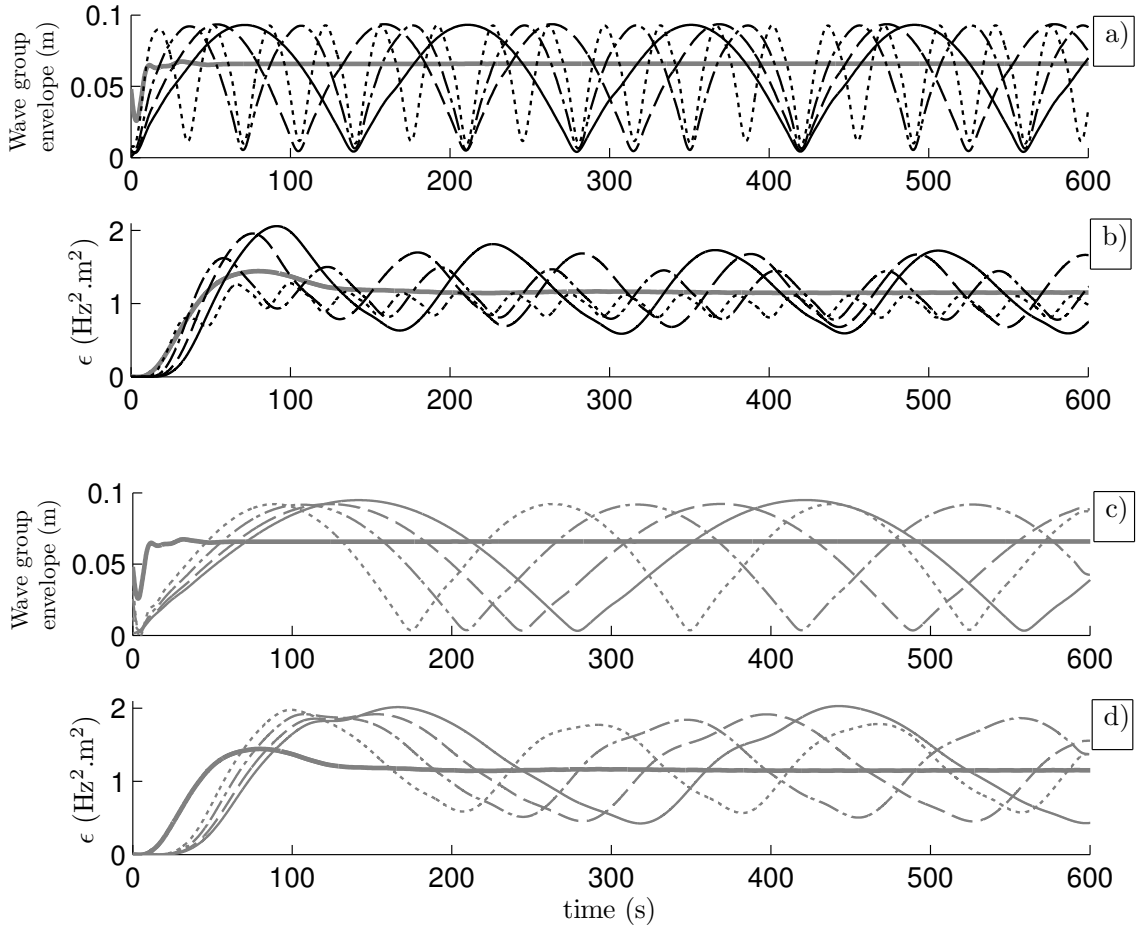

Figure 5.26 – a) and c) Time evolution of the wave group envelope at $x = 5$ m for the bichromatic simulations, only the upper part of the wave envelope is shown, for clarity purpose. ; b) and d) low-pass filtered enstrophy for the corresponding simulations. (—): monochromatic forcing, $T_0 = 3.5$ s (simulation M_2). $(\cdots)$: $T_g = 35$ s (simulation B_1); $(- \cdot -)$: $T_g = 70$ s (simulation B_2); $(--)$: $T_g = 105$ s (simulation B_3); $(-)$: $T_g = 140$ s (simulation B_4). $(\cdots)$: $T_g = 175$ s (simulation B_5); $(- \cdot -)$: $T_g = 210$ s (simulation B_6); $(--)$: $T_g = 245$ s (simulation B_7); $(-)$: $T_g = 280$ s (simulation B_8).

the higher the enstrophy maximum during a group period, however the enstrophy is modulated by the wave group and oscillates around the same mean value which is the equilibrium enstrophy of the equivalent monochromatic wave.

If we focus now on the bichromatic case with a longer wave group period $T_g = 140$ s, we observe a slight asymmetry in the enstrophy modulation around the equilibrium value. Looking at the modulation between two trough $t = 450$ s and $t = 590$ s, the maximum enstrophy is reached at $t = 505$ s, which means that the increasing phase lasts 55 s, and the decreasing phase lasts 85 s. This is due to the different mechanisms involved in the vorticity generation and the vorticity decay. In the case of the vorticity generation, as the wave amplitude grows, the vorticity generated by wave breaking interacts with the vorticity field already present, with a positive feedback that increases further the vorticity. On the contrary, when the wave amplitude is decreasing, the feedback decreases too, and the dissipation by friction becomes strong. As evidenced in the previous section the spin-up is more rapid while the enstrophy decrease monitored by friction has much larger time scales.

For longer wave group periods ($T_g > 175$ s, simulations $B5 - B8$), we observe that the enstrophy in the oscillatory state present three phases. At first when the wave amplitude start increasing, the enstrophy start increasing with the same growth rate for these 4 simulations for approximately the first 50 seconds of the wave group. Then the enstrophy keeps increasing, but with a lower growth rate. Finally when the wave amplitude in the group start decreasing, the enstrophy decreases too with a constant rate, similar in the 4 simulations.

This indicates that the circulation in the nearshore zone reaches a quasi-equilibrium after some time, related to the spin-up time, when the enstrophy reaches a value of approximately 1.5 $\mathrm{Hz}^2.\mathrm{m}^2$.

The vorticity time-stack for different wave group periods are plotted in Figures 5.27 and 5.28. For the bichromatic wave forcing with wave group period $T_g = 35$ s (simulation B_1), we observe that the cross-shore position of the vortex is modulated by the wave group. When the wave amplitude is low the vortex is found in the band 11 m $< y <$ 17 m and when the wave amplitude increase, the vortex position changes abruptly, passing to the band 14 m $< y <$ 18 m. This abrupt change is due to the fact the waves with the lower amplitude of the group do not break, and do not generate significant vorticity, to influence the vortex. The vorticity generation in the vortex center also increases with the wave of higher amplitude.

For the bichromatic with a wave group period $T_g = 70$ s, the behaviour is similar, the vortex moving slowly seaward when the wave amplitude decreases, and going shoreward when the wave amplitude increases and the wave start breaking again. The vorticity

evolution at $x = 15$ m, $y = 7$ m shows that the evolution is asymmetric, when the wave amplitude increases the vorticity increases slowly for 45 seconds and when the wave amplitude start decreasing, the vorticity decreases to reach its minimum in only 15 seconds. This caused by the different terms that are preponderant in the increasing phase it is the vorticity generation due to dissipation by wave breaking and the vorticity advection, and in the decreasing phase it is the dissipation by friction that becomes important.

We also notice that when the wave amplitude decreases, negative vorticity is generated at the off-shore boundary. When the wave forcing increases, the vortices are stronger and the shear between the two vortices in the rip channel increases too. This shear advects vorticity from the negative vortex toward the rip neck, and is later found in the seaward boundary of the positive vortex.

For the other bichromatic wave forcing with wave period ranging from $T_g = 105$ s to $T_g = 280$ s (simulations B_3-B_8)the evolution is similar hence we can explain the dynamics one time for all these simulations. At first when the wave amplitude starts increasing the vorticity is not affected by the waves due to the low amplitude and we observe that the vortex is moving shoreward. When the wave amplitude is high enough to generate vorticity by dissipation due to wave breaking, the vortex starts moving seaward, with high vorticity in the center of the vortex. After approximately 70 seconds, the vorticity starts decreasing, even though the wave amplitude keeps increasing. This behaviour is similar to the one observed for the spin-up in the monochromatic simulations and lasts for the same period of 70 seconds. After this spin-up time, the vorticity decreases rapidly to a value oscillating near 0.2 s^{-1} and when it reaches this value, the vorticity keeps increasing, but a slower pace. With the vorticity decrease is also associated an expansion of the vortex from the band 12 m $< y <$ 16 m to the band 12 m $< y <$ 18 m. When the wave amplitude starts decreasing the vorticity at first does not decrease, as the wave amplitude is still high and generates enough vorticity to remain in quasi-equilibrium. When the wave amplitude is low enough, the vorticity starts to decrease and the vortex start expanding.

5.6.2 Evolution of the circulation cells

The evolution of the center of mass averaged over one wave period (Figure 5.29) are different for the JONSWAP, the monochromatic and the bichromatic simulations. For the JONSWAP wave forcing (simulation J_0) the two vortices center move constantly to adapt to the wave forcing, spreading toward a center position at $x = 16$ m, $y = 7$ m for the positive vortex (red) and $x = 16.5$ m, $y = 15.5$ m for the negative vortex

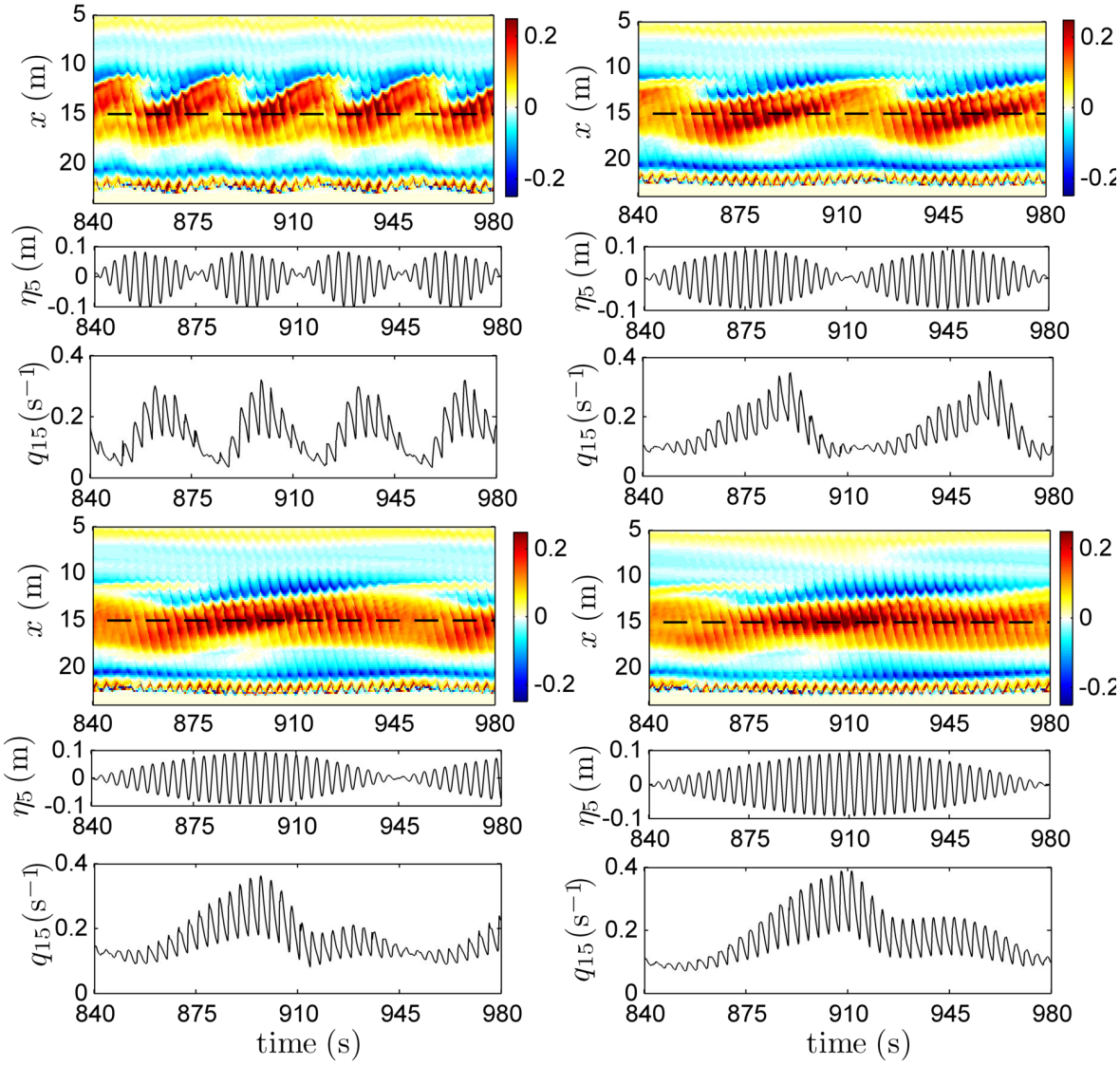

Figure 5.27 – Cross-shore vorticity time stack at $y = 7$ m, corresponding free surface water height time series at $x = 5$ m (η_5) and vorticity time-series at $x = 15$ m, $y = 7$ m (q_{15}) corresponding to the black dashed line in the vorticity time-stack, for a bichromatic wave forcing. Upper left panels: $T_g = 35$ s (simulation B_1). Upper right panels: $T_g = 70$ s (simulation B_2). Lower left panels: $T_g = 105$ s (simulation B_3). Lower right panels: $T_g = 140$ s (simulation B_4).

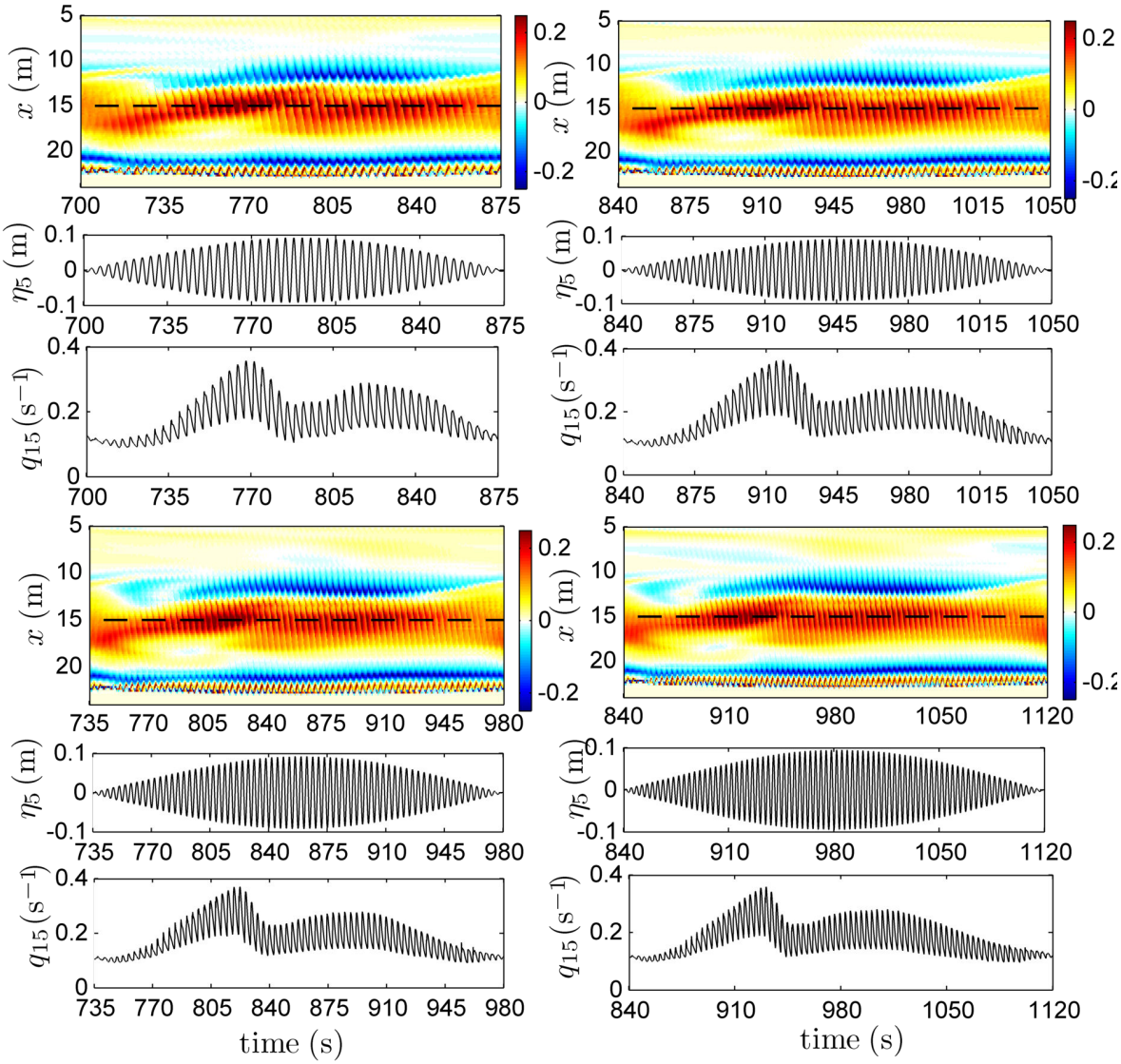

Figure 5.28 – Cross-shore vorticity time stack at $y = 7$ m, corresponding free surface water height time series at $x = 5$ m (η_5) and vorticity time-series at $x = 15$ m, $y = 7$ m (q_{15}) corresponding to the black dashed line in the vorticity time-stack, for a bichromatic wave forcing. Upper left panels: $T_g = 175$ s (simulation B_5). Upper right panels: $T_g = 210$ s (simulation B_6). Lower left panels: $T_g = 245$ s (simulation B_7). Lower right panels: $T_g = 280$ s (simulation B_8).

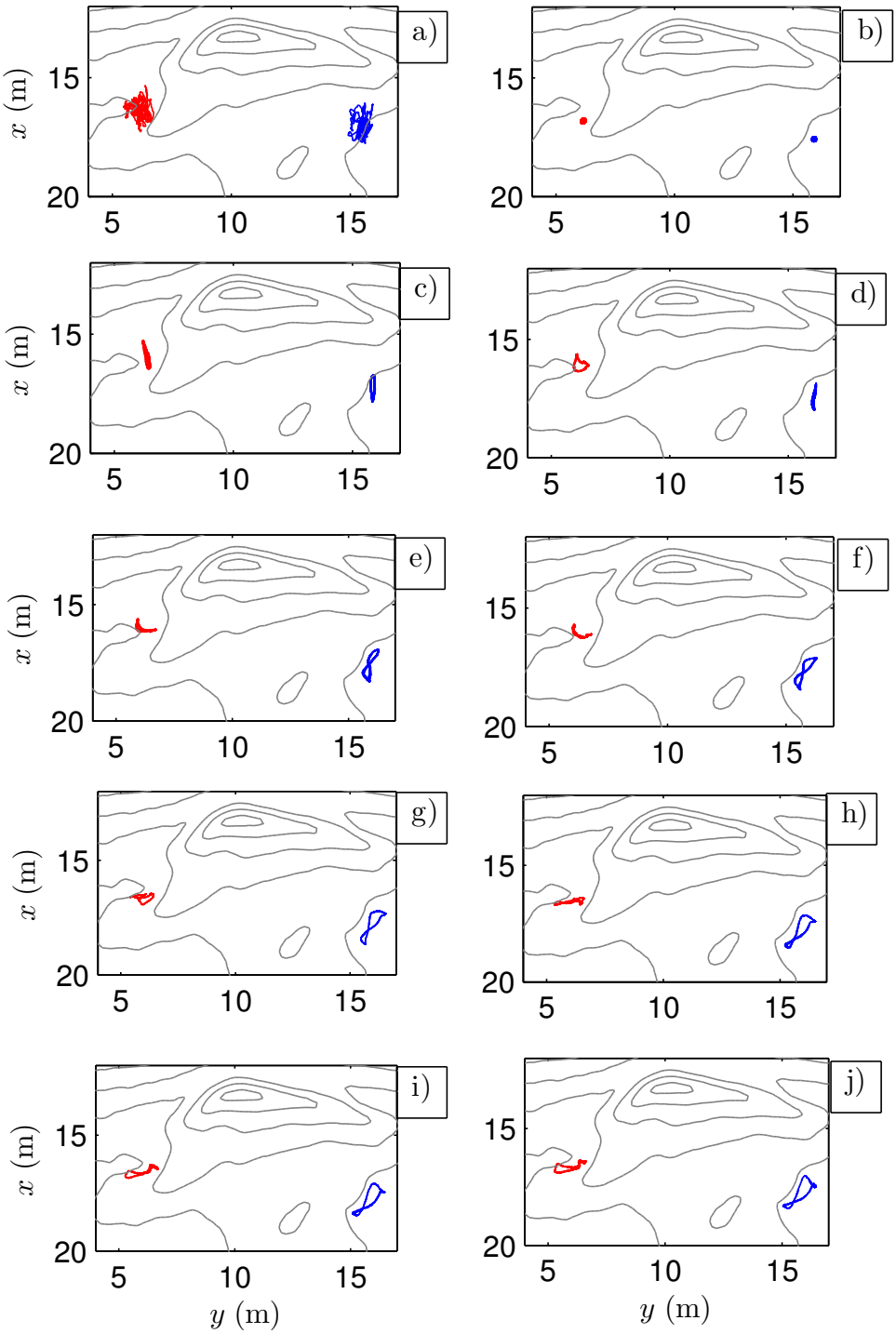

Figure 5.29 – Trajectories for the averaged center of mass over one period of the positive vortex $[\overline{x_v^+}, \overline{y_v^+}]$ (red) and negative vortex $[\overline{x_v^-}, \overline{y_v^-}]$ (blue). a) JONSWAP wave forcing (simulation J_0) b) monochromatic wave forcing $T = 3.5$ (simulation M_2); (c-i) bichromatic wave forcing: b) $T_g = 35$ s (simulation B_1); d) $T_g = 70$ s (simulation B_2); e) $T_g = 105$ s (simulation B_3); f) $T_g = 140$ s (simulation B_4); g) $T_g = 175$ s (simulation B_5); h) $T_g = 210$ s (simulation B_6); i) $T_g = 245$ s (simulation B_7); j) $T_g = 280$ s (simulation B_8).

(blue). Their positions respect to the mean position does not change too much, as they move less than 2 meters in the cross-shore or the longshore direction. For the monochromatic wave forcing (simulation M_2) the vortices remain in the same position in a state of quasi-equilibrium.

For the bichromatic wave forcing, we observe that the vortices center start to move due to the wave grouping. For the wave group period $T_g = 35$ s (simulation B_1) the motion of the vortices is essentially cross-shore, moving by roughly 2 meters during one wave group. As shown in the previous section, for this simulation the wave group period is lower than the spin-up time, hence the vortices move freely with the wave group and the vortices do not reach a quasi-equilibrium.

As the wave group period increases, the motion of the vortices changes too. The trajectory of the positive vortex (red) changes to a longshore oscillation of approximately 2 meters, and the negative vortex (blue) trajectory moves in the cross-shore and the longshore position. For $T_g > 135$ s (simulations B_5-B_8), the trajectory of the vortices is very similar. This also shows the importance of the spin-up time, as when the wave group period is large than this spin up time, the behaviour of the vortices does not change drastically.

The evolution of the distance between the vortex centres d_v over one group period also changes with the group period. For the bichromatic wave forcing with $T_g = 35$ s (simulation B_1) the distance between the vortex centres is relatively constant, this is explained due to the cross-shore movement of the vortices, and they seem to move at the same pace seaward or shoreward. When the wave group period increases we observe that the distance between the two vortices start to evolve with the wave group period. When the wave amplitude is low, the two vortices come closer to one another, as the waves do not generate significant vorticity, the mutual advection of the vortices moves them closer. As the wave amplitude increases, the distance starts increasing as the vortices move toward their equilibrium position. When the wave amplitude decreases, at first the distance remains constant, and when the wave amplitude is low, the vorticity generated by the waves is not significant and the vortices start to move closer again. We also note that the motion of the vortex centres due to the wave forcing is slower than the motion of the vortices due to mutual advection.

The distance spectra (Figure 5.31) shows that the vortices motion is dictated by the wave group period, as for the bichromatic forcing considered, the peak in frequency is found at the wave group period, consistent with the time evolution of the vortices.

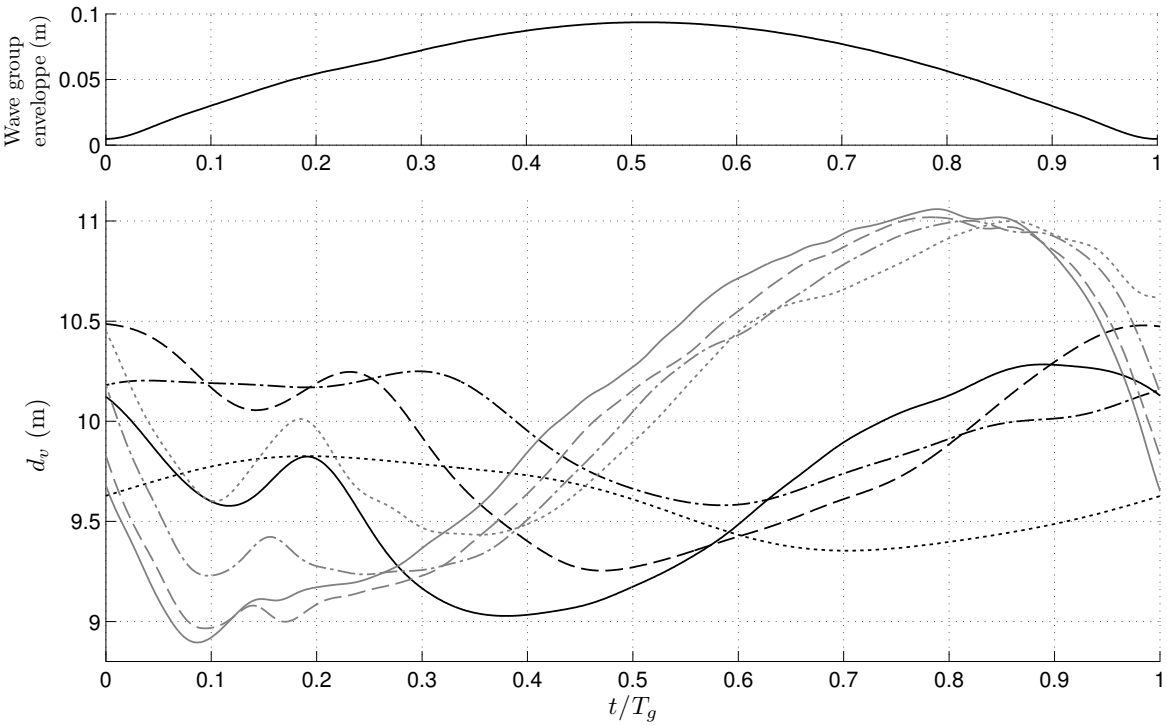

Figure 5.30 – Upper panel: Evolution of the wave group envelope over one group period T_g. Lower panel: Evolution of the distance between the center of mass of the vortices d_v over one group period. $(\cdots)$: $T_g = 35$ s (simulation B_1); $(- \cdot -)$: $T_g = 70$ s (simulation B_2); $(--)$: $T_g = 105$ s (simulation B_3); $(-)$: $T_g = 140$ s (simulation B_4); $(\cdots)$: $T_g = 175$ s (simulation B_5); $(- \cdot -)$: $T_g = 210$ s (simulation B_6); $(--)$: $T_g = 245$ s (simulation B_7); $(-)$: $T_g = 280$ s (simulation B_8).

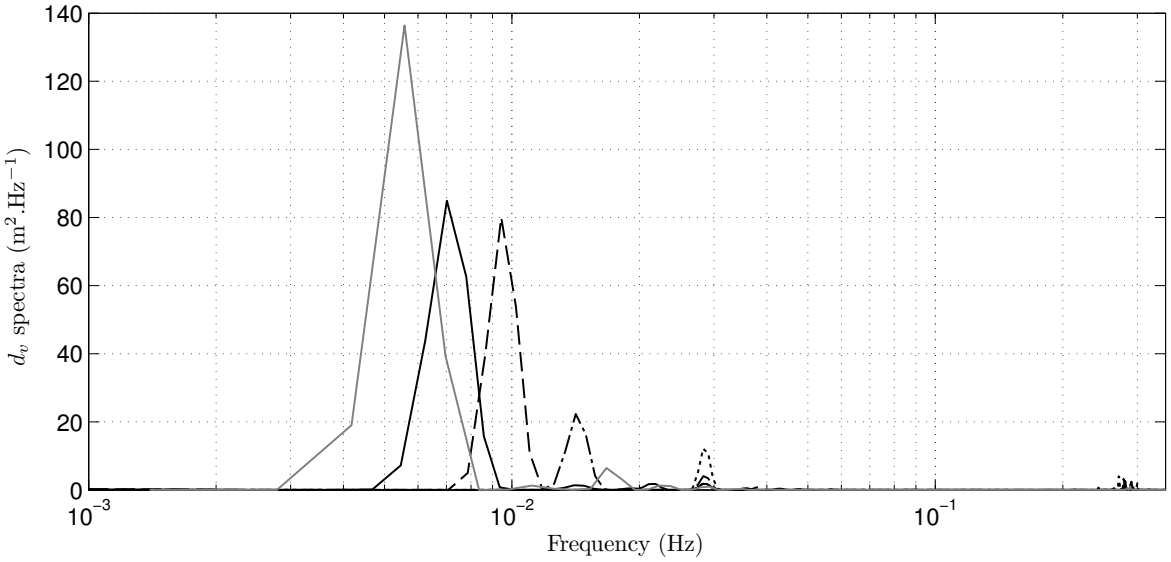

Figure 5.31 – Spectra of the distance between the center of mass of the two vortices d_v for the bichromatic cases. $(\cdots)$: $T_g = 35$ s (simulation B_1); $(- \cdot -)$: $T_g = 70$ s (simulation B_2); $(--)$: $T_g = 105$ s (simulation B_3); $(-)$: $T_g = 140$ s (simulation B_4); $(-)$: $T_g = 175$ s (simulation B_5).

5.6.3 Rip current velocities

One of the main feature of the rip current is the rip current ejection that is a great hazard for swimmers. Using the monochromatic case and the bichromatic cases, we intend to understand the evolution of the rip current velocities. To observe the variation in the rip current velocity, we focus on point at $x = 15$ m, $y = 10$ m, in the center of the rip channel.

The rip current evolution are plotted in Figure 5.32. We observe that the rip current velocity is mainly cross-shore oriented, as it ranges from -0.4 m/s to 0.3 m/s in the cross-shore direction, and from -0.05 m/s to 0 m/s in the longshore direction. If we look at the spatial distribution of the rip current velocity, the most probable case is of seaward oriented cross-shore velocity, with low longshore velocity v_{rip}. The observation of the velocities time series explains this distribution, as the cross-shore velocity u_{rip} is clearly skewed, being more time seaward oriented than shoreward oriented in a wave period. During a wave period, u_{rip} becomes positive with the passing of the wave, but 0.7 s after the wave, the velocity in the rip current becomes negative, and decreases until the next wave comes. This explain that the wave-averaged rip current velocity is $\overline{u_{rip}} \approx -0.15$ m/s.

As the longshore rip current velocity v_{rip} is one order of magnitude lower compared

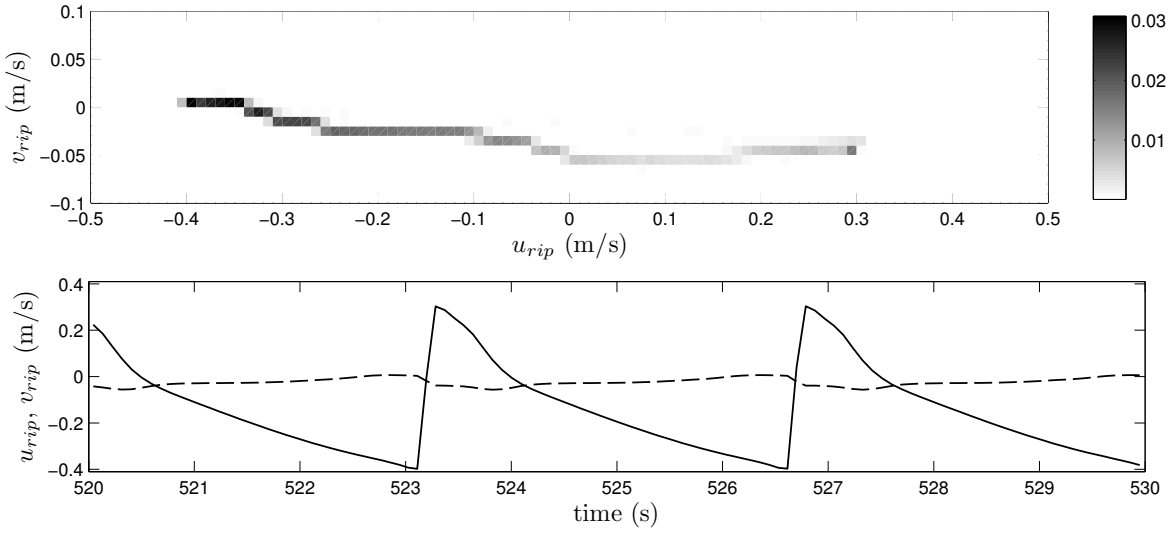

Figure 5.32 – Upper panel: spatial distribution of the cross-shore and longshore velocities u_{rip}, v_{rip} inside the rip channel, at $x = 15$ m, $y = 10$ m for a monochromatic wave forcing (simulation M_2). Lower panel: Time-series of u_{rip} $(-)$, v_{rip} $(--)$ over 10 seconds. For u_{rip}, the positive velocity is shoreward oriented, for v_{rip} the positive velocity is oriented toward $y = 30$ m.

to the cross-shore velocity u_{rip}, we focus on the cross-shore velocity u_{rip} for the bichromatic wave forcing simulations. For $T_g = 35$ s (simulation B_1) we observe a skewed cross-shore velocity profile with most of the values negative over one group period, explaining the negative averaged velocity (Figure 5.33). The cross-shore velocity averaged over one group period $< u_{rip} >_{T_g}$ is shown in Figure 5.34. The strongest averaged velocity in the rip current is obtained for the monochromatic case (a negative cross-shore velocity corresponds to a seaward oriented velocity), as with the bichromatic cases, the averaged cross-shore velocity is lower. We also note that the averaged cross-shore velocity reaches an equilibrium value, around -0.125 m/s that does not change for $T_g > 105$ s. This is another indication that for long enough wave group periods, the nearshore circulation reaches a quasi-equilibrium state.

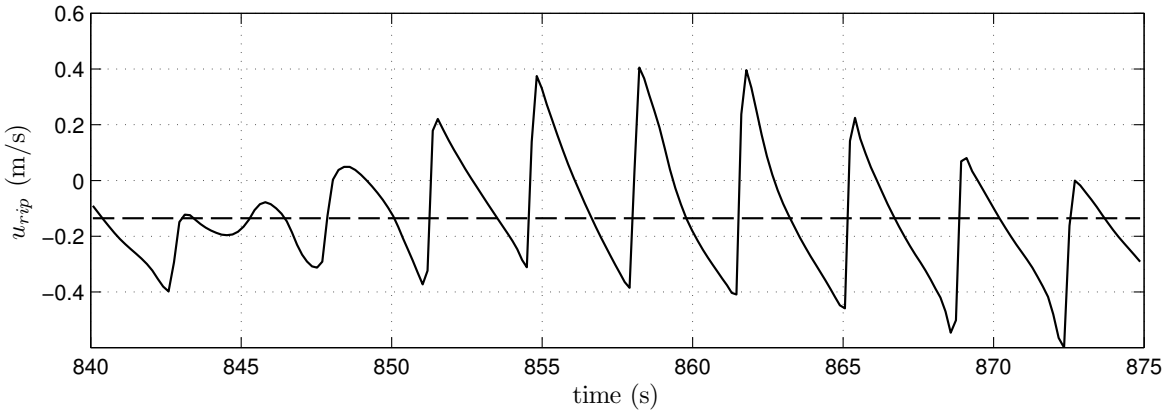

Figure 5.33 – Evolution of u_{rip} $(-)$ for the bichromatic $T_g = 35$ s case (simulation B_1), at $x = 15$ m, $y = 10$ m, in the center of the rip channel. The dashed line represents the averaged cross-shore velocity $< u_{rip} >_{T_g}$ over a group period in the same position.

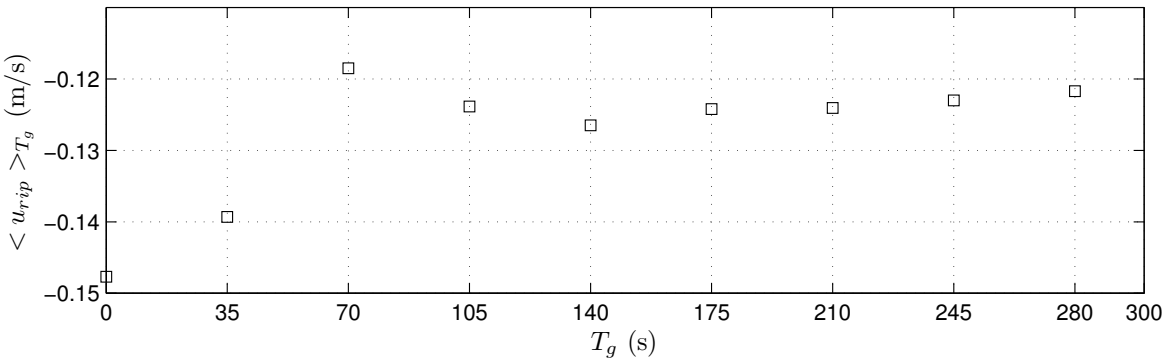

Figure 5.34 – Evolution of the cross-shore velocity averaged over a group period $< u_{rip} >_{T_g}$ with the wave group period T_g. $T_g = 0$ s corresponds to the monochromatic case.

5.7 Conclusion

Using the numerical model from [Marche *et al.*, 2007 ; Guerra *et al.*, 2014] that has been validated for the bathymetry and wave forcing considered, we studied the evolution of the circulation and vorticity in the nearshore zone. Using the potential vorticity balance equation in the case of a monochromatic wave forcing, we studied the relative importance of each term, in term of vorticity generation, displacement or dissipation.

We observe that the enstrophy, related to the vorticity present in the nearshore zone is related to the friction and the vorticity production term. The potential vorticity balance allowed to understand the mechanisms of vorticity generation and advection with a monochromatic normally incident wave forcing.

For a monochromatic wave forcing, we observed using a scaling law, that the mean vorticity results from the equilibrium between the vorticity production by wave breaking and the vorticity advection by the mean currents.

The friction also influences the vorticity in the nearshore zone, as when the friction decreases, the enstrophy increases. The friction is also responsible for the vorticity decay, and the decay rate increases with an increased friction.

For the bichromatic wave forcing, we observed that the nearshore zone reaches an equilibrium when increasing the wave group period, and that the enstrophy reaches a threshold for large wave group periods, the time to reach this threshold being similar to the spin-up of the vorticity in our case.

Chapter 6

Conclusion

6.1 Coastal bottom boundary layer

A unidimensional $k-\omega$ model has been proposed and validated on smooth and rough bottoms, against experimental and numerical results. The incorporation of the advective terms, as well as the mean pressure gradient, improves the model capacity to reproduce the variations of the bottom boundary layer under oscillatory flows on the beach.

Using the wave forcing from an experiment on a wave flume in the LEGI with a mobile bed and a bichromatic wave forcing, the $k-\omega$ numerical model reproduces the vertical distribution of non-linearities in the boundary layer.

The decrease in asymmetry and increase in skewness as we approach the still bed predicted by the model is well observed in the experiment. The numerical results show however a variation in a much smaller vertical scale than the experiment. By ad-hoc coupling of the numerical results on a fixed bed with the vertical displacements of the still bed, we observe a similar vertical diffusion, implying that this diffusion is caused by the still bed vertical motion, and not by an increased roughness height caused by the sheet-flow layer.

Using a theoretical formula [Abreu *et al.*, 2010] to estimate the relationship between the asymmetry outside the boundary layer and the skewness near the bottom over a wide range of skewed and asymmetric waves, a linear correspondence between this two quantities is found, that is similar to the experiment by [Berni *et al.*, 2013]. We can state that the process that transforms asymmetry into skewness in the coastal bottom boundary layer is a general feature of oscillatory boundary layers, that could lead to a better prediction of the sediment transport.

6.2 Vorticity and circulation in the nearshore zone

The 2D depth-averaged numerical model based on the Non Linear Shallow Water equations ([Marche *et al.*, 2007],[Guerra *et al.*, 2014]) has been validated with a wide set of data, of free surface and velocity evolution from the MODLIT experiment [Michallet *et al.*, 2010 2013]. The model is able to reproduce the energy dissipation gradients related to wave breaking, as well as the energy transfer from the JONSWAP band to the infragravity band. These energy dissipation gradients are an important proxy for vorticity generation [Brocchini *et al.* [2004]; Bonneton *et al.* [2010]]. The numerical model is also accurate in estimating the nearshore circulation and vorticity associated, compared to the lagrangian drifters ([Castelle *et al.*, 2010]). The model also reproduces some of the seiching modes that occur between the breaking point and the shoreline.

Using this numerical model and the potential vorticity balance derived from the vorticity equation of Bonneton *et al.* [2010] as a diagnosis tool, we studied the evolution of the circulation and vorticity in the nearshore zone, for a JONSWAP wave forcing, as well as monochromatic and bichromatic ones.

We observe that the enstrophy, related to the vorticity present in the nearshore zone is controlled by friction and vorticity wave generation. The potential vorticity balance allowed to understand the mechanisms of vorticity generation and advection with a monochromatic normally incident wave forcing.

For a monochromatic wave forcing, we observed that the mean vorticity results from the equilibrium between the vorticity production by wave breaking and the vorticity advection by the mean currents that can be summarized with a scaling law that predicts vorticity levels in the surf zone.

The friction also influences the vorticity in the nearshore zone, as when the friction decreases, the enstrophy increases. The friction is also responsible for the vorticity decay, and the decay rate increases with an increased friction.

For the bichromatic wave forcing, we observed that the nearshore zone reaches an equilibrium when increasing the wave group period, and that the enstrophy reaches a threshold for large wave group periods, the time to reach this threshold being similar to the spin-up of the vorticity in our case.

6.3 Perspectives

The coastal bottom boundary layer is important to obtain better predictions of the sediment transport in the surf zone. The influence of the mobile bed on this boundary layer is an important topic, and the mechanisms involved with this bed mobility is

still under investigation. Future work will be focused on the modelling of such vertical bottom motions within the $k-\omega$ framework, by incorporating the bed mobility directly into the equations.

The mechanisms of generation and decay of the potential vorticity in the nearshore zone can be further developed by coupling the numerical hydrodynamic model with Lagrangian drifters through the incorporation of the Lagrangian Particle Tracking model from Escauriaza et Sotiropoulos [2011] to the numerical model. Lagrangian drifters can be used to observe the nearshore dispersion on a rip current, for different wave forcing over an uneven bathymetry.

Bibliography

U.N. atlas of the oceans. `http://www.oceansatlas.org/`.

Abreu T., Silva P. A., Sancho F., et Temperville A. Analytical approximate wave form for asymmetric waves. *Coast. Eng.*, 57(7):656–667, 2010. ISSN 0378-3839.

Abreu T., Michallet H., Silva P. A., Sancho F., van der A D., et Ruessink B. G. Bed shear stress under skewed and asymmetric oscillatory flows. *Coast. Eng.*, 73:1–10, 2013.

Almar R., Bonneton P., Michallet H., Cienfuegos R., B.G. Ruessink, et Tissier M. On the use of the radon transform in studying nearshore wave dynamics. Dans *Proceeding of Coastal Dynamics, 24-28 June 2013, Arcachon, France*, 2013.

Arthur R. S. A note on the dynamics of rip currents. *Journal of Geophysical Research*, 67:2777–2779, 1962.

Baldock T. E., O'Hare T. J., et Huntley D. A. Long wave forcing on a barred beach. *Journal of Fluid Mechanics*, 503:321–343, 2004.

Barthélemy E. Nonlinear shallow water theories for coastal waves. *Surveys in Geophysics*, 25(3):315–337, 2004.

Berni C., Suarez L., Michallet H., et Barthélemy E. Asymmetry and skewness in the bottom boundary layer: small scale experiment and numerical model. Dans *Proc. 33rd Int. Conf. Coast. Eng.*, page waves.25, 2012.

Berni C., Barthélemy E., et Michallet H. Surf zone cross-shore boundary layer velocity asymmetry and skewness: an experimental study on a mobile bed. *Journal of Geophysical Research: Oceans*, 118(4):2188–2200, 2013.

Bonneton P. Modelling of periodic wave transformation in the inner surf zone. *Ocean Engineering*, 34:1459–1471, 2007.

Bonneton P., Bruneau N., Castelle B., et Marche F. Large-scale vorticity generation due to dissipating waves in the surf zone. *Discrete and continuous dynamical systems Series B*, 13(4):729–738, 2010.

Bonneton P., Barthelemy E., Chazel F., Ciefuegos R., Lannes D., Marche F., et Tissier M. Recent advances in serre-green naghdi modelling for wave transformation, breaking and run-up processes. *European Journal of Mechanics B/ Fluids*, 30:589–597, 2011a.

Bonneton P., Chazel F., Lannes D., Marche F., et Tissier M. A splitting approach for the fully nonlinear and weakly dispersive green-naghdi model. *Journal of Computational Physics*, 230:1479–1498, 2011b.

Boussinesq J. Théorie des ondes et des remous qui se propagent le long d'un canal rectangulaire, en communiquant au liquide contenu dans ce canal, des vitesses sensiblement pareilles de la surface au fond. *J. Math. Pures Appl. 2ieme série*, 17:55–108, 1872.

Bowen A. J. Rip currents 1. theoretical inverstigations. *Jounral of Geophysical Research*, 74(23):5467–5478, 1969.

Brocchini M., Kennedy A., Soldini L., et Mancinelli A. Topographically controlled, breaking-wave induced macro-vortices. part 1. widely separated breakwaters. *Journal of Fluid Mechanics*, 507:289–307, 2004.

Bruneau N., Bonneton P., Castelle B., et Pedreros R. Modeling rip current circulations and vorticity in a high-energy mesotidal-macrotidal envieronment. *Journal of Geophysical Research*, 116(C07026), 2011.

Buhler O. et Jacobson T. E. Wave-driven currents and vortex dynamics on barred beaches. *Journal of Fluid Mechanics*, 449:313–339, 2001.

Castelle B., Michallet H., Marieu V., Leckler , Dubardier Lambert, Berni C., Bonneton P., Barthélemy E., et Bouchette F. Laboratory experiment on rip current circulations over a moveable bed: Drifter measurements. *J. Geophys. Res.*, 115:C12008, 2010.

Chavanis P. H. et Sommeria J. Statistical mechanics of the shallow water system. *Phisical Review E*, 65(026302), 2002.

Chen Q., Dalrymple R. A., Kirby J. T., Kennedy A. B., et Haller M. C. Boussinesq modeling of a rip current system. *Journal of Geophysical Research*, 104(C9):20617–20637, 1999.

Cienfuegos R., Barthélemy E., et Bonneton P. A fourth-order compact finite volume scheme for fully nonlinear and weakly dispersive boussinesq-type equations. part ii: Boundary conditions and validation. *Int. J. Numer. Methods in Fluids*, 53:1423–1455, 2007.

Cienfuegos R., Barthélemy E., et Bonneton P. Wave-breaking model for boussinesq-type equations including roller effects in the mass conservation equation. *Journal of Waterway, Port, Coastal and Ocean Engineering*, 136:10–26, 2010.

Dalrymple R. A., MacMahan J. H., Reniers A. J. H. M., et Nelko V. Rip currents. *Annual Review of Fluid Mechanics*, 43:551–581, 2011.

Del Canto S. M. et Paskoff R. P. Carterísticas y evolución geomerfológica actual de algunas playas de chile central, entre valparaíso y san antonio (v región). *Revista de GeografÃa Norte Grande*, 10:31–45, 1983.

Dibajnia M. et Watanabe A. Sheet flow under nonlinear waves and currents. Dans *Coast. Eng.*, pages 2015–2028. ASCE, 1992.

Dohmen-Janssen C. M., Hassan W. N., et Ribberink J. S. Mobile-bed effects in oscillatory sheet flows. *Journal of Geophysical Research*, 106(C11):27103–27115, 2001.

Dohmen-Janssen C. M., Kroekenstoel D. F., Hassan W. N., et Ribberink J. S. Phase lags in oscillatory sheet flow: experiments and bed load modelling. *Coast. Eng.*, 46 (1):61–87, 2002.

Elgar S. Relationships involving third moments and bispectra of a harmonic process. *Acoustics, Speech and Signal Processing, IEEE Transactions on*, 35(12):1725–1726, 1987.

Elgar S., Gallagher E. L., et Guza R. T. Nearshore sand bar migration. *Journal of Geophysical Research*, 106(C06):11623–11627, 2001.

Escauriaza C. et Sotiropoulos S. Lagrangian model of bed-load transport in turbulent junction flows. *J. Fluid Mech*, 666:36–76, 2011.

Fowler R. E. et Dalrymple R. A. Wave group forced nearshore circulation. Dans *In Proc. 22nd Int. Conf. Coast. Eng.*, pages 729–42, 1990.

Fritz Hermann M., Petroff Catherine M., Catalan Patricio A., Cienfuegos Rodrigo, Winckler Patricio, Kalligeris Nikos, Weiss Robert, Barrientos Sergio E., Meneses Gianina, Valderas-Bermejo Carolina, Ebeling Carl, Papadopoulos Athanassios, Contreras Manuel, Almar Rafael, Carlos Dominguez Juan, et Synolakis Costas E. Field

Survey of the 27 February 2010 Chile Tsunami. *PURE AND APPLIED GEOPHYSICS*, 168(11):1989–2010, 2011.

Fuhrman D. R., Fredsoe J., et Sumer B. M. Bed slope effects on turbulent wave boundary layers: 2. comparison with skewness, asymmetry and other effects. *Journal of Geophysical Research*, 114(C03025), 2009a.

Fuhrman D. R., Fredsoe J., et Sumer B. M. Bed slope effects on turbulent wave boundary layers: 1. model validation and quantification of rough-turbulent results. *Journal of Geophysical Research*, 114(C03024), 2009b.

Fuhrman D. R., Dixen M., et Jacobsen N. G. Phisically-consistent wall boundary conditions for the k-ω turbulence model. *Journal of Hydraulic Research*, 48(6):793–800, 2010.

Fuhrman D. R., Schloer S., et Sterner J. Rans-based simulation of turbulent wave boundary layer and sheet-flow sediment transport processes. *Coastal Engineering*, 73:151–166, 2013.

Gallagher E.L., Elgar S., et Guza RT. Observations of sand bar evolution on a natural beach. *J. Geophys. Res.*, 103(C2):3203–3215, 1998.

Geiman J. D. et Kirby J. T. Unforced oscillation of rip-current vortex cells. *Journal of Physical Oceanography*, 43:477–497, 2013.

Grasso F., Michallet H., et Barthélemy E. Sediment transport associated with morphological beach changes forced by irregular asymmetric, skewed waves. *J. Geophys. Res.*, 116(C3):C03020, 2011.

Green A. E. et Naghdi P. M. A derivation of equations for wave propagation in water of variable depth. *Journal of Fluid Mechanics*, 78:237–246, 1976.

Guerra M., Cienfuegos R., Escauriaza C., Marche F., et Galaz J. Modeling rapid flood propagation over natural terrains using a well-balanced scheme. *Journal of Hydraulic Engineering*, accepted, 2014.

Guizien K., Dohmen-Janssen M., et Vittori G. 1dv bottom boundary layer modeling under combined wave and current: Turbulent separation and phase lag effects. *Journal of Geophysical Research*, 108(C1):3016, 2003.

Haller et Dalrymple R. A. Rip current instabilities. *Journal of Fluid Mechanics*, 433: 161–192, 2001.

Haller , Dalrymple R. A., et Svendsen I. A. Modeling rip currents and nearshore circulation. Dans *Ocean Wave Measurement and Analysis, Am. Soc. of Civ. Eng., Virginia Beach, VA.*, 1997.

Hasselman K., Barnett T. P., Bouws E., Carlson D. E., et Hasselmann P. Measurements of wind-wave growth and swell decay during the joint north sea wave project (jonswap). *Deutsche Hydrographische Zeitschrift*, 8(12), 1973.

Henderson S. M., Allen J. S., et Newberger P. A. Nearshore sandbar migration predicted by an eddy-diffusive boundary layer model. *J. Geophys. Res.,* 109, C05025, 109, 2004.

Holmedal L. E. et Myrhaug D. Wave-induced steady streaming, mass transport and net sediment transport in rough turbulent ocean bottom boundary layers. *Continental Shelf Research*, 29:911–926, 2009.

Holthuijsen L. H. *Waves in oceanic and coastal waters.* Cambridge University Press, 2007.

Hsu T.-J. et Hanes D. M. Effects of wave shape on sheet flow sediment transport. *J. Geophys. Res.,* 109, C05025, 2004.

Jaramillo E., Dugan J. E., Hubbard D. M., Melnick D., Manzano M., DUarte C., Campos C., et Sanchez R. Ecological implications of extreme events: Footprints of the 2010 earthquake along the chilean coast. *PLoS ONE*, 7(5):e35348, 2012.

Jensen B. L., Sumer B. M., et FredsœJ. Turbulent oscillatory boundary layers at high reynolds numbers. *J. Fluid Mech.*, 206:265–297, 1989.

Johnson D. et Pattiaratchi C. Boussinesq modelling of transient rip currents. *Coastal Engineering*, 53:419–439, 2006.

Kennedy A. B., Chen Q., Kirby J. T., et Dalrymple R. A. Boussinesq modelling of wave transformation, breaking and run-up. i: one dimension. *ASCE Journal of Waterway, Port, Coastal and Ocean Engineering*, 126(1):48–56, 2000.

King D.B. *Studies in oscillatory flow bedload sediment transport.* Thesis, Univ. of Calif., 1991.

Kobayashi N., Silva G. D., et Watson K. Wave transformation and swash oscillation on gentle and steep slopes. *Journal of Geophysical Research*, 94:951–966, 1989.

Kok J. C. Resolving the dependence on freestream values for the k-w turbulence model. *AIAA Journal*, 38(7):1292–1295, 2000.

Kolmogorov A. N. Local structure of turbulence in incompressible viscous fluid for very large reynolds number. *Doklady Akademiya Nauk SSSR*, 30:299–303, 1941.

Kolmogorov A. N. Equations of turbulent motion of an incompressible fluid. *Izvestia Academy of Sciences, USSR; Physics*, 6(1 and 2):56–58, 1942.

Kostense J.K. Measurements of surf beat and set-down beneath wave groups. *Coastal Engineering Proceedings*, 1(19), 1984.

Kraichnan R. H. et Montgomery D. Two-dimensional turbulence. *Rep. Prog. Phys*, 43: 547–620, 1980.

Kranenburg W. M., Ribberink J. S., Uittenbogaard RE, et Hulscher S. J. M. H. Net currents in the wave bottom boundary layer: on waveshape streaming and progressive wave streaming. *AIAA Journal*, 38(7):1292–1295, 2012.

Kranenburg W. M., Ribberink J. S., Schretlen J. J. L. M., et Uittenbogaard RE. Sand transport beneath waves: the role of progressive wave streaming and other free surface effects. *Journal of Geophysical Research, Earth Surface*, 118:122–139, 2013.

Launder B. E. et Spalding D. B. *Mathematical models of turbulence.* Academic Press, London, 1972.

Liang Q. et Marche F. Numerical resolution of well-balances shallow water equations with complex source terms. *Adv. Water Resour.*, 32:873–884, 2009.

Lin C. et Hwung H. H. Observation and measurement of the bottom boundary layer flow in the prebreaking zone of shoaling waves. *Ocean Engineering*, 29:1479–1502, 2002.

Long J. W. et Ozkan-Haller H. T. Low-frequency characteristics of wave-group forced vortices. *Journal of Geophysical Research*, 114(C08004), 2009.

Longuet-Higgins M. S. On the statistical distribution of the wave heights of sea waves. *Journal of Marine Research*, 11:245–266, 1952.

Longuet-Higgins M. S. et Stewart R. W. Radiation stresses in water waves: a physical discussion with applications. *Deep Sea Research*, 11:529–63, 1964.

Lubin Pierre, Vincent Stéphane, Caltagirone Jean-Paul, et Abadie Stéphane. Fully three-dimensional direct numerical simulation of a plunging breaker. *Comptes Rendus Mecanique*, 331(7):495–501, 2003.

Lubin Pierre, Vincent Stéphane, Abadie Stéphane, et Caltagirone Jean-Paul. Three-dimensional large eddy simulation of air entrainment under plunging breaking waves. *Coastal engineering*, 53(8):631–655, 2006.

MacMahan J. H., Reniers A. J. H. M., Thornton E. B., et Stanton T. P. Infragravity rip current pulsations. *Journal of Geophysical Research*, 109(C01033), 2004.

MacMahan J. H., Thornton E. B., et Reniers A. J. H. M. Rip current review. *Coastal Engineering*, 53:191–208, 2006.

MacMahan J. H., Brown J., Brown J., Thornton E. B., Reniers A. J. H. M., Stanton T. P., Henriquez M., Gallagher E., Morrison J., Austin M. J., Scott T. M., et Senechal N. Mean lagrangian flow behavior on an open coast rip-channelen beach: a new perspective. *Marine Geology*, 268:1–15, 2010.

Madsen P.A., SÃ¸rensen O.R., et SchÃ¤ffer H.A. Surf zone dynamics simulated by a boussinesq type model. part i: Model description and cross-shore motion of regular waves. *Coastal Engineering*, 32(4):255 – 287, 1997a.

Madsen P.A., SÃ¸rensen O.R., et SchÃ¤ffer H.A. Surf zone dynamics simulated by a boussinesq type model. part ii: surf beat and swash oscillations for wave groups and irregular waves. *Coastal Engineering*, 32(4):289 – 319, 1997b.

Marche F., Bonneton P., Fabrie , et Seguin . Evaluation of well-balanced bore-capturing schemes for 2d wetting and drying processes. *Int. J. Numer. Methods in Fluids*, 53: 867–894, 2007.

Martínez et Salinas . Morfodinámica y evolución reciente de playa tunquén, chile central. *Revista BiologÃa y OceanografÃa Marina*, 44:203–215, 2009.

Mei C. C. *The applied dynamics of ocean surface waves*, volume 1. World Scientific Pub Co Inc, 1989.

Michallet H., Castelle B., Bouchette F., Lambert , Berni C., Barthélemy E., Bonneton P., et Sous . Modélisation de la morphodynamique d'une plage barrée tridimensionnelle. Dans *Proc. Journée Natl. Génie Côtier - Génie Civ.*, volume 11, pages 379–386, 2010.

Michallet H., Cienfuegos R., Barthélemy E., et Grasso F. Kinematics of waves propagating and breaking on a barred beach. *European Journal of Mechanics B/Fluids*, 30:624–634, 2011.

Michallet H., Castelle B., Barthélemy E., Berni C., et Bonneton P. Physical modelling of three-dimensional intermediate beach morphodynamics. *Journal of Geophysical Research: Earth Surface*, 118:1045–1059, 2013.

Mignot E. et Cienfuegos R. On the application of a boussinesq model to river flows including shocks. *Coast. Eng.*, 56:23–31, 2009.

Nielsen P. *Coastal Bottom Boundary Layers and Sediment Transport*. World Scientific, Singapore, 1992.

Nielsen P. Sheet flow sediment transport under waves with acceleration skewness and boundary layer streaming. *Coast. Eng.*, 53:749–758, 2006.

Paskoff R. Potential implications of sea-level rise for france. *Journal of Coastal Research*, 20(2):424–434, 2004.

Patankar S. V. *Numerical Heat Transfer and Fluid Flow*. Taylor and Francis Group, 1980.

Peregrine D. H. Surf zone currents. *Theoret. Comput. Fluid Dynamics*, 10:295–309, 1998.

Reniers A.J.H.M., MacMahan J.H., Beron-Vera F. J., et Olascoaga M.J. Rip-current pulses tied to lagrangian coherent structures. *Coast. Eng.*, 53:209–222, 2006a.

Reniers A.J.H.M., MacMahan J.H., Thornton E.B., et Stanton T.P. Modelling infragravity motions on a rip-channel beach. *Coast. Eng.*, 53:209–222, 2006b.

Roelvink D., Reniers A., van Dongeren A., van Thiel de Vries J., McCall R., et Lescinski J. Modelling storm impacts on beaches, dunes and barrier islands. *Coast. Eng.*, 56: 1133–1152, 2009.

Ruessink B. G., Michallet H., Abreu T., Sancho F., et others . Observations of velocities, sand concentrations, and fluxes under velocity-asymmetric oscillatory flows. *J. Geophys. Res.*, 116(C3):C03004, 2011.

Saffman P. G. A model for inhomogeneous turbulent flow. *proceedings of the Royal Society of London. Series A, Mathematical and Physical*, 317(1530):417–433, 1970.

Sana A. et Tanaka H. Review of k-ϵ model to analyze oscillatory boundary layers. *Journal of Hydraulic Engineering*, 126(9):701–710, 2000.

Serre F. Contribution à l'étude des écoulements permanents et variables dans les canaux. *Houille Blanche*, 8:374–388, 1953.

Shaffer H. A. Infragravity waves induced by short-wave groups. *Journal of Fluid Mechanics*, 247:551–588, 1993.

Shepard F. P. Undertow, rip tide or "rip current". *Science*, 84:181–82, 1936.

Shepard F. P., Emory K.O., et La Fond E. C. Rip currents: a process of geological importance. *J. Geol.*, 49:337–69, 1941.

Shepard F.P. et Inman D. L. Nearshore circulation. Dans *Proc. of the 1st Conference on Coastal Engineering, Berkeley, CA, Council on Wave Research*, pages 50–59, 1950.

Shi F., Kirby J. T., Harris J. C., Geiman J. D., et Grilli S. T. A high-order adaptive time-stepping tvd solver for boussinesq modelling of breaking waves and coastal inundations. *Ocean modelling*, 43-44:36–51, 2012.

Sleath J. F. A. Turbulent oscillatory flow over rough beds. *J. Fluid Mech.*, 182:369–409, 1987.

Sparrow K., Pokrajac D., et van der A D. The effect of bed permeability on oscillatory boundary layer flow. Dans *Proc. 33rd Int. Conf. Coast. Eng.*, page waves.26, 2012.

Spydell M. et Feddersen F. Lagrangian drifters dispersion in the surf zone: directionnaly spread, normally incident waves. *Journal of Physical Oceanography*, 39:809–830, 2009.

Suarez L., Barthélemy E., Berni C., Chauchau J., Michallet H., et Cienfuegos R. Vertical distribution of skewness and asymmetry in a boundary layer on a mobile bed. experiment and $k - \omega$ model comparison. *La Houille Blanche, International Water Journal*, accepted, 2014.

Sumer B. M., Laursen T. S., et Fredsoe J. Wave boundary layer in a convergent tunel. *Coastal Engineering*, 20:317–342, 1993.

Suntoyo et Tanaka H. Effect of bed roughness on turbulent boundary layer and net sediment transport under asymmetric waves. *Coastal Engineering*, 56:960–969, 2009.

Symonds G, Huntley D. H., et Bowen A. J. Two-dimensional surf beat: long wave generation by a time-varying breakpoint. *Journal of geophysicial Research*, 87(C1): 492–498, 1982.

Thornton E., Dalrymple R. A., Drake T., Gallagher E., Guza R. T., Hay A., Holman R. A., Kaihatu J., Lippmann T. C., et Ozkan-Haller T. State of nearshore processes research. Technical report, Naval Postgraduate School, Monterey, 2000.

Thornton E. B. et Guza R. T. Transformation of wave height distribution. *Journal of Geophysical Research*, 88:5925–5938, 1983.

Tissier M., Bonneton P., Marche F., Chazel F., et Lannes D. A new approach to handle wave breaking in fully non-linear boussinesq models. *Coastal Engineering*, 67:54–66, 2012.

van der A D. A., O'Donoghue T., et Ribberink J. S. Measurements of sheet flow transport in acceleration-skewed oscillatory flow and comparison with practical formulations. *Coast. Eng.*, 57(3):331–342, 2010.

van der A D. A., O'Donoghue T., Davies A. G., et Ribberink J. S. experimental study of the turbulent boundary layer in acceleration-skewed oscillatory flow. *Journal of Fluid Mechanics*, 684:251–283, 2011.

van Dongeren A., Battjes J., Janssen T., Van Noorloos J., Steenhauer K., Steenbergen G., et Reniers A. Shoaling and shoreline dissipation of low-frequency waves. *Journal of Geophysical Research- Oceans*, 112(C02011), 2007.

Villagran M., Cienfuegos R., Catalan P., et Almar R. Morphological response of central chile sandy beaches to the 8.8 mw 2010 earthquake and tsunami. Dans *Proceeding of Coastal Dynamics, 24-28 June 2013, Arcachon, France*, 2013.

Vittori G. et Verzicco R. Direct simulation of transition in an oscillatory boundary layer. *J. Fluid Mech.*, 371:207–232, 1998.

Von Karman T. Mechanische Ähnlichkeit und turbulenz. *Nachrichten von der Gesellschaft der Wissenschaften zu GÃ¶ttingen, Fachgruppe 1 (Mathematik)*, 1930. (also as: "Mechanical Similitude and Turbulence", Tech. Mem. NACA, no. 611, 1931).

Wei G. et Kirby J. T. A time-dependent numerical code for extended boussinesq equations. *Journal of waterway, Port, Coastal and Ocean engineering*, 120:256–261, 1995.

Wilcox D. C. *Turbulence modeling for CFD*. DCW Industries, Inc.„ La Canada, CA, 2nd edition, 1998.

Wilcox D. C. *Turbulence modeling for CFD*. DCW Industries, Inc.„ La Canada, CA, 3rd edition, 2006.

Wilcox D. C. Formulation of the k-w turbulence model revisited. *AIAA Journal*, 46 (11):2823–2838, 2008.

Wilcox D. C. et Rubesin M. W. Progress in turbulence modeling for complex flow fields including effects of compressibility. *NASA*, TP-1517, 1980.

Yu Jie. On the instability leading to rip currents due to wave-current interaction. *Journal of Fluid Mechanics*, 549:403–428, 2006.

Yu Jie et Slinn D. N. Effects of wave current interaction on rip currents. *Journal of Geophysical Research*, 108(C3):3088, 2003.

Annexes

Appendix A

Turbulence modelling - Numerical resolution

A.1 1D version of the $k-\omega$ equations

The horizontal velocity $u(z,t)$, the turbulence kinetic energy $k(z,t)$ and the specific dissipation rate $\omega(z,t)$, are described in a 1D framework:

$$\frac{\partial u}{\partial t} = -\frac{1}{\rho}\frac{\partial p}{\partial x} + \frac{\partial}{\partial z}\left((\nu + \nu_T)\frac{\partial u}{\partial z}\right) \tag{A.1}$$

$$\frac{\partial k}{\partial t} = \nu_T \left(\frac{\partial u}{\partial z}\right)^2 - \beta^* k\omega + \frac{\partial}{\partial z}\left[\left(\nu + \sigma_k \alpha^* \frac{k}{\omega}\right)\frac{\partial k}{\partial z}\right] \tag{A.2}$$

$$\begin{cases} \dfrac{\partial \omega}{\partial t} = \dfrac{\alpha\omega}{k}\nu_t \left(\dfrac{\partial u}{\partial z}\right)^2 - \beta\omega^2 + \dfrac{\partial}{\partial z}\left[\left(\nu + \sigma_\omega \alpha^* \dfrac{k}{\omega}\right)\dfrac{\partial \omega}{\partial z}\right] \\ \text{[Wilcox, 1998 ; Guizien } \textit{et al.}\text{, 2003]} \\ \dfrac{\partial \omega}{\partial t} = \dfrac{\alpha\omega}{k}\nu_t \left(\dfrac{\partial u}{\partial z}\right)^2 - \beta\omega^2 + \dfrac{\partial}{\partial z}\left[\left(\nu + \sigma_\omega \alpha^* \dfrac{k}{\omega}\right)\dfrac{\partial \omega}{\partial z}\right] + \dfrac{\sigma_d}{\omega}\dfrac{\partial k}{\partial z}\dfrac{\partial \omega}{\partial z} \\ \text{[Wilcox, 2006]} \end{cases} \tag{A.3}$$

A.2 Numerical Resolution

A.2.1 Resolution scheme

We solve the system of equations using the implicit finite control volume method of Patankar [1980] which is described hereafter, on an exponential grid. We improve this

method by determining the turbulence kinetic energy k and the specific dissipation rate ω in the staggered grid.

Determination of the computational grid

We can choose the type of the grid, depending on the area where we want the more points

Geometric grid

to describe the geometric grid, we use the initial conditions z_0 the bottom boundary, and z_h the upper boundary, and also the number of nodes N_0

We define the grid with the equation A.4:

$$\begin{cases} (z)_1 & = z_0 \\ (z)_{j+1} & = (z)_j + z_0 R^j \quad \forall j \geq 1 \end{cases} \tag{A.4}$$

where R represent the common ratio of the geometric series, which is not known beforehand. To determine R we use the properties of a geometric series:

$$(z)_{N_0} = z_0 \sum_{i=0}^{N_0} R^i = z_h \tag{A.5}$$

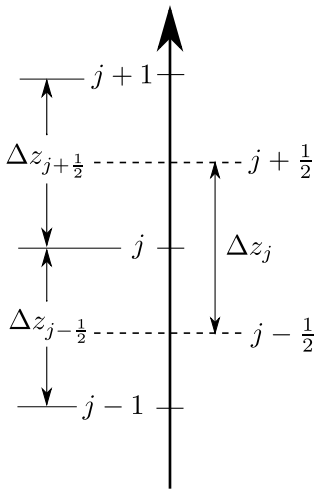

Figure A.1 – Computational grid sketch. The horizontal velocity u is determined at point j, while the turbulence kinetic energy k and the specific dissipation rate ω are determined on the midpoints $j + 1/2$ and $j - 1/2$

the midpoints are located at the center of each cell, as shown in figure A.1:

$$(z)_{j+1/2} = z_j + \frac{(z)_{j+1} - (z)_j}{2} \tag{A.6}$$

We also define two points that will be used as ghost points in the boundaries:

$$\begin{aligned} z_{-\frac{1}{2}} &= \frac{z_0}{2} \\ z_{N_0+\frac{1}{2}} &= z_h + \frac{z_0 R^{N_0-1}}{2} \end{aligned} \tag{A.7}$$

Regular grid

The regular grid is a grid where all points are evenly spaced:

$$(z)_{j+1} = \frac{j}{N}(z_h - z_0) + z_0 \tag{A.8}$$

mixed grid

the mixed grid is partly geometric at the bottom, and regular at the top. For this type of grid, and to avoid discrepancies at the frontier, the frontier is located where $\Delta z_{geom} = \Delta z_{regular}$

Geometric grid at the boundaries

the geometric grid at the boundaries is used when we need more resolution at the top and bottom boundaries. We use two geometric grid of length $(z_h - z_0)/2$.

Comparison different grid types In the figure A.2, we see the difference between the different types of grid.

We see that the regular grid has low resolution at the bottom boundary, and therefore is seldom used. From now on, unless stated otherwise, the grid will be geometric.

A.2.2 Horizontal Velocity equation

original terms

The following step is to derive the discretization equation and to integrate them over a control volume.

We integrate the equation (A.1) over a control volume centered in the point j, and over a time step Δt:

$$\int_{j-\frac{1}{2}}^{j+\frac{1}{2}} \int_t^{t+\Delta t} \frac{\partial u}{\partial t}\, dt\, dz = \int_{j-\frac{1}{2}}^{j+\frac{1}{2}} \int_t^{t+\Delta t} \left(\frac{\partial U}{\partial t} - \frac{1}{\rho}\frac{\partial \bar{P}}{\partial x} \right) dt\, dz + \int_{j-\frac{1}{2}}^{j+\frac{1}{2}} \int_t^{t+\Delta t} \frac{\partial}{\partial z}\left((\nu + \nu_t)\frac{\partial u}{\partial z} \right) dt\, dz \tag{A.9}$$

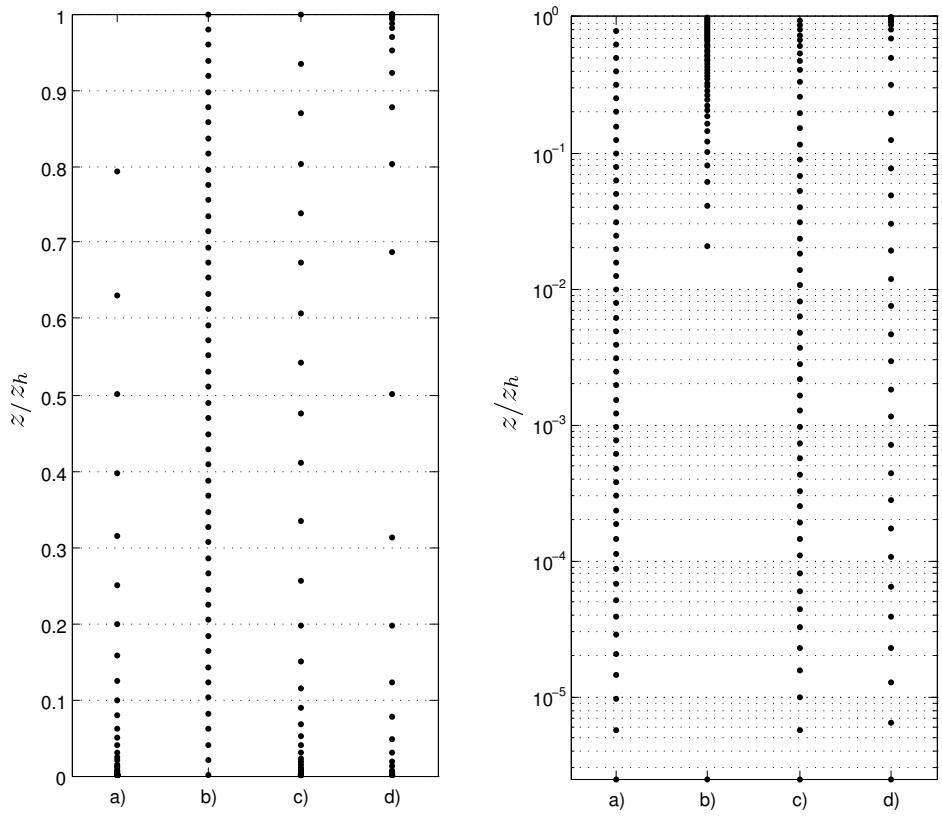

Figure A.2 – Grid point distribution. The grid span from $z_0 = 10^{-6}$ m to $z_h = 0.4$ m, with $N_0 = 50$ grid points. a) geometric grid, b) regular grid, c) mixed grid with a geometric grid between $2.5 \cdot 10^{-6} < z/z_h < 1/3$ and a regular grid between $1/3 < z/z_h < 1$, d) geometric grid at the boundaries. The left panel represents the grid in regular scale, the right panel shows the same grids on logarithmic scale.

For time integration, we will use a fully implicit method:

$$\int_t^{t+\Delta t} u_j \; dt = u_j^{t+\Delta t} \Delta t \tag{A.10}$$

For readability purpose, we will drop the superscript $t + \Delta t$, and assume that u, k and ω stand for the new values that are unknown at step $t + \Delta t$:

$$u^{t+\Delta t} \equiv u \;,\; k^{t+\Delta t} \equiv k \;,\; \omega^{t+\Delta t} \equiv \omega \tag{A.11}$$

Therefore:

$$\int_{j-\frac{1}{2}}^{j+\frac{1}{2}} \int_t^{t+\Delta t} \frac{\partial u}{\partial t} \; dt \; dz = (u_j - u_j^t) \Delta z_j \tag{A.12}$$

$$\int_{j-\frac{1}{2}}^{j+\frac{1}{2}} \int_{t}^{t+\Delta t} \left(\frac{\partial U}{\partial t} - \frac{1}{\rho} \frac{\partial \bar{P}}{\partial x} \right) \, dt \, dz = (U - U^t) \Delta z_j - \frac{1}{\rho} \frac{\partial \bar{P}}{\partial x} \Delta t \Delta z_j \tag{A.13}$$

$$\int_{j-\frac{1}{2}}^{j+\frac{1}{2}} \int_{t}^{t+\Delta t} \frac{\partial}{\partial z} \left((\nu + \nu_t) \frac{\partial u}{\partial z} \right) \, dt \, dz = \left[(\Gamma_u)_{j+\frac{1}{2}} \left(\frac{\partial u}{\partial z} \right)_{j+\frac{1}{2}} - (\Gamma_u)_{j-\frac{1}{2}} \left(\frac{\partial u}{\partial z} \right)_{j-\frac{1}{2}} \right] \Delta t \tag{A.14}$$

Where $(\Gamma_u)_j = \nu + (\nu_T)_j$. To calculate the derivatives at the points $j - \frac{1}{2}$ and $j + \frac{1}{2}$, we use the nearby points:

$$\left(\frac{\partial u}{\partial z} \right)_{j+\frac{1}{2}} = \left(\frac{u_{j+1} - u_j}{\Delta z_{j+1/2}} \right) \tag{A.15}$$

$$\left(\frac{\partial u}{\partial z} \right)_{j-\frac{1}{2}} = \left(\frac{u_j - u_{j-1}}{\Delta z_{j-1/2}} \right) \tag{A.16}$$

we then obtain:

$$\begin{aligned} &\left[(\Gamma_u)_{j+\frac{1}{2}} \left(\frac{\partial u}{\partial z} \right)_{j+\frac{1}{2}} - (\Gamma_u)_{j-\frac{1}{2}} \left(\frac{\partial u}{\partial z} \right)_{j-\frac{1}{2}} \right] \Delta t \\ &= \Delta t \left[\frac{(\Gamma_u)_{j+\frac{1}{2}}}{\Delta z_{j+\frac{1}{2}}} u_{j+1} + \frac{(\Gamma_u)_{j-\frac{1}{2}}}{\Delta z_{j-\frac{1}{2}}} u_{j-1} - \left(\frac{(\Gamma_u)_{j+\frac{1}{2}}}{\Delta z_{j+\frac{1}{2}}} + \frac{(\Gamma_u)_{j-\frac{1}{2}}}{\Delta z_{j-\frac{1}{2}}} \right) u_j \right] \end{aligned} \tag{A.17}$$

By defining the terms:

$$A_N(j) = -\frac{\Delta t}{\Delta z_j} \left(\frac{(\Gamma_u)_{j+\frac{1}{2}}}{\Delta z_{j+\frac{1}{2}}} \right) \tag{A.18a}$$

$$A_S(j) = -\frac{\Delta t}{\Delta z_j} \left(\frac{(\Gamma_u)_{j-\frac{1}{2}}}{\Delta z_{j-\frac{1}{2}}} \right) \tag{A.18b}$$

$$A_P(j) = 1 - A_N(j) - A_S(j) \tag{A.18c}$$

$$D_u(j) = -\frac{1}{\rho} \frac{\partial \bar{P}}{\partial x} \Delta t + u_j^t + U - U^t \tag{A.18d}$$

$$\tag{A.18e}$$

we obtain the following discrete equation for points $j \in [2 : N_0 - 1]$:

$$A_N(j) u_{j+1} + A_P(j) u_j + A_S(j) u_{j-1} = D_u(j) \tag{A.19}$$

The subscript $_P$ refers to the central point considered, while the $_N$ subscript refers to the point directly above (or "North") and the $_S$ subscript refers to the point directly

below ("South").

Boundary conditions

Lower boundary condition

At the bottom boundary $z = z_0$ corresponding to $j = 0$ (figure A.3) the horizontal velocity u and the turbulent kinetic energy k are equal to zero and the specific dissipation rate is set to the value ω_{wall}, as defined in chapter 2.

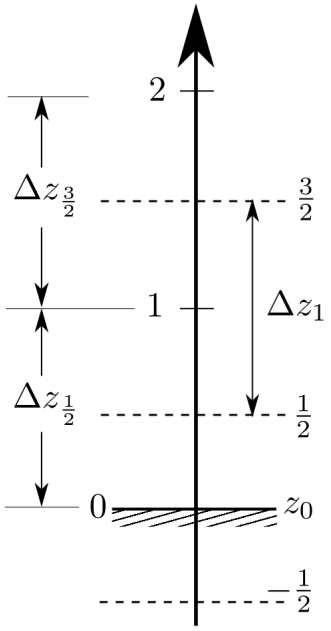

Figure A.3 – Grid point sketch at the bottom boundary

The discrete equation for u is straightforward, as it is defined on the normal grid:

$$A_N(1)u_1 + A_P(1)u_0 = 0 \tag{A.20}$$

with

$$A_N(1) = 0\ , \quad A_P(1) = 1 \tag{A.21}$$

Upper boundary condition

At the upper boundary $z = z_h$ corresponding to $j = N_0$ (figure A.4) the vertical gradient of turbulent kinetic energy k and specific dissipation rate ω are equal to zero. We can define two boundary conditions for the horizontal velocity u, the velocity at the boundary can be equal to the velocity outside the boundary layer, or the gradient

of velocity in this point can be equal to zero.

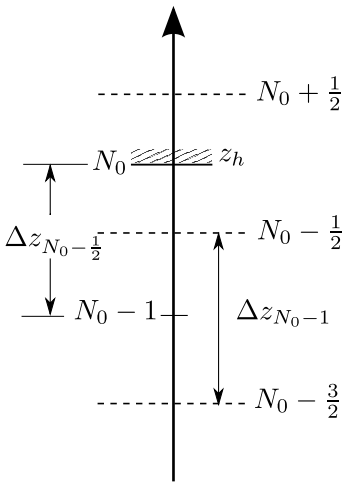

Figure A.4 – Grid point sketch at the upper boundary

- If we define the horizontal velocity at the top boundary to be equal to the velocity outside the boundary layer U_∞, the integration between the points $j = N_0 - \frac{1}{2}$ and $j = N_0 + \frac{1}{2}$ gives:

$$\int_{N_0-\frac{1}{2}}^{N_0+\frac{1}{2}} \int_t^{t+\Delta t} \frac{\partial u}{\partial t}\, dt\, dz = (u_{N_0} - u^t_{N_0})\Delta z_{N_0} = (u_{N_0} - U^t_\infty)\Delta z_{N_0} \tag{A.22}$$

$$\int_{N_0-\frac{1}{2}}^{N_0+\frac{1}{2}} \int_t^{t+\Delta t} \left(\frac{\partial U}{\partial t} - \frac{1}{\rho}\frac{\partial \bar{P}}{\partial x}\right) dt\, dz = (U_\infty - U^t_\infty)\Delta z_{N_0} - \frac{1}{\rho}\frac{\partial \bar{P}}{\partial x}\Delta t \Delta z_{N_0} \tag{A.23}$$

$$\int_{N_0-\frac{1}{2}}^{N_0+\frac{1}{2}} \int_t^{t+\Delta t} \frac{\partial}{\partial z}\left(\Gamma_u \frac{\partial u}{\partial z}\right) dt\, dz = \left[(\Gamma_u)_{N_0+\frac{1}{2}} \left(\frac{\partial u}{\partial z}\right)_{N_0+\frac{1}{2}} - (\Gamma_u)_{N_0-\frac{1}{2}} \left(\frac{\partial u}{\partial z}\right)_{N_0-\frac{1}{2}}\right] \Delta t \tag{A.24}$$

We suppose that the velocity outside the boundary layer is constant, therefore

$\left(\frac{\partial u}{\partial z}\right)_{N_0+\frac{1}{2}} = 0.$

$$\begin{aligned}\int_{N_0-\frac{1}{2}}^{N_0+\frac{1}{2}} \int_t^{t+\Delta t} \frac{\partial}{\partial z}\left(\Gamma_u \frac{\partial u}{\partial z}\right)\, dt\, dz &= -(\Gamma_u)^t_{N_0-\frac{1}{2}} \left(\frac{\partial u}{\partial z}\right)_{N_0-\frac{1}{2}} \Delta t \\ &= -(\Gamma_u)^t_{N_0-\frac{1}{2}} \left(\frac{u_{N_0} - u_{N_0-1}}{\Delta z_{N_0-1/2}}\right) \Delta t \\ &= -(\Gamma_u)^t_{N_0-\frac{1}{2}} \left(\frac{U_\infty - u_{N_0-1}}{\Delta z_{N_0-1/2}}\right) \Delta t \end{aligned} \tag{A.25}$$

By defining the terms:

$$A_S(N_0) = -\frac{\Delta t}{\Delta z_{N_0}} \frac{(\Gamma_u)^t_{N_0-\frac{1}{2}}}{\Delta z_{N_0-\frac{1}{2}}} \tag{A.26a}$$

$$A_P(N_0) = 1 \tag{A.26b}$$

$$D_u(N_0) = -\frac{1}{\rho}\frac{\partial \bar{P}}{\partial x}\Delta t + U_\infty(1 + A_S(N_0)) \tag{A.26c}$$

we obtain the following discrete equation for point N_0:

$$A_P(N_0)u_{N_0} + A_S(N_0)u_{N_0-1} = D_u(N_0) \tag{A.27}$$

- If we define the boundary condition as $\left.\frac{\partial u}{\partial z}\right|_{N_0} = 0$, the resulting equation is similar to the other boundary condition, except that the term U^t_∞ is replaced by the term $u^t_{N_0}$ in equations A.22 and A.25.

  By defining the terms:

$$A_S(N_0) = -\frac{\Delta t}{\Delta z_{N_0}} \frac{(\Gamma_u)^t_{N_0-\frac{1}{2}}}{\Delta z_{N_0-\frac{1}{2}}} \tag{A.28a}$$

$$A_P(N_0) = 1 - A_S(N_0) \tag{A.28b}$$

$$\tag{A.28c}$$

$$D_u(N_0) = -\frac{1}{\rho}\frac{\partial \bar{P}}{\partial x}\Delta t + U_\infty - U^t_\infty + u^t_{N_0} \tag{A.28d}$$

  we obtain the following discrete equation for point N:

$$A_P(N_0)u_{N_0} + A_S(N_0)u_{N_0-1} = D_u(N_0) \tag{A.29}$$

additional terms: advection

discretization of the vertical velocity

We first need to discretize the vertical velocity w. We evaluate the integral discretely:

$$\begin{aligned} w_j &= \frac{1}{c}\int_{z(1)}^{z(j)} \left.\frac{\partial u}{\partial t}\right|_y dy \\ &= \frac{1}{c}\sum_{m=1}^{j-1}\int_{z(m)}^{z(m+1)} \left.\frac{\partial u}{\partial t}\right|_y dy \\ &\sim \frac{1}{c}\sum_{m=1}^{j-1} \left.\frac{\partial u}{\partial t}\right|_{m+\frac{1}{2}} \Delta z_{m+\frac{1}{2}} \\ &\sim \frac{1}{c}\sum_{m=1}^{j-1} \frac{u^t_{m+\frac{1}{2}} - u^{t-\Delta t}_{m+\frac{1}{2}}}{\Delta t}\Delta z_{m+\frac{1}{2}} \end{aligned} \tag{A.30}$$

The sum starts at $m = 1$ because the vertical velocity is zero at the bottom: $w(z_0) = 0$. The temporal derivative is estimated using the previous time steps t and $t - \Delta t$, as the terms at time step $t + \Delta t$ are unknown, and since it is an implicit discretization, the linear system to be solved would not involve a tridiagonal matrix, making the problem more complicated.

When using an iteration loop, we can estimate a new value for the vertical velocity at each iteration step:

$$w_j \sim \frac{1}{c}\sum_{k=1}^{j-1} \frac{u^1_{k+\frac{1}{2}} - u^t_{k+\frac{1}{2}}}{\Delta t}\Delta z_{k+\frac{1}{2}} \tag{A.31}$$

Where u^1 is the iterated value for the horizontal velocity

Discretization of the advection terms

- For the horizontal velocity equation, we integrate the terms between the points $j - \frac{1}{2}$ and $j + \frac{1}{2}$:

$$\begin{aligned} \int_{j-\frac{1}{2}}^{j+\frac{1}{2}}\int_{t}^{t+\Delta t} -\frac{u}{c}\frac{\partial u}{\partial t} + w\frac{\partial u}{\partial z}\, dtdz &= -\frac{1}{c}u^t_j\Delta z_j \int_t^{t+\Delta t}\frac{\partial u}{\partial t}\, dt + w^t_j\Delta t\int_{j-\frac{1}{2}}^{j+\frac{1}{2}}\frac{\partial u}{\partial z}\, dz \\ &\sim -\frac{1}{c}u^t_j\Delta z_j(u_j - u^t_j) + w^t_j\Delta t(u^t_{j+\frac{1}{2}} - u^t_{j-\frac{1}{2}}) \end{aligned} \tag{A.32}$$

the terms A_N and A_S remain unchanged, the terms A_P and D_u are modified:

$$A_P(j) = 1 - A_N(j) - A_S(j) - \frac{u_j^t}{c} \tag{A.33a}$$

$$D_u(j) = -\frac{1}{\rho}\frac{\partial \bar{P}}{\partial x}\Delta t + u_j^t + U_j - U_j^t - \frac{(u_j^t)^2}{c} - w_j^t \frac{\Delta t}{\Delta z_j}(u_{j+\frac{1}{2}}^t - u_{j-\frac{1}{2}}^t) \tag{A.33b}$$

The values $u_{j+\frac{1}{2}}^t$ and $u_{j-\frac{1}{2}}^t$ are estimated by linear interpolation. The linear system remains the same as the one in equation A.19

- In the lower boundary, the equation is similar to equation A.20.

- In the upper boundary, the equation changes with the chosen boundary condition.

  In the case where the boundary condition is $u_{N_0} = U_\infty$, the integration of the advection terms gives:

$$\begin{aligned}
\int_{N_0-\frac{1}{2}}^{N_0+\frac{1}{2}} \int_t^{t+\Delta t} -\frac{u}{c}\frac{\partial u}{\partial t}\, dtdz &\sim -\frac{1}{c} u_{N_0}^t \Delta z_{N_0}(u_{N_0} - u_{N_0}^t) \\
&\sim -\frac{1}{c} U_\infty^t \Delta z_N (U_\infty - U_\infty^t) \qquad \text{(A.34)} \\
\int_{N_0-\frac{1}{2}}^{N_0+\frac{1}{2}} \int_t^{t+\Delta t} w\frac{\partial u}{\partial z}\, dtdz &\sim w_{N_0}^t \Delta t (u_{N_0+\frac{1}{2}}^t - u_{N_0-\frac{1}{2}}^t) \qquad \text{(A.35)}
\end{aligned}$$

  The values $u_{N_0+\frac{1}{2}}^t$ is set to U_∞, and $u_{N_0-\frac{1}{2}}^t$ is estimated by linear interpolation:

$$u_{N_0-\frac{1}{2}}^t = \frac{U_\infty + u_{N_0-1}^t}{2} \tag{A.36}$$

  Therefore

$$u_{N_0+\frac{1}{2}}^t - u_{N_0-\frac{1}{2}}^t = \frac{1}{2}(U_\infty - u_{N_0-1}^t) \tag{A.37}$$

  and

$$\int_{N_0-\frac{1}{2}}^{N_0+\frac{1}{2}} \int_t^{t+\Delta t} w\frac{\partial u}{\partial z}\, dtdz \sim w_{N_0}^t \frac{\Delta t}{2}(U_\infty^t - u_{N_0-1}^t) \tag{A.38}$$

The terms of the linear system are then:

$$D_u(N_0) = -\frac{1}{\rho}\frac{\partial \bar{P}}{\partial x}\Delta t + U_\infty(1 + A_S(N_0)) + \frac{1}{c}U_\infty(U_\infty - U_\infty^t) - w_{N_0}^t \frac{\Delta t}{2\Delta z_{N_0}}(U_\infty - u_{N_0-1}^t) \tag{A.39}$$

The terms $A_P(N_0)$ and $A_S(N_0)$ remain the same as equations 2.65c and A.26a

- In the case where the velocity gradient is equal to 0, we have:

$$\int_{N_0-\frac{1}{2}}^{N_0+\frac{1}{2}} \int_t^{t+\Delta t} w\frac{\partial u}{\partial z}\, dtdz = 0 \tag{A.40}$$

and the coefficients of the discrete equation are changed to:

$$A_P(N_0) = 1 - A_S(N_0) - \frac{u_{N_0}^t}{c} \tag{A.41}$$

$$D_u(N_0) = -\frac{1}{\rho}\frac{\partial \bar{P}}{\partial x}\Delta t + U_\infty - U_\infty^t + u_{N_0}^t - \frac{(u_{N_0}^t)^2}{c} \tag{A.42}$$

A.2.3 Turbulent Kinetic Energy equation

Original terms

We define the turbulent kinetic energy k at the mid-points of the control volume, to insure a better precision in the system. By doing so, we do not need to interpolate the values at the j points. The equation (A.2) is integrated over a control volume centered in the point $j + \frac{1}{2}$, and over a time step Δt:

$$\int_j^{j+1}\int_t^{t+\Delta t} \frac{\partial k}{\partial t}\, dt\, dz = \int_j^{j+1}\int_t^{t+\Delta t} \left(\nu_T \left(\frac{\partial u}{\partial z}\right)^2 - \beta k\omega\right)\, dt\, dz + \int_j^{j+1}\int_t^{t+\Delta t} \frac{\partial}{\partial z}\left((\nu + \sigma_k\frac{k}{\omega})\frac{\partial k}{\partial z}\right)\, dt\, dz \tag{A.43}$$

We integrate over time using a first order fully implicit control volume scheme:

$$\int_j^{j+1}\int_t^{t+\Delta t} \frac{\partial k}{\partial t}\, dt\, dz = (k_{j+\frac{1}{2}} - k_{j+\frac{1}{2}}^t)\Delta z_{j+\frac{1}{2}} \tag{A.44}$$

$$\int_j^{j+1}\int_t^{t+\Delta t}\nu_T\left(\frac{\partial u}{\partial z}\right)^2\,dt\,dz \sim (\nu_T)^t_{j+\frac{1}{2}}\left(\frac{\partial u}{\partial z}\right)^2_{j+\frac{1}{2}}\Delta t\Delta z_{j+\frac{1}{2}}$$
$$\sim (\nu_T)^t_{j+\frac{1}{2}}\left(\frac{u_{j+1}-u_j}{\Delta z_{j+\frac{1}{2}}}\right)^2\Delta t\Delta z_{j+\frac{1}{2}}$$
$$\sim (\nu_T)^t_{j+\frac{1}{2}}\left(\frac{u^t_{j+1}-u^t_j}{\Delta z_{j+\frac{1}{2}}}\right)^2\Delta t\Delta z_{j+\frac{1}{2}} \tag{A.45}$$

$$\int_j^{j+1}\int_t^{t+\Delta t}\beta^* k\omega dt\,dz \sim (\beta^*)^t_{j+\frac{1}{2}}k_{j+\frac{1}{2}}\omega^t_{j+\frac{1}{2}}\Delta t\Delta z_{j+\frac{1}{2}} \tag{A.46}$$

by defining $(\Gamma_k)_j = \nu + \sigma_k\dfrac{k_j}{\omega_j}$, we have:

$$\int_j^{j+1}\int_t^{t+\Delta t}\frac{\partial}{\partial z}\left(\Gamma_k\frac{\partial k}{\partial z}\right)\,dt\,dz \sim \left[(\Gamma_k)^t_{j+1}\left(\frac{\partial k}{\partial z}\right)_{j+1} - (\Gamma_k)^t_j\left(\frac{\partial k}{\partial z}\right)_j\right]\Delta t$$
$$\sim \left[(\Gamma_k)^t_{j+1}\frac{k_{j+\frac{3}{2}}-k_{j+\frac{1}{2}}}{\Delta z_{j+1}} - (\Gamma_k)^t_j\frac{k_{j+\frac{1}{2}}-k_{j-\frac{1}{2}}}{\Delta z_j}\right]\Delta t \tag{A.47}$$

As k and ω are defined at the mid-points, the turbulent viscosity ν_T is also defined at those points. Therefore to calculate $(\Gamma_k)_j$ we need to use an interpolation (linear or cubic).

By defining the terms:

$$B_N(j) = -\frac{\Delta t}{\Delta z_{j+\frac{1}{2}}}\frac{(\Gamma_k)^t_{j+1}}{\Delta z_{j+1}} \tag{A.48a}$$
$$B_S(j) = -\frac{\Delta t}{\Delta z_{j+\frac{1}{2}}}\frac{(\Gamma_k)^t_j}{\Delta z_j} \tag{A.48b}$$
$$B_P(j) = 1 - B_N(j) - B_S(j) + (\beta^*)^t_{j+\frac{1}{2}}\omega^t_{j+\frac{1}{2}}\Delta t \tag{A.48c}$$
$$D_k(j) = k^t_{j+\frac{1}{2}} + (\nu_T)^t_{j+\frac{1}{2}}\left(\frac{u^t_{j+1}-u^t_j}{\Delta z_{j+\frac{1}{2}}}\right)^2\Delta t \tag{A.48d}$$

we obtain the following equation for point $j+\frac{1}{2}$, with $j \in [2\cdots N-2]$:

$$B_N(j)k_{j+\frac{3}{2}} + B_P(j)k_{j+\frac{1}{2}} + B_S(j)k_{j-\frac{1}{2}} = D_k(j) \tag{A.49}$$

Boundary conditions

Lower boundary condition

- the turbulent kinetic energy is defined at the point $j = \frac{1}{2}$, therefore we have to find discretization equation in $j = \frac{1}{2}$, as the boundary condition is $k(z = z_0) = k_0 = 0$:

$$\begin{aligned}\int_0^1 \int_t^{t+\Delta t} \frac{\partial k}{\partial t}\, dt\, dz &= \int_0^1 \int_t^{t+\Delta t} \left(\nu_T \left(\frac{\partial u}{\partial z}\right)^2 - \beta k\omega\right)\, dt\, dz \\ &+ \int_0^1 \int_t^{t+\Delta t} \frac{\partial}{\partial z}\left((\nu + \sigma_k \frac{k}{\omega})\frac{\partial k}{\partial z}\right)\, dt\, dz \end{aligned} \tag{A.50}$$

We integrate over time using a first order fully implicit control volume scheme:

$$\int_0^1 \int_t^{t+\Delta t} \frac{\partial k}{\partial t}\, dt\, dz = (k_{\frac{1}{2}} - k^t_{\frac{1}{2}})\Delta z_{\frac{1}{2}} \tag{A.51}$$

$$\begin{aligned}\int_0^1 \int_t^{t+\Delta t} \nu_T \left(\frac{\partial u}{\partial z}\right)^2\, dt\, dz &= (\nu_T)^t_{\frac{1}{2}} \left(\frac{\partial u}{\partial z}\right)^2_{\frac{1}{2}} \Delta t \Delta z_{\frac{1}{2}} \\ &= (\nu_T)^t_{\frac{1}{2}} \left(\frac{u^t_1 - u^t_0}{\Delta z_{\frac{1}{2}}}\right)^2 \Delta t \Delta z_{\frac{1}{2}} \\ &= (\nu_T)^t_{\frac{1}{2}} \left(\frac{u^t_1}{\Delta z_{\frac{1}{2}}}\right)^2 \Delta t \Delta z_{\frac{1}{2}} \end{aligned} \tag{A.52}$$

$$\int_0^1 \int_t^{t+\Delta t} \beta^* k\omega dt\, dz = (\beta^*)^t_{\frac{1}{2}} k_{\frac{1}{2}} \omega^t_{\frac{1}{2}} \Delta t \Delta z_{\frac{1}{2}} \tag{A.53}$$

$$\begin{aligned}\int_0^1 \int_t^{t+\Delta t} \frac{\partial}{\partial z}\left(\Gamma_k \frac{\partial k}{\partial z}\right)\, dt\, dz &= \left[(\Gamma_k)_1 \left(\frac{\partial k}{\partial z}\right)_1 - (\Gamma_k)_0 \left(\frac{\partial k}{\partial z}\right)_0\right] \Delta t \\ &= \left[(\Gamma_k)_1 \frac{k_{\frac{3}{2}} - k_{\frac{1}{2}}}{\Delta z_1} - (\Gamma_k)_0 \frac{k_{\frac{1}{2}} - k_{-\frac{1}{2}}}{\Delta z_0}\right] \Delta t \end{aligned} \tag{A.54}$$

At the bottom boundary layer, we consider that k is equal to 0 below z_0, therefore

$k_{-\frac{1}{2}} = 0$. The discretization is then:

$$\int_0^1 \int_t^{t+\Delta t} \frac{\partial}{\partial z}\left(\Gamma_k \frac{\partial k}{\partial z}\right)\, dt\, dz = \left[(\Gamma_k)_1 \frac{k_{\frac{3}{2}} - k_{\frac{1}{2}}}{\Delta z_1} - \nu \frac{k_{\frac{1}{2}}}{\Delta z_0}\right] \Delta t \tag{A.55}$$

By defining the terms:

$$B_N(1) = -\frac{\Delta t}{\Delta z_{\frac{1}{2}}} \frac{(\Gamma_k)_1}{\Delta z_1} \tag{A.56a}$$

$$B_P(1) = 1 - B_N(1) + \frac{\Delta t}{\Delta z_{\frac{1}{2}}} \frac{\nu}{\Delta z_0} + (\beta^*)^t_{\frac{1}{2}} \omega^t_{\frac{1}{2}} \Delta t \tag{A.56b}$$

$$D_k(1) = k^t_{\frac{1}{2}} + (\nu_T)^t_{\frac{1}{2}} \left(\frac{u^t_1}{\Delta z_{\frac{1}{2}}}\right)^2 \Delta t \tag{A.56c}$$

we obtain the following equation for the boundary condition $j = \frac{1}{2}$:

$$B_N(1) k_{\frac{3}{2}} + B_P(1) k_{\frac{1}{2}} = D_k(1) \tag{A.57}$$

- If we consider the boundary condition with a zero-gradient, the second term in equation A.54 is equal to zero, and the coefficients at point $j = \frac{1}{2}$ becomes:

$$B_N(1) = -\frac{\Delta t}{\Delta z_{\frac{1}{2}}} \frac{(\Gamma_k)_1}{\Delta z_1} \tag{A.58a}$$

$$B_P(1) = 1 - B_N(1) + (\beta^*)^t_{\frac{1}{2}} \omega^t_{\frac{1}{2}} \Delta t \tag{A.58b}$$

$$D_k(1) = k^t_{\frac{1}{2}} + (\nu_T)^t_{\frac{1}{2}} \left(\frac{u^t_1}{\Delta z_{\frac{1}{2}}}\right)^2 \Delta t \tag{A.58c}$$

Upper boundary condition

The upper boundary condition for the turbulent kinetic energy k is: $\left.\frac{\partial k}{\partial z}\right|_N = 0$

We integrate between the points $N-1$ and N:

$$\int_{N-1}^{N} \int_t^{t+\Delta t} \frac{\partial k}{\partial t}\, dt\, dz = (k_{N-\frac{1}{2}} - k^t_{N-\frac{1}{2}}) \Delta z_{N-\frac{1}{2}} \tag{A.59}$$

$$\int_{N-1}^{N}\int_{t}^{t+\Delta t}\nu_T\left(\frac{\partial u}{\partial z}\right)^2\,dt\,dz = (\nu_T)^t_{N-\frac{1}{2}}\left(\frac{\partial u}{\partial z}\right)^2_{N-\frac{1}{2}}\Delta t\Delta z_{N-\frac{1}{2}}$$
$$= (\nu_T)^t_{N-\frac{1}{2}}\left(\frac{u^t_N - u^t_{N-1}}{\Delta z_{N-\frac{1}{2}}}\right)^2\Delta t\Delta z_{N-\frac{1}{2}}$$
$$= (\nu_T)^t_{N-\frac{1}{2}}\left(\frac{U_\infty - u^t_{N-1}}{\Delta z_{N-\frac{1}{2}}}\right)^2\Delta t\Delta z_{N-\frac{1}{2}} \tag{A.60}$$

$$\int_{N-1}^{N}\int_{t}^{t+\Delta t}\beta^* k\omega dt\,dz = (\beta^*)^t_{N-\frac{1}{2}}k_{N-\frac{1}{2}}\omega^t_{N-\frac{1}{2}}\Delta t\Delta z_{N-\frac{1}{2}} \tag{A.61}$$

$$\int_{N-1}^{N}\int_{t}^{t+\Delta t}\frac{\partial}{\partial z}\left(\Gamma_k\frac{\partial k}{\partial z}\right)\,dt\,dz = \left[(\Gamma_k)_N\underbrace{\left(\frac{\partial k}{\partial z}\right)_N}_{=0} - (\Gamma_k)_{N-1}\left(\frac{\partial k}{\partial z}\right)_{N-1}\right]\Delta t$$
$$= \left[-(\Gamma_k)_{N-1}\frac{k_{N-\frac{1}{2}} - k_{N-\frac{3}{2}}}{\Delta z_{N-1}}\right]\Delta t \tag{A.62}$$

By defining the terms:

$$B_N(N-1) = 0 \tag{A.63a}$$
$$B_S(N-1) = -\frac{\Delta t}{\Delta z_{N-\frac{1}{2}}}\frac{(\Gamma_k)_{N-1}}{\Delta z_{N-1}} \tag{A.63b}$$
$$B_P(N-1) = 1 - B_S(N-1) + (\beta^*)^t_{N-\frac{1}{2}}\omega^t_{N-\frac{1}{2}}\Delta t \tag{A.63c}$$
$$D_k(N-1) = k^t_{N-\frac{1}{2}} + (\nu_T)^t_{N-\frac{1}{2}}\left(\frac{U^t_\infty - u^t_{N-1}}{\Delta z_{N-\frac{1}{2}}}\right)^2\Delta t \tag{A.63d}$$

we obtain the following equation for the boundary condition $j = N - \frac{1}{2}$:

$$B_P(N-1)k_{N-\frac{1}{2}} + B_S(N-1)k_{N-\frac{3}{2}} = D_k(N-1) \tag{A.64}$$

If the boundary condition for u is $\frac{\partial u}{\partial z} = 0$, the term U_∞ in equation A.60 is replaced by u^t_N.

advection terms

- For the turbulent kinetic energy equation, we integrate the terms between the points j and $j+1$:

$$\begin{aligned}\int_j^{j+1}\int_t^{t+\Delta t} w\frac{\partial k}{\partial z}\,dtdz &= w^t_{j+\frac{1}{2}}\Delta t\int_j^{j+1}\frac{\partial k}{\partial z}\,dz \\ &= w^t_{j+\frac{1}{2}}\Delta t(k^t_{j+1}-k^t_j) \end{aligned} \tag{A.65}$$

$$\begin{aligned}\int_j^{j+1}\int_t^{t+\Delta t} -\frac{u}{c}\frac{\partial k}{\partial t}\,dtdz &= -\frac{u^t_{j+\frac{1}{2}}}{c}\Delta z_{j+\frac{1}{2}}\int_t^{t+\Delta t}\frac{\partial k}{\partial t}\,dz \\ &= -\frac{u^t_{j+\frac{1}{2}}}{c}\Delta z_{j+\frac{1}{2}}(k_{j+\frac{1}{2}}-k^t_{j+\frac{1}{2}}) \end{aligned} \tag{A.66}$$

The coefficients B_P and D_k from equation A.49 are then changed to:

$$B_P(j) = 1-B_N(j)-B_S(j)+(\beta^*)^t_{j+\frac{1}{2}}\omega^t_{j+\frac{1}{2}}\Delta t-\frac{u^t_{j+\frac{1}{2}}}{c}\Delta z_{j+\frac{1}{2}}(k_{j+\frac{1}{2}}-k^t_{j+\frac{1}{2}}) \tag{A.67}$$

$$D_k(j) = k^t_{j+\frac{1}{2}}+(\nu_T)^t_{j+\frac{1}{2}}\left(\frac{u^t_{j+1}-u^t_j}{\Delta z_{j+\frac{1}{2}}}\right)^2\Delta t - w^t_{j+\frac{1}{2}}\frac{\Delta t}{\Delta z_{j+\frac{1}{2}}}(k^t_{j+1}-k^t_j) \tag{A.68}$$

The values k^t_j and k^t_{j+1} are estimated by linear interpolation.

- In the lower boundary layer, with the boundary condition $k_{z_0}=0$ there is one additional term to the equation:

$$\begin{aligned}\int_0^{1}\int_t^{t+\Delta t} w\frac{\partial k}{\partial z}\,dtdz &= w^t_{\frac{1}{2}}\Delta t\int_0^{1}\frac{\partial k}{\partial z}\,dz \\ &= w^t_{\frac{1}{2}}\Delta t(k^t_1-k^t_0) \\ &= w^t_{\frac{1}{2}}\Delta t k^t_1 \end{aligned} \tag{A.69}$$

$D_k(1)$ is then changed to:

$$D_k(1) = k^t_{\frac{1}{2}}+(\nu_T)^t_{\frac{1}{2}}\left(\frac{u^t_1}{\Delta z_{\frac{1}{2}}}\right)^2\Delta t - w^t_{\frac{1}{2}}\frac{\Delta t}{\Delta z_{\frac{1}{2}}}k^t_1 \tag{A.70}$$

- If the boundary condition is $\left.\frac{\partial k}{\partial z}\right|_{z_0} = 0$, we need to find k_0.

$$\left.\frac{\partial k}{\partial z}\right|_{z_0} = 0 \Rightarrow k_{\frac{1}{2}} = k_{-\frac{1}{2}} \Rightarrow k_{\frac{1}{2}} = k_0 \tag{A.71}$$

The additional term is then:

$$\int_0^1 \int_t^{t+\Delta t} w\frac{\partial k}{\partial z}\, dtdz = w_{\frac{1}{2}}^t \Delta t(k_1^t - k_{\frac{1}{2}}^t) \tag{A.72}$$

- In the upper boundary layer, there is also one additional term to the equation:

$$\begin{aligned}\int_{N-1}^{N} \int_t^{t+\Delta t} w\frac{\partial k}{\partial z}\, dtdz &= w_{N-\frac{1}{2}}^t \Delta t \int_{N-1}^{N} \frac{\partial k}{\partial z}\, dz \\ &= w_{N-\frac{1}{2}}^t \Delta t(k_N^t - k_{N-1}^t)\end{aligned} \tag{A.73}$$

$D_k(N-1)$ is then changed to:

$$D_k(N-1) = k_{N-\frac{1}{2}}^t + (\nu_T)_{N-\frac{1}{2}}^t \left(\frac{u_N^t - u_{N-1}^t}{\Delta z_{N-\frac{1}{2}}}\right)^2 \Delta t - w_{N-\frac{1}{2}}^t \frac{\Delta t}{\Delta z_{N-\frac{1}{2}}}(k_N^t - k_{N-1}^t) \tag{A.74}$$

A.2.4 Specific dissipation rate equation

Original terms

We define the specific dissipation rate ω at the mid-points of the control volume,the same way we do with the turbulent kinetic energy k. We first discretize the equation for the [Wilcox, 1998] formulation, and then add the term for the [Wilcox, 2006] formulation.

[Wilcox, 1998] formulation

We need to integrate the equation (A.3) over a control volume centered in the point $j + \frac{1}{2}$, and over a time step Δt:

$$\begin{aligned}\int_j^{j+1} \int_t^{t+\Delta t} \frac{\partial \omega}{\partial t}\, dt\, dz &= \int_j^{j+1} \int_t^{t+\Delta t} \left(\gamma \frac{\omega}{k}\nu_T \left(\frac{\partial u}{\partial z}\right)^2 - \beta\omega^2\right)\, dt\, dz \\ &+ \int_j^{j+1} \int_t^{t+\Delta t} \frac{\partial}{\partial z}\left(\Gamma_\omega \frac{\partial \omega}{\partial z}\right)\, dt\, dz\end{aligned} \tag{A.75}$$

We integrate over time using a first order fully implicit control volume scheme:

$$\int_j^{j+1}\int_t^{t+\Delta t}\frac{\partial\omega}{\partial t}\,dt\,dz=(\omega_{j+\frac{1}{2}}-\omega^t_{j+\frac{1}{2}})\Delta z_{j+\frac{1}{2}} \tag{A.76}$$

$$\begin{aligned}\int_j^{j+1}\int_t^{t+\Delta t}\gamma\frac{\omega}{k}\nu_T\left(\frac{\partial u}{\partial z}\right)^2\,dt\,dz&=\gamma\frac{\omega^t_{j+\frac{1}{2}}}{k^t_{j+\frac{1}{2}}}(\nu_T)_{j+\frac{1}{2}}\left(\frac{\partial u}{\partial z}\right)^2_{j+\frac{1}{2}}\Delta t\Delta z_{j+\frac{1}{2}}\\&=\gamma\frac{\omega^t_{j+\frac{1}{2}}}{k^t_{j+\frac{1}{2}}}(\nu_T)_{j+\frac{1}{2}}\left(\frac{u^t_{j+1}-u^t_j}{\Delta z_{j+\frac{1}{2}}}\right)^2\Delta t\Delta z_{j+\frac{1}{2}}\end{aligned} \tag{A.77}$$

$$\int_j^{j+1}\int_t^{t+\Delta t}\beta\omega^2 dt\,dz=\beta\omega_{j+\frac{1}{2}}\omega^t_{j+\frac{1}{2}}\Delta t\Delta z_{j+\frac{1}{2}} \tag{A.78}$$

by defining $\Gamma_\omega=\nu+\sigma_\omega\dfrac{k}{\omega}$, we have:

$$\begin{aligned}\int_j^{j+1}\int_t^{t+\Delta t}\frac{\partial}{\partial z}\left(\Gamma_\omega\frac{\partial\omega}{\partial z}\right)\,dt\,dz&=\left[(\Gamma_\omega)_{j+1}\left(\frac{\partial\omega}{\partial z}\right)_{j+1}-(\Gamma_\omega)_j\left(\frac{\partial\omega}{\partial z}\right)_j\right]\Delta t\\&=\left[(\Gamma_\omega)_{j+1}\frac{\omega_{j+\frac{3}{2}}-\omega_{j+\frac{1}{2}}}{\Delta z_{j+1}}-(\Gamma_\omega)_j\frac{\omega_{j+\frac{1}{2}}-\omega_{j-\frac{1}{2}}}{\Delta z_j}\right]\Delta t\end{aligned} \tag{A.79}$$

$(\Gamma_\omega)_j$ is defined by interpolation(linear, cubic or [Patankar, 1980]).

By defining the terms:

$$C_N(j)=-\frac{\Delta t}{\Delta z_{j+\frac{1}{2}}}\frac{(\Gamma_\omega)^t_{j+1}}{\Delta z_{j+1}} \tag{A.80a}$$

$$C_S(j)=-\frac{\Delta t}{\Delta z_{j+\frac{1}{2}}}\frac{(\Gamma_\omega)^t_{j}}{\Delta z_{j}} \tag{A.80b}$$

$$C_P(j)=1-C_N(j)-C_S(j)+\beta\omega^t_{j+\frac{1}{2}}\Delta t \tag{A.80c}$$

$$D_\omega(j)=\omega^t_{j+\frac{1}{2}}+\gamma\frac{\omega^t_{j+\frac{1}{2}}}{k^t_{j+\frac{1}{2}}}(\nu_T)_{j+\frac{1}{2}}\left(\frac{u^t_{j+1}-u^t_j}{\Delta z_{j+\frac{1}{2}}}\right)^2\Delta t \tag{A.80d}$$

we obtain the following equation for point $j+\frac{1}{2}$ with $j\in[2:N-2]$:

$$C_N(j)\omega_{j+\frac{3}{2}}+C_P(j)\omega_{j+\frac{1}{2}}+C_S(j)\omega_{j-\frac{1}{2}}=D_\omega(j) \tag{A.81}$$

[Wilcox, 2006] formulation

If we consider the [Wilcox, 2006] formulation, we have to discretize the cross diffusion term:

$$\int_j^{j+1}\int_t^{t+\Delta t}\frac{\sigma_d}{\omega}\frac{\partial k}{\partial z}\frac{\partial \omega}{\partial z}dt\ dz = \frac{\sigma_d}{\omega^t_{j+\frac{1}{2}}}\left(\frac{\partial k}{\partial z}\right)^t_{j+\frac{1}{2}}\left(\frac{\partial \omega}{\partial z}\right)^t_{j+\frac{1}{2}}\Delta t\Delta z_{j+\frac{1}{2}} \tag{A.82}$$

The partial derivatives of k and ω are estimated using the nearby points:

$$\left(\frac{\partial k}{\partial z}\right)^t_{j+\frac{1}{2}} = \frac{k^t_{j+1}-k^t_j}{\Delta z_{j+\frac{1}{2}}} \tag{A.83}$$

$$\left(\frac{\partial \omega}{\partial z}\right)^t_{j+\frac{1}{2}} = \frac{\omega^t_{j+1}-\omega^t_j}{\Delta z_{j+\frac{1}{2}}} \tag{A.84}$$

the new formulation of term $D_\omega(j)$ is then:

$$\begin{aligned} D_\omega(j) &= \omega^t_{j+\frac{1}{2}} + \gamma\frac{\omega^t_{j+\frac{1}{2}}}{k^t_{j+\frac{1}{2}}}(\nu_T)_{j+\frac{1}{2}}\left(\frac{u^t_{j+1}-u^t_j}{\Delta z_{j+\frac{1}{2}}}\right)^2\Delta t \\ &+ \frac{\sigma_d}{\omega^t_{j+\frac{1}{2}}}\frac{k^t_{j+1}-k^t_j}{\Delta z_{j+\frac{1}{2}}}\frac{\omega^t_{j+1}-\omega^t_j}{\Delta z_{j+\frac{1}{2}}}\Delta t \end{aligned} \tag{A.85}$$

Boundary conditions

Lower boundary condition

The specific dissipation rate ω is also defined at the point $j=\frac{1}{2}$, we use the same method as with the turbulent kinetic energy k:

$$\begin{aligned} \int_0^1\int_t^{t+\Delta t}\frac{\partial \omega}{\partial t}\ dt\ dz &= \int_0^1\int_t^{t+\Delta t}\left(\gamma\frac{\omega}{k}\nu_T\left(\frac{\partial u}{\partial z}\right)^2-\beta\omega^2\right)\ dt\ dz \\ &+ \int_0^1\int_t^{t+\Delta t}\frac{\partial}{\partial z}\left(\Gamma_\omega\frac{\partial \omega}{\partial z}\right)\ dt\ dz \end{aligned} \tag{A.86}$$

$$\int_0^1\int_t^{t+\Delta t}\frac{\partial \omega}{\partial t}\ dt\ dz = (\omega_{\frac{1}{2}}-\omega^t_{\frac{1}{2}})\Delta z_{\frac{1}{2}} \tag{A.87}$$

$$\int_0^1 \int_t^{t+\Delta t} \gamma \frac{\omega}{k} \nu_T \left(\frac{\partial u}{\partial z}\right)^2 \, dt \, dz = \gamma \frac{\omega_{\frac{1}{2}}^t}{k_{\frac{1}{2}}^t} (\nu_T)_{\frac{1}{2}} \left(\frac{\partial u}{\partial z}\right)_{\frac{1}{2}}^2 \Delta t \Delta z_{\frac{1}{2}}$$
$$= \gamma \frac{\omega_{\frac{1}{2}}^t}{k_{\frac{1}{2}}^t} (\nu_T)_{\frac{1}{2}} \left(\frac{u_1 - u_0}{\Delta z_{\frac{1}{2}}}\right)^2 \Delta t \Delta z_{\frac{1}{2}}$$
$$= \gamma \frac{\omega_{\frac{1}{2}}^t}{k_{\frac{1}{2}}^t} (\nu_T)_{\frac{1}{2}} \left(\frac{u_1}{\Delta z_{\frac{1}{2}}}\right)^2 \Delta t \Delta z_{\frac{1}{2}} \tag{A.88}$$

$$\int_0^1 \int_t^{t+\Delta t} \beta \omega^2 dt \, dz = \beta \omega_{\frac{1}{2}} \omega_{\frac{1}{2}}^t \Delta t \Delta z_{\frac{1}{2}} \tag{A.89}$$

$$\int_0^1 \int_t^{t+\Delta t} \frac{\partial}{\partial z} \left(\Gamma_\omega \frac{\partial \omega}{\partial z}\right) \, dt \, dz = \left[(\Gamma_\omega)_1 \left(\frac{\partial \omega}{\partial z}\right)_1 - (\Gamma_\omega)_0 \left(\frac{\partial \omega}{\partial z}\right)_0\right] \Delta t$$
$$= \left[(\Gamma_\omega)_1 \frac{\omega_{\frac{3}{2}} - \omega_{\frac{1}{2}}}{\Delta z_1} - \nu \frac{\omega_{\frac{1}{2}} - \omega_{-\frac{1}{2}}}{z_{\frac{1}{2}} - z_{-\frac{1}{2}}}\right] \Delta t \tag{A.90}$$

At the bottom boundary, we have $\omega_0 = \omega_{wall}$ and $(\Gamma_\omega)_0 = \nu$. At the point $j = -\frac{1}{2}$, we assume that the value is equal to the one at $j = 0$:

$$\omega_{-\frac{1}{2}} = \omega_{wall} \tag{A.91}$$

the discretized term is then:

$$\int_0^1 \int_t^{t+\Delta t} \frac{\partial}{\partial z} \left(\Gamma_\omega \frac{\partial \omega}{\partial z}\right) \, dt \, dz = \left[(\Gamma_\omega)_1 \frac{\omega_{\frac{3}{2}} - \omega_{\frac{1}{2}}}{\Delta z_1} - \nu \frac{\omega_{\frac{1}{2}} - \omega_{wall}}{\Delta z_0}\right] \Delta t \tag{A.92}$$

By defining the terms:

$$C_N(1) = -\frac{\Delta t}{\Delta z_{\frac{1}{2}}} \frac{(\Gamma_\omega)_1}{\Delta z_1} \tag{A.93a}$$

$$C_P(1) = 1 - C_N(1) + \frac{\Delta t}{\Delta z_{\frac{1}{2}}} \frac{\nu}{\Delta z_0} + \beta \omega_{\frac{1}{2}}^t \Delta t \tag{A.93b}$$

$$D_\omega(1) = \omega_{\frac{1}{2}}^t + \gamma \frac{\omega_{\frac{1}{2}}^t}{k_{\frac{1}{2}}^t} (\nu_T)_{\frac{1}{2}} \left(\frac{u_1}{\Delta z_{\frac{1}{2}}}\right)^2 \Delta t + \frac{\Delta t}{\Delta z_{\frac{1}{2}}} \frac{\nu \omega_{wall}}{\Delta z_0} \tag{A.93c}$$

we obtain the following equation for the boundary condition at the point $j = \frac{1}{2}$:

$$C_N(1) \omega_{\frac{3}{2}} + C_P(1) \omega_{\frac{1}{2}} = D_\omega(1) \tag{A.94}$$

If we consider the [Wilcox, 2006] formulation, we have to discretize the cross diffusion term:

$$\int_0^1 \int_t^{t+\Delta t} \frac{\sigma_d}{\omega} \frac{\partial k}{\partial z} \frac{\partial \omega}{\partial z} dt \; dz = \frac{\sigma_d}{\omega^t_{\frac{1}{2}}} \left(\frac{\partial k}{\partial z} \right)^t_{\frac{1}{2}} \left(\frac{\partial \omega}{\partial z} \right)^t_{\frac{1}{2}} \Delta t \Delta z_{\frac{1}{2}} \tag{A.95}$$

The partial derivatives of k and ω are estimated using the nearby points:

$$\left(\frac{\partial k}{\partial z} \right)^t_{\frac{1}{2}} = \frac{k^t_1 - k^t_0}{\Delta z_{\frac{1}{2}}} = \frac{k^t_1}{\Delta z_{\frac{1}{2}}} \tag{A.96}$$

$$\left(\frac{\partial \omega}{\partial z} \right)^t_{\frac{1}{2}} = \frac{\omega^t_1 - \omega^t_0}{\Delta z_{\frac{1}{2}}} = \frac{\omega^t_1 - \omega^t_{wall}}{\Delta z_{\frac{1}{2}}} \tag{A.97}$$

and the resulting coefficient for $D_\omega(1)$ is then:

$$\begin{aligned} D_\omega(1) &= \omega^t_{\frac{1}{2}} + \gamma \frac{\omega^t_{\frac{1}{2}}}{k^t_{\frac{1}{2}}} (\nu_T)_{\frac{1}{2}} \left(\frac{u_1}{\Delta z_{\frac{1}{2}}} \right)^2 \Delta t + \frac{\Delta t}{\Delta z_{\frac{1}{2}}} \frac{\nu \omega_{wall}}{\Delta z_0} \\ &+ \frac{\sigma_d}{\omega^t_{\frac{1}{2}}} \frac{k^t_1}{\Delta z_{\frac{1}{2}}} \frac{\omega^t_1 - \omega^t_{wall}}{\Delta z_{\frac{1}{2}}} \Delta t \end{aligned} \tag{A.98}$$

Upper boundary condition

The upper boundary condition for the specific dissipation rate ω is: $\left. \frac{\partial \omega}{\partial z} \right|_N = 0$

We integrate between the points $N-1$ an N:

$$\int_{N-1}^{N} \int_t^{t+\Delta t} \frac{\partial \omega}{\partial t} \; dt \; dz = (\omega_{N-\frac{1}{2}} - \omega^t_{N-\frac{1}{2}}) \Delta z_{N-\frac{1}{2}} \tag{A.99}$$

$$\begin{aligned} \int_{N-1}^{N} \int_t^{t+\Delta t} \gamma \frac{\omega}{k} \nu_T \left(\frac{\partial u}{\partial z} \right)^2 \; dt \; dz &= \gamma \frac{\omega^t_{N-\frac{1}{2}}}{k^t_{N-\frac{1}{2}}} (\nu_T)_{N-\frac{1}{2}} \left(\frac{\partial u}{\partial z} \right)^2_{N-\frac{1}{2}} \Delta t \Delta z_{N-\frac{1}{2}} \\ &= \gamma \frac{\omega^t_{N-\frac{1}{2}}}{k^t_{N-\frac{1}{2}}} (\nu_T)_{N-\frac{1}{2}} \left(\frac{u_N - u_{N-1}}{\Delta z_{N-\frac{1}{2}}} \right)^2 \Delta t \Delta z_{N-\frac{1}{2}} \\ &= \gamma \frac{\omega^t_{N-\frac{1}{2}}}{k^t_{N-\frac{1}{2}}} (\nu_T)_{N-\frac{1}{2}} \left(\frac{U_\infty - u_{N-1}}{\Delta z_{N-\frac{1}{2}}} \right)^2 \Delta t \Delta z_{N-\frac{1}{2}} \end{aligned} \tag{A.100}$$

$$\int_{N-1}^{N} \int_t^{t+\Delta t} \beta \omega^2 dt \; dz = \beta \omega_{N-\frac{1}{2}} \omega^t_{N-\frac{1}{2}} \Delta t \Delta z_{N-\frac{1}{2}} \tag{A.101}$$

$$\int_{N-1}^{N}\int_{t}^{t+\Delta t}\frac{\partial}{\partial z}\left(\Gamma_\omega\frac{\partial\omega}{\partial z}\right)\,dt\,dz=\left[(\Gamma_\omega)_N\underbrace{\left(\frac{\partial\omega}{\partial z}\right)_N}_{=0}-(\Gamma_\omega)_{N-1}\left(\frac{\partial\omega}{\partial z}\right)_{N-1}\right]\Delta t$$
$$=\left[-(\Gamma_\omega)_{N-1}\frac{\omega_{N-\frac{1}{2}}-\omega_{N-\frac{3}{2}}}{\Delta z_{N-1}}\right]\Delta t \tag{A.102}$$

By defining the terms:

$$C_S(N-1)=-\frac{\Delta t}{\Delta z_{N-\frac{1}{2}}}\frac{(\Gamma_\omega)_{N-1}}{\Delta z_{N-1}} \tag{A.103a}$$

$$C_P(N-1)=1-C_S(N-1)+\beta\omega^t_{N-\frac{1}{2}}\Delta t \tag{A.103b}$$

$$D_\omega(N-1)=\omega^t_{N-\frac{1}{2}}+\gamma\frac{\omega^t_{N-\frac{1}{2}}}{k^t_{N-\frac{1}{2}}}(\nu_T)_{N-\frac{1}{2}}\left(\frac{U_\infty-u_{N-1}}{\Delta z_{N-\frac{1}{2}}}\right)^2\Delta t \tag{A.103c}$$

we obtain the following equation for the boundary condition at the point $j=N-\frac{1}{2}$:

$$C_P(N-1)\omega_{N-\frac{1}{2}}+C_S(N-1)\omega_{N-\frac{3}{2}}=D_\omega(N-1) \tag{A.104}$$

If the upper boundary condition for the horizontal velocity is $\frac{\partial u}{\partial z}=0$, we have to replace the term U_∞ by u_N in equation A.100.

If we consider the [Wilcox, 2006] formulation, we have to discretize the cross diffusion term:

$$\int_{N-1}^{N}\int_{t}^{t+\Delta t}\frac{\sigma_d}{\omega}\frac{\partial k}{\partial z}\frac{\partial\omega}{\partial z}dt\,dz=\frac{\sigma_d}{\omega^t_{N-\frac{1}{2}}}\left(\frac{\partial k}{\partial z}\right)^t_{N-\frac{1}{2}}\left(\frac{\partial\omega}{\partial z}\right)^t_{N-\frac{1}{2}}\Delta t\Delta z_{N-\frac{1}{2}} \tag{A.105}$$

The spatial derivatives of k and ω are estimated using the nearby points:

$$\left(\frac{\partial k}{\partial z}\right)^t_{N-\frac{1}{2}}=\frac{k^t_N-k^t_{N-1}}{\Delta z_{N-\frac{1}{2}}} \tag{A.106}$$

$$\left(\frac{\partial\omega}{\partial z}\right)^t_{N-\frac{1}{2}}=\frac{\omega^t_N-\omega^t_{N-1}}{\Delta z_{N-\frac{1}{2}}} \tag{A.107}$$

We interpolate linearly the values k_{N-1} and ω_{N-1}. For the values k_N, and ω_N we have:

$$k_{N-\frac{1}{2}}=k_N+(z_N-z_{N-\frac{1}{2}})\left.\frac{\partial k}{\partial z}\right|_N=k_N \tag{A.108}$$

$$\omega_{N-\frac{1}{2}} = \omega_N + (z_N - z_{N-\frac{1}{2}}) \left.\frac{\partial \omega}{\partial z}\right|_N = \omega_N \tag{A.109}$$

The term defined in equation A.103c is changed to:

$$\begin{aligned} D_\omega(N-1) &= \omega^t_{N-\frac{1}{2}} + \gamma \frac{\omega^t_{N-\frac{1}{2}}}{k^t_{N-\frac{1}{2}}} (\nu_T)_{N-\frac{1}{2}} \left(\frac{U^t_\infty - u^t_{N-1}}{\Delta z_{N-\frac{1}{2}}} \right)^2 \Delta t \\ &+ \frac{\sigma_d}{\omega^t_{N-\frac{1}{2}}} \left(\frac{\partial k}{\partial z}\right)^t_{N-\frac{1}{2}} \left(\frac{\partial \omega}{\partial z}\right)^t_{N-\frac{1}{2}} \Delta t \end{aligned} \tag{A.110}$$

advection term

- For the specific dissipation rate equation, we integrate the terms between the points j and $j+1$:

$$\begin{aligned} \int_j^{j+1} \int_t^{t+\Delta t} w \frac{\partial \omega}{\partial z} \, dt dz &= w^t_{j+\frac{1}{2}} \Delta t \int_j^{j+1} \frac{\partial \omega}{\partial z} \, dz \\ &= w^t_{j+\frac{1}{2}} \Delta t (\omega^t_{j+1} - \omega^t_j) \end{aligned} \tag{A.111}$$

  The term D_ω in equation **??** is then changed to:

$$\begin{aligned} D_\omega(j) &= \omega^t_{j+\frac{1}{2}} + \gamma \frac{\omega^t_{j+\frac{1}{2}}}{k^t_{j+\frac{1}{2}}} (\nu_T)_{j+\frac{1}{2}} \left(\frac{u_{j+1} - u_j}{\Delta z_{j+\frac{1}{2}}} \right)^2 \Delta t \\ &+ \frac{\sigma_d}{\omega^t_{j+\frac{1}{2}}} \frac{k^t_{j+1} - k^t_j}{\Delta z_{j+\frac{1}{2}}} \frac{\omega^t_{j+1} - \omega^t_j}{\Delta z_{j+\frac{1}{2}}} \Delta t \\ &- w^t_j \frac{\Delta t}{\Delta z_{j+\frac{1}{2}}} (\omega^t_{j+1} - \omega^t_j) \end{aligned} \tag{A.112}$$

  The values ω^t_j and ω^t_{j+1} are estimated by linear interpolation.

- In the lower boundary layer, there is one additional term in D_ω to the equation:

$$\begin{aligned} \int_0^1 \int_t^{t+\Delta t} w \frac{\partial \omega}{\partial z} \, dt dz &= w^t_{\frac{1}{2}} \Delta t \int_0^1 \frac{\partial \omega}{\partial z} \, dz \\ &= w^t_{\frac{1}{2}} \Delta t (\omega^t_1 - \omega^t_0) \\ &= w^t_{\frac{1}{2}} \Delta t (\omega^t_1 - \omega_{wall}) \end{aligned} \tag{A.113}$$

- In the upper boundary layer, there is also one additional term in D_ω to the

equation:

$$\begin{aligned}
\int_{N-1}^{N}\int_{t}^{t+\Delta t} w\frac{\partial \omega}{\partial z}\,dtdz &= w^t_{N-\frac{1}{2}}\Delta t\int_{N-1}^{N}\frac{\partial \omega}{\partial z}\,dz \\
&= w^t_{N-\frac{1}{2}}\Delta t(\omega^t_N - \omega^t_{N-1}) \\
&= w^t_{N-\frac{1}{2}}\Delta t(\omega^t_{N-\frac{1}{2}} - \omega^t_{N-1}) \qquad \text{(A.114)}
\end{aligned}$$

Appendix B

Seiching

B.1 Theoretical seiching modes

As we intend to analyse low frequency motions in the wave basin, we need to determine the wave basin seiching. Seiches occur on enclosed or partially enclosed bodies of water. This body of water resonates to its natural frequencies when excited, allowing the development of a standing wave.

The wave forcing in an enclosed basin produces seiches due to the wave reflection and the wave grouping, allowing a transfer of wave energy to lower frequencies. It is therefore important to estimate these natural frequencies, since they are amplified.

The MODLIT wave basin seiches are determined as explained in Haller et Dalrymple [2001], using the two-dimensional shallow water equation for variable depth:

$$\eta_{tt} - (gh\eta_x)_x - (gh\eta_y)_y = 0 \tag{B.1}$$

with η the water surface elevation, h the water depth, and subscripts representing derivatives. The seiche modes are assumed periodic in time and in the longshore direction, and with an arbitrary distribution in the cross-shore direction:

$$\eta(x, y, t) = \zeta_m(x) \cos(\frac{n\pi y}{W}) \cos(\sigma t) \tag{B.2}$$

where m is the cross-shore mode number associated to its cross-shore waveform ζ_m, n is the longshore mode number, W is the width of the basin, and σ is the wave frequency. If we substitute equation B.2 into equation B.1, and assuming a longshore uniform bathymetry ($h_y = 0$), we obtain an equation for the seiche modes:

$$-gh\zeta_{m_{xx}} - gh_x\zeta_{m_x} + \frac{ghn^2\pi^2}{W^2}\zeta_m = \sigma^2\zeta_m \tag{B.3}$$

T (s)	$n=0$	$n=1$	$n=2$
$m=0$		33.26	20.28
$m=1$	25.97	19.48	12.50
$m=2$	12.42	11.64	9.70

Table B.1 – Period of the lowest frequency modes.

As mentioned in Haller et Dalrymple [2001], a variable transformation $\xi = \zeta_m \cdot x$ and a change in orientation such as $x = 0$ at the shoreline, and $x = L$ at the wavemaker is used, to implement the shoreline boundary condition of a finite wave amplitude. With these changes, the equation governing the seiche modes in the wave basin is now:

$$-gh\xi_{xx} + \left(\frac{2gh}{x} - gh_x\right)\xi_x + \left(\frac{gh_x}{x} - \frac{2gh}{x^2} + \frac{ghn^2\pi^2}{W^2}\right)\xi = \sigma^2\xi \tag{B.4}$$

with the boundary conditions:

$$\xi = 0 \qquad x = 0 \tag{B.5}$$

$$\zeta_x(L) = \xi_x(L) - \frac{\xi(L)}{L} = 0 \qquad x = L \tag{B.6}$$

Now, equation B.4 can be seen as an eigenvalue problem, with eigenvalues σ^2. Note that the arbitrary cross-shore wave form ζ_m is related to the eigenvector ξ of the eigenvalues σ^2. This eigenvalue problem is solved using a finite difference method. The derivatives h_x, ζ_x and ζ_{xx} are discretized using central differences ($O(\Delta x^2)$), which lead to a matrix form of the eigenvalue problem.

One of the hypotheses to find the seiching modes assumed an alongshore uniform bathymetry. In our case, as the wave basin dimensions are larger than the longshore non-uniformity, we consider the alongshore averaged bathymetry to obtain the natural modes.

The eigenvalues corresponding to higher frequencies are more likely to be affected by frictional damping, therefore we focus on the lowest frequency modes, which are more energetic. These modes corresponds to $n = [0, 1, 2]$, $m = [0, 1, 2]$.

Table B.1 lists the periods of the waves corresponding to these modes. We observe that the main seiche modes are located in the infragravity band.

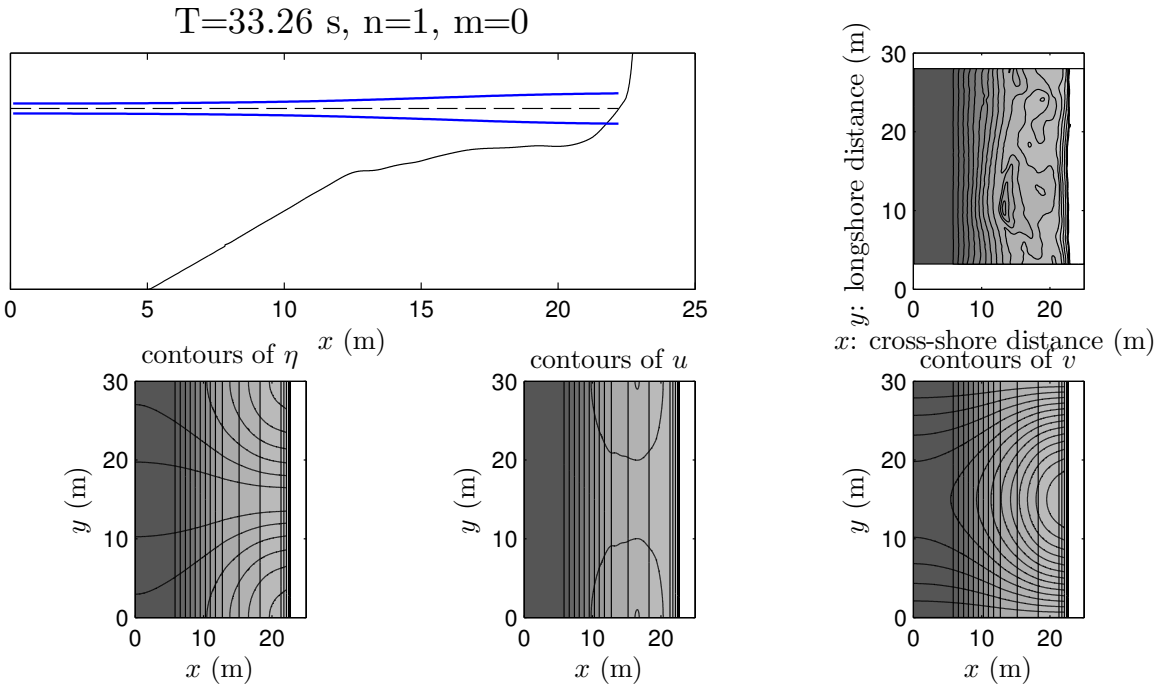

Figure B.1 – seiche, n=1, m=0. In the upper left panel are plotted the alongshore averaged cross-shore profile as a black line, the still water level as a black dotted line and the plain blue lines as the extreme free surface displacement at $x = 15$ m. The upper right panel shows the isolines of the original bathymetry considered. The lower panel shows the contour of the free surface η, the cross-shore velocity u and the longshore velocity v as black line, and the isolines of the alongshore averaged bathymetry shown as vertical lines.

B.2 Main seiching modes

The main seiching modes can be seen in Figures B.2, B.3, B.1, B.4, B.5. The mode with the larger period corresponds to the mode $n = 1$, $m = 0$, with a theoretical period $T = 33.26$ s, and it is the main longshore mode, with 1 longshore node, and no cross-shore node.

The main cross-shore mode corresponds to the mode $n = 0$, $m = 1$, with 1 cross-shore node and no longshore node, with a period $T = 25.97$ s. The second cross-shore mode, with $n = 0$, $m = 2$ has a period $T = 12.42$ s, close to the half of the period of the main cross-shore mode.

There are also two modes, with one longshore node, and one and two cross-shore nodes, which are the modes $n = 1$, $m = 1$ and $n = 1$, $m = 2$, with periods of respectively $T = 19,48$ s and $T = 11.64$ s. The period of the latest is also close to the half of the $n = 1$, $m = 1$ mode.

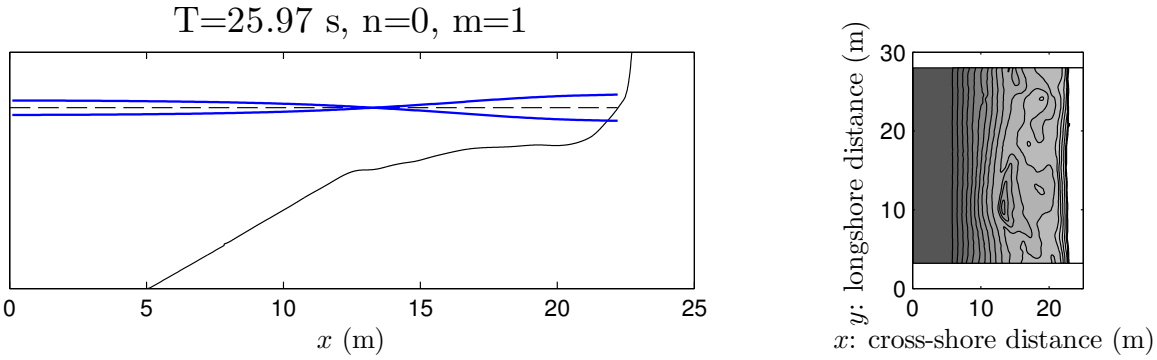

Figure B.2 – seiche, n=0, m=1. Captions, see Figure B.1.

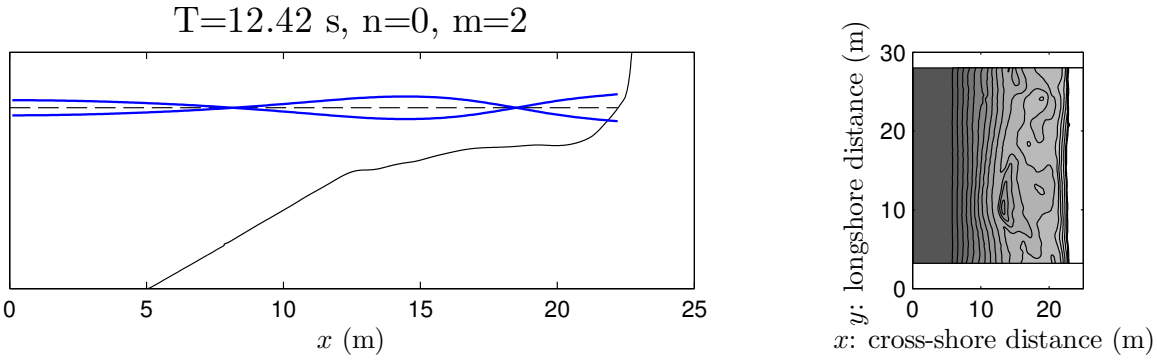

Figure B.3 – seiche, n=0, m=2. Captions, see Figure B.1

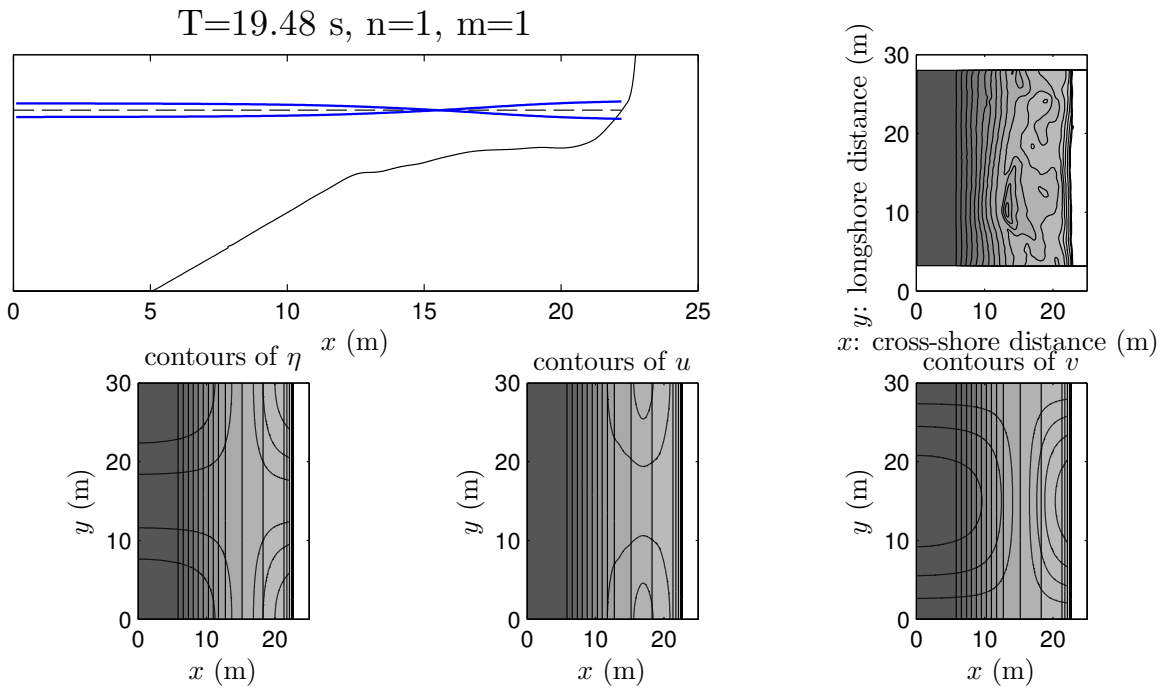

Figure B.4 – seiche, n=1, m=1. Captions, see Figure B.1

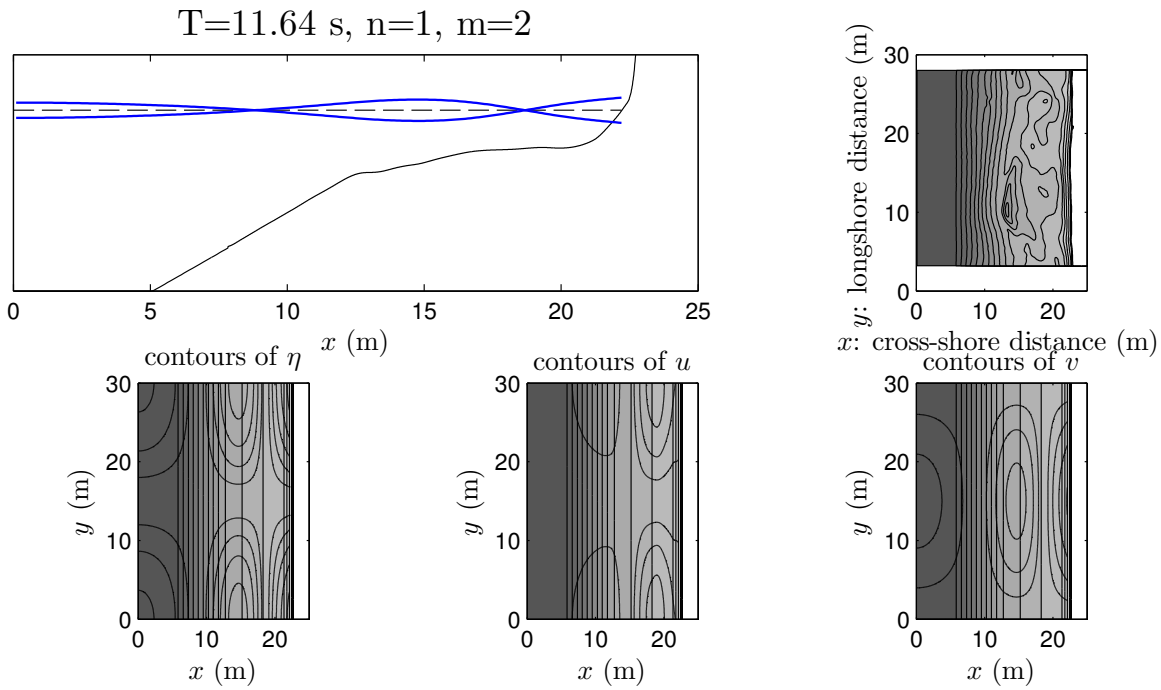

Figure B.5 – seiche, n=1, m=2 Captions, see Figure B.1

It has been suggested that nearshore dynamics fluctuations can be related to infragravity wave motions [Fowler et Dalrymple, 1990]. In the experiments these low frequency motions are generated by the selection of particular modal frequencies in the wave grouping of the JONSWAP spectrum. The resonant frequencies selected by the basin geometry and bottom topography appear as peaks in the free surface elevation spectrum (Figures 4.13 and 4.19). The aim of this section is to understand the characteristics of this low frequency spectrum and how much is reproduced by the numerical model. We recall that the numerical model has an offshore absorption/generation boundary that mimics what would be a real life beach.

We compare the theoretical seiching modes with the experimental results for experiment 30 (t=21:00-26:00). We obtain the experimental spectral wave energy in a cross-shore profile located at $y = 10$ m. To obtain these cross-shore profiles, we use the following method:

1. we estimate for each point in the cross-shore profile the wave spectrum, with the time series at 50 Hz for the experimental data, and the time-series interpolated at the same frequency for the numerical model, in order to compare the spectra.

2. for each natural mode frequency determined by the theoretical model of Haller et Dalrymple [2001], we extract from the spectra the amplitude a_η corresponding to these frequencies. The amplitude $a_\eta(x_0, f_0)$ in meters for a frequency f_0 at a cross-shore distance x_0 from the wavemaker is estimated with the formula:

$$a_\eta(x_0 f_0) = \sqrt{S_{\eta\eta}(x_0, f_0)\Delta f_0} \tag{B.7}$$

   where Δf_0 is the frequency band around the chosen frequency f_0. In our case, we choose $\Delta f_0 = 0.01$ Hz.

3. To compare these amplitudes with the theoretical model, we use the cross-shore waveform at these frequencies $\zeta_m(x)$. This amplitude is then multiplied by a factor in order to obtain the same amplitude of the experimental wave gauge located at $x = 21.325$ m, nearest to the shoreline. For the modes with $n = 0$ or $n = 1$ longshore mode, the profiles were taken at $y = 8.17$ m, to obtain information from the wave gauges at $x = 5$ m. For the mode $n = 2$ with two longshore nodes, the cross-shore profiles were taken at $y = 15$ m, where the amplitude is high, and to obtain information on the wave gauge at $x = 5$ m also.

If we first compare the theoretical seiching modes with the experimental data in Figure B.6 we observe that the main cross-shore seiching mode at $T = 25.97$ s ($n = 0$,

$m = 1$) is well predicted by the theory, as well as the seiching mode with 2 cross-shore nodes and one longshore node at $T = 12.42$ s ($n = 1$, $m = 2$) . The main theoretical longshore mode at $T = 33.26$ s ($n = 1$, $m = 0$) is different in the experiment which shows a cross-shore node at $x = 14$ m at this frequency. For the $n = 1$, $m = 1$ mode at $T = 19.48$ s, the profiles are similar for $x > 15$ m, but the experiment shows a node at $x = 9$ m, not present in the theory. The $n = 1$, $m = 2$ mode at $T = 11.64$ s shows some similarities, as the position of the two cross-shore nodes are well predicted by the theory but the theoretical wave amplitude over-estimates the one from the experiment. The $n = 2$, $m = 0$ mode at $T = 20.28$ s is similar for $x > 10$ m, but different for $x < 10$ m as the experiment indicates that there is a node at $x = 10$ m at this frequency. For the $n = 2$, $m = 1$ mode at $T = 12.50$ s, the experimental results are similar to the theory. Finally for the $n = 2$, $m = 2$ mode at $T = 9.70$ s, the nodes at $x = 11$ m and $x = 19$ m are the same, but for $x < 10$ m the behaviour is different.

The numerical results present some similarities with the experiment concerning the two main cross-shore modes ($n = 0$, $m = 1$ and $n = 0$, $m = 2$), in terms of the cross-shore position of the nodes however the amplitude is lower, and for $x < 10$ m the wave amplitude does not increase in the model, due to the open boundary condition that does not add cross-shore resonance. The main longshore mode $n = 1$, $m = 0$ is fairly well reproduced, probably due to the fact that the waves can resonate in the model between the two closed boundaries. For the remaining modes, there are some discrepancies between the model and the experiment at the theoretical seiching mode frequencies, with still similar waveform for $x > 10$ m, but with lower amplitude for the modes ($n = 1$, $m = 2$), ($n = 2$, $m = 1$) and ($n = 2$, $m = 2$).

Using the the theoretical approach it is possible to assess the importance of the "natural" standing waves. By natural we mean those that would appear in a real life beach for which there is no seaward boundary. These natural modes have been thought to be standing waves resonating between the mean wave breaking point and the shoreline, the shoreline being an antinode. Symonds *et al.* [1982] showed that the cross-shore variation of the breakpoint caused by the wave grouping induces standing waves between the breaking point and the shoreline. By introducing a partial transmission of the wave grouping into the surf zone in addition to a varying breaking point, Shaffer [1993] improved the prediction of these standing waves in a 1D cross-shore situation. In the case of barred beaches, Baldock *et al.* [2004] found resonant modes between the bar position and the shoreline, similar to seiche modes.

Most of Shaffer [1993]'s calculation assume that the bound wave transmission, which can also be viewed as the high frequency wave groupiness transmission in the surf-zone, was non-existent. The numerical work by Madsen *et al.* [1997b] on the Kostense [1984]

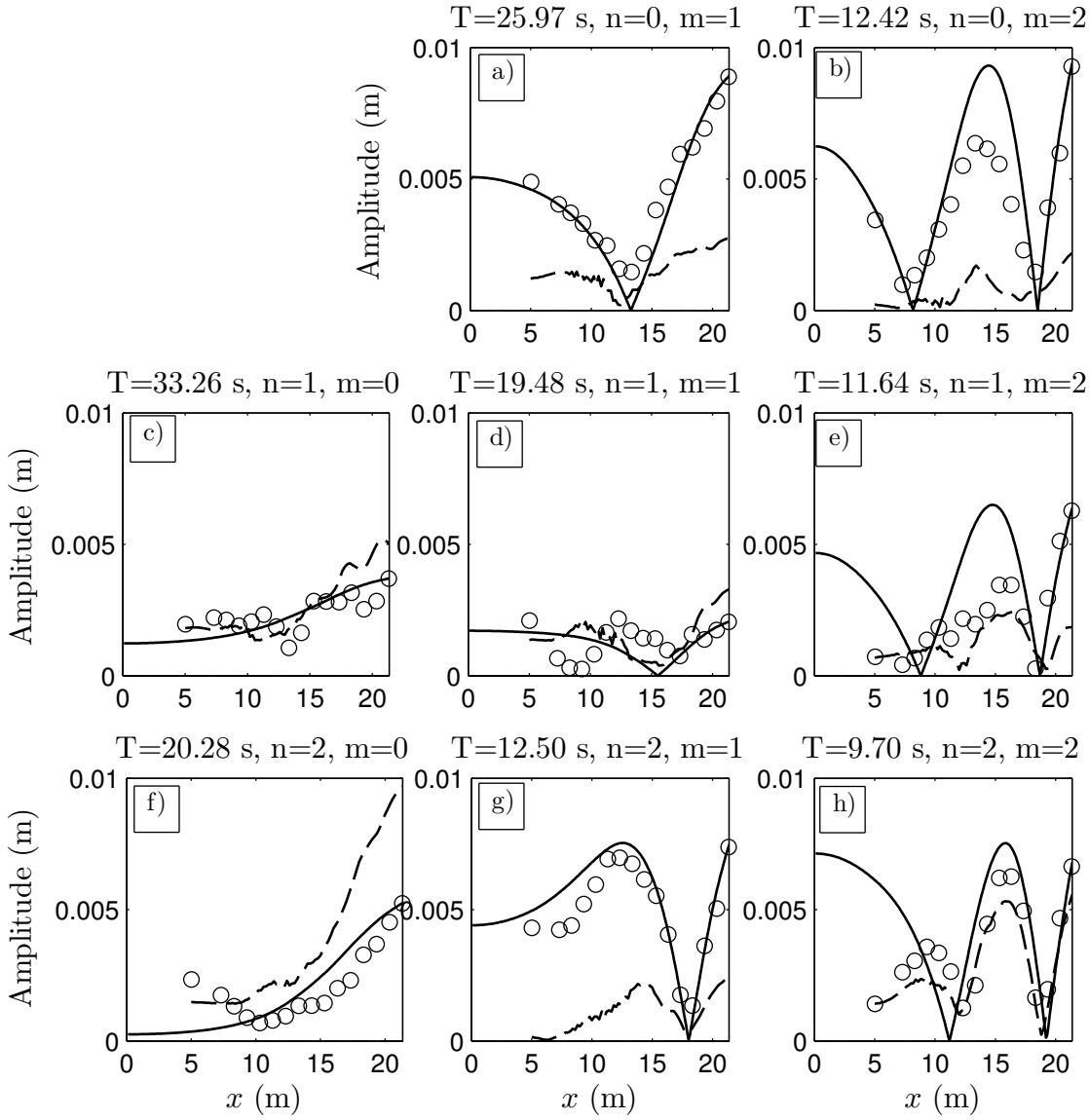

Figure B.6 – Modal structure of the entire basin. Comparison between the theoretical seiching modes, and the experimental wave energy for experiment 30 (t=21:00-26:00). T represents the theoretical period of the seiching mode, n the number of longshore nodes, m the number of cross-shore nodes. The cross-shore profile is chosen at $y = 8.17$ m for $n = 0$ and $n = 1$, and at $y = 15$ m for $n = 2$. Circles: experimental seiching modes at the theoretical periods; line: theoretical seiching modes; dashed line: numerical model

experiments seem to show that there is a certain amount of transmission in the case of these experiments. They even show that in contrast to Symonds *et al.* [1982] theory the break point is in the vicinity of the node of a standing wave between this location and the shore line. Our experiments also exhibit partial groupiness transmission as seen at x=13.3 on fig. 4.20. Kostense [1984] experiments are from a non-dimensional point of view very close to the LHF ones. Indeed the non-dimensional parameter Shaffer [1993] $m_0 * f_p/f_{lo}$ with m the beach slope, f_p the peak JONSWAP frequency and f_{lo} the characteristic frequency of the infragravity band, similar to the β_b defined by van Dongeren *et al.* [2007], is between 0.1 and 0.4 in the LHF experiments while ranging between 0.2 and 0.5 for the bichromatic experiments on a plane beach of Kostense [1984].

The theoretical modes are found supposing there exist a node at $x = 11$ m near the wave breaking. This is equivalent to assuming that the break point acts as a piston prescribing the velocity. The theoretical seiching modes are then compared to the experimental results and the numerical model, in a cross-shore profile located at $y = 10$ m. This comparison can be seen in Figure B.7.

The theoretical seiching modes can be separated in three different types. The first type are the modes with 1 cross-shore nodes ($m = 1$) with periods of $T = 10.75$ s, $T = 10.47$ s and $T = 9.74$ s (respectively $n = 0$, $n = 1$, $n = 2$), that are similar. The second type with 2 cross-shore modes ($m = 2$) also have very similar periods , that only slightly depend of the longshore modes, as their period are $T = 6.58$ s, $T = 6.52$ s and $T = 6.33$ s (respectively $n = 0$, $n = 1$, $n = 2$). The third type corresponds to the modes without alongshore nodes $m = 0$, and consist of the two modes with the larger periods $T = 25.76$ s and $T = 19.32$ s (respectively $n = 1$ and $n = 2$).

The theoretical seiching modes between the wave breaking and the shoreline are consistent with the experimental results for the $m = 1$ and $m = 2$ modes. For the $m = 1$ modes, the peaks are located at $x \approx 15$ m, close to the theoretical results, and for the $m = 2$ modes, the peaks at $x \approx 13$ m and $x \approx 18$ m are well reproduced. The amplitudes for the main cross-shore mode ($n = 0$, $m = 1$) are similar, although we note that the period for the main longshore mode in this case is similar to the period of the main cross-shore mode of the basin in Figure B.6. The modes with two cross-shore nodes ($m = 2$) are fairly well reproduced in the experiment, as well as the ($n = 1$, $m = 1$) mode. The longshore modes ($m = 0$) are not present in the experiment, as we see that at these theoretical frequencies, the existing modes are modes of the complete basin.

If we observe now the numerical model results at the theoretical period of the seiching modes, the cross-shore profiles present similarities with the experiment in

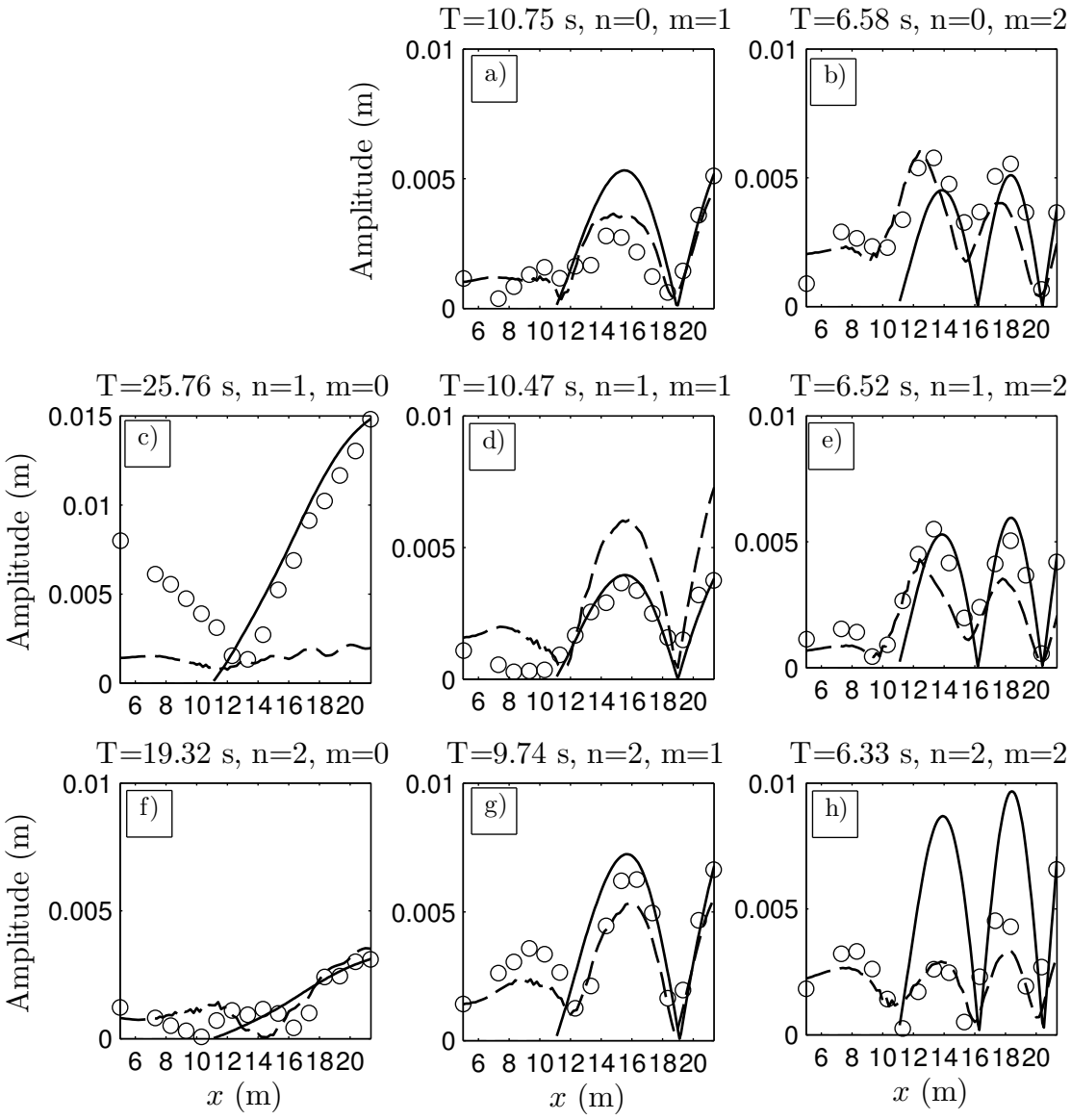

Figure B.7 – Modal structure of the part of the basin bound by $x = 11$ m and the shoreline. Comparison between the theoretical seiching modes, and the experimental wave energy for experiment 30 (t=21:00-26:00). T represents the theoretical period of the seiching mode, n the number of longshore nodes, m the number of cross-shore nodes. The cross-shore profile is chosen at $y = 8.17$ m for $n = 0$ and $n = 1$, and at $y = 15$ m for $n = 2$. Circles: experimental seiching modes at the theoretical periods; line: theoretical seiching modes; dashed line: seiching modes determined by the model.

terms of position of the cross-shore nodes. The $m = 1$ modes present a peak at $x \approx 15$ m, with amplitudes close to the experimental ones. The $m = 2$ modes are also well reproduced, with the two peaks at cross-shore positions similar to the experiment, with a lower amplitude though. The longshore modes present discrepancies with the experimental profiles and the theoretical ones.

From the study of the seiching modes, we can conclude that although the model does not reproduce well the basin seiching modes, excepting the main longshore mode, due to the open boundary condition at $x = 5$ m, we still observe some seiching modes resonating between the shoreline and the breaking point, explaining the presence of energy in the infragravity band. We can observe some of these seiching modes by looking at the free surface spectral profiles, in the previous section. This could be the reason why the numerical model shows some modal structure, even though there is an open boundary condition at $x = 5$ m.

Appendix C

Congreso Latinoamericano de Ingeniería Hidráulica - Latin IAHR - Noviembre 2011 - Punta del Este - Uruguay

IAHR **AIIH**

XXIV CONGRESO LATINOAMERICANO DE HIDRÁULICA
PUNTA DEL ESTE, URUGUAY, NOVIEMBRE 2010

MODELACIÓN DEL ARRASTRE DE SEDIMENTOS SOBRE UNA DUNA DE ARENA Y SU EVOLUCIÓN MORFODINÁMICA

L. Suarez[1,2], R. Cienfuegos[1], E. Barthélémy[2] y H. Michallet[2]
[1]Departamento de Ingeniería Hidráulica y Ambiental; Pontificia Universidad Católica de Chile
[2] Laboratoire des Ecoulements Géophysiques et Industriels; Institut National Polytechnique de Grenoble, France
E-mail: lsuarez2@uc.cl, racienfu@ing.puc.cl, eric.barthelemy@hmg.inpg.fr, herve.michallet@hmg.inpg.fr

RESUMEN:

Para estudiar el arrastre de sedimento sobre una duna de arena, modelamos la evolución morfológica de una duna bidimensional sometida a un flujo uniforme, de manera unidimensional, en un canal abierto. El transporte de sedimento se relaciona con la forma, la pendiente y la altura de la duna. Para poder estimar la evolución de la duna, utilizamos un esquema de tipo NOCS acoplado con un módulo de avalancha localizado. Comparamos los datos experimentales con una parametrización del transporte de sedimento a partir de la pendiente de la duna (Rossi y Michallet, 2003), y con un modelo que determina el transporte a partir de una parametrización del esfuerzo de corte (Coleman, 2006).

La parametrización de Rossi y Michallet(2003) permite tener una buena representación del movimiento de la duna bajo un flujo uniforme, pero es necesario conocer la altura crítica de inicio del arrastre de sedimento, lo que solamente un modelo que calcula el esfuerzo de corte local nos puede entregar.

ABSTRACT:

Experiments were performed to examine the movement and transport of a two-dimensional sand dune of large dimensions in an open channel flow. The sediment discharge is related to the dune's shape, height and upstream slope. To model the dune evolution, we use a NOCS scheme coupled with an avalanche module. We compare experimental data with a parameterization of the sediment transport which depends on the slope of the stoss side of the dune (Rossi & Michallet, 2003) and with a parameterization of the local bed shear stress (Coleman, 2006).

Rossi & Michallet (2003) parameterization can provide good results for the dune evolution, but it is necessary to know the critical height of initiation of sediment transport, which only a model with local shear stress estimation can provide.

PALABRAS CLAVES:

Morfodinámica, Esfuerzo de corte, transporte de sedimento

INTRODUCCIÓN

La estimación de tasas de arrastre de sedimentos y la evolución morfodinámica de playas de arena bajo el efecto de corrientes y oleaje es un problema altamente complejo. En este trabajo pretendemos, por un lado contribuir a mejorar el entendimiento de los procesos asociados y por otro, desarrollar una herramienta numérica capaz de entregar una buena predicción de la evolución espacio-temporal de fondos de arena bajo el efecto de hidrodinámico.

Con el objeto de calibrar un modelo numérico morfodinámico, utilizaremos datos experimentales sobre la evolución de una duna de arena bidimensional en canal abierto en condiciones subcríticas. Estas experiencias se llevaron a cabo en el Laboratoire des Ecoulements Geophysiques et Industriels (LEGI) de Grenoble en Francia. Mediante ultrasonido, se realizó un seguimiento del movimiento de la duna bajo el efecto de un flujo unidireccional determinándose sus parámetros geométricos importantes (altura, forma, pendientes, etc.). Además se cuenta con estimaciones de la velocidad de desplazamiento de la cresta de la duna.

La información experimental sirve para calibrar un modelo de transporte de fondo unidmensional, que permita predecir el movimiento de la duna. La hidrodinámica se resuelve a partir de las ecuaciones de Saint-Venant, y la evolución del fondo se resuelve a partir de un esquema de tipo NOCS (Non Oscillatory Central Scheme) acoplado con un módulo de avalancha cuando la pendiente de la duna supera la pendiente crítica. La tasa de transporte de fondo se calcula a partir de los esfuerzos de corte sobre el fondo, estimados con un modelo de capa límite turbulenta de tipo k-ω, a partir de una parametrización del transporte de sedimento de Rossi (2003), y a partir de una parametrización del esfuerzo de corte de Coleman (2006).

Con este modelo esperamos obtener una mejor predicción del transporte de fondo sobre la duna al disponer de series de tiempo del esfuerzo de corte aplicado eliminando la necesidad de usar la velocidad media como estimador del transporte de sedimentos.

OBJETIVOS

Un escurrimiento sobre un lecho de arena puede generar formas de fondo, y a su vez éstas pueden modificar el escurrimiento. Se trata por lo tanto de un proceso altamente acoplado. El flujo se comporta de distintas maneras al enfrentarse a una duna. Antes de entrar en contacto con ella, el flujo es uniforme, mientras que al llegar al pie de la duna, se acelera hasta alcanzar su cresta. Después de la cresta, tenemos una zona de recirculación debida al fenómenos de separación. La Figura 1 nos muestra los distintos fenómenos que ocurren cuando el flujo pasa sobre una duna. A partir del experimento de Rossi y Michallet (2003), examinaremos el comportamiento de una duna de arena bidimensional bajo el efecto de un escurrimiento abierto.

Las diferentes zonas del escurrimiento son las siguientes:

- aguas arriba (definido como AA) de la duna, el flujo es uniforme
- entre el pie de la duna y la cresta de la duna, el flujo se acelera
- entre la cresta de la duna y el punto donde el flujo vuelve a ocupar toda la columna de agua se produce una capa de mezcla debido a la separación del flujo
- aguas abajo (definido como aa) del punto de unión el flujo se re-establece transportando estructuras turbulentas coherentes producidas en la capa de mezcla

Los mecanismos de transporte de sedimento están íntimamente ligados a estos cuatro tipos de flujo que existen en presencia de una duna.

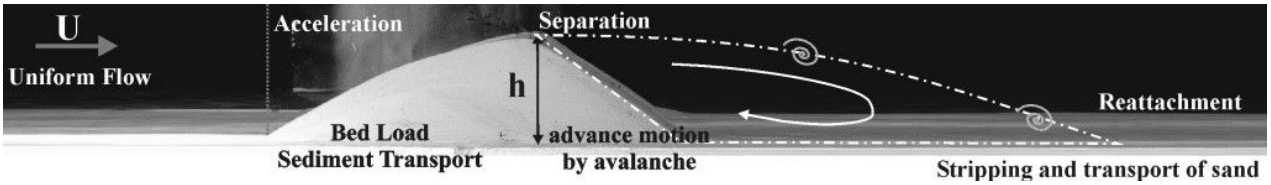

Figura 1.- Ilustración de los mecanismos de transporte (Rossi 2003)

La aceleración del flujo permite aumentar el esfuerzo de corte hasta que en cierto punto de la duna se vuelve superior al esfuerzo de corte crítico necesario para transportar sedimentos. Aguas abajo de la cresta de la duna, la separación del flujo permite a la arena caer y avanzar produciendo una acumulación de sedimento y un desplazamiento general de la duna por medio de avalanchas localizadas y sucesivas.

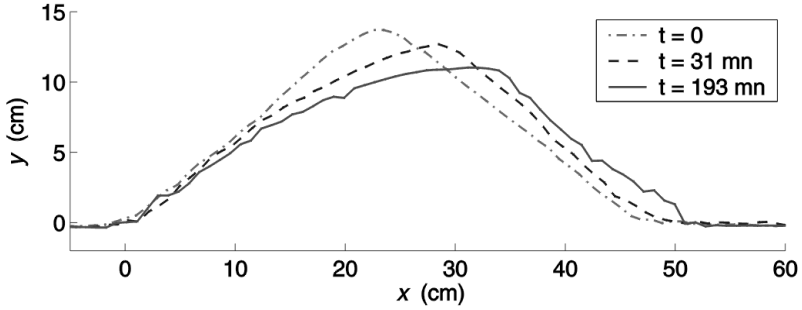

Figura 2.- evolución de la morfología de una duna (Rossi, 2003)

Nuestro objetivo consiste en modelar el transporte de sedimento de fondo sobre la duna. El transporte de sedimento suspendido no se tomará en cuenta en este caso debido a que en los experimentos la velocidad del escurrimiento es muy cercana a la velocidad límite de inicio del movimiento, por lo que el transporte de sedimento suspendido es poco relevante.

En el caso de una única duna de dimensiones importantes respecto de la profundidad del flujo, como la consideramos en este artículo (altura inicial de la duna es cercana a la mitad de la profundidad del flujo AA), el espesor de la capa límite debe ser claramente diferente AA de la duna, y en la parte en donde el flujo se acelera. En la zona de aceleración, el transporte de sedimentos es impermanente debido a que la duna se encuentra en movimiento. Las observaciones experimentales de la duna realizadas por Rossi (2003) servirán evaluar la parametrización producida por él además de otros modelos de transporte de sedimento que utlizan directamente el esfuerzo de corte producido por el flujo.

Descripción del Experimento

Los experimentos de Rossi y Michallet (2003), nos entregan datos, sobre el movimiento de una duna sometido a un flujo uniforme. Los experimentos se desarrollaron en un canal de PVC, de 350 mm de ancho, 400 mm de alto, y 10 m de largo, con una sección de paredes de vidrio de 2 m. Para los experimentos, el canal se llena de agua y el sedimento se deposita uniformemente en todo el ancho para luego crear una duna triangular con una pendiente crítica de avalancha (de más o menos 32 grados). Aguas abajo del canal, una compuerta vertical permite controlar el caudal y el nivel. El flujo modifica entonces la forma de la duna. Los perfiles del lecho fueron obtenidos con sonda de ultrasonido viajando a velocidad constante. Un pulso de frecuencia 2.25 MHz es reflejado por el fondo y la señal capturada. El tiempo de viaje de la pulsación ultrasónica es entonces convertido en

profundidad. Los perfiles de velocidad fueron obtenidos con un aparato de velocimetría acústica doppler (Acoustic Doppler Velocimeter). La velocidad media del flujo puede ser deducida con un margen de error de 10%. Nos enfocaremos en dos tipos de experimentos, el primero con una duna constituida de arena gruesa (d_{50}=0.9 mm), y el segundo con una duna hecha de arena más fina (d_{50}=0.2 mm).

Modelación Hidrodinámica

Para la parte hidrodinámica, se empleará un método basado en las ecuaciones de Saint-Venant. Consiste en calcular la superficie libre a partir de las ecuaciones de Saint-Venant estacionarias, unidimensionales y despreciando la fricción.

$$U \cdot H = U_0 \cdot H_0 \qquad [1]$$

$$H_0 + \frac{1}{2g} U_0^2 = H + h + \frac{1}{2g} U^2 \qquad [2]$$

La ecuación de conservación [1] permite expresar U a partir de H, U_0 y H_0, y se inyecta en la ecuación [2]:

$$H^3 + \left(h - H_0 + \frac{1}{2g} U_0^2 \right) H^2 + \frac{1}{2g} U_0^2 H_0^2 = 0 \qquad [3]$$

Por lo que podemos encontrar H resolviendo [3], y a partir de [2] encontrar U, obteniendo directamente la altura de agua y la velocidad media en cada punto del dominio. Elegimos este modelo hidrodinámico por la simplicidad de implementación y la rapidez de cálculo. Para determinar el transporte de sedimento debido al flujo, podemos utilizar la parametrización de Rossi y Michallet (2003) y compararla con fórmulas de transporte basadas en esfuerzos de corte en el fondo.

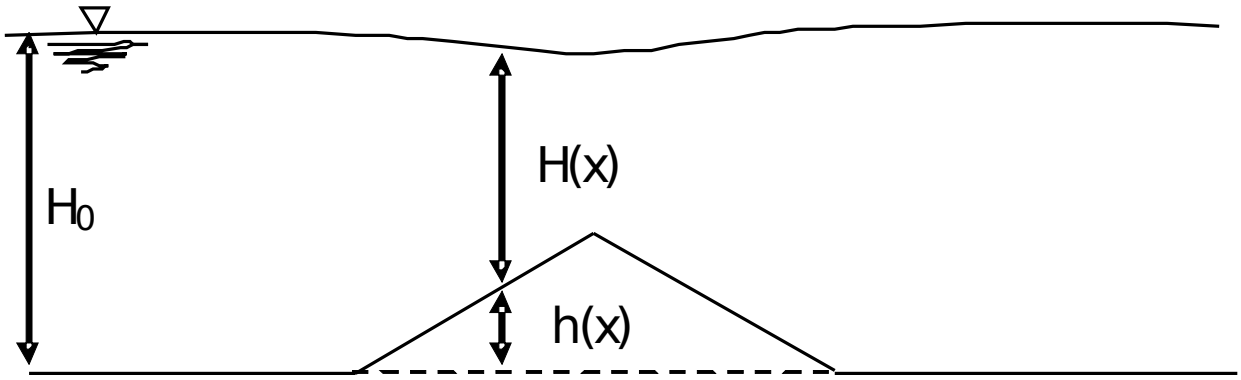

Figura 3.- Esquema de una duna al inicio de los experimentos. La pendiente de la duna corresponde al ángulo de estabilidad del sedimento (32°).

Parametrización de Rossi y Michallet (2003)

Existen muchas relaciones en la literatura para estimar la tasa de transporte de sedimento de fondo con lechos horizontales de arena. El aproche probabilístico (Einstein, 1942) o el aproche energético (Bagnold, 1956), generalmente relacionan el transporte de sedimento con el exceso de esfuerzo de corte. Como el esfuerzo de corte en la duna no puede ser determinado directamente, el transporte de sedimento en la cresta de la duna se relaciona con la velocidad media del flujo sobre la cresta de la duna con la formula de Meyer-Peter and Müller (1948):

$$q_s = A\,U_{top}^3 \qquad [4]$$

o

$$q_s = A\,Cf(\alpha)\left(U_{top}^2 - U_c^2\right)^{3/2} . \qquad [5]$$

La ecuación [5] incluye la velocidad crítica asociada al umbral de esfuerzo de corte que se necesita para iniciar el transporte de arena y un coeficiente de forma $Cf(\alpha)$. Este coeficiente considera los efectos de la aceleración del flujo y la forma de la duna, y el coeficiente A solamente depende del diámetro del arena.

$$Cf(\alpha) = (\tan\alpha)^n = \left(\frac{h - h_c}{x - x_c}\right)^n . \qquad [6]$$

El efecto de la pendiente debe ser considerado para corregir levemente la estimación de la tasa de transporte de sedimento sobre fondos inclinados. La idea es que el transporte de sedimento se ve modificado por la gravedad. En nuestro caso, donde tenemos una gran estructura sedimentaria, las cosas son diferentes. En la parte posterior de la duna, el transporte de sedimento es controlado por un proceso de avalanchas, por lo que el transporte en esa parte es igual al que tiene lugar en la cresta. En la parte de la duna que enfrenta el flujo, la pendiente positiva aumenta el transporte de sedimento bajo el efecto del flujo la capa límite produce un aumento considerable en la velocidad de corte local. Como la aceleración del flujo está relacionada con la pendiente de la duna, la parametrización propuesta por Rossi y Michallet (2003) trata de tomar este efecto en cuenta.

Sand D_{50} (mm)	h_0 (mm)	U_{ext} (mm/s)	U (mm/s)	h_w (mm)	h_c (mm)
0.9	176	362	319	281	0
0.9	128	354	312	281	0
0.9	177	268	236	297	54.6
0.9	177	239	210	306	82.9
0.2	150	338	297	270	0
0.2	150	300	264	283	25.7
0.2	150	280	246	287	44.1
0.2	126.5	275	242	290	48.5
0.2	150	265	233	295	58.1
0.2	134	28	218	304	75.8
0.2	150	240	211	304	82.9

Tabla 1: Condiciones experimentales de deformación de la duna: h_0 es la altura inicial de la duna, U_{ext} es la velocidad AA fuera de la capa límite, U es la velocidad media AA, h_w es la profundidad AA, y h_c es la altura crítica para el inicio del transporte de sedimento sobre la duna.

Sand	U (mm/s)	n	A (s^2/mm)	σ_A (s^2/mm)	σ_A/A
Coarse	all	1	$3.4\ 10^{-6}$	$5.2\ 10^{-7}$	16 %
Fine	≤ 246	4.3	$2.1\ 10^{-5}$	$8.8\ 10^{-6}$	42 %
Fine	≥ 264	1.4	$2.5\ 10^{-6}$	$5.1\ 10^{-7}$	21 %

Tabla 2: Valores de los coeficientes (5-6): *n*, *A* y la desviación estándar de *A*, para las diferentes arenas usadas.

Queremos a partir de esos datos experimentales y de la parametrización asociada, poder validar la metodología de simulación propuesta y cuantificar las mejoras obtenidas respecto a enfoques tradicionales. En nuestro caso, el transporte de sedimentos se estimará a partir del esfuerzo de corte sobre el fondo calculado de dos maneras distintas: por un modelo convencional (Coleman 2006), y por un modelo de capa límite turbulenta de tipo k-ω (Wilcox, 1992).

Modelo de capa límite turbulenta de Wilcox (1992)

La velocidad de fricción se estima a partir de un modelo de capa límite turbulenta unidimensional de tipo k-ω (Wilcox, 1992). Para encontrar la velocidad de fricción, es necesario resolver el siguiente sistema al interior de la capa límite turbulenta:

$$\frac{\partial u}{\partial t}=-\frac{1}{\rho_0}\frac{\partial p}{\partial x}+\frac{\partial}{\partial z}\left(\left(\nu+\nu_t\right)\frac{\partial u}{\partial z}\right) \quad [7]$$

$$\frac{\partial k}{\partial t}=\nu_t\left(\frac{\partial u}{\partial z}\right)^2-\beta*k\omega+\frac{\partial}{\partial z}\left(\left(\nu+\sigma*\nu_t\right)\frac{\partial k}{\partial z}\right) \quad [8]$$

$$\frac{\partial \omega}{\partial t}=-\nu_t\left(\frac{\partial u}{\partial z}\right)^2-\beta\omega^2+\frac{\partial}{\partial z}\left(\left(\nu+\sigma\nu_t\right)\frac{\partial \omega}{\partial z}\right) \quad [9]$$

Donde u es la velocidad horizontal dentro de la capa límite, k es la energía cinética turbulenta, y ω la tasa de disipación de energía.

Tenemos también la relación siguiente:

$$\frac{\partial p}{\partial x}=\rho_0 g\frac{\partial h}{\partial x} \quad [10]$$

Por lo que a causa de la forma de la duna, el gradiente de presión va a cambiar, lo que influirá en el esfuerzo de corte. Es posible entonces determinar la velocidad de fricción sobre todo el dominio a partir de la forma de la duna. Luego, podemos determinar la tasa de transporte de sedimento, a partir de la formula de Meyer Peter & Müller (1948). Para calcular la velocidad de fricción, nos enfocamos en la parte de pendiente positiva de la duna, donde el flujo se acelera. Entonces para cada punto calculamos el perfil de velocidad cerca del fondo a partir de un modelo k-ω. El modelo k-ω utiliza la velocidad media y del gradiente de presión para obtener la estimación del esfuerzo de corte sobre el fondo. El esfuerzo de corte se determina a partir de la relación:

$$\tau_0=\rho u_{*0}^2 \quad [11]$$

donde

$$u_{*0}=\rho\left(\nu+\nu_t\right)\frac{\partial u}{\partial z} \quad [12]$$

Estimación del esfuerzo de corte en el fondo (Coleman 2006)

Para poder evaluar los resultados, hemos utilizado la formula de Coleman (2006) para estimar los esfuerzos de corte sobre el fondo.

Las teorías de formación de duna reconocen que los cambios de fase entre el flujo, el lecho, y el transporte de sedimento son necesarios para que se modifique la forma de la duna. Para cada test, podemos evaluar el esfuerzo de corte local a partir de la ecuación [11] en cada punto de la parte anterior de la duna asumiendo un perfil logarítmico para la velocidad:

$$u_{¿0} = \bar{u} / \left[2.5 \ln (z / z_0) \right] \qquad [13]$$

y adoptando para la altura de rugosidad hidrodinámica el valor (Nikuradse, 1933):

$$z_0 = d_{50} / 30 \ . \qquad [14]$$

Modelación de la evolución morfodinámica del fondo (Marieu 2008)

Para estimar la evolución del fondo, vamos a utilizar las estimaciones de transporte de sedimento de fondo en la parte río arriba de la duna y resolver la siguiente ecuación de conservación de la masa para la fase sólida:

$$\frac{\partial h}{\partial t} + \frac{1}{1-n} \frac{\partial q}{\partial x} = 0 \qquad [15]$$

Donde *n* es la porosidad de la arena.

Esta ecuación se resuelve a partir de un esquema de tipo NOCS (Non Oscillatory Central Scheme) utilizado por Marieu (2008). Este esquema es una extensión natural de segundo orden del esquema de primer orden de Lax-Freidrich.

El cálculo de elevación de fondo *h* al paso de tiempo *n+1* se calcula a partir de una etapa de corrección:

$$h_i^{n+1} = \frac{1}{2}(h_{i+1}^n - h_{i-1}^n) + \frac{1}{4}(h_{i-1}^{'} - h_{i+1}^{'}) - \frac{\Delta t}{2\Delta \mathrm{x}}(q_{i+1}^{n+\frac{1}{2}} - q_{i-1}^{n+\frac{1}{2}}) \qquad [16]$$

donde *h'* es la aproximación de la derivada de la elevación del fondo *h*, y $q_i^{n+\frac{1}{2}}$ es la aproximación de la derivada del flujo q en el punto i en el tiempo n+1/2:

$$q_i^{n+\frac{1}{2}} = q(h_i^{n+\frac{1}{2}}) \qquad [17]$$

$$h_i^{n+\frac{1}{2}} = h_i^n - \frac{\Delta t}{2\Delta \mathrm{x}} q_i^{'} \qquad [18]$$

Para calcular las aproximaciones de las derivadas de *h* y *q*, se utilizan los β-limitadores. Entonces, la aproximación de la derivada de una función φ en el punto i se define de la siguiente manera:

$$\varphi_i^{'} = MinMod\left[\beta(\varphi_i - \varphi_{i-1}), \frac{1}{2}(\varphi_{i+1} - \varphi_{i-1}), \beta(\varphi_{i+1} - \varphi_i) \right] \qquad [19]$$

donde β es el parámetro del limitador, y la función MinMod se define por:

$$MinMod\left(x_1, x_2, x_3\right) = \begin{cases} \min\left(x_1, x_2, x_3\right) & si\ x_k > 0\ \forall k = 1,2,3 \\ \max\left(x_1, x_2, x_3\right) & si\ x_k < 0\ \forall k = 1,2,3 \\ 0 & si\ no \end{cases} \quad [20]$$

Cuando β=1, se trata del limitador MinMod, y cuando β=2, se habla del limitador Superbee, más preciso que el limitador MinMod pero tiende a aplanar más las crestas.

A partir de la velocidad de fricción, se calcula una tasa de transporte a partir de la fórmula de Meyer Peter & Müller. Se determina el volumen de sedimento que pasa la cresta de la duna, y se aplica el modulo de avalancha para que se siga moviendo la duna.

Es una necesidad incluir un algoritmo para modelar las avalanchas de arena que se producen en la cresta de la duna. De no tener avalanchas, después de la etapa morfológica, algunas pendientes pueden tener pendientes superiores a la pendiente máxima que puede existir físicamente, por lo que se debe manejar con precaución el cálculo de estas pendientes. Marieu (2008) propone buscar las celdas de la grilla donde la pendiente local es superior a la pendiente crítica para corregirlas hasta llegar al ángulo de reposo del sedimento. La corrección se efectúa cambiando los dos nodos de la celda de tal manera que el volumen de sedimento quede constante. El algoritmo es entonces iterado hasta llegar a la convergencia.

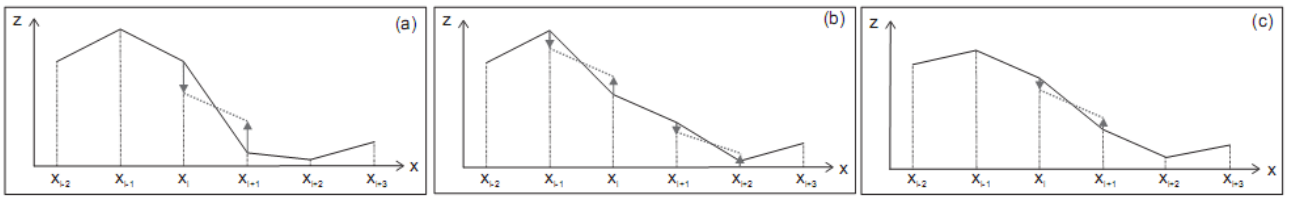

Figura 4 dos iteraciones del algoritmo de avalancha descrito por Marieu (2007). (a) fondo inicial, (b) primera iteración, (c) segunda iteración. Las pendientes superiores al ángulo de estabilidad son corregidas, resultando una transferencia de sedimento de la cresta hacia la parte baja de la duna. Las líneas sólidas representan el fondo, y las líneas en puntos representan el ángulo de reposo del sedimento.

Evaluación de resultados

Queremos lograr modelar de manera satisfactoria los distintos fenómenos que ocurren cuando un flujo interactúa con una duna de arena. Los datos proporcionados permiten predecir la evolución de la cresta de la duna según el tipo de arena, y la altura de agua y velocidad AA, y esperamos poder llegar a una estimación precisa del movimiento de la duna en el tiempo. Además nos interesa evaluar las diferencias respecto a los distintos modelos hidrodinámicos. Queremos también obtener series de tiempo del esfuerzo de corte para ver su evolución con el cambio morfológico de la duna debido al flujo.

Para verificar que los resultados son concordantes, utilizamos una formula de transporte determinada por Rossi y Michallet (2003) respecto al movimiento de la duna.

No se lograron al momento de la redacción de este articulo resultados satisfactorios con el modelo de capa límite turbulenta k-ω. Las condiciones iníciales presentan gradientes de presión importantes en la zona de la pendiente de la duna que se encuentre al ángulo de reposo. Por consiguiente, el esfuerzo de corte calculado es relativamente fuerte, y la tasa de transporte de sedimento resulta poco realista. Sin embargo, comparamos los resultados experimentales con la parametrización de Rossi y Michallet (2003) y la estimación del esfuerzo de corte de Coleman (2006).

El esfuerzo de corte estimado por la fórmula de Coleman (2006) se encuentra en la figura 5. Notamos que el esfuerzo de corte tiende a aumentar cuando se acerca a la cresta de la duna, lo que concuerda con la realidad, donde la aceleración del flujo produce un aumento mayor del esfuerzo de corte.

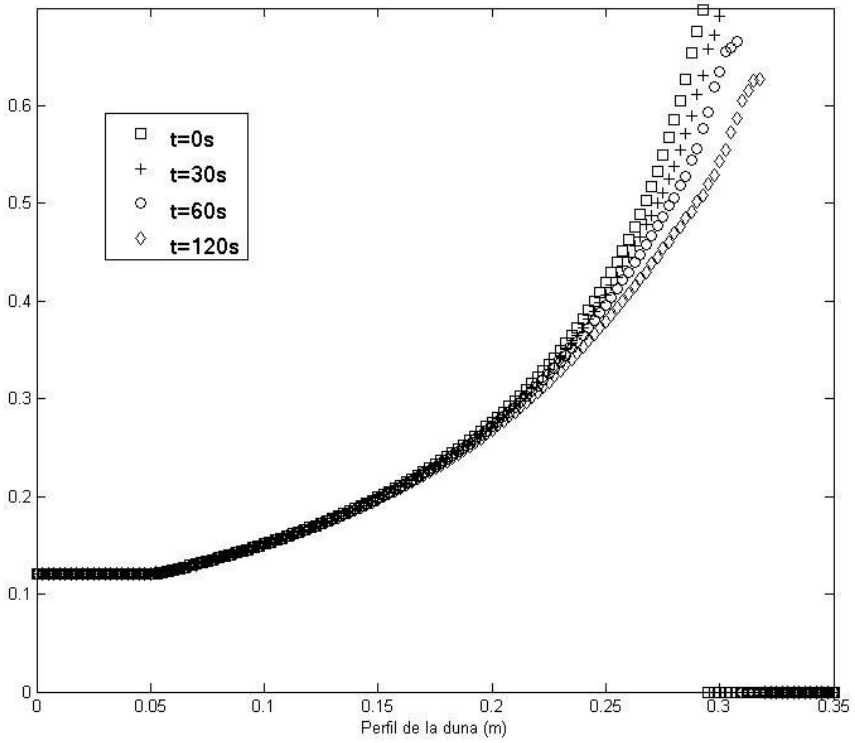

Figura 5- Evolución del esfuerzo de corte, durante el tiempo. Experimento 1, d_{50}=0.9mm, h_0=0.177 m, x_c=0.134 m, h_c=0.0829 m; Uw=0.210 m/s, H_w=0.306 m

La primera observación es respecto a la evolución de la posición de la cresta de la duna (Figuras 6 y 7). Los dos modelos tienden a desplazar la cresta de la duna más rápido que en los experimentos. También se nota que el modelo de Rossi y Michallet, a pesar de tener diferencias en la posición, llega a un límite después de cierto tiempo logrando un estado cuasi estable, mientras que en el modelo con esfuerzo de corte, la cresta de la duna sigue avanzando regularmente en el tiempo, lo que muestra que el equilibrio no se ha logrado aún.

El hecho que los modelos aumenten el desplazamiento real de la duna puede deberse a la implementación del modulo de avalancha en la etapa morfodinámica, ya que existen distintas maneras de encontrar la cresta de la duna antes de utilizar el modulo de avalancha. Por lo visto, es necesario validar el modelo de avalancha comparando con otro modelo, tal como el de Paarlberg, (2007), donde el sedimento que pasa la cresta de la duna se distribuye sobre toda la parte posterior de la duna.

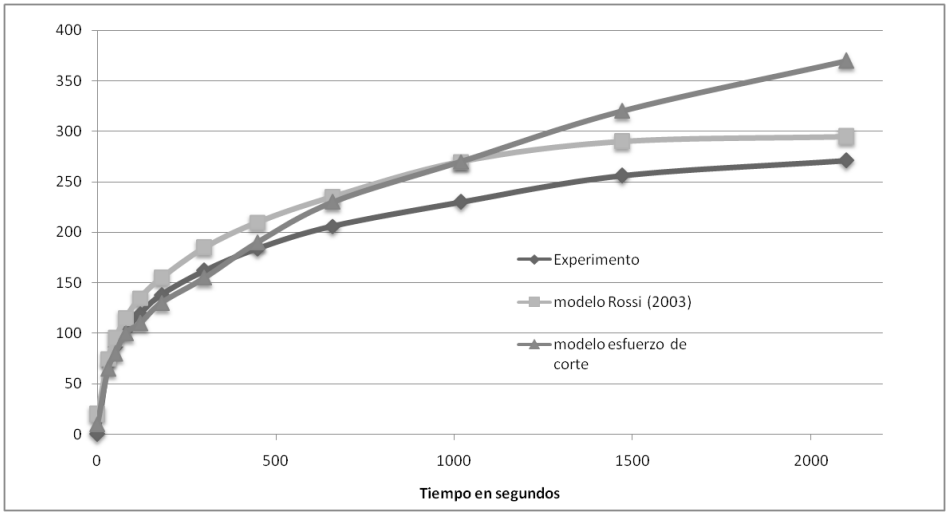

Figura 6- Evolución de la posición de la cresta de la duna en mm, durante el tiempo. Experimento 1, d_{50}=0.9mm, h_0=0.177 m, x_c=0.134 m, h_c=0.0829 m; Uw=0.210 m/s, H_w=0.306 m

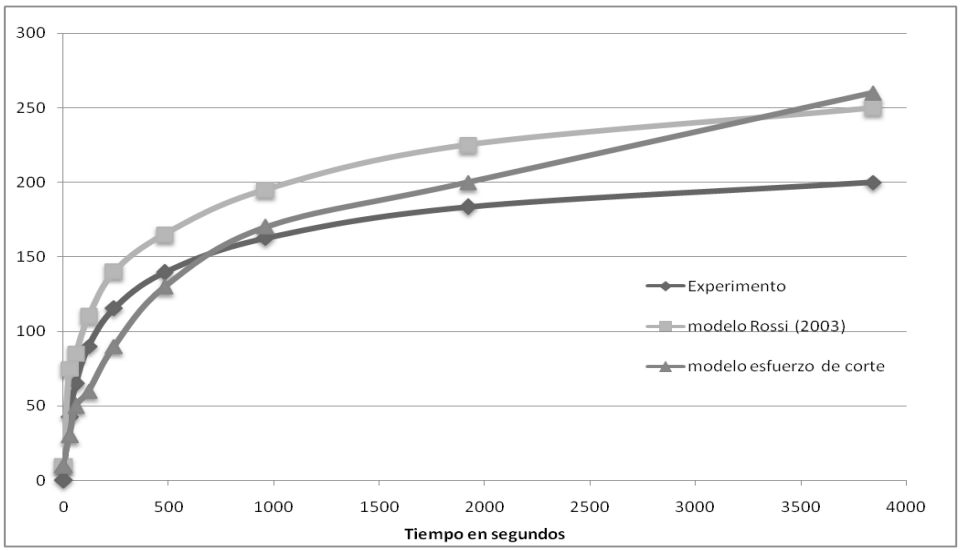

Figura 7.- Evolución de la posición de la cresta de la duna en mm, durante el tiempo. Experimento 2, d_{50}=0.9mm, h_0=0.177 m, x_c=0.088 m, h_c=0.054 m; Uw=0.235 m/s, H_w=0.297 m

Cuando observamos la evolución de la altura de la cresta (Figuras 8 y 9), podemos notar que los modelos logran acercarse a los datos experimentales. Para el experimento 2, se nota igualmente que el modelo de Rossi y Michallet llega a un cierto equilibrio, para tiempos parecidos a los datos experimentales, mientras que el modelo de esfuerzo de corte sigue transportando más sedimento.

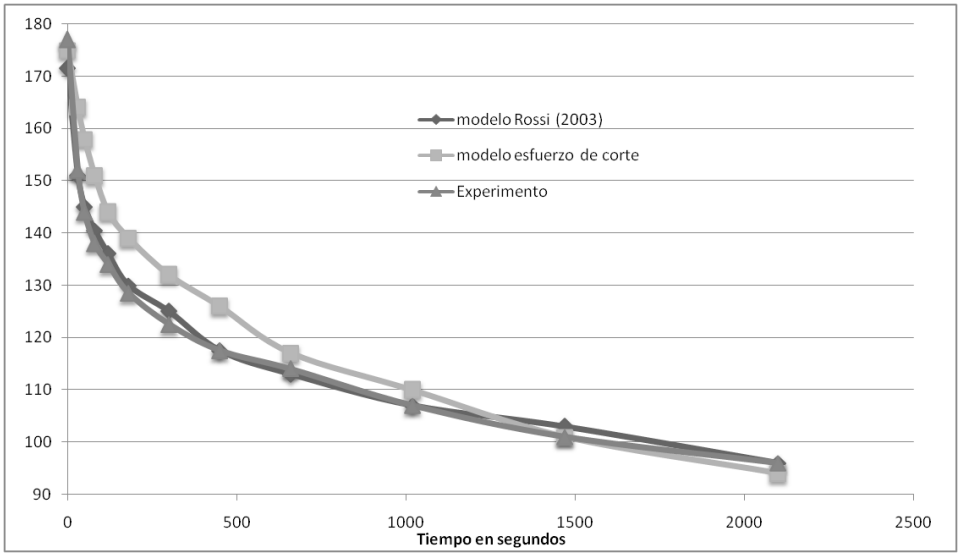

Figura 8.- Evolución de la altura de la cresta de la duna en mm, durante el tiempo. Experimento 1, d_{50}=0.9mm, h_0=0.177 m, x_c=0.134 m, h_c=0.0829 m; Uw=0.210 m/s, H_w=0.306 m

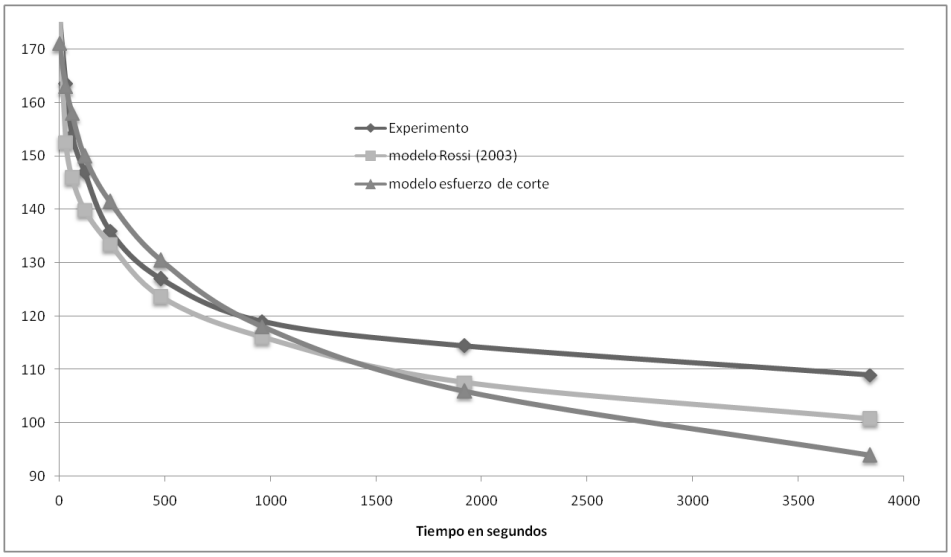

Figura 9.- Evolución de la altura de la cresta de la duna en mm, durante el tiempo. Experimento 2, d_{50}=0.9mm, h_0=0.177 m, x_c=0.088 m, h_c=0.054 m; Uw=0.235 m/s, H_w=0.297 m

CONCLUSIONES

Modelamos la evolución morfológica de una duna sometida a un flujo uniforme, de manera unidimensional. El transporte de fondo en la parte AA de la duna es estimado a partir del esfuerzo de corte calculado a partir de una parametrización de Coleman (2006), y evolución morfodinámica de la duna se modela a partir de un esquema de tipo NOCS acoplado con un módulo de avalancha localizado. Comparamos los datos experimentales obtenidos con una parametrización del transporte de sedimento a partir de la pendiente de la duna (Rossi y Michallet, 2003), y con un modelo que determina el transporte a partir de una parametrización del esfuerzo de corte (Coleman, 2006).

Cabe destacar que a pesar de los mejores resultados obtenidos por el modelo realizado a partir de la parametrización de Rossi y Michallet (2003), es necesario para que ese modelo funcione conocer la altura crítica donde se inicia el transporte de sedimento sobre la duna, lo que se puede determinar solamente por el esfuerzo de corte. Es la razón por la cual un modelo que permita modelar de manera satisfactoria el esfuerzo de corte en fondos con pendientes fuertes permitiría una mejor modelación del transporte de sedimente sobre una duna.

REFERENCIAS

Bagnold, R.A., (1956), "The flow of cohesionless grains in fluids", *Phil. Trans. Roy. Soc. London, Ser. A*, 249 (964), 235-297.

Coleman, S. E., Nikora, V. I., McLean, S. R. Clunie, T. M., Schlicke, T., and Melville W. (2006), "Equilibrium hydrodynamics concept for developing dunes", *Physics of fluids, 18, 105104*

Einstein, H.A., (1942), "Formulae for transportation of bed-load", *Trans. ASCE*, **107**, 561-577.

Marieu, V., Bonneton, P., Foster, D. L. and Ardhuin F. (2008), "Modeling of vortex ripple morphodynamics", *J. Geophys. Res., 113, C09007*

Meyer-Peter, E., and R. Müller (1948), "*Formulas for bed-load transport"*, in Proceeding of the International Association of Hydraulic Research, 3rd Annual Conference, Stokholm, pp. 39– 64.

Nikuradse, J. (1933), "*Stromungsgesestz in rauhren rohren, vdi-forschungsheft 361"*

Paarlberg, A. J., Dohmen-Janssen, C. M., Hulscher, S. J. M. H. and Termes P. (2009), "Modeling river dune evolution using a parametrization of flow separation", *J. Geophys. Res., 114, F01014*

Rossi, L., Michallet, H. and Bonneton, P. (2003) "Morphodynamique d'une dune, couplage avec l'écoulement", *9ème congrès de l'Association des Sédimentologistes Français.*

Wilcox, D. C., (1992) "The remarkable ability of turbulence model equations to describe transition", *Fifth Symposium on Numerical and Physical aspects of Aerodynamical Flows*, 13– 15 January, Calif. State Univ., Long Beach, Calif., 1992.

Appendix D

Journées Nationales Génie Civil - Génie Cotier - June 2012 - Cherbourg - France -

Distributions verticales d'asymétrie et de skewness dans une couche limite sur fond mobile : comparaison expériences-modèle *k-ω*

Léandro SUAREZ [1,2], Eric BARTHELEMY [2], Céline BERNI [2], Julien CHAUCHAT [2]

1. Departamento de Ingeniería Hidráulica y Ambiental, Pontificia Universidad Católica de Chile, Vicuña Mackenna 4860, casilla 306, correo 221, Santiago de Chile, Chile. *lsuarez2@uc.cl*
2. Laboratoire des Ecoulements Géophysiques et Industriels (UJF, GINP, CNRS), BP53, 38041 Grenoble Cedex 9, France *eric.barthelemy@legi.grenoble-inp.fr ; celine.berni@legi.grenoble-inp.fr ; julien.chauchat@legi.grenoble-inp.fr*

Résumé :
Lorsque les vagues se rapprochent du rivage, leurs non linéarités augmentent, et prennent une importance considérable dans l'interaction entre les vagues et le fond. Ces interactions se produisent principalement dans la couche limite turbulente.
Des expériences sur un modèle physique de vagues non linéaires sur fond mobile (BERNI, 2011), nous permettent d'obtenir les profils de vitesse ainsi que l'évolution du fond de manière couplée. Les données expérimentales obtenues suggèrent une transformation au sein de la couche limite, le skewness adimensionnel augmentant et l'asymétrie adimensionnelle diminuant au fur et à mesure que l'on se rapproche du fond. Par ailleurs on constate (DICK & SLEATH, 1991) que l'échelle verticale de diffusion de cette couche limite est plus importante sur fond mobile que sur fond fixe.
Notre objectif est de reproduire ces 2 aspects à partir d'un modèle de couche limite turbulente de type *k-ω* (WILCOX, 2006 ; GUIZIEN *et al*., 2003) et de pouvoir obtenir une meilleure description sur l'évolution des non-linéarités des vagues au sein de la couche limite. Le modèle numérique utilisé est capable de calculer la couche limite turbulente sur un fond fixe. En modélisant les mouvements du fond et en les couplant avec l'évolution de la couche limite, nous reproduisons les principales caractéristiques de l'évolution de la couche limite turbulente sur un fond mobile.
Mots-clés :
Couche limite turbulente – Non-linéarité – Fond mobile – Modèle numérique *k-ω*
Abstract:
As the waves approach the coast, non-linearities become increasingly important. The interactions between the waves and the bottom occur within the turbulent boundary layer, which is why its study represents a mean to understand the evolution of these non-linearities near the coast.

Experimental measurements (BERNI, 2011), concerning non-linear waves on a mobile bed, provide velocity profiles and bed position in a coupled way. These data suggest a transformation within the boundary layer, with a non-dimensional skewness increasing and a non-dimensional asymmetry diminishing as we approach the bottom.
We intend to reproduce this phenomenon with a k-ω numerical model (WILCOX, 2006; GUIZIEN *et al.*, 2003), and get a better resolution on the non-linearities evolution inside the turbulent boundary layer. The numerical model is able to determine the velocity within the boundary layer on a fixed bed, by modeling the bed mobility and coupling it with the k-ω model, we are able to reproduce the experimental results observed, which would indicate that the bed mobility is responsible for a vertical diffusion within the boundary layer.
Keywords:
Turbulent boundary layer – Non linearity – Mobile bed – k-ω numerical model

1. Introduction

La couche limite turbulente sous les vagues est sujette à différents processus, et représente une zone importante pour déterminer la contrainte de cisaillement au fond ainsi que les processus de transport de sédiment. A l'approche de la côte, la levée des vagues produit des non-linéarités, qui, influent sur la contrainte de cisaillement sur le fond. La connaissance de cette contrainte est utile pour permettre d'estimer le transport sédimentaire, d'autant plus que celui-ci s'effectue sur fond mobile.
Dans cet article, nous nous limiterons à l'étude de la couche limite turbulente sous des vagues non-linéaires et sur un fond mobile. De récentes expériences sur fond mobile (BERNI, 2011) ont permis de dégager d'intéressantes propriétés concernant les non-linéarités dans la couche limite turbulente. Le but de cet article est de reproduire les comportements observés à l'aide d'un modèle numérique 1D de type k-ω (WILCOX, 2006 ; GUIZIEN *et al.*, 2003) qui donne des résultats sur fond fixe.

2. Matériel et méthodes

2.1 Expérience

L'expérience s'est déroulée dans le canal à houle du Laboratoire des Écoulements Géophysiques et Industriels (LEGI) dont le schéma se trouve figure 1. Ce canal mesure 36 m de long, 55 cm de large et 1,30 m de haut, et ses parois latérales sont constituées de verre. Le sédiment présent dans le fond du canal est en matière plastique (PMMA) de faible masse volumique (ρ_s=1190 g L^{-1}), ce qui permet d'assurer une similitude des nombres de Froude et de Shields.

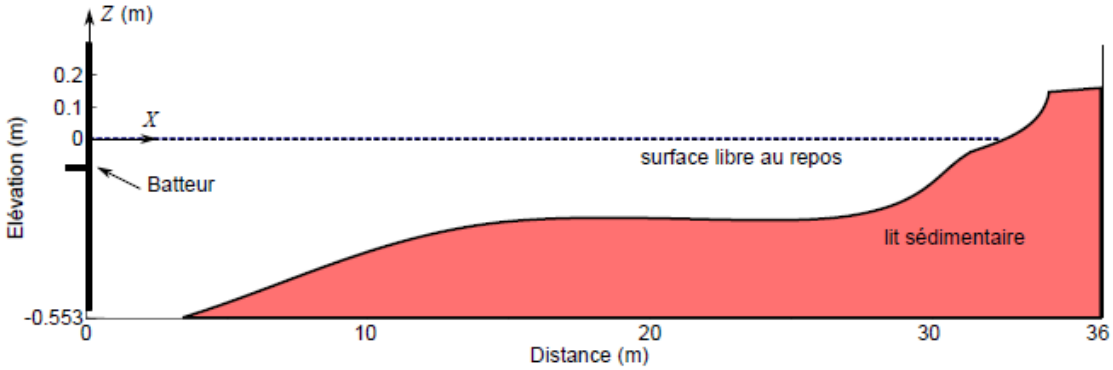

Figure 1. Schéma du canal à houle du LEGI. Un batteur piston en x=0 engendre deux paquets d'ondes, bichromatiques.

La houle utilisée pour l'expérience est de type bichromatique, i.e. la somme de deux ondes sinusoïdales de fréquence proche et d'amplitude égale, afin d'obtenir une onde de haute fréquence de période T=2,5 s modulée par une onde de basse fréquence (figure 2). Le forçage de l'expérience consiste en une série de 23 paquets d'onde, et nous nous focalisons sur une séquence de 10 secondes dans chaque paquet, correspondant à 4 vagues passant au droit des capteurs, comme indiqué sur la figure 2.

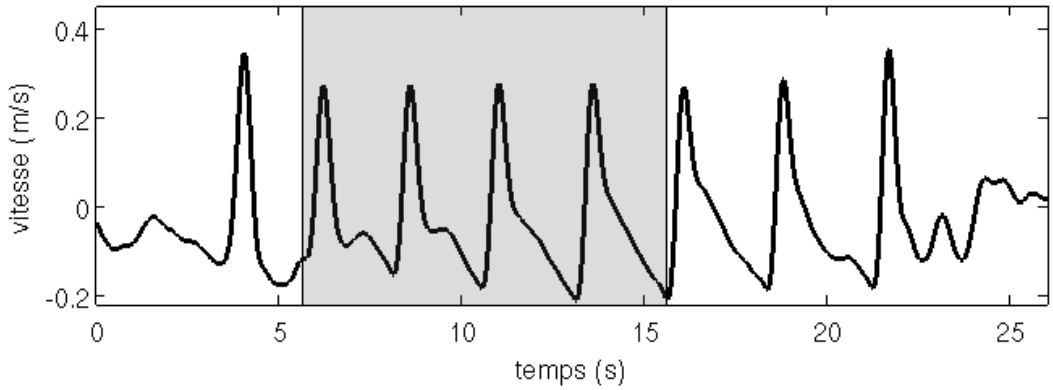

Figure 2. Vitesse moyenne sur les 23 réalisations du paquet d'ondes envoyé à chaque réalisation. En grisé, les 10 secondes prises en compte dans chaque réalisation.

A l'aide d'un profileur acoustique ADVP, BERNI (2011) obtient la position du fond, ainsi que le profil de vitesse, avec une résolution spatiale verticale de l'ordre de 3 mm. Ce profil de vitesse permet de déterminer les valeurs de skewness *Sk*, caractérisant une dissymétrie en vitesse, ainsi que d'asymétrie *As*, qui caractérisent une dissymétrie d'accélération à toutes les altitudes. Le Skewness et l'Asymétrie sont calculés comme les moments d'ordre 3 de la vitesse et de l'accélération respectivement.

Alors que l'asymétrie diminue au fur et à mesure que l'on se rapproche du fond, le skewness augmente avant de baisser à nouveau. Nous voulons voir si ce comportement est reproduit par un modèle numérique 1D de type *k-ω*, décrit ci-après.

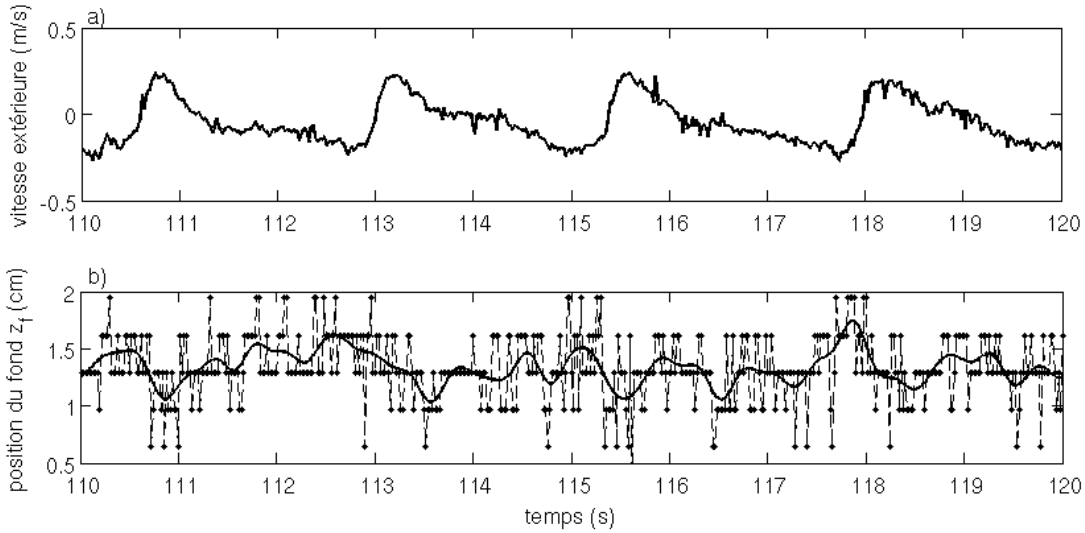

Figure 3. a) vitesse u à l'extérieur de la couche limite, pendant 10 secondes. b) positions du fond mesurées (traits tiretés) et filtrées (trait plein).

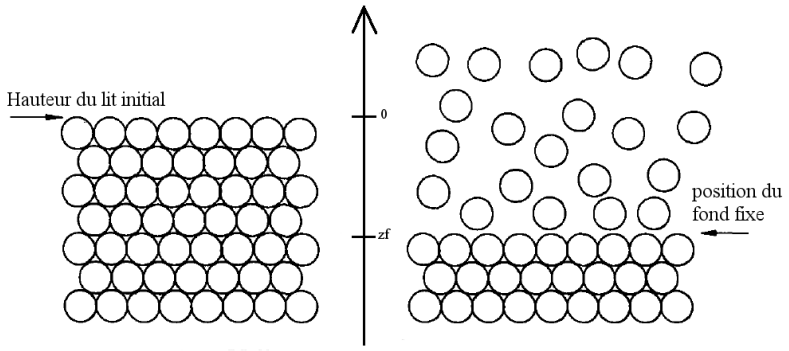

Figure 4. Définition du lit initial et de la position du lit fixe d'après DICK & SLEATH (1991). La position z=0 correspond à la hauteur du lit initial.

2.2 Modèle numérique

Pour la partie numérique nous utiliserons une modèle de couche limite turbulente 1D de type *k-ω* (WILCOX 2006 ; GUIZIEN *et al.*, 2003) dans sa version à bas nombre de Reynolds. La vitesse horizontale dans la couche limite *u*, l'énergie cinétique turbulente *k* et le taux de dissipation d'énergie *ω* sont solutions des équations (1-3) :

$$\frac{\partial u}{\partial t} = -\frac{1}{\rho}\frac{\partial \bar{P}}{\partial x} + \frac{\partial U}{\partial t} + \frac{\partial}{\partial z}\left((\nu + \nu_t)\frac{\partial u}{\partial z}\right) \quad (1)$$

$$\frac{\partial k}{\partial t} = \nu_t \left(\frac{\partial u}{\partial z}\right)^2 - \beta^* k\omega + \frac{\partial}{\partial z}\left((\nu + \sigma_k \nu_t)\frac{\partial k}{\partial z}\right) \quad (2)$$

$$\frac{\partial \omega}{\partial t} = \alpha \nu_t \frac{\omega}{k}\left(\frac{\partial u}{\partial z}\right)^2 - \beta\omega^2 + \frac{\partial}{\partial z}\left((\nu + \sigma_\omega \nu_t)\frac{\partial \omega}{\partial z}\right) \quad (3)$$

Les coefficients et conditions aux limites à utiliser sont explicités dans (GUIZIEN *et al.*, 2003). La série temporelle de vitesse extérieure $u_\infty(t)$ utilisée comme condition à la limite pour le modèle numérique, est la série de vitesse obtenue expérimentalement à la hauteur pour laquelle on observe le maximum de la vitesse *Urms*, qui correspond à $z=3,6$ *cm*. Cette vitesse est celle utilisée dans les 23 séquences, mises bout à bout, et on itère le modèle numérique jusqu'à obtenir une convergence suffisante.
Concernant la rugosité équivalente k_s utilisée dans le modèle, celle ci est prise égale à $k_s=5\theta d_{50,}$ comme suggéré pour des écoulements de type sheet-flow par (WILSON, 1989 ; DICK & SLEATH, 1991), où θ représente le nombre de Shields, et d_{50} le diamètre médian du sédiment.

2.3 Caractéristiques des évolutions du lit fixe

Grâce aux données fournies par l'ADVP, nous pouvons déterminer la position $z_f(t)$ du niveau du fond fixe (BERNI, 2011). La résolution verticale de l'ordre de 3 mm s'observe sur la figure 5. Néanmoins, la position aléatoire du fond z_f peut être modélisée par une fonction de densité de probabilité, dont les paramètres statistiques sont ceux déterminés empiriquement. Nous pouvons voir sur la figure 5, une distribution normale obtenue avec la déviation standard de la position du fond, ainsi qu'une distribution de Pearson de type IV ayant les mêmes moments d'ordre 2, 3 et 4 que la distribution.

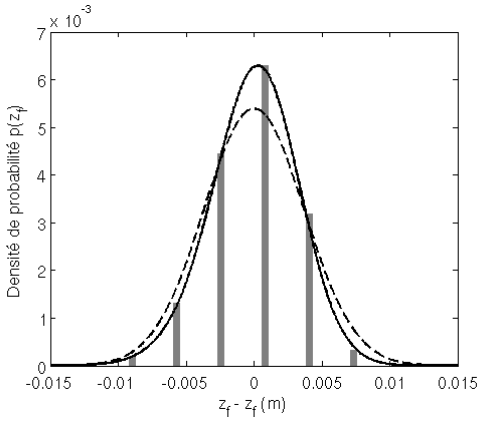

Figure 5. fonctions de densité de probabilité p(zf) équivalente à la distribution des positions du fond, qui correspondent à une distribution normale (traits tiretés) et à une distribution de type Pearson (trait plein) avec les mêmes paramètres statistiques. L'histogramme représente la distribution des données expérimentales.

3. Résultats

3.1 Modèle numérique sur fond fixe

Les résultats obtenus avec le modèle numérique k-ω sur fond fixe (figure 6) montrent que le modèle numérique reproduit le comportement observé lors de l'expérience, c'est à dire une augmentation de la skewness près du fond, ainsi qu'une diminution de l'asymétrie, mais le pic ne se situe pas à la même hauteur. En effet, en définissant $\delta=(2\nu/\omega)^{0,5}$ qui correspond à la longueur de Stokes, le modèle numérique sur fond fixe nous donne un maximum de skewness pour $z=2\delta$, contre un maximum situé à $z=25\delta$ pour l'expérience, et la vitesse *Urms* prédit une vitesse maximale pour $z=3.5\delta$, alors que les données expérimentales situent le pic à $z=35\delta$. Il semble que le modèle numérique est capable de reproduire les phénomènes non-linéaires observés dans la couche limite, mais la diffusivité verticale n'est pas suffisante. Si on regarde les résultats obtenus avec une rugosité 10 fois supérieure aux valeurs théoriques pour des couches limites oscillantes sur fond mobile, on observe bien sur la figure 6 une diffusion verticale des valeurs moyennes de *Urms*, *As* et *Sk*, mais pas suffisantes pour pouvoir expliquer la diffusivité verticale des valeurs expérimentales.

3.2 Effets de fond fixe variable

Nous voulons donc vérifier si en couplant le modèle numérique, implémenté pour un fond fixe, avec les positions du fond z_f, il est possible d'expliquer en partie cette diffusion verticale observée expérimentalement.

Nous disposons de manière synchronisée d'une série temporelle de vitesse $u_\infty(t)$ et de position du lit $z_f(t)$. On construit alors à l'aide du modèle numérique k-ω une série synchronisée de vitesse de $u(z,t)$ pour toute altitude dans la couche limite. La moyenne d'ensemble sera alors :

$$U(z) = \frac{1}{N}\sum_{j=1}^{N} u(z - z_f(j)) \qquad (4)$$

N étant le nombre total de points de la série de $u_\infty(t)$.

Comme nous pouvons le voir dans la figure 6, ce couplage nous donne des profils de vitesse, d'asymétrie et de skewness en escaliers, du fait de la résolution de l'ADVP qui ne nous permet pas de connaître la position du fond avec plus de précision. On remarque tout de même qu'aux hauteurs correspondantes aux points de mesures, les valeurs du modèle sont proches des valeurs expérimentales pour la vitesse, ainsi que pour le skewness pour des hauteurs inférieures à 20δ.

De façon plus approximative et décorrélée dans le temps, nous pouvons approcher les profils verticaux déterminées expérimentalement par moyenne d'ensemble, comme la convolution du $Urms_0(z)$, $Sk_0(z)$ et $As_0(z)$ (profils verticaux sur fond fixe) par la densité de probabilité $p(z_f)$ des positions du fond, ainsi :

$$Urms(z) = \int_{-\infty}^{\infty} p(z_f) Urms_0(z - z_f) df\, z_f \tag{5}$$

Cette formulation est semblable au couplage avec la position du fond, avec la différence que les positions du lit et les profils de vitesses correspondants ne sont plus synchronisés dans le temps. Une formule similaire est mise en œuvre pour estimer *As(z)* et *Sk(z)*.

Les profils obtenus par convolution (figure 6) donnent des résultats proches des valeurs expérimentales, et ont des pentes semblables aux données expérimentales lorsque l'on se trouve près du fond, pour $z<20\delta$. Ces résultats semblent indiquer que la diffusion verticale au niveau des profils moyens de vitesse, d'asymétrie et de skewness peut en partie s'expliquer par la mobilité du fond, qui agit comme un diffuseur pour les valeurs moyennes. Cependant, certaines caractéristiques des valeurs moyennes échappent à cette approche. En particulier le pic expérimental de skewness en z=25δ.

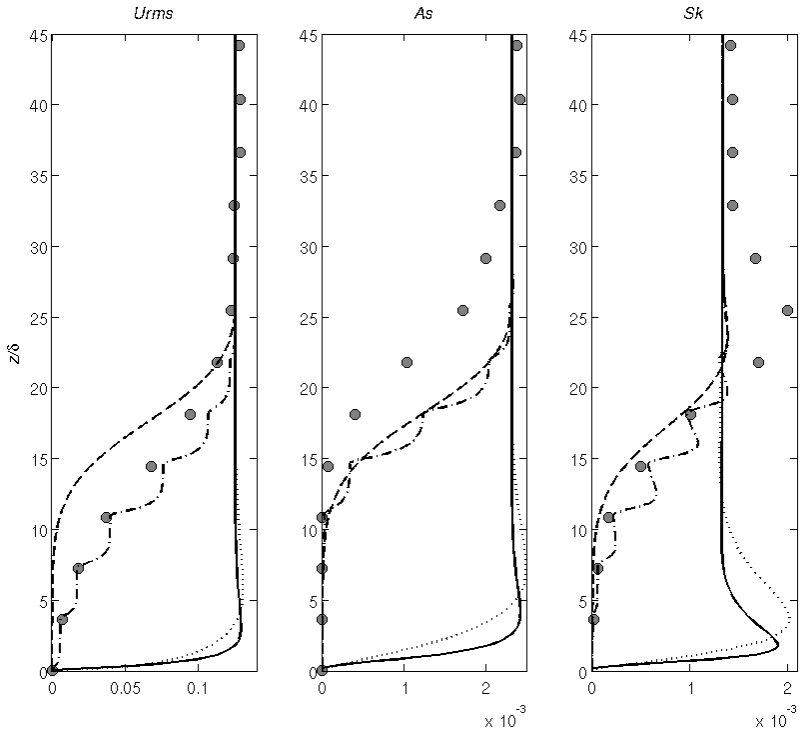

Figure 6. Profils moyens de vitesse Urms, d'asymétrie As et de skewness Sk sur l'ensemble des réalisations. (●) représente les profils obtenus expérimentalement par moyenne d'ensemble à chaque altitude, (-) les profils Urms0, Sk0 et As0 du modèle numérique obtenus en considérant une rugosité de fond égale à 10 fois la rugosité théorique,(--) les profils obtenus par convolution décorrélée avec une distribution de type Pearson, (-.-.) les profils obtenus par couplage entre la position du fond et les profils de vitesses sur fond fixe.

4. Conclusions

Un post-traitement combinant des résultats d'un modèle numérique 1D de type k-ω avec une série temporelle de positions du niveau du lit fixe permet d'obtenir des profils d'asymétrie et de skewness semblables à ceux obtenus avec les données expérimentales, et permettent en partie d'expliquer une diffusivité verticale de ces paramètres sur fond mobile.

L'aspect intéressant de la validation du modèle, est que les caractéristiques non linéaires au sein de la couche limite se retrouvent au niveau des ordres de grandeur. Il faudrait plus en avant étudier l'évolution des non-linéarités au sein de la couche limite, qui sont importantes dans l'estimation de la contrainte de cisaillement et de son déphasage par rapport à la vitesse extérieure à la couche limite.

5. Remerciements

Le premier auteur remercie CONICYT de lui avoir accordé une bourse de doctorat, la Pontificia Universidad Católica, ainsi que le laboratoire LEGI pour son accueil.

6. Références bibliographiques

BERNI C. (2011). *Processus de mobilisation et de transport de sédiments dans la zone de déferlement*, Thèse de l'Université de Grenoble, 231 p.

DICK J.E., SLEATH J.F.A. (1991). *Velocities and concentrations in oscillatory flow over beds of sediment.* Journal of Fluid Mechanics, Vol. 233, pp 165-196. doi:10.1017/S0022112091000447

GUIZIEN K., DOHMEN-JANSSEN C.M., VITTORI G. (2003). *1DV bottom boundary layer modelling under combined wave and current: suspension ejection events and phase lag effects.* J. Geophys. Res., 108(C1): 3016. doi:10.1029/2001JC001292

WILCOX D.C. (2006). *Turbulence Modeling for CFD, 3rd edition.* DCW Industries, Inc., La Canada CA

WILSON K.C. (1989). *Mobile-bed friction at high shear stress,* Journal of Hydraulic Engineering, Vol 115, No 6, pp 825-830. doi:10.1061/(ASCE)0733-9429(1989)115:6(825)

Appendix E

International Conference on Coastal Engineering - July 2012 - Santander - Spain

LAGRANGIAN DRIFTER MODELLING OF AN EXPERIMENTAL RIP CURRENT

Leandro Suarez[1 2], Rodrigo Cienfuegos[2], Cristian Escauriaza[2], Eric Barthélemy[1] and Hervé Michallet[1]

Mean circulations on an experimental uneven bathymetry are studied using a numerical model. A non-uniform alongshore wave forcing on a uneven mobile bathymetry create mean circulation on a rip channel. A 2D numerical hydrodynamic model integrates the non-linear shallow-water equations taking intrinsically into account the energy dissipation by capturing broken waves in a shock-capturing finite-volume framework, also considering friction losses and an accurate description of the moving shoreline in the swash zone. The numerical model is validated with wave height and velocity experimental data.

Keywords: rip currents, non-linear shallow-water equations , lagrangian drifters

INTRODUCTION

When approaching the coast the propagation of random wave fields over uneven bathymetries triggers spatio-temporal non-uniformities in wave breaking, inducing energy dissipation gradients in the surf zone. These gradients generates mean currents, important for the nearshore, because of their influence in mixing, dispersion sediment transport and beach morphology.

Under close to normal wave incidence conditions, we often observe the appearance of rip channels (figure 1), which are strong offshore directed jets, that can be hazardous for swimmers.

In this work we aim at investigating and characterizing with a numerical model the nearshore circulation forced by a random wave field propagating over nonuniform bathymetry in comparison with 3D morphodynamic laboratory experiments of rip channels.

METHODS

Laboratory Experiments

The experiments (Michallet et al. [2010]) took place in the LHF (Sogréah/Grenoble-INP) wave tank (figure figure 2), with dimensions of $30 \times 30m^2$. The waves originate from a 60 parallel segmented piston-type wavemaker, of $50cm$ width each and covering the $30m$ tank width, allowing to produce a differential wave forcing between the segments.

To access the water levels and velocities during the experiment, three fixed capacitive wave gauges located at $X = 5.01\ m,\ Y = 8.17\ m$, $X = 5.03\ m,\ Y = 15.0\ m$ and $X = 5.05\ m,\ Y = 21.75\ m$, a moving sliding rail equipped with capacitive wave gauges can take cross-shore profile measures, and can provide information about longshore profiles as we move it alongshore.

Velocity measurements were obtained with three Acoustic Doppler Velocimeter (ADV), one fixed at $X = 10.00\ m, Y = 15.00\ m$, and two located on the sliding rail. The ADV provides the three components of the velocity at a fixed point located at 4-8 cm above the bed for the different measurement positions.

The acquisition frequency is set to 50 Hz for the capacitive wave gauges, and to 64 Hz for the ADV velocities.

A laser profiler mounted on a motorized trolley located on the sliding rail measured the beach morphology every day, in the bathymetric survey area, between $7.84\ m < x < 22.84\ m$ in the cross-shore direction, and $3.12\ m < y < 28.02\ m$ in the longshore direction, these area being limited by the sliding rail configuration.

The wave climate consisted in irregular shore-normal waves complying with a JONSWAP spectrum. Different wave conditions were tested during the experiment, but in this article we only focus on a wave sequence of 20 minutes concerning the numerical modelling ($H_{m0} = 18cm$, $T_p = 3.5s$).

In order to create an alongshore non-uniformity in the incoming waves, the wave amplitude in the center of the wave flume was damped, resulting in alongshore variations of H_{rms} as can be seen in figure 3. This alongshore non-unifomity enhanced a rip instability. We define H_{rms} as the root mean square of the wave sequence, and H_{m0} as the significant wave height estimated by integrating the wave spectrum in the full frequency range. The relation between these two terms is $H_{m0} = 1.416 H_{rms}$.

[1]LEGI UMR 5519, Domaine universitaire, BP 53, 38041 Grenoble cedex 9, France

[2]Departamento de Ingenieria Hidráulica y Ambiental, Pontificia Universidad Católica de Chile, Vicuña Mackenna, Chile

Figure 1: **Rip currents in the Tunquen Beach, Chile (from Martínez & Salinas [2009])**

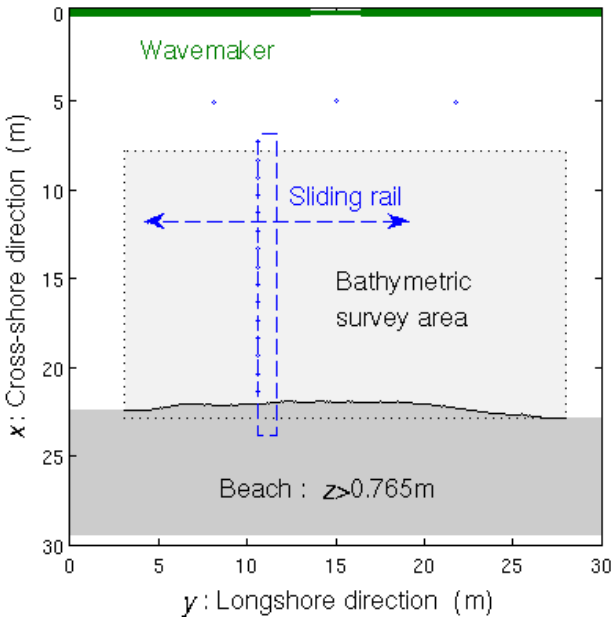

Figure 2: **Schematcis representation of LHF wave tank. the X axis corresponds to the cross-shore postion, the wavemakeris located at $X = 0\ m$, the shoreline is at $X \approx 22\ m$. The Y axis correponds to the alongshore position**

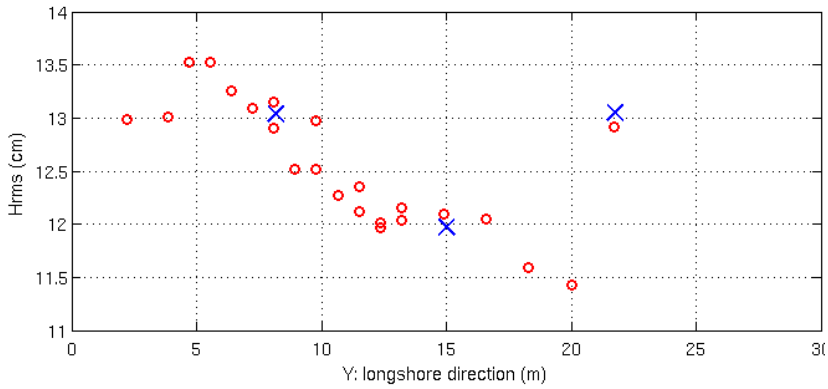

Figure 3: Incident wave climate: H_{rms} obtained by the capacitive wave gauges, located at $X = 5m$ from the wavemaker (blue X), and at $X = 7.30m$ (red O). We clearly observe the diminution of H_{rms} in the middle of the tank, result of the damped movement of the wavemaker located in the middle

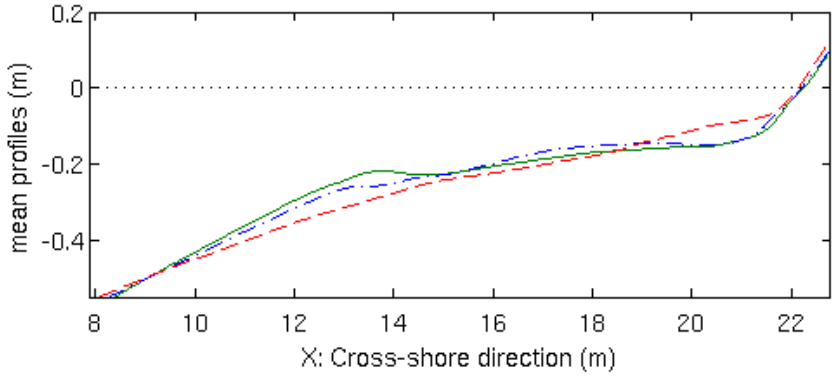

Figure 4: Mean cross-shore bathymetric profiles at $t = 0h00$ (green line), $t = 26h00$ (blue dash) and $t = 51h40$ (red dot dash). Still water level is represented in black dots.

We consider the initial beach at $t = 00 : 00$, when the wave forcing considered starts. This original bathymetry is relatively uniform alongshore, with a bar at $x \approx 13m$. The experiment we consider lasts for $51h40$, with a wave sequence of 20 minutes, repeated continuously. Every 20 minutes the sliding rail was moved alongshore to gather data in the whole survey area.

There are two phenomenons that explain the bathymetric evolution. The first one consist in the wave non-uniformity alongshore, which create rip channels and an heterogeneity alongshore. The second one is related to the mild wave conditions, and consist in an onshore sediment transport (figure 4). Therefore, during this experiment, the beach never reached a quasi-steady state. The characteristic time of this two phenomenon are different, the accretion occurring at a greater time scale than the alongshore non-uniformity.

The alongshore wave forcing non-uniformity result in an alongshore non-uniformity in the bathymetry, and the formation of rip channels (figure 5). At $t = 26h00$, we observe an onshore migration of the bar, as well as the formation of rip channels and shallow shoals. at $t = 51h40$, we observe the filling of the rip channels previously formed, as the accretion phase continues.

During the LHF experiment, rip currents characteristics were investigated with the use of Drifters measurements (Castelle et al. [2010]). Those drifters consisted in balloons filled with water, of diameter 5-10 cm

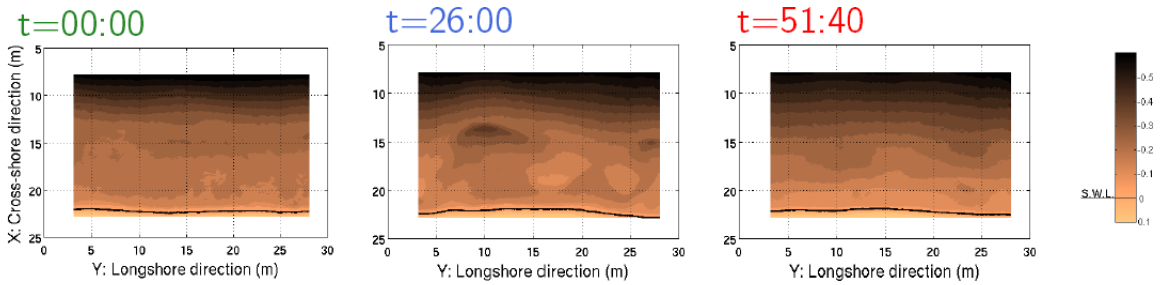

Figure 5: Beach Bathymetry at $t = 0h00$ (a), $t = 26h00$ (b) and $t = 51h40$ (c). The still water level is marked by a thick black line

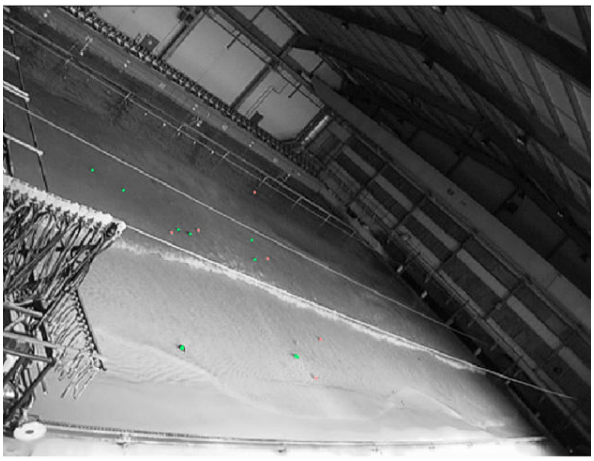

Figure 6: Sample of captured video images with drifters (from Castelle et al. [2010]).

deployed in the surf zone during the different runs, for a period of 30 to 60 minutes. The duration of the drifters experiments compared to the morphological time-scale of the experiment allows to assume a fixed bed during the drifters movement.

A shore-mounted video-camera was used to track the drifters during the wave forcing (see figure 6): The images obtained were then rectified to obtain the Cartesian coordinates of the drifters. The drifters movement were obtained by a semi-automatic method, by indicating manually the drifter position every 6 seconds.

Cross-shore and alongshore velocities were estimated from a linear interpolation in position and time of each sequential position of the drifter position at a 1 s time step over a 30 s duration, and mean currents were calculated.

NUMERICAL MODELLING

The numerical model is a 2D depth averaged model, using the Non-linear Shallow Water Equations (NSWE), valid for long waves. The main hypotheses of this set of equations are incompressibility, homogeneous fluid and hydrostatic pressure distribution.

The non-dimensional form of the NSWE can be written:

$$\frac{\partial Q}{\partial t} + \frac{\partial \overline{F}}{\partial x} + \frac{\partial \overline{G}}{\partial y} = S(Q) \tag{1}$$

where Q is the vector of hydrodynamic variables, function of h the water depth,u and v respectively the cross-shore and longshore depth-averaged velocities, $\overline{F}$ and $\overline{G}$ represent the flux vectors in each Cartesian

direction, and S is the source term vector considering bed slope and friction. The terms of the equation are defined as:

$$Q = \begin{pmatrix} h \\ hu \\ hv \end{pmatrix}, \overline{F}(Q) = \begin{pmatrix} hu \\ hu^2 + \frac{1}{2Fr^2}h^2 \\ huv \end{pmatrix}, \overline{G}(Q) = \begin{pmatrix} hv \\ huv \\ hv^2 + \frac{1}{2Fr^2}h^2 \end{pmatrix} \quad (2)$$

$$S(Q) = \begin{pmatrix} 0 \\ -\frac{h}{Fr^2}\frac{\partial z}{\partial x} - S_{fx} \\ -\frac{h}{Fr^2}\frac{\partial z}{\partial y} - S_{fy} \end{pmatrix}$$

with Fr as the Froude number, $\frac{\partial z}{\partial x}$ and $\frac{\partial z}{\partial y}$ as the bed-slope, S_{fx} and S_{fy} as the friction source term

The non-dimensional form of the NSWE, given by Equations (2), are solved using a finite volume well-balanced scheme, which incorporates separately the friction and bed-slope in the momentum source terms (Marche et al. [2007],Guerra et al. [2010]) . The numerical procedure consists of an initial step in which the friction source term in the momentum equations is incorporated employing a semi-implicit method. (Liang & Marche [2009])

In a second hyperbolic NSWE step, the variables are reconstructed at the cell interfaces and the fluxes are found through the solution of the Riemann problem at the cell interfaces using a non-conservative form of the governing equations. This methodology gives the numerical model the well-balanced property by considering the bed-slope in the spatial discretization schemes using a MUSCL type reconstruction method to reach a second order accuracy. The discretized form of the governing equations is integrated in time using a multi-stage Runge-Kutta scheme.

The drifters movement was modelled by a Lagrangian Particle Tracking model (Escauriaza & Sotiropulos [2011]). One assumption we make is that the drifters have no mass, and therefore no inertia forces, so they follow exactly the water flow. The governing equation of the model to obtain the particle trajectory is the following:

$$\frac{dx_i}{dt} = v_i \quad (3)$$

with x_i and v_i represent the ith component of the drifter position and velocity. Thanks to this Lagrangian Particle Tracking model, we are able to follow particles of water during the wave forcing.

The model boundary conditions are shown in figure 7: the boundaries 2 ($Y = 0\ m$) and 3 ($Y = 30\ m$) corresponds to closed boundaries, to reflect the closed basin. The boundary 4 ($X = 25\ m$) corresponds to a moving shoreline, with a dry/wet interface (Marche et al. [2007]). The boundary 1 ($X = 5\ m$) consider an absorption/generation condition (Cienfuegos et al. [2007], Mignot & Cienfuegos [2009])

For the present simulation, we considered a rectangular grid, with a regular spacing $\Delta x = \Delta y = 0.10m$, leading to roughly $60,000$ nodes.

The absorption/generation condition considers an incoming input wave height and solve a Riemann problem at the boundary, between the incoming wave height and the outgoing wave height, to find the proper wave height at the boundary. For the wave height input, the wave height near the wavemaker was not available. Therefore we considered the closest wave gauges to the wavemaker, that consisted in three static wave gauges located at 5 meters from the wavemaker, precisely at $X = 5\,m$, and $Y = 8.17\,m$, $Y = 15\,m$, $Y = 21.75\,m$ respectively. The wave input at each node is then interpolated alongshore, using the three wave gauges. Resulting wave forcing is shown in figure 8.

Concerning the incident condition wave, there is a difference between the experimental data, and the numerical model. The absorption/generation condition considers an open boundary, and the wave basin is closed one. The latter implies that reflection at the wavemaker is not included in the numerical model, so that resonant conditions due to the semi-enclosed basin in the experimental data will not be amplified in the simulations. The influence of the wavemaker can be seen mostly in the resonant modes of the basin, occurring at low frequency. For our numerical model, we prefer to use a high-pass filter and not to force incident wave conditions with infragravity energy. The model should be able to transfer energy from the short-wave band to the low frequency band, without resonant mode amplification.

MODEL VALIDATION

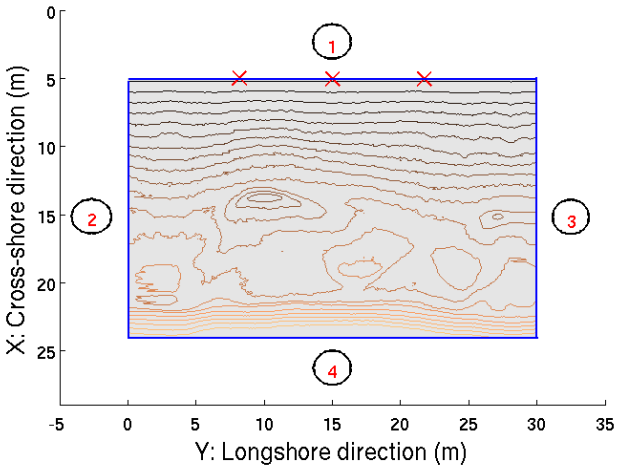

Figure 7: Boundary conditions of the numerical model. The red crosses mark the location of the wave gauges used for estimating the wave input

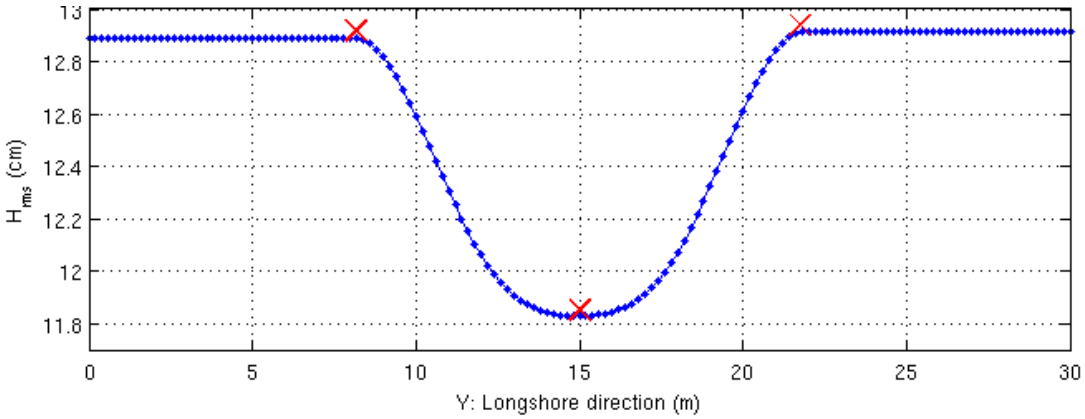

Figure 8: H_{rms} of experimental wave gauges at a distance $X = 5\ m$ from the wavemaker (red crosses), the thin blue line represent the H_{rms} of the interpolated input wave.

The model is validated with the bathymetry shown in figure 5 b) and represent a bathymetry with two rip channels formed, at $Y = 10\ m$ and $Y = 26\ m$.

We first validate the numerical model by checking the wave height statistical properties. To that end, we compare H_{rms} in a cross-shore profile, located at the middle of the basin alongshore, at $Y = 15\ m$. The spectra were calculated over a 20 minute sequence,at a 50 Hz frequency for both the wave gauges and the numerical data. The first spectrum 9 a), at a distance $X = 5\ m$ from the wavemaker, corresponds to the absorption/generation boundary condition of the numerical model. The spectrum indicates that the numerical model is able to reproduce the input wave height in the frequency band between $0.15\ Hz$ and $1\ Hz$. In the frequency band below $0.15\ Hz$, the differences in peak frequencies can be explained by the numerical boundary condition, where the reflection by the wavemaker is not included.

The second spectrum (figure 9 b)), at a distance $X = 10\ m$, shows a good concordance in the frequency band between $0.15\ Hz$ and $1\ Hz$, with some discrepancies under $0.15\ Hz$. The spectrum at $X = 15\ m$ is located after the wave breaking, and even though the frequency band around the peak frequency, between $0.15\ Hz$ and $0.4\ Hz$ is well reproduced, over $0.4\ Hz$ the numerical model shows less energy than the wave measurements. The spectrum at $X = 20\ m$ is located near the shoreline, and the peak frequency band of the numerical model is also concordant with the experimental data. The numerical model reproduce energy transfer to the low frequencies near the shoreline, in term of values, even though the peaks are not well reproduced.

We then consider a spectral H_{rms} cross-shore profile located a $Y = 15\ m$ alongshore (figure 10). The spectral H_{rms} represent the integral of the wave height spectrum, and is related to the energy dissipated by wave breaking. The first thing to note is that the experimental spectral H_{rms} at the open boundary at $X = 5\ m$ is reproduced by the numerical model. The numerical model shows an increase between $X = 5\ m$ and $X = 10\ m$, reaching its peak, and then decrease with a constant slope until $X = 19\ m$. The decrease in energy dissipation corresponds to energy dissipation by wave breaking. The experimental data show a slow increase, until $X = 12\ m$, and then a decrease with an almost constant slope. The main difference between the experiment and the model is the wave breaking location, in the numerical model it occurs $2\ m$ before, but the observed gradient in the spectral H_{rms} decrease is similar in both cases.

The numerical model is also validated using velocity observations. During the experiment, an Acoustic Doppler Velocimeter mounted on the sliding rail, measured the three component of the instantaneous velocities at a frequency of $64\ Hz$. The ADV was located at approximately $5\ cm$ from the bottom. The numerical model provides cross-shore and alongshore depth averaged velocities, therefore we can only compare the experimental and numerical velocities qualitatively, by assuming that the ADV is outside of the boundary layer and its measurements are representative of depth-averaged velocities.

We compare the mean velocities in an alongshore profile, at a distance $X = 14.71\ m$ of the wavemaker, where the wave breaking has already occurred. We observe (figure 11) that the numerical model reproduce the velocity variations. Concerning the cross-shore mean velocity, the maximum off-shore velocity are located at approximately $Y = 10\ m$, and $Y = 24\ m$ where the rip channels are located, as can be seen in figure 5. The alongshore velocities also present similarities in their variation, increasing between $Y = 0\ m$ and $Y = 12\ m$, and then decreasing for $Y > 12\ m$.

The comparison gives confidence to the numerical results, although they are only qualitative.

RESULTS

Using the numerical model, we estimated the mean velocities over a $1200\ s$ simulation, and compared these circulations with experimental data. Using Lagrangian drifters, Castelle et al. [2010] obtained mean circulation velocities for different bathymetries. We compare the results over the bathymetry at $t = 26:00$ in the middle of the accretion phase, where the beach is relatively non-uniform, with two rip-channels (figure 12).

The mean circulations modelled for the first bathymetry clearly show the two circulation cells of the rip current located at $Y = 11\ m$, that correspond to the ones that can be seen with the drifters circulation. The center of the circulation cells in the simulation, at $X = 15\ m$, $Y = 7\ m$ for one, $X = 16\ m$, $Y = 15\ m$ for the other, are similar to the position found using drifters. The rip channel with strong offshore mean velocities, of the order of $0.1\ m/s$, can be seen at $Y = 10\ m$. The order of magnitude of the rip channel velocity in the numerical model is equivalent to the drifter circulation speed in the rip channel.

In the region of the second rip channel at $Y = 26\ m$, there is no data available to determine the drifter circulation. The numerical model predicts in this area another rip, but the circulation cell is not clearly observed.

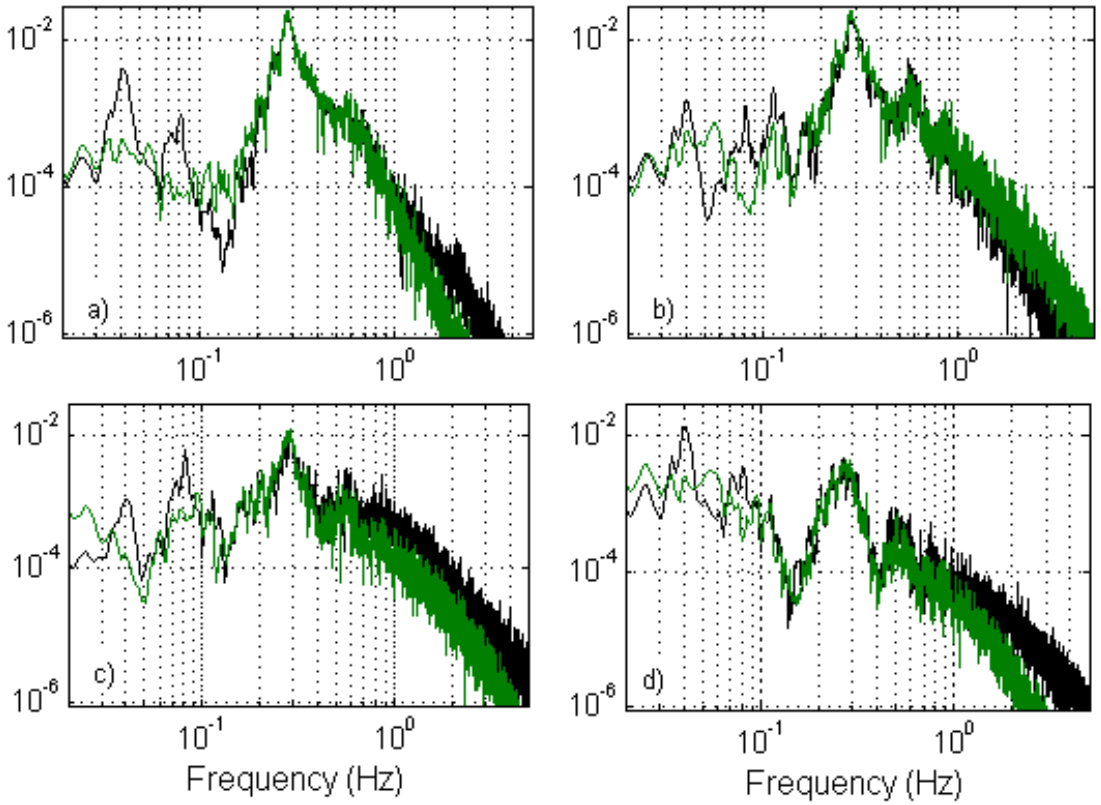

Figure 9: Spectral wave height of experimental wave gauges (black) and of the numerical model (green) at distances (a) $X = 5.01m$, (b)$X = 10.31m$, (c)$X = 15.31m$,(d) $X = 20.34m$, from the wavemaker. The alongshore distance is $Y = 15m$, at the center of the basin.

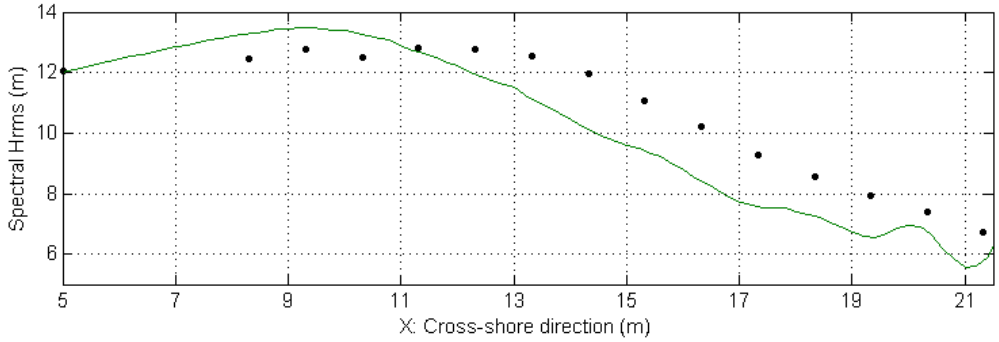

Figure 10: Cross-shore variation of Spectral H_{rms} from measured (black dots) and computed (green line) free surface time series, at an alongshore distance $Y = 15\ m$

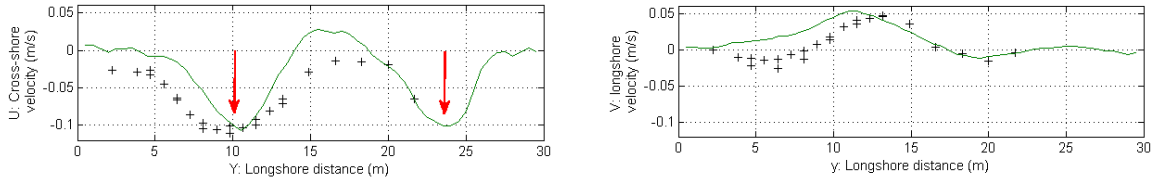

Figure 11: Cross-shore and alongshore mean velocity over the alongshore profile $Y = 15m$

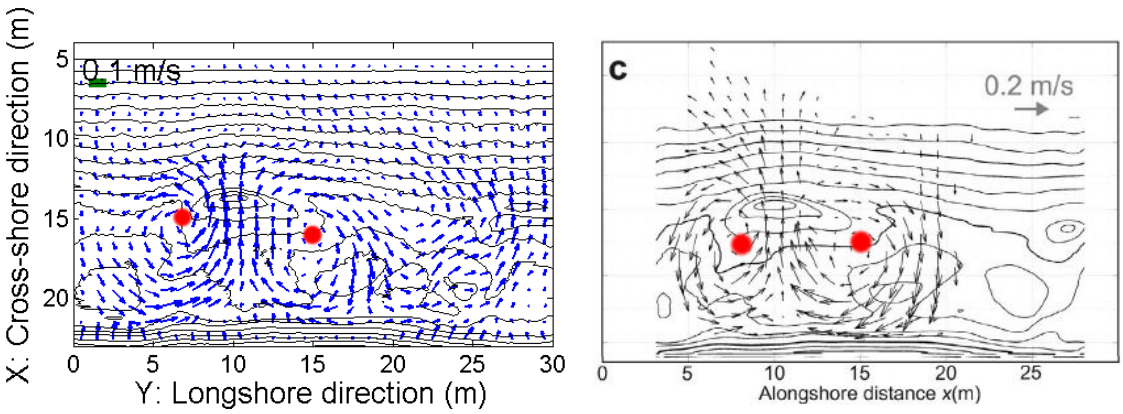

Figure 12: Mean velocity circulation over a 1200s simulation (left), and circulation estimated by drifters circulation (from Castelle et al. [2010], over a bathymetry at $t = 26 : 00$). The red dots indicates the position of the circulation cells center

Using the hydrodynamic results provided by the numerical model, we can model the movement of drifters induced by the wave forcing on the bathymetry at $t = 26 : 00$. The particle trajectories are smoothed in time over a 6s period, for clarity purpose:

$$x_0(t) = \frac{1}{6}\int_{t-3}^{t+3} x(t)dt\ , \quad y_0(t) = \frac{1}{6}\int_{t-3}^{t+3} y(t)dt\ ,$$

where $x(t)$,$y(t)$ represent the drifter position at time t, and $x_0(t)$,$y_0(t)$ represent the drifter mean position over 6 seconds at time t.

The particles initial positions are near the shoreline, at $X = 20\ m$, and between $4\ m < Y < 16\ m$. This correspond to the zone between the shoreline and the two cell circulations of the rip current. The smoothed trajectories of the particles (figure 13) clearly shows that almost all particles enter the rip channel, which is a preferred pathway. We then observe that some particles are caught in the recirculation cells, and realize several revolutions during the 1200s simulation time. Some particles are ejected from the circulation when passing through the rip channel.

CONCLUSION

A 2D numerical model can reproduce mean circulations on an uneven bathymetry, with a non-uniform wave forcing. There exist an early breaking in the numerical model, but the energy dissipation due to wave breaking is close to the experimental data, and the wave height spectra are well reproduced. There is a good overall qualitative agreement between experimental and numerical Lagrangian drifters.

By incorporating dispersion in the hydrodynamic numerical model, we could reproduce the shoaling before breking, and obatin better estimations of circulations. Concerning the Lagrangian drifters movement, by adding inertia to the particle movement, we could compare their movement with the lagrangian drifters experimental data, concerning drifters ejection in the rip channel.

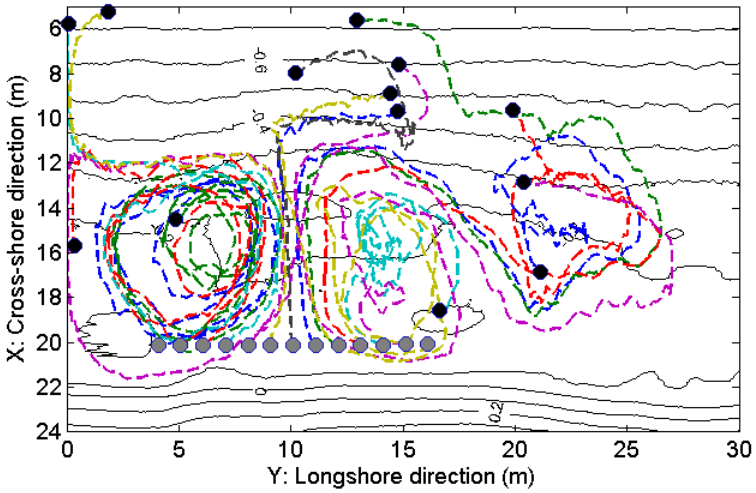

Figure 13: Drifter smoothed trajectories for a 1200 second simulation, over a bathymetry at $t = 26 : 00$. The grey dots represent the drifters' initial position, at $t = 0s$, the black dots represent their position at $t = 1200\ s$.

ACKNOWLEDGEMENTS

Project MODLIT (RELIEFS/INSU, SHOM-DGA) with additional financial support from COPTER (ANR) with help from SOGREAH Consultants

This research has been funded by the CONICYT grant from Conicyt, Chile and the LEGI Laboratory, France

REFERENCES

Castelle, B. Michallet, H., Marieu, V., Leckler, Dubardier, Lambert, Berni, C., Bonneton, Barthélemy, and Bouchette (2010). Laboratory experiment on rip current circulations over a moveable bed: Drifter measurements. *J. Geophys. Res.*, 115C12008.

Cienfuegos, Barthélemy, Bonneton (2007). A fourth-order compact finite volume scheme for fully nonlinear and weakly dispersive Boussinesq-type equations. Part II: Boundary conditions and validation. *Int. J. Numer. Methods in Fluids*, 531423-1455.

Escauriaza, C. and Sotiropoulos, F. (2011), Lagrangian model of bed-load transport in turbulent junction flows, *J. Fluid Mech*, 666, 36-76.

Guerra, M. Cienfuegos, R., Escauriaza, C., Rosa (2010), Modelación numérica 2D de crecidas extremas y zonas de inundación en coordenadas curvilíneas generalizadas *XXIV Congreso latinoaméricano de hidraúlica, Punta del Este, Uruguay*

Liang, Q. & Marche, F. (2009). Numerical resolution of well-balances shallow water equations with complex source terms. *Adv. Water Resour.*, 32873-884.

Marche, Bonneton, Fabrie, Seguin, (2007). Evaluation of well-balance bore-capturing schemes for 2D wetting and drying processes. *Int. J. Numer. Methods in Fluids*, 53867-894.

Martínez, C., Salinas S. (2006). Morfodinámica y evolución reciente de playa Tunquén, Chile central. *Revista BiologÃa y OceanografÃa Marina*, 44 (1) 203-215.

Michallet, Castelle, Bouchette, Lambert, Berni, Barthélemy, Bonneton, Sous (2010). Modélisation de la morphodynamique d'une plage barrée tridimensionnelle. *Proc. Journée Natl. Génie Côtier - Génie Civ.*, 11 379-386.

Mignot, E. & Cienfuegos, R. (2009). On the application of a Boussinesq model to river flows including shocks. *Coast. Eng.*, 5623-31.

Appendix F

Coastal Dynamics - July 2013 - Arcachon - France

Coastal Dynamics 2013
Paper No. 197

VORTICITY EVOLUTION AND RELATED LOW-FREQUENCY MOTIONS ON A RIP-CURRENT WITH A NON-UNIFORM ALONGSHORE WAVE FORCING

Leandro Suarez[1,2], Rodrigo Cienfuegos[1,3] Eric Barthélemy[2], Hervé Michallet[2]

Abstract

Experimental results on a rip formed over a heterogeneous beach with a mobile sandy bed are analyzed using a 2D depth-averaged Non Linear Shallow Water Equations (NSWE) model. The numerical model is validated comparing results with measured wave height values and velocity time series recorded by Acoustic Doppler Velocimeters (ADV) showing good agreement with experimental data. The numerical model is then used to produce a much longer simulation under the same conditions in order to obtain reliable information on the Very Low Frequency (VLF) band. By computing H_{rms} and U_{rms} in this frequency band we are able to observe pulsations that correlate with the slow evolution of the rip current, and the contribution of the VLF to the vorticity dynamics. We also show that a peak of energy exists in the VLF range in the position of the center of the recirculation rip cell, and the rip-current offshore velocity. We analyze model results using time series and spectral analysis of free surface, velocities and vorticity. A large amount of energy in the VLF range is observed in the vorticity generated in the surf zone. By looking closer at one rip-vortex, we show that the position of the center of the recirculation cell moves with time scales in the VLF spectral range. The rip-current offshore velocity pulsates at VLF frequencies.

Key words: Rip Current, Vorticity, Circulation, Very Low Frequency Motion

1. Introduction

Rip-currents are offshore oriented jets that originate in the surf zone, that constitute a hazard for swimmers, and represent one of the main mechanisms responsible for the mixing and circulation in the surf zone. The rips are created from the breaking of a low incident-angle random wave field over real topographies, which often enhance spatio-temporal variations of the breakpoint location due to the heterogeneity of beach bathymetry and/or the wave forcing. Under this situation, differential intensities in wave breaking energy dissipation can generate vertical vorticity at the scale of wave-averaged flows [Brocchini et al., 2004; Bonneton et al., 2010]. This wave generated vorticity then self-organizes in macrovortices with horizontal scales much larger than the local water depth. These macrovortices are responsible for producing these strong currents. In nature, the rips are always evolving, as natural wave conditions do, and the seabed is also changing due to sediment transport. Hence, there is a feedback between the wave forcing, the beach bathymetry and rip vorticity dynamics, which has not been completely clarified so far.

In this work we intend to study and analyze the generation and spatio-temporal evolution of macrovortices in a numerical rip and their link with Very Low-Frequency (VLF) motions in the surf zone. To that end, results from a 2DH numerical model, validated with experimental data of an established rip current, will be used to understand the connection existing between vorticity and VLF waves.

2. Methods

2.1. *Laboratory experiment*

[1]Departamento de Ingeniería Hidráulica y Ambiental, Pontificia Universidad Católica de Chile, Vicuña Mackenna 4860, casilla 306, correo 221, Santiago de Chile, Chile. lsuarez2@uc.cl; racienfu@ing.puc.cl
[2] Grenoble INP, UJF, UMR5519, LEGI, BP53, 38041 Grenoble Cedex 9, France. eric.barthelemy@legi.grenoble-inp.fr ; herve.michallet@legi.grenoble-inp.fr
[3] National Research Center for Integrated Natural Disasters Management CONICYT/FONDAP/15110017 program.

The experiment [Castelle et al., 2010; Michallet et al., 2013] took place in the LHF ("Laboratoire Hydraulique de France") wave basin, of dimension 30m x 30m, with a still water level of h_0=0.765m at the wavemakers. It is a scaled experiment, with a length similitude of 1/10, and a time similitude of 1/3 according to the Froude similarity.

The beach bathymetry was prepared with a mobile bed of fine sand sediment of median diameter d_{50}=0.166mm. The scale of the experiment allowed to fulfill the Rouse similitude, but not the Shields one, resulting in the presence of sand ripples. At the end of each day, the wave basin was slowly emptied, so as not to alter the beach bathymetry, and the beach morphology was measured by means of a laser profiler mounted on a motorized trolley located on the sliding beam, at a resolution of 1 cm cross-shore and 10 cm longshore, with a vertical accuracy of 1 mm. The bathymetric survey zone was restricted by the movement of the sliding rail, to the area between 7.84m<x<22.84m in the cross-shore direction, and 3.12m<y<28.02m alongshore (see Figure 1).

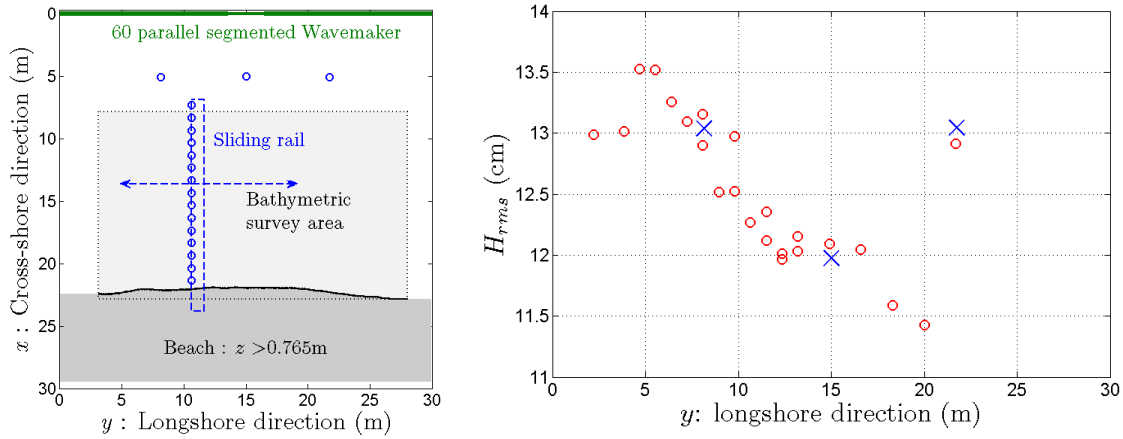

Figure 1. a) Schematic view of the wave basin from Michallet et al. [2013]. The capacitive wave gauges are represented as blue circles. The position x=0 corresponds to the position of the wavemakers. There are three fixed capacitive gauges, at x=5m. b) H_{rms} alongshore distribution, at x=5m (blue crosses) and at x=7.30m (red dots). The wave damping can be seen at the center of the wave basin at x=5m.

The water height was measured by capacitive wave gauges, three of them located permanently at the cross-shore position x=5m, and respectively at y=8.17m, y=15.0m, y=21.75m. Other wave gauges were located on a sliding rail in order to measure cross-shore transects of wave height evolution.

The basin is equipped on one side with 60 independent piston-type wavemakers that prescribe the shore-normal non-uniform alongshore-irregular wave forcing. The wave forcing is a mild wave climate JONSWAP spectrum with a significant wave height H_{m0}=18 cm and a peak period of T_p=3.5s. A damped motion of the wavemakers at the center of the wave front (see figure 1b) imposed a non-uniform alongshore wave forcing in the experiment, 20 minutes wave series were considered, and repeated continuously during each experiment. The wave damping can be seen at x=5m, as well as the H_{rms} heterogeneity at x=7.30m, due to the heterogeneity of the bathymetry.

At the beginning of the experiment, the bathymetry was relatively uniform, and the alongshore non-uniformity of the wave forcing established a differential breaking, that led to circulations in the wave basin. These circulations led to sediment transport and beach evolution, resulting in a 3D heterogeneous bathymetry (see Michallet et al. [2013] for details on the bathymetric evolution).

For the validation of the numerical model, we use the experimental results associated with a bathymetry that is relatively non-uniform alongshore, with the presence of two rip channels, located at y=10m and y=26m. We will specifically focus on the circulation cells and rip channel located at Y=10m (see figure 2 a). Even though after each run, the bathymetry was slightly modified in the experiment, for the numerical model we consider a fixed bathymetry, and observe the circulation induced by the wave forcing.

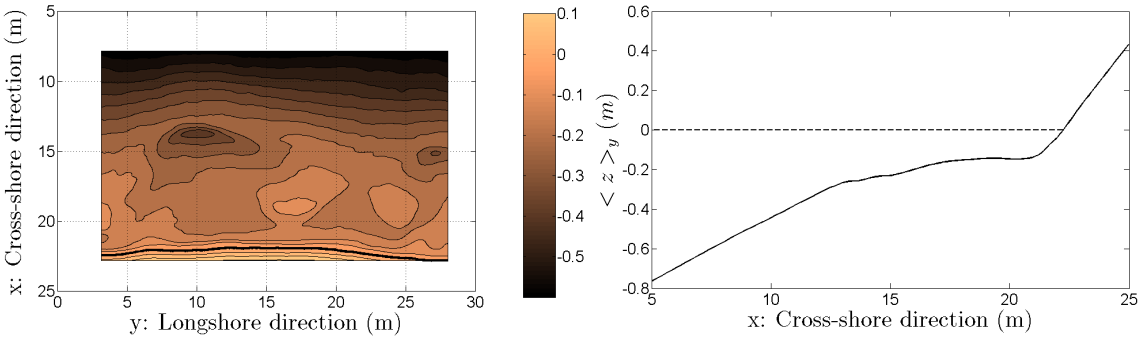

Figure 2. Left panel: bathymetry used for the validation of the numerical model. Right panel: mean alongshore profile as a thick line (-) and Still Water Level (SWL) represented as a dashed line (- -).

2.2. *Numerical modeling and validation*

The numerical simulations are performed using a 2D depth-averaged Non-linear Shallow Water Equations (NSWE) solver. The main hypotheses of this set of equations are incompressibility, homogeneous fluid and hydrostatic pressure distribution. This solver deals effectively with breaking energy dissipation, bed friction, and the run-up and run-down of waves and bores in the swash zone [Marche et al., 2007; Liang & Marche, 2009; Guerra et al., 2010].
The non-dimensional form of the NSWE can be written as:

$$\frac{\partial Q}{\partial t} + \frac{\partial \overline{F}}{\partial t} + \frac{\partial \overline{G}}{\partial t} = S(Q) \tag{1}$$

where Q is the vector of hydrodynamic variables, function of h, the water depth, u and v respectively the cross-shore and longshore depth-averaged velocities, F and G represent the flux vectors in each Cartesian direction, and S is the source term vector considering bed slope and friction. The terms of the equation are defined as:

$$Q = \begin{pmatrix} h \\ hu \\ hv \end{pmatrix} \qquad \overline{F}(Q) = \begin{pmatrix} hu \\ hu^2 + \frac{1}{2Fr^2}h^2 \\ huv \end{pmatrix} \qquad \overline{G}(Q) = \begin{pmatrix} hv \\ huv \\ hv^2 + \frac{1}{2Fr^2}h^2 \end{pmatrix}$$

$$S(Q) = \begin{pmatrix} 0 \\ -\frac{h}{Fr^2}\frac{\partial z}{\partial x} - S_{fx} \\ -\frac{h}{Fr^2}\frac{\partial z}{\partial y} - S_{fy} \end{pmatrix} \tag{2}$$

with Fr as the Froude number, z as the bed elevation, S_{fx} and S_{fy} as the friction source term.

The numerical simulation was performed on a rectangular grid, with grid spacing of Δx = 0.10m and Δy = 0.20m, leading to nearly 30,000 nodes. Concerning the bathymetry, the grid resolution is not sufficient to observe the ripples, therefore we smooth the bathymetry with a median mask of 50cmx50cm. This bathymetry is then interpolated to obtain a grid resolution of 0.1m x 0.2m.
For the model boundary conditions we consider the following: the lateral boundaries (y=0m) and (y=30m)

are set to closed boundaries; at the shoreline (x=25 m) a wet/dry moving boundary condition is employed [Marche et al., 2007]; at the offshore limit of the numerical model (x=5 m) an absorption/generation boundary condition is considered [Cienfuegos et al., 2007; Mignot and Cienfuegos, 2009].It is important to note, that at the offshore boundary, the incoming JONSWAP wave climate is prescribed without any low frequency energy content and with a random phase distribution (see figure 3).

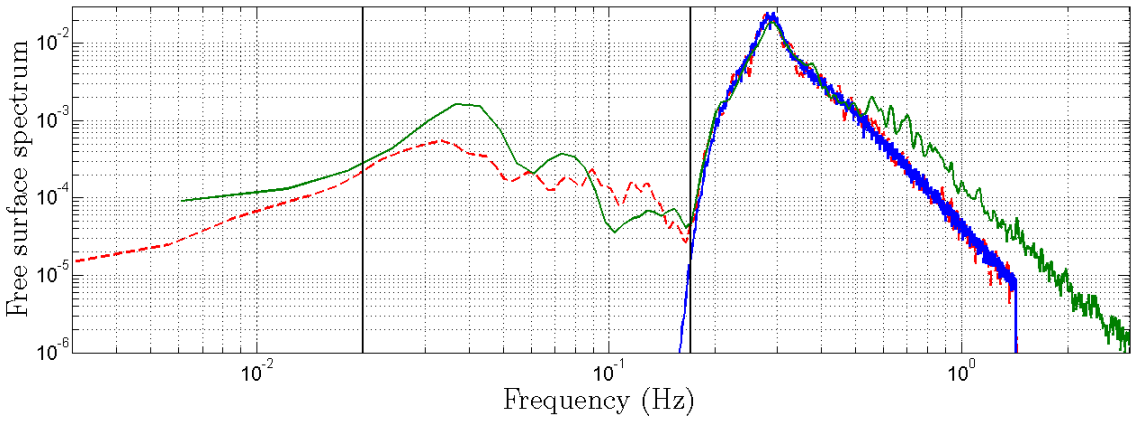

Figure 3. Synthetic JONSWAP spectrum of the free surface, used as boundary condition at x=5m (blue line); spectrum of the experimental data measured at x=5 m, y=8.71 m (green line); spectrum of the data obtained by the numerical model at x=5m, y=8m (dashed red line).

A complete recording of the measured free surface time series at the boundary of the domain was not available from the experiments. Hence for the boundary forcing, we consider the closest wave gauges to the wavemaker, precisely at x=5 m, and y=8.17 m, y=15 m, y=21.75 m respectively and interpolate the time series alongshore. The procedure also takes into account the signal prescribed to the wavemakers, which is a shore-normal JONSWAP spectrum with damped amplitude at the center (see figure 1b).

Low frequency energy will appear as a consequence of the wave propagation processes and partial reflections. In the experimental wave basin, the reflection of long waves at the wakemakers is unavoidable, while in the numerical model, long waves exit the domain freely. The latter will explain some of the differences observed in the structure of infragravity waves and resonant modes as discussed later.

To assess the confidence in the numerical model in reproducing wave propagation and low frequency motions, we perform a simulation of 1,200s, forcing the offshore boundary with the measured free surface time series (at x=5m) and the interpolation procedure already described. Experimental observations of wave gauges (free surface), and ADVs (velocities), are used for validation purposes.

The model hydrodynamics has been validated for mean circulations comparing its results with wave height data and velocity measurements [Suarez et al., 2012] showing that it is able to reproduce the energy dissipation gradients which are an important proxy for vorticity generation [Brocchini et al., 2004; Bonneton et al., 2010].

We now complement the validation of the model results by analyzing the free surface spectrum distribution in the alongshore direction at x=16m and in the cross-shore direction at y=6m and y=9m. These profiles were also chosen to obtain information at the vortex center of the recirculation cell, located near x=16m, y=6m (figure 4). For that we perform a simulation of 1,200s, forcing the offshore boundary with the measured free surface time series (at x=5m) and the interpolation procedure already described. Model results are compared with free surface time series measured by wave gauges, and velocity values recorded with ADVs.

In the longshore spectral distribution of figure 5, we observe that the signature of the JONSWAP spectrum is present in all the positions of the profile, in good agreement with experimental data. We also observe a trough in the spectrum at y=15m, at a frequency of 0.055 Hz, and three bumps alongshore, at a frequency of 0.125 Hz. This might correspond to the basin alongshore seiching but further analysis is required to confirm this. The numerical model succeeds in reproducing these features.

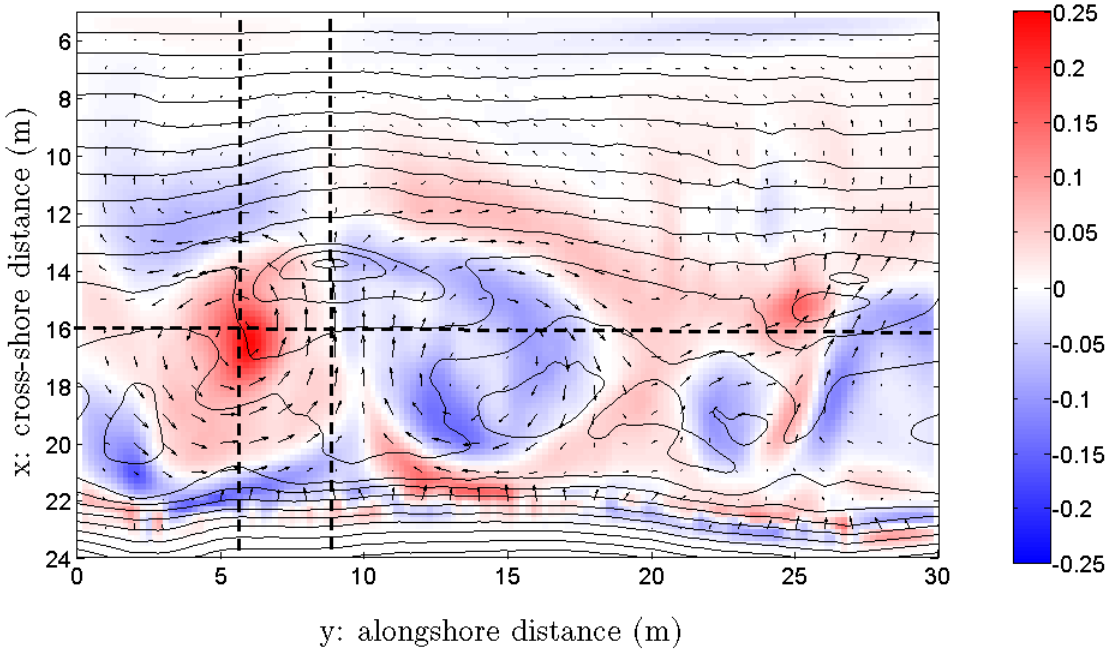

Figure 4. Mean circulation (arrows) and mean vorticity (color) in rad/s^{-1} induced by the non-uniform alongshore wave forcing and the bathymetry heterogeneity. The thin lines represent the isobaths, the wavemaker is located at the position x=0m. The dashed lines represent the cross-shore profile at y=6m (used in figure 6, 9, 10), y=9m (used in figure 10) and the longshore profile at x=16m (used in figure 5).

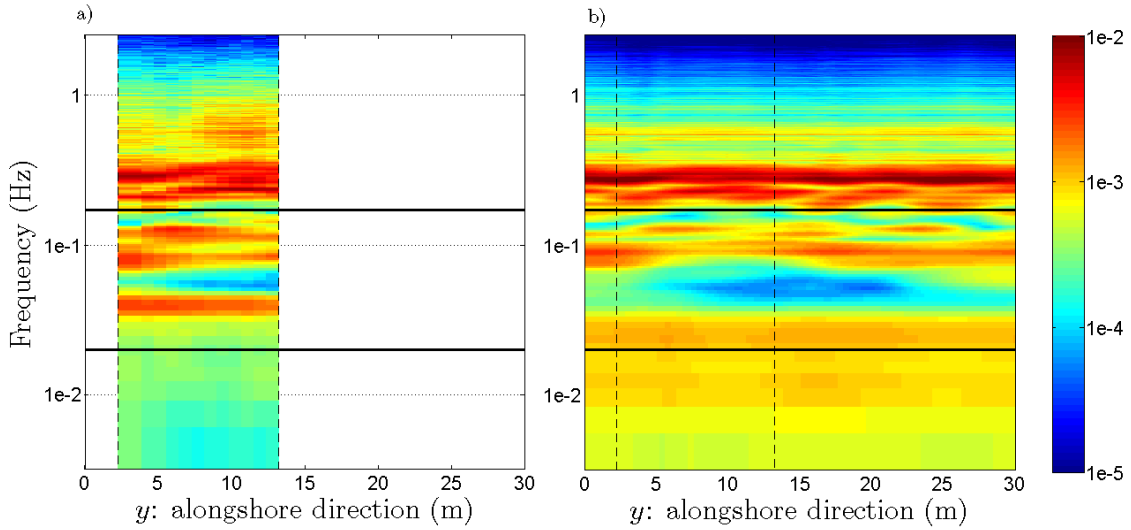

Figure 5. Longshore evolution of the free surface spectra, at x=16m (see figure 4). The thick black lines represents the limits between the VLF band and the infra-gravity band (f_1=2 10^{-2} Hz) and the limit between the infragravity band and the JONSWAP spectrum band (f_2=1.7 10^{-1} Hz). Color scale is logarithmic. a) experimental results, computation duration 1,200s, b) numerical model results, computation duration 1,200s.

Concerning the cross-shore spectral distribution of figure 6, the experimental results show clearly the basin cross-shore seiching, with a fundamental mode at frequency 0.04 Hz, lying in the infra-gravity band. This mode does not appear in the numerical model results since an absorbing/generating boundary condition is employed offshore, but overall the spectral distribution is similar in the experiment and in the numerical results. We also observe both, in the data and the model, a modal structure at a frequency of 0.07 Hz. This quasi-standing mode is confined between x=12m (the breaking point) and the shoreline. It exhibits anti-nodes at the breaking point and the shoreline and a node at x=18m. It might correspond to a quasi-standing long-wave oscillating between the breaking point and the shoreline.

Since the numerical model succeeds in representing the most important features of the complex wave and low frequency motion dynamics, we perform next simulations with longer time series using the same JONSWAP forcing, without energy content in the low frequencies and with a random phase distribution.

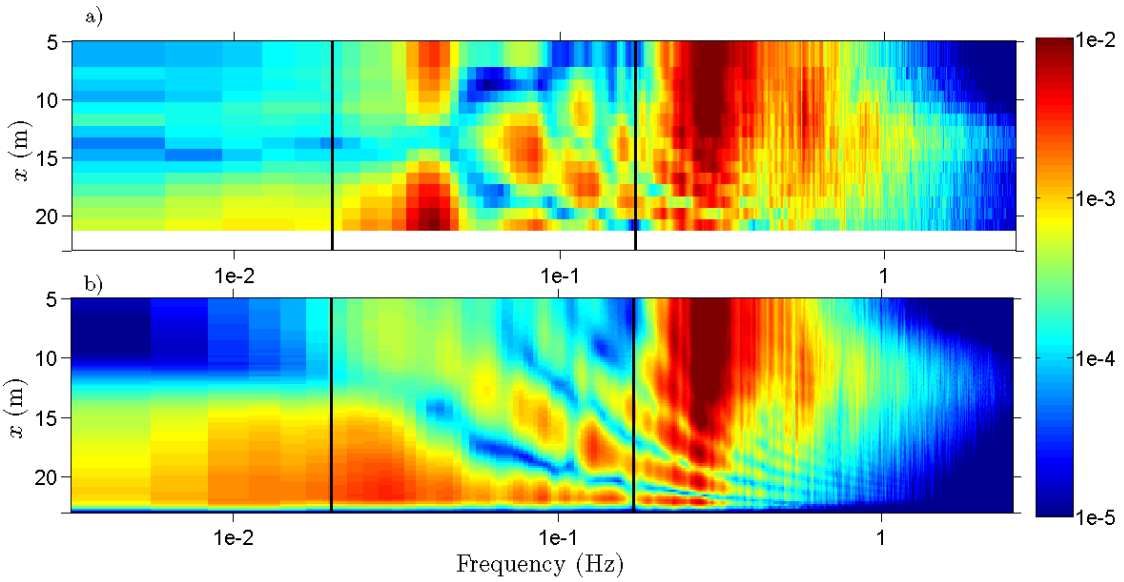

Figure 6. Cross-shore evolution of the free surface spectra, at y=6m (see figure 4). The thick black lines are described in figure 5. a) Experimental results, computation duration 1,200s. b) Numerical model, computation duration 1,200s. Color scale is logarithmic.

3. Analysis of VLF motions

To study low frequency motions at the VLF range, we must first define the different spectral ranges. As suggested by MacMahan et al. [2006]: the infra-gravity band is limited at periods between 25s and 250s, which would correspond in the experiment to periods between 8.3 s and 83 s defining a frequency band of 0.012 to 0.12 Hz. The VLF is limited to periods between 5-30 min, which in the experiment corresponds to periods between 100 and 600s defining a frequency band of 0.0017 to 0.01 Hz. In the present analysis, we choose the limit between the VLF spectral range and the infragravity one at f_1=2.10^{-2} Hz (T=50 s), this is substantiated by the clear separation observed in the experiments (see figure 6). The limit between infra-gravity and the JONSWAP spectrum is fixed at f_2=1.7.10^{-1} Hz (T=6 s).

3.1. *Spatial distribution of σ_η and U_{rms}*

Since we expect the rip currents to pulsate at frequencies lower than the wave period, in the infra-gravity-band and in the very low frequency band we decided to run the model during longer time than the experiment in order to obtain a better resolution in the VLF spectral range. We use a seaward boundary free

surface elevation time series complying a JONSWAP spectrum,of duration 10,800s.

To understand the spatial distribution of the different spectral range motions, we compute the energy content of free surface displacements and velocities. The latter is of course related to kinetic energy of these motions. The values of σ_η and U_{rms} in each spectral range (figures 7 and 8) are estimated as follows:

$$\sigma_\eta = \sqrt{\int_{band} S_{\eta\eta}(f)\,df} \tag{3}$$

$$U_{rms} = \sqrt{\int_{band} \left[S_{uu}(f) + S_{vv}(f)\right] df} \tag{4}$$

where $S_{\eta\eta}$ is the power density spectrum of the free surface displacements, S_{uu} and S_{vv} are the power density spectra of the cross-shore and alongshore velocity respectively and f is the frequency. We also estimate the total σ_η and U_{rms}, and obtain a spatial map of the total energy content in this variables (figures 7 and 8).

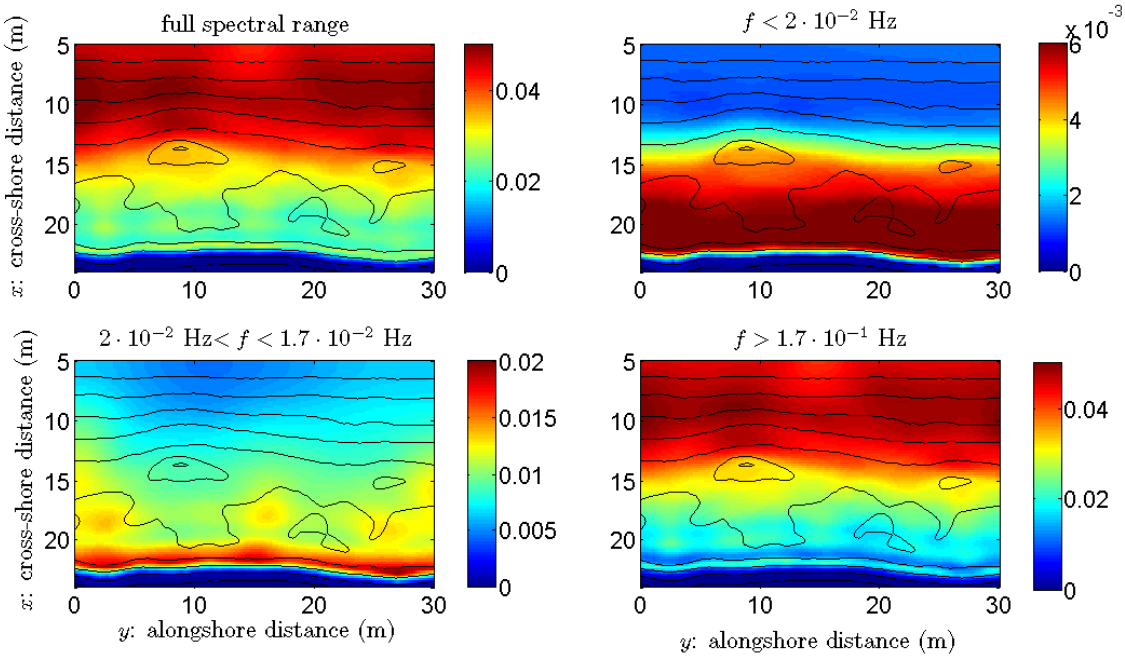

Figure 7. Free surface standard deviation σ_η estimated with equation (3). Upper left panel: integration on the full spectrum, Upper right panel: integration on the VLF band. Lower left panel: integration on the infragravity band. Lower right panel: integration on the JONSWAP high-frequency spectrum range.

In the total energy map of the free surface displacements σ_η (figure 7) we observe the wave damping in the middle, at x=5m and y=15m. At x~12m the differential breaking produced by the bathymetry combined with the wave forcing is clearly evidenced. This is the source of the vortices generation. In the VLF band, the free surface energy content is an order of magnitude lower and confined between the breaking point and the shoreline, between x=15m and y=21m. The JONSWAP high-frequency range is similar to the total spectral energy as one would expect. The infragravity band motion shows a spatial structure with higher amplitudes at the horns of the shore-attached bars located near x=18-19m. This could be explained by wave amplification over the shoal, since at the same location U_{rms} is also maximum (figure 8). Note that the VLF range motions are spatially uniform with no modal structures. This means that the very slow modulations of the mean water level by the VLF motion is uniform over the entire surf zone.

The U_{rms} maps are plotted in figure 8. The shoaling of the waves is evidenced in the total U_{rms} map where U_{rms} is the strongest near the breaking point. As for the free surface displacements, the high frequency range contribution to the total energy is dominant with a very close spatial structure between the

two. The maps show a significant amount (50%) of kinetic energy present in the infragravity band. As for the free surface displacement, the maximum energy is located on the horns of the shore-connected bars. The VLF kinetic energy is spatially distributed very differently compared to the free surface energy spectrum. High kinetic VLF energy is located at strong mean vorticity locations (figure 4) and does not seem to be forced by large-scale vortex stretching.

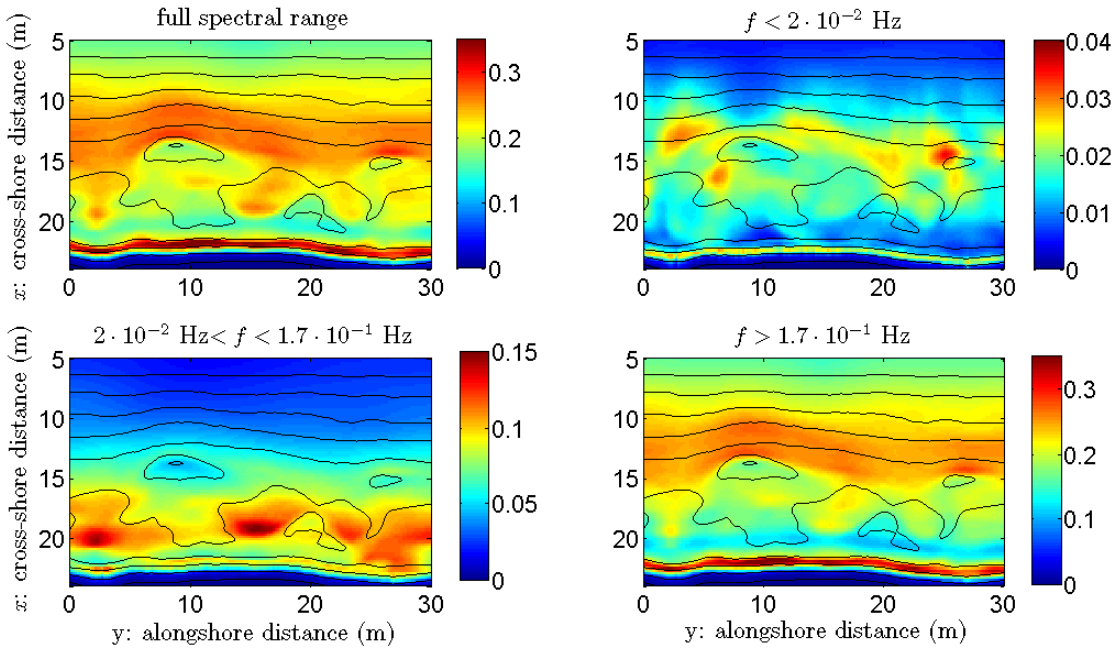

Figure 8. U_{rms} estimated with equation (4). Upper left panel: integration on the full spectrum, Upper right panel: integration on the VLF band. Lower left panel: integration on the infragravity band. Lower right panel: integration on the Jonswap high-frequency spectrum.

3.2. *Vorticity motions and variations*

It is now clear that VLF energy is present in the velocity field. Using the numerical results, we analyze hereinafter the vorticity dynamics focusing in low-frequency motions (pulsations).

Using the numerical model, we are able to observe the macrovortices formation and their evolution over 10,800 s. In Figure 4, the mean circulation and vorticity fields clearly show a strong dipole vortex and a rip current at x=16m, y=12m, and a smaller one at x=18m, y=25m. The rip current located at y=26 m is less obvious probably due to the interaction of the flow with the lateral boundary.

In order to characterize the vorticity fluctuations within the rip, a time-stack of vorticity in the same cross-shore profile (y=6m) is plotted in figure 9. In this plot, the individual wave-attached vorticity propagation is visible. The trajectories show how the waves slow down as they propagate towards the shore. More interestingly, coherent patterns of fluctuating motions at a time scale of 50 s, much longer than the peak frequency of the wave forcing, are observed.

Figure 9 shows the importance of low-frequency motions in the vorticity. A closer view in two cross-shore profiles (figure 10) at y=6m and y=10m, indicates that the vorticity appears in the cross-shore profile after the breaking. At y=6m, corresponding to the cross-shore profile centered in the recirculation cell, we observe in the infragravity band three ridges with the higher vorticity energy at x=13m, x=15m and x=18m. These three bands correspond to the center of the vortex, and the two arms that rotate slowly around it. We also observe in the VLF band some energy, much stronger within the vortex.

By using a 50 s low-pass filter to focus on the VLF motions (figure 11), we observe that the very slow modulations of the rip current velocity U_{rip} are highly correlated with the cross-shore evolutions of the

vortex center distance R_{vort}. The vortex's center position is defined as the location of the maximum vorticity within the region 14m<x<18m, 4m<y<7m, and R_{vort} represents the distance between this position to the mean vortex's center position. On the other hand, the wave energy measured by computing the H_{rms} on a 50 s running mean average does not seem to have a high correlation with the rip current cross-shore velocities. The latter would suggest to that the very slow motions of the macro-vortices are not caused by the modulation in the incident wave energy.

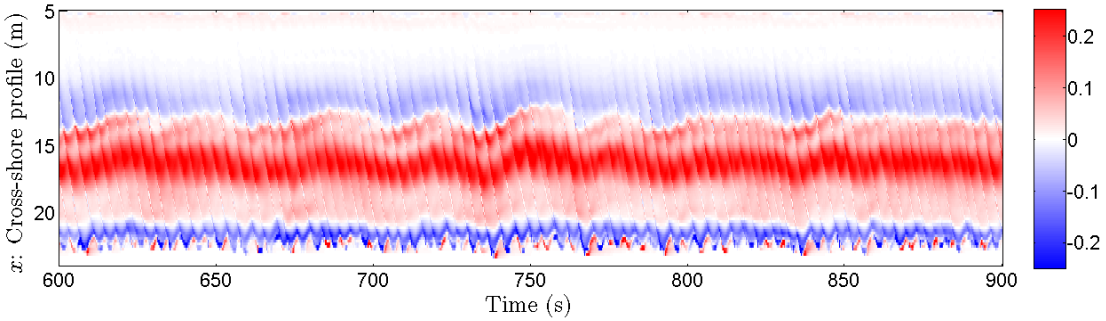

Figure 9. Vorticity time-stacks over a cross-shore profile at y=6m (see figure 4), in rad/s.

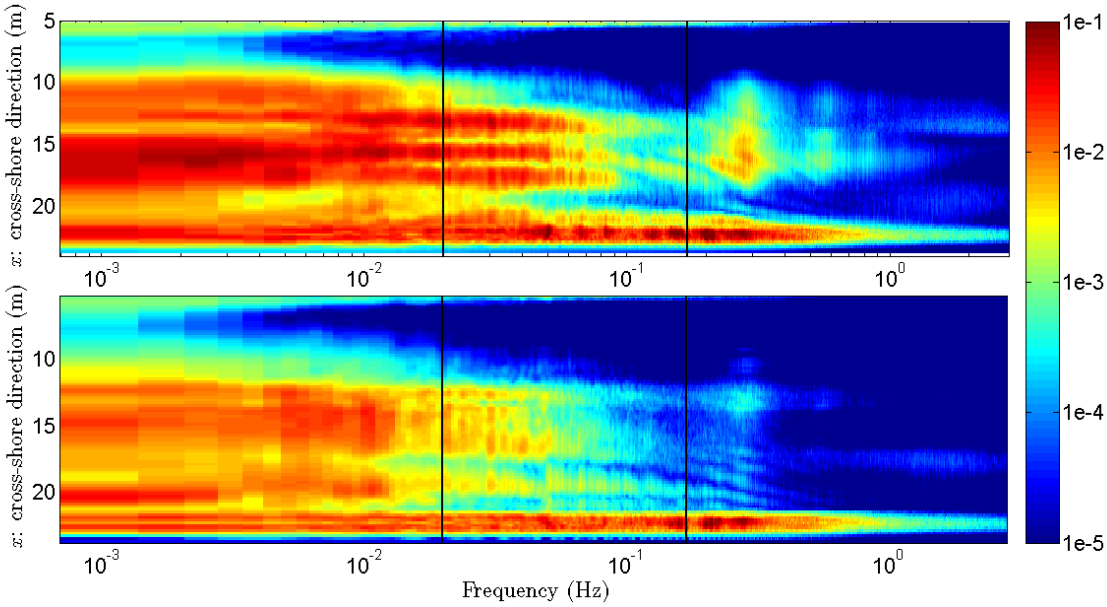

Figure 10. Cross-shore evolution of the vorticity spectra. Upper panel: profile at y=6m, passing through the center of the macro-vortex (see figure 4). Lower panel: y=9m, passing through the rip channel. Color scale is logarithmic.

4. Conclusion

After validating a 2DH numerical model on an experimental rip, we produce longer time series of free surface and velocities forcing the model with the same JONSWAP spectrum used in the experiment. This allows us to increase the spectral resolution in lower frequencies to investigate the VLF modulations of free surface, velocity and vorticity. The vorticity energy in the rip macro-vortices is mainly found in the VLF and infragravity bands. The numerical results also show that there is a slow modulation in the vortex position that is correlated with the VLF low-pass filtered cross-shore velocity. From time to time, a strong jump in offshore velocities in the rip channel is observed; the same behavior occurs in the time series of the

vortex position. Further investigation is required to better understand the link between wave forcing, bathymetric coupling, and the pulsations in the rip. On the other hand, the numerical results suggest that the low-pass filtered wave energy does not correlate with the very slow modulation of the macro-vortex.

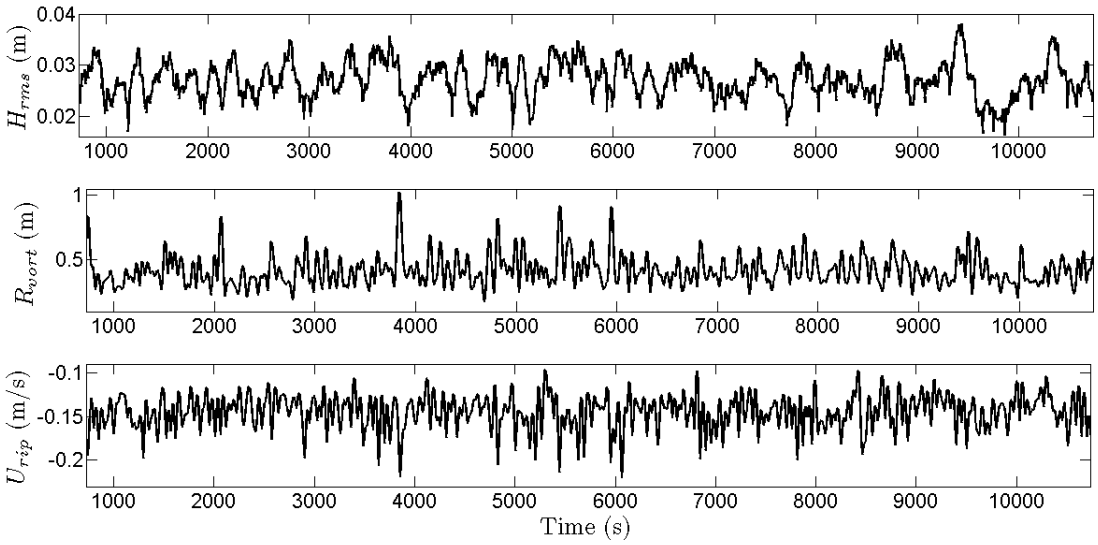

Figure 11. Upper panel: low-pass filtered (50 s running mean average) H_{rms} (m/s). Middle panel: 50 s low-pass filtered cross-shore position of the vortex center with regard to the mean cross-shore position center (m). Lower panel: 50 s low-pass filtered cross-shore velocity within the rip channel (m/s), x=16m, y=9m. Offshore values are negative.

Acknowledgements

The technical support of SOGREAH/ARTELIA is gratefully acknowledged. The project was partially funded by MODLIT (RELIEFS/INSU, SHOM-DGA) with additional financial support from COPTER (ANR). Partial support was provided by Fondecyt 1120878. The first author would like to acknowledge the support of CONICYT of Chile through PhD grant No.21100415.

References

Bonneton P., Bruneau N., Marche F., Castelle B.,(2010), Large scale vorticity generation due to dissipating waves in the surf zone, *Discrete and continuous dynamical systems – Series B*, 13, 729-738

Brocchini M., Kennedy A., Soldini L., Mancinelli A., (2004), *Topographically controlled, breaking-wave induced macro-vortices. Part 1. Widely separated breakwaters*. Journal of Fluid Mechanics, 507, pp 289-307

Castelle, B., Michallet H., Marieu V., Leckler F., Dubardier B., Lambert A., Berni C., Bonneton P., Barthélemy E., and Bouchette F. (2010), *Laboratory experiment on rip current circulations over a moveable bed: Drifter measurements*, J. Geophys. Res., 115, C12008, doi:10.1029/2010JC006343.

Guerra, M.; Cienfuegos, R.; Escauriaza, C.; Rosa, E., *Modelación numérica 2D de crecidas extremas y zonas de inundación en coordenadas curvilíneas generalizadas,* XXIV Congreso latinoaméricano de hidraúlica, Punta del Este, Uruguay

MacMahan, J.H., Thornton, E.B., Reniers, A.J.H.M., 2006. Rip current review. Coast. Eng. 53, 191–208. doi:10.1016/j.coastaleng.2005.10.009.

Marche F., Bonneton P., Fabrie P.,Seguin N.,(2007), *Evaluation of well-balanced bore-capturing schemes for 2D wetting and drying processes,* International Journal for Numerical Methods in Fluids, 53, 5, 867-894

Suarez L., Cienfuegos R., Escauriaza C., Barthélemy E., Michallet H. (2012) *Lagrangian Drifter Modelling of an Experimental Rip Current,* Proceedings of the 33rd International Conference on Coastal Engineering.

H. Michallet, B. Castelle, E. Barthélemy, C. Berni, P. Bonneton, (2013). Submitted to J. Geophys. Res. (Earth Surface). *Physical modeling of three-dimensional intermediate beach morphodynamics.*